

AD_____

Award Number: W81XWH-05-1-0041

TITLE: Prostate Dose Escalation by Innovative Inverse Planning-Driven IMRT

PRINCIPAL INVESTIGATOR: Lei Xing, Ph.D.

CONTRACTING ORGANIZATION: Stanford University
Stanford, CA 94305-5401

REPORT DATE: November 2007

TYPE OF REPORT: Annual

PREPARED FOR: U.S. Army Medical Research and Materiel Command
Fort Detrick, Maryland 21702-5012

DISTRIBUTION STATEMENT: Approved for Public Release;
Distribution Unlimited

The views, opinions and/or findings contained in this report are those of the author(s) and should not be construed as an official Department of the Army position, policy or decision unless so designated by other documentation.

REPORT DOCUMENTATION PAGE				Form Approved OMB No. 0704-0188	
Public reporting burden for this collection of information is estimated to average 1 hour per response, including the time for reviewing instructions, searching existing data sources, gathering and maintaining the data needed, and completing and reviewing this collection of information. Send comments regarding this burden estimate or any other aspect of this collection of information, including suggestions for reducing this burden to Department of Defense, Washington Headquarters Services, Directorate for Information Operations and Reports (0704-0188), 1215 Jefferson Davis Highway, Suite 1204, Arlington, VA 22202-4302. Respondents should be aware that notwithstanding any other provision of law, no person shall be subject to any penalty for failing to comply with a collection of information if it does not display a currently valid OMB control number. PLEASE DO NOT RETURN YOUR FORM TO THE ABOVE ADDRESS.					
1. REPORT DATE (DD-MM-YYYY) 01-11-2007		2. REPORT TYPE Annual		3. DATES COVERED (From - To) 1 Nov 2006 – 31 Oct 2007	
4. TITLE AND SUBTITLE Prostate Dose Escalation by Innovative Inverse Planning-Driven IMRT				5a. CONTRACT NUMBER	
				5b. GRANT NUMBER W81XWH-05-1-0041	
				5c. PROGRAM ELEMENT NUMBER	
6. AUTHOR(S) Lei Xing, Ph.D. E-Mail: lei@reyes.stanford.edu				5d. PROJECT NUMBER	
				5e. TASK NUMBER	
				5f. WORK UNIT NUMBER	
7. PERFORMING ORGANIZATION NAME(S) AND ADDRESS(ES) Stanford University Stanford, CA 94305-5401				8. PERFORMING ORGANIZATION REPORT NUMBER	
9. SPONSORING / MONITORING AGENCY NAME(S) AND ADDRESS(ES) U.S. Army Medical Research and Materiel Command Fort Detrick, Maryland 21702-5012				10. SPONSOR/MONITOR'S ACRONYM(S)	
				11. SPONSOR/MONITOR'S REPORT NUMBER(S)	
12. DISTRIBUTION / AVAILABILITY STATEMENT Approved for Public Release; Distribution Unlimited					
13. SUPPLEMENTARY NOTES					
14. ABSTRACT: The goal of this project is to develop innovative inverse planning techniques for prostate radiation therapy. In the last funding period significant progress has been made toward the goal of the project. In the past funding year, the PI group has contributed greatly to advance prostate radiation therapy techniques. A few important milestones have been achieved toward the goal of the project. These include: (i) Investigated intrafraction prostate motion and its influence on prostate radiation therapy; (ii) Developed method for auto-propagation of contours from planning CT to CBCT for on-line/off-line inverse planning; (iii) Established a novel technique to enhance on-board cone-beam CT and to effectively reduce the radiation dose incurred in the scanning process; (iv) Setup a framework for adaptive inverse planning based on a voxel specific penalty scheme; (v) Evaluated the feasibility of using on-board cone-beam CT for on-treatment dose calculation and developed a reliable electron density mapping algorithm for CBCT-based IMRT optimization; and (vi) Provided a robust procedure for retrospective dose reconstruction in IMRT dose delivery. These works are both timely and important and should have measurable impact on prostate cancer management.					
15. SUBJECT TERMS Prostate Cancer					
16. SECURITY CLASSIFICATION OF:			17. LIMITATION OF ABSTRACT UU	18. NUMBER OF PAGES 223	19a. NAME OF RESPONSIBLE PERSON USAMRMC
a. REPORT U	b. ABSTRACT U	c. THIS PAGE U			19b. TELEPHONE NUMBER (include area code)

Table of Contents

	Page
Introduction.....	4
Body.....	4
Key Research Accomplishments	7
Reportable Outcomes.....	8
Conclusions.....	9
References.....	10
Appendices.....	11

I. INTRODUCTION

This Idea Award (PC040282/W81XWH05-1-0041), entitled “Prostate Dose Escalation by Innovative Inverse Planning-Driven IMRT”) was awarded to the principal investigator (PI) for the period of Nov 1, 2004—Oct. 31, 2007. This is the annual report for the third funding period (Nov. 1, 2006 – Oct. 31, 2007). Due to a delay in having a postdoctoral fellow with right training background on board during the course of the project, an one year no-cost-extension was filed and granted by DOD. The scheduled completion date will be Oct. 31, 2008.

The goal of this project is to improve current prostate IMRT by establishing a novel inverse planning framework. Under the generous support from the U.S. Army Medical Research and Materiel Command, the PI’s research team has made significant progress toward the general goal of the project and contributed greatly to prostate cancer research. A number of significant conference abstracts and refereed papers have been resulted from the support. The preliminary data obtained under the support of the grant has also enabled the PI to start new research initiatives. In this report, the past year’s research activities of the PI are highlighted.

II. RESEARCH AND ACCOMPLISHMENTS

We have worked on several important projects in the past year to improve the existing prostate radiation therapy. These can be categorized as: (1) Intrafractional prostate motion in hypofractionated prostate radiation therapy¹ (Appendix 10); (2) Automated contour propagation for prostate plan re-optimization²⁻⁴ (Appendices 3, 8, 9 & 11) and image registration (Appendices 5, 6 & 9); (3) Adaptive prostate radiation therapy planning^{5, 6} (Appendices 1 & 2); (4) dose reduction and image enhancement of CBCT for adaptive radiation therapy⁷⁻⁹ (Appendix 13); and (5) IMRT dose reconstruction^{10, 11} (Appendices 7 & 12). By using the new inverse planning techniques, we can now significantly improve the radiation dose distributions as compared with the current practice. The study should have widespread impact on clinical prostate IMRT in the future.

Intrafraction prostate motion: Intra-fractional organ motion has long been recognized as one of the major limiting factors of prostate dose escalation in conformal radiation therapy and IMRT¹²⁻¹⁴. A detailed knowledge of prostate motion would help to understand the nature and degree of the adverse influence of the uncertainty and provide guidance in dealing with the issue. The known motion can also be included into inverse planning process to minimize its adverse dosimetric influence^{15, 16}. We have recently studied

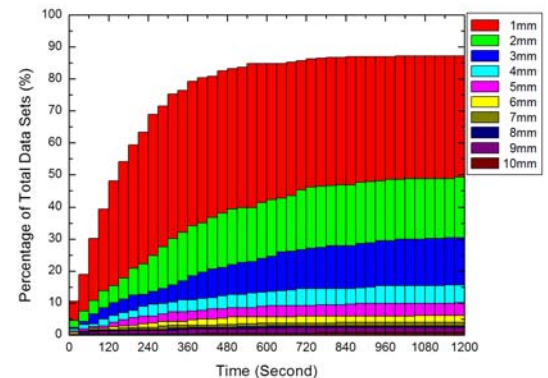


Figure 1 A plot of the percentage of data sets for the prostate target to move more than 1mm (red), 2mm (green), 3mm (blue), 4mm (light green), 5mm (magenta), ..., for sampling durations of 30 s, 60 s, 90 s, 120 s,

the intra-fractional prostate motion in the hypofractionated treatments of 21 prostate cancer patients¹ (Appendix 10). During the treatment of these patients, a stereoscopic kV X-ray system was used to obtain the position of the prostate target through the monitoring of implanted gold fiducial markers. During the treatment, the deviation is examined every 30 - 40 s. It was found that almost all these cases show a certain degree of prostate movement. The spread of prostate position increases as the time elapses. As summarized in figure 1, at 30 s, a motion larger than 2mm exists in about ~5% of data sets. The percentage is increased to 8%, 11%, and 14% at 60s, 90 s, and 120 s, respectively. Our study emphasizes the importance of real-time imaging during prostate radiation therapy, in particularly a hypofractionated treatment. We are working on effective means of compensating the intra-fractional movement to ensure adequate dose coverage of the tumor target.

Automated contour propagation and deformable image registration: automated contour propagation is a critical step in online or offline IMRT planning based on the on-treatment cone beam CT images. We have investigated a few automated contour propagation strategies from pCT to CBCT¹⁷. This includes (i) deformable registration of two input images¹⁸; (ii) sparse volume sampling along manually outlined contours²; and (iii) warping of narrow band encompassing the manually segmented contour with and without the incorporation of *a priori*

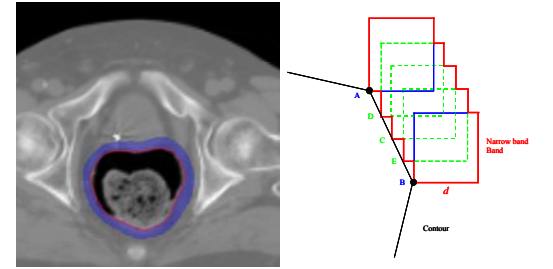


Fig. 2 A sketch of narrow band surrounding a rectal contour (left). Right: a band construction connecting two vortices A and B.

tissue features (see Fig. 2 for a sketch)^{2, 3, 4, 19}. The narrow band approach outperforms all existing methods in computational efficiency (speed and memory usage), accuracy and robustness, especially if correspondence between two images acquired at different times do not exist due to variations in the image content (such as a change in rectal filling). We found that the incorporation of pre-associated tissue features identified by SIFT method greatly enhances the performance of warping algorithm and makes reliable contour mapping possible for some challenging cases. In Fig. 3 we show the results of a digital phantom experiment, in which an image (1a) is intentionally deformed into two dramatically different ones (3b & 3c). Overall, the mapped contours can capture the main features of the two dramatic deformations, and conforms to the rectum boundaries. In obtaining the result, a total of 52 control points were identified by the SIFT calculation. For clarity, a selection of the control point associations is displayed in Fig. 3. The number of control points identified here is far more than that commonly used in regular TPS calculation, allowing an improved deformable warping of the narrow band. The displacement field derived by TPS is shown in Fig. 3c together with the known displacements (Fig. 3d). The subtraction of the two displacement fields (Fig. 3e) shows that the average deviation of the displacement is less than 1.6mm. The feasibility study here shows significant promise of the SIFT-based narrow band approach for auto-segmenting CBCT images. This work has been submitted to International Journal of

Radiation Oncology, Biology, Physics for consideration of publication. The postdoc who carried out the study were recently received the ASTRO Basic Science Travel Award for this work.

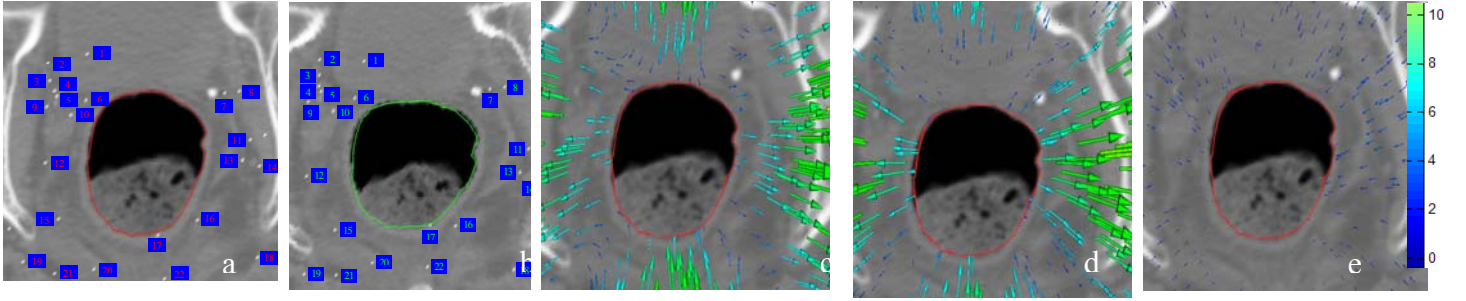


Fig. 3, Left two panels: control points identified by SIFT in a 2D image and its deformation. The TPS-derived displacement field, intentionally introduced displacement field and their subtract are shown in 3rd, 4th, and 5th panel, respectively.

Strategies of CBCT dose reduction and quality enhancement: Onboard CBCT imaging²⁰⁻²² plays an essential role in the success of adaptive prostate IMRT. We are developing methods for enhancing the performance of CBCT^{7, 9} and reduce radiation dose incurred during frequent CBCT scanning (Appendix 13). To assure the functionality of the system we have also developed an image phantom and software tool for the onboard imaging system (Appendix 6). Generally, the patient has already had a planning CT (and possibly one or more CBCT) before an on-treatment CBCT is acquired. The earlier imaging data can be utilized as *a priori* knowledge to enhance the CBCT images in subsequent scans and to reduce the radiation dose in routine CBCT imaging process. Previously, we have successfully demonstrated that, the image quality of a 4D CT or 4D PET phase can be improved significantly by incorporating measured noise spectrum and “borrowing” information from other phases, providing a viable solution to a longstanding problem of the competition between spatial and temporal resolutions²³. Application of this strategy to CBCT significantly reduces the view-aliasing artifacts and leads to high quality images for therapeutic guidance⁷⁻⁹. Our hope here is that the information from previous pCT or CBCTs can be incorporated effectively through deformable registration in image or even raw data space⁵ so that the radiation dose of CBCT acquisition and/or image quality can be improved dramatically. This will greatly facilitate the future CBCT-based dose calculation, image registration and IMRT planning.

Retrospective IMRT dose reconstruction: With the development of highly conformal radiation therapy techniques such as IMRT and BCRT, how to accurately deliver the high radiation dose to the prostate target(s) and verify the dose distribution while sparing the sensitive structures becomes a major concern. Study has been carried out to reconstruct prostate IMRT dose distribution using CBCT and planned fluence maps from the planning system²⁴. This maneuver is based on the assumption that the planned fluences can be faithfully realized by the delivery system. In reality, there might be errors associated with the leaf motion and fractional MU delivery such as overshoot, undershoot segmental MU, dropped segments, and beam delivery during leaf motion²⁵. A more pragmatic approach is to use the fluences actually delivered for the treatment; therefore, we propose to retrieve the MLC log-file which records the leaf position of each individual leaf and the fractional MU status during

the actual delivery from the MLC workstation and derive the delivered fluence map from it. We have recently established a methodology and procedure to reconstruct the dose based on a series of on-treatment CBCTs and the log-files taking into account the changes of the patient's anatomy (Appendices 7 & 12). A manuscript reporting this work has now been published¹¹. In this study, the respective MLC log-files were retrieved and converted into fluence maps using a preliminary fluence model²⁶. The dose was then reconstructed on the corresponding CBCT. The reconstructed dose distribution, dosimetric endpoints, and DVHs were compared to the original plans. Dosimetric changes as large as 10% were observed for some critical organs due to the anatomic variations caused by setup inaccuracy, organ deformation, tumor shrinkage or weight loss or both, re-emphasizing the need for adaptive replanning. The dose reconstruction is valuable to examine the actual dose delivered to the patient. It also affords an objective dosimetric basis for the clinical decision on whether a re-planning is necessary during the course of treatment, and provides a valuable platform for heading toward ART.

Voxel specific penalty scheme based inverse planning for adaptive prostate radiation therapy: To ensure adequate dose coverage of the prostate while sparing the rectum and bladder in the presence of daily anatomical change in prostate IMRT, we are developing an adaptive inverse planning strategy for improved prostate radiotherapy. Newly emerged onboard CBCT is used to acquire the volumetric anatomical information of a patient prior to treatment on a routine basis. With the image registration and contour mapping as described above, an IMRT treatment plan is adaptively modified with consideration of organ deformation and delivered doses. For the margins used in current prostate IMRT, we found that seminal vesicle, bladder and rectum doses benefited most from the adaptive therapy basis. In addition, our study suggested that correcting the patient's daily setup just through the translation and rotation is often not enough and accounting for the organ deformation is important, especially if the target margin is to be reduced for dose escalation or for hypofractionated treatment. The new optimization framework has recently been published in *Physics in Medicine and Biology*⁶ (Appendix 2). We are continuing this effort in incorporating the voxel specific penalty into the plan re-optimization process²⁷. We anticipate that the voxel specific penalty will not only substantially improve the dose distribution, but also provide an effective tool for near real-time modification/fine-tuning of the treatment plan. This new adaptive IMRT scheme will substantially improve the current IMRT treatment plan optimization and dose delivery process.

III. KEY RESEARCH ACCOMPLISHMENTS

- Investigated intrafraction prostate motion and its influence on prostate IMRT.
- Developed method for auto-propagation of contours from planning CT to CBCT for on-line/off-line inverse planning.

- Established a novel technique to enhance on-board cone-beam CT and to effectively reduce the radiation dose incurred in the scanning process.
- Setup a framework for adaptive inverse planning based on a voxel specific penalty scheme.
- Provided a robust procedure for retrospective dose reconstruction in IMRT dose delivery, which can be incorporated as part of the feedback information for the following IMRT treatment planning and delivery.

IV. REPORTABLE OUTCOMES

The following is a list of publications resulted from the grant support in the last funding period.

Refereed publications:

1. Yang Y, Schreibmann E., Li T, **Xing L**, Evaluation of dosimetric accuracy of kV cone beam CT-based dose calculation, *Physics in Medicine and Biology*, 52, 685-705, 2007.
2. Timmerman R. D., Kavanagh B. D., Cho L. C., Papiez L., **Xing L**, Stereotactic body radiation therapy in multiple organ sites, *J Clin Oncol* 25, 947-52, 2007.
3. Chao M, Schreibamnn E, Li T, **Xing L**, Automated contour mapping using sparse volume sampling for 4D radiation therapy, *Medical Physics* 34, 4023-29, 2007.
4. de la Zerda A, Armbruster B, **Xing L**, Formulating adaptive radiation therapy (ART) treatment planning into a closed-loop control framework, *Physics in Medicine and Biology* 52, 4137-4153, 2007.
5. Mao W, Li T, **Xing L**, Image registration in sinogram space, *Medical Physics*, Medical Physics 34, 3596-3602, 2007.
6. Wiersma R, **Xing L**, Geometric and dosimetric accuracies of gated IMRT, *Med Phys* 34, 3962-70, 2007.
7. Li T, Koogn A, **Xing L**, Enhanced 4D Cone-Beam Computed Tomography Using an On-Board Imager, *Medical Physics* 34, 3688-95, 2007. – figures featured in the cover of the issue of the journal.
8. **Xing L**, Siebers J, and Keall P, Software solutions for real-time adaptive image-guided radiotherapy, *Seminar in Radiation Oncology* 17, 245-57, 2007.
9. Paquin D, Levy D, **Xing L**, Hybrid multistage landmark and deformable image registration, *Math. Biosciences Eng.* 4, 711-37, 2007.
10. Lee L., Le Q, **Xing L**, Retrospective IMRT dose reconstruction based on cone-beam CT and MLC log-file, *International Journal of Radiation Oncology, Biology, Physics*, in press.
11. Chao M, Schreibamnn E, Li T, **Xing L**, Automated contour mapping with a regional deformable model, *International Journal of Radiation Oncology, Biology, Physics*, in press.
12. Xie Y, Djajaputra D, King C, Hossain S, Ma L, **Xing L**, Intrafraction motion of prostate in hypofractionated radiation therapy, *International Journal of Radiation Oncology, Biology, Physics*, submitted, 2007.
13. Wang C, Chao M, Lee L., **Xing L**, MRI-based dose calculation, *Medical Physics*, submitted, 2007.
14. Mao, Wiersma R, **Xing L**, Using prior knowledge to facilitate the auto-detection of implanted fiducials, *Medical Physics*, submitted, 2007.
15. Mao W, **Xing L**, Design of Multi-Purpose Phantom and Automated Software Analysis Tool for Quality Assurance of Onboard kV/MV Imaging System, *Medical Physics*, conditionally accepted, 2007.
16. Wiersma R. and **Xing L**, Real-time monitoring of implanted fiducials using onboard kV and treatment MV beams, *Medical Physics*, conditionally accepted, 2007.
17. Xie Y, Chao M, Lee P, and **Xing L**, Auto-mapping of rectum contour for prostate adaptive therapy inverse planning, *International Journal of Radiation Oncology, Biology, Physics*, submitted, 2007.
18. Wang J, Li T, Liang Z, **Xing L**, Dose reduction in kV cone beam CT for radiation therapy, *Medical Physics*, submitted, 2007.

Book and Book Chapters

1. Keall P and **Xing L**, Image Guided and Adaptive Therapy, *The Textbook of Radiation Oncology*, Phillips T and Leibel S (editors), Saunders, 2008.
2. Xia P, Almos H, **Xing L**, Intensity Modulated Radiation Therapy, *The Textbook of Radiation Oncology*, Phillips T and Leibel S (editors), Saunders, 2008.
3. **Xing L**, Lagen K, Timmerman R, Image Guided Adaptive Radiation Therapy, in *Image Guided and Adaptive Therapy*, Timmerman R. and Xing L (editors), *Image Guided and Adaptive Radiation Therapy*, Lippincott, Williams, and Wilkins, Baltimore, MD, in processing (to appear in 2008).

-
4. **Xing L**, Image Guided Intensity Modulated Radiation Therapy, in Mathematical Methods in Biomedical Imaging and IMRT, Censor Y, Jiang M, Louis A.K (Editors), Springer-Verlag, 2008.

Conference abstract

1. Chao M, Schreibmann E, Li T, Xing L, Automated Propagation of Contours Between 4DCT Images Using a Regional Deformable Model, oral presentation in 2007 AAPM Annual Meeting, Minneapolis, MN.
2. Xing L, Functional Imaging, invited talk in 2007 AAPM Annual Meeting, Minneapolis, MN.
3. Callaghan T, Levy D, Xing L, IMRT Inverse Planning with Voxel-Based Penalty Scheme, poster presentation in 2007 AAPM Annual Meeting, Minneapolis, MN.
4. A de la Zerda, B Armbruster, L Xing, A Closed-Loop Control Framework for Adaptive Radiation Therapy (ART), oral presentation in 2007 AAPM Annual Meeting, Minneapolis, MN.
5. K Lee, Q Le, L Xing, Retrospective IMRT Dose Reconstruction Based On CBCT and the MLC Positional Log-File Recorded During Treatment, oral presentation in 2007 AAPM Annual Meeting, Minneapolis, MN.
6. W Mao, L Xing, A Phantom and Software Analysis Tool for Quality Assurance (QA) of LINAC with Onboard KV X-Ray Imaging Device, oral presentation in 2007 AAPM Annual Meeting, Minneapolis, MN.
7. W Mao, T Li, N Wink, L Xing, CT Image Registration in Sinogram Space, oral presentation in 2007 AAPM Annual Meeting, Minneapolis, MN.
8. C Wang, M Chao, L Xing, Electron Density Mapping for MRI-Based Treatment Planning, oral presentation in 2007 AAPM Annual Meeting, Minneapolis, MN.
9. T Li, L Papiez, R Timmerman, H Choy, A Koong, L Xing, High-Quality Four-Dimensional CBCT Reconstruction with Virtual Projections, oral presentation in 2007 AAPM Annual Meeting, Minneapolis, MN.
10. R.D. Wiersma, L Xing, Temporal Precision of Gated Step-And-Shoot Intensity Modulated Radiation Therapy, oral presentation in 2007 AAPM Annual Meeting, Minneapolis, MN.
11. R.D. Wiersma, L Xing, Temporal, Dosimetric, and Geometric Precision of Gated Step-And-Shoot Intensity Modulated Radiation Therapy, oral presentation in 2007 AAPM Annual Meeting, Minneapolis, MN.
12. Xing L, 4D CT and PET Imaging, invited talk in 2007 RSNA Annual Meeting, Chicago, IL.
13. J. Wang, M. Chao, **L. Xing**, Toward Clinical Implementation of Adaptive Treatment Planning: Auto-Propagation of Contours from Planning CT to CBCT, *International Journal of Radiation Oncology Biology Physics* 69, S43.
14. R.D. Wiersma and **L. Xing** Dosimetric Consequences of Electronic Delay on Gated Radiation Therapy, *International Journal of Radiation Oncology Biology Physics* 69, Page S131-S132.
15. **L. Lee**, Q. Le, T. La and **L. Xing**, IMRT Dose Reconstruction on CBCT: A Platform for Head-and-Neck Adaptive Therapy, *International Journal of Radiation Oncology Biology Physics* 69, 2007, Page S412.
16. Y. Xie, **L. Xing**, D. Paquin, D. Levy, Deformable Image Registration with Inclusion of Auto-Detected Homologous Tissue Features, *International Journal of Radiation Oncology Biology Physics* 69, 2007, S646-S647
17. **Xing L**, Korreman S, Keall P, Image Guided Intensity Modulated Radiation Therapy, invited talk in 2007 annual Meeting of ESTRO, Barcelona, Spain, Sept, 2007.
18. de la Zerda A, Armbrush B, **Xing L**, Adaptive Prostate Radiation Therapy, oral presentation in 2007 annual Meeting of ESTRO, Barcelona, Spain, Sept, 2007.

US Patent

None.

V. CONCLUSIONS

In the past funding year, the PI group has contributed greatly to advance prostate radiation therapy techniques. A few important milestones have been achieved toward the goal of the project. These include: (i) Investigated intrafraction prostate motion and its influence on prostate radiation therapy; (ii) Developed method for auto-propagation of contours from planning CT to CBCT for on-line/off-line inverse planning; (iii) Established a novel technique to enhance on-board cone-beam CT and to effectively reduce the radiation dose incurred in the scanning process; (iv) Setup a framework for adaptive inverse planning based on a voxel

specific penalty scheme; (v) Evaluated the feasibility of using on-board cone-beam CT for on-treatment dose calculation and developed a reliable electron density mapping algorithm for CBCT-based IMRT optimization; and (vi) Provided a robust procedure for retrospective dose reconstruction in IMRT dose delivery. Integration and further refinement of the above tools are in progress.

References:

1. Xie, Y.; Djajaputra, D.; King, C.; Hossain, S.; Ma, L.; Xing, L., Intrafraction motion of prostate in hypofractionated radiation therapy. *Int J Radiat Oncol Biol Phys* **2007**, submitted.
2. Chao, M.; Schreibmann, E.; Li, T.; Xing, L., Automated Contour Mapping using Sparse Volume Sampling for 4D Radiation Therapy. *Medical Physics* **2007**, *34*, 4023-29.
3. Chao, M.; Li, T.; Schreibmann, E.; Koong, A.; Xing, L., Automated Contour Mapping with a Regional Deformable Model. *Int J Radiat Oncol Biol Phys* **2007**, in press.
4. Xie, Y.; Ming, C.; Lee, P.; Xing, L., Auto-mapping of rectum contour for prostate adaptive therapy inverse planning. *Int J Radiat Oncol Biol Phys* **2007**, submitted.
5. de la Zerda, A.; Armbruster, B.; Xing, L., Inverse Planning for Adaptive Radiation Therapy Using Dynamic Algorithm. *International Journal of Radiation Oncology Biology Physics* **2006**, *66*, (11), S123-S124.
6. de la Zerda, A.; Armbruster, B.; Xing, L., Formulating adaptive radiation therapy (ART) treatment planning into a closed-loop control framework. *Phys Med Biol* **2007**, *52*, (14), 4137-53.
7. Li, T.; Xing, L., Optimizing 4D cone-beam CT acquisition protocol for external beam radiotherapy. *Int J Radiat Oncol Biol Phys* **2007**, *67*, (4), 1211-9.
8. Li, T.; Xing, L.; McGuinness, C.; Munro, P.; Loo, B.; Koong, A., Four-dimensional cone-beam CT using an on-board imager. *Medical Physics* **2006**, *33*, 3825-3833.
9. Li, T.; Koong, A.; Xing, L., Enhanced 4D Cone-Beam Computed Tomography Using an On-Board Imager. *Medical Physics* **2007**, *34*, 3688-95.
10. Lee, L.; Le, Q.; L, X. In *Retrospective IMRT Dose Reconstruction Based On Cone-Beam Computed Tomography (CBCT) and the MLC Positional Log-File Recorded During Treatment*, 2007 Annual Meeting of AAPM, Minneapolis, MN, 2007; Minneapolis, MN, 2007.
11. Lee, L.; Le, Q.; Xing, L., Retrospective IMRT Dose Reconstruction Based On Cone-Beam Computed Tomography (CBCT) and the MLC Positional Log-File Recorded During Treatment. *Int J Radiat Oncol Biol Phys* **2007**, p in press.
12. Kupelian, P.; Willoughby, T.; Mahadevan, A.; Djemil, T.; Weinstein, G.; Jani, S.; Enke, C.; Solberg, T.; Flores, N.; Liu, D.; Beyer, D.; Levine, L., Multi-institutional clinical experience with the Calypso System in localization and continuous, real-time monitoring of the prostate gland during external radiotherapy. *Int J Radiat Oncol Biol Phys* **2007**, *67*, (4), 1088-98.
13. Willoughby, T. R.; Kupelian, P. A.; Pouliot, J.; Shinohara, K.; Aubin, M.; Roach, M., 3rd; Skrumeda, L. L.; Balter, J. M.; Litzenberg, D. W.; Hadley, S. W.; Wei, J. T.; Sandler, H. M., Target localization and real-time tracking using the Calypso 4D localization system in patients with localized prostate cancer. *Int J Radiat Oncol Biol Phys* **2006**, *65*, (2), 528-34.
14. Langen, K. M.; Jones, D. T., Organ motion and its management. *Int J Radiat Oncol Biol Phys* **2001**, *50*, 265-78.
15. Li, J. G.; Xing, L., Inverse planning incorporating random organ motion. *Medical Physics* **2000**, *27*, 1368-1372.
16. Bortfeld, T.; Jokivarsi, K.; Goitein, M.; Kung, J.; Jiang, S. B., Effects of intra-fraction motion on IMRT dose delivery: statistical analysis and simulation. *Physics in Medicine & Biology* **2002**, *47*, (13), 2203-20.
17. Xie, Y.; Chao, M.; Lee, P.; Xing, L., Tissue Feature-Based Rectal Contour Propagation from Planning CT to Cone Beam CT for Adaptive Radiation Therapy. *Int J Radiat Oncol Biol Phys* **2007**, submitted.
18. Schreibmann, E.; Chen, G. T.; Xing, L., Image interpolation in 4D CT using a BSpline deformable registration model. *Int J Radiat Oncol Biol Phys* **2006**, *64*, (5), 1537-50.
19. Chao, M.; Schreibmann, E.; Li, T.; Xing, L., Automated Propagation of Region-Of-Interest Contours Between 4DCT Images Using a Regional Deformable Model. *Medical Physics* **2007**, , 2515.
20. Jaffray, D. A.; Siewerdsen, J. H.; Wong, J. W.; Martinez, A. A., Flat-panel cone-beam computed tomography for image-guided radiation therapy. *Int J Radiat Oncol Biol Phys* **2002**, *53*, (5), 1337-49.

21. Xing, L.; Thorndyke, B.; Schreibmann, E.; Yang, Y.; Li, T. F.; Kim, G. Y.; Luxton, G.; Koong, A., Overview of image-guided radiation therapy. *Med Dosim* **2006**, 31, (2), 91-112.
22. Xing, L.; Siebers, J.; Keall, P., Computational challenges for image-guided radiation therapy: framework and current research. *Semin Radiat Oncol* **2007**, 17, (4), 245-57.
23. Li, T.; Schreibmann, E.; Thorndyke, B.; Tillman, G.; Boyer, A.; Koong, A.; Goodman, K.; Xing, L., Radiation Dose Reduction in 4D Computed Tomography. *Medical Physics* **2005**, 32, 3650-60
24. Yang, Y.; Schreibmann, E.; Li, T.; Wang, C.; Xing, L., Evaluation of on-board kV cone beam CT (CBCT)-based dose calculation. *Phys Med Biol* **2007**, 52, (3), 685-705.
25. Wiersma, R.; Xing, L., Spatial and Temporal Precision of Gated Step-And-Shoot Intensity Modulated Radiation Therapy. *Medical Physics* **2007**, 34, 3962-70.
26. Xing, L.; Li, J. G., Computer verification of fluence maps in intensity modulated radiation therapy. *Medical Physics* **2000**, 27, 2084-92.
27. Yang, Y.; Xing, L., Inverse treatment planning with adaptively evolving voxel-dependent penalty scheme. *Med Phys* **2004**, 31, (10), 2839-44.

Appendices -- manuscripts published/submitted

1. Yang Y, Schreibmann E, Li T, Xing L, Evaluation of dosimetric accuracy of kV cone beam CT-based dose calculation, *Physics in Medicine and Biology*, 52, 685-705, 2007.
2. de la Zerda A, Armbruster B, Xing L, Formulating adaptive radiation therapy (ART) treatment planning into a closed-loop control framework, *Physics in Medicine and Biology* 52, 4137-4153, 2007.
3. Chao M, Schreibamnn E, Li T, Xing L, Automated contour mapping using sparse volume sampling for 4D radiation therapy, *Medial Physics* 34, 4023-29, 2007.
4. Mao W, Li T, Xing L, Image registration in sinogram space, *Medical Physics* 34, 3596-3602, 2007.
5. Paquin D, Levy D, Xing L, Hybrid multistage landmark and deformable image registration, *Math. Biosciences Eng.* 4, 711-37, 2007.
6. Mao W, Lee L, Xing L, Design of multi-purpose phantom and automated software analysis tool for quality assurance of onboard kV/MV imaging system, *Medical Physics* 35, 1497-1506, 2008.
7. Lee L., Le Q, Xing L, Retrospective IMRT dose reconstruction based on cone-beam CT and MLC log-file, *International Journal of Radiation Oncology, Biology, Physics*, 70, 634-644, 2008.
8. Chao M, Schreibamnn E, Li T, Xing L, Automated contour mapping with a regional deformable model, *International Journal of Radiation Oncology, Biology, Physics*, 70, 599-608. 2008.
9. Xing L, Siebers J, and Keall P, Software solutions for real-time adaptive image-guided radiotherapy, *Seminar in Radiation Oncology* 17, 245-57, 2007.
10. Xie Y, Djajaputra D, King C, Hossain S, Ma L, Xing L, Intrafraction motion of prostate in hypofractionated radiation therapy, *International Journal of Radiation Oncology, Biology, Physics*, conditionally accepted, 2007.
11. Xie Y, Chao M, and Xing L, Auto-mapping of rectum contour for prostate adaptive therapy inverse planning, *International Journal of Radiation Oncology, Biology, Physics*, conditionally accepted, 2007.
12. Lee L, Mao W, and Xing L, The use of EPID-measured leaf sequence files for IMRT dose reconstruction in adaptive radiation therapy, *Medical Physics*, submitted, 2008.
13. Wang J, Li T, Liang J, Xing L: Dose reduction for kilovoltage cone-beam computed tomography in radiation therapy. *Physics in Medical Biology*, conditionally accepted, 2008.

Appendix ---Reprints and preprints

1. Yang Y, Schreibmann E., Li T, Xing L, Evaluation of dosimetric accuracy of kV cone beam CT-based dose calculation, *Physics in Medicine and Biology*, 52, 685-705, 2007.
2. de la Zerda A, Armbruster B, Xing L, Formulating adaptive radiation therapy (ART) treatment planning into a closed-loop control framework, *Physics in Medicine and Biology* 52, 4137-4153, 2007.
3. Chao M, Schreibamnn E, Li T, Xing L, Automated contour mapping using sparse volume sampling for 4D radiation therapy, *Medial Physics* 34, 4023-29, 2007.
4. Mao W, Li T, Xing L, Image registration in sinogram space, *Medical Physics* 34, 3596-3602, 2007.
5. Paquin D, Levy D, Xing L, Hybrid multistage landmark and deformable image registration, *Math. Biosciences Eng.* 4, 711-37, 2007.
6. Mao W, Lee L, Xing L, Design of multi-purpose phantom and automated software analysis tool for quality assurance of onboard kV/MV imaging system, *Medical Physics* 35, 1497-1506, 2008.
7. Lee L., Le Q, Xing L, Retrospective IMRT dose reconstruction based on cone-beam CT and MLC log-file, *International Journal of Radiation Oncology, Biology, Physics*, 70, 634-644, 2008.
8. Chao M, Schreibamnn E, Li T, Xing L, Automated contour mapping with a regional deformable model, *International Journal of Radiation Oncology, Biology, Physics*, 70, 599-608. 2008.
9. Xing L, Siebers J, and Keall P, Software solutions for real-time adaptive image-guided radiotherapy, *Seminar in Radiation Oncology* 17, 245-57, 2007.
10. Xie Y, Djajaputra D, King C, Hossain S, Ma L, Xing L, Intrafraction motion of prostate in hypofractionated radiation therapy, *International Journal of Radiation Oncology, Biology, Physics*, conditionally accepted, 2007.
11. Xie Y, Chao M, and Xing L, Auto-mapping of rectum contour for prostate adaptive therapy inverse planning, *International Journal of Radiation Oncology, Biology, Physics*, conditionally accepted, 2007.
12. Lee L, Mao W, and Xing L, The use of EPID-measured leaf sequence files for IMRT dose reconstruction in adaptive radiation therapy, *Medical Physics*, submitted, 2008.
13. Wang J, Li T, Liang J, Xing L: Dose reduction for kilovoltage cone-beam computed tomography in radiation therapy. *Physics in Medical Biology*, conditionally accepted, 2008.



Evaluation of on-board kV cone beam CT (CBCT)-based dose calculation*

Yong Yang, Eduard Schreibmann, Tianfang Li, Chuang Wang
and Lei Xing

Department of Radiation Oncology, Stanford University School of Medicine,
875 Blake Wilbur Drive, Stanford, CA 94305-5847, USA

E-mail: lei@reyes.stanford.edu

Received 14 September 2006, in final form 6 November 2006

Published 12 January 2007

Online at stacks.iop.org/PMB/52/685

Abstract

On-board CBCT images are used to generate patient geometric models to assist patient setup. The image data can also, potentially, be used for dose reconstruction in combination with the fluence maps from treatment plan. Here we evaluate the achievable accuracy in using a kV CBCT for dose calculation. Relative electron density as a function of HU was obtained for both planning CT (pCT) and CBCT using a Catphan-600 calibration phantom. The CBCT calibration stability was monitored weekly for 8 consecutive weeks. A clinical treatment planning system was employed for pCT- and CBCT-based dose calculations and subsequent comparisons. Phantom and patient studies were carried out. In the former study, both Catphan-600 and pelvic phantoms were employed to evaluate the dosimetric performance of the full-fan and half-fan scanning modes. To evaluate the dosimetric influence of motion artefacts commonly seen in CBCT images, the Catphan-600 phantom was scanned with and without cyclic motion using the pCT and CBCT scanners. The doses computed based on the four sets of CT images (pCT and CBCT with/without motion) were compared quantitatively. The patient studies included a lung case and three prostate cases. The lung case was employed to further assess the adverse effect of intra-scan organ motion. Unlike the phantom study, the pCT of a patient is generally acquired at the time of simulation and the anatomy may be different from that of CBCT acquired at the time of treatment delivery because of organ deformation. To tackle the problem, we introduced a set of modified CBCT images (mCBCT) for each patient, which possesses the geometric information of the CBCT but the electronic density distribution mapped from the pCT with the help of a BSpline deformable image registration software. In the patient study, the dose computed with the mCBCT was used as a surrogate of the ‘ground truth’. We found that the CBCT electron density calibration curve differs moderately from that of pCT. No significant fluctuation

* Part of this work was presented in 2006 Annual Meeting of American Association of Physicists in Medicine.

was observed in the calibration over the period of 8 weeks. For the static phantom, the doses computed based on pCT and CBCT agreed to within 1%. A notable difference in CBCT- and pCT-based dose distributions was found for the motion phantom due to the motion artefacts which appeared in the CBCT images (the maximum discrepancy was found to be $\sim 3.0\%$ in the high dose region). The motion artefacts-induced dosimetric inaccuracy was also observed in the lung patient study. For the prostate cases, the mCBCT- and CBCT-based dose calculations yielded very close results ($<2\%$). Coupled with the phantom data, it is concluded that the CBCT can be employed directly for dose calculation for a disease site such as the prostate, where there is little motion artefact. In the prostate case study, we also noted a large discrepancy between the original treatment plan and the CBCT (or mCBCT)-based calculation, suggesting the importance of inter-fractional organ movement and the need for adaptive therapy to compensate for the anatomical changes in the future.

(Some figures in this article are in colour only in the electronic version)

1. Introduction

Modern radiation therapy techniques, such as 3D conformal radiotherapy (3DCRT) and intensity-modulated radiation therapy (IMRT), provide unprecedented means for producing exquisitely shaped radiation doses that closely conform to the tumour dimensions while sparing sensitive structures. As a result of greatly enhanced dose conformality, more accurate beam targeting becomes an urgent issue in radiation therapy. In current practice, uncertainties exist in tumour target localization due to intra- and inter-organ motions during the course of radiation treatment. As thus, large safety margins around the tumour targets and sensitive structures are introduced to cope with the otherwise insoluble patient localization problem. The use of non-optimal margins compromises the patient care and adversely affects the treatment outcome (Coolens *et al* 2006, Hector *et al* 2000, Hugo *et al* 2003, Litzenberg *et al* 2006, Ruan *et al* 2006, Webb 2006). The need to improve targeting in high precision radiation therapy has recently spurred a flood of research activities in image-guided radiation therapy (IGRT) (Xing *et al* 2006).

CBCT-based upon flat-panel technology integrated with a medical linear accelerator has recently become available from linac vendors for therapy guidance. The volumetric images may be used to verify and correct the planning patient setup in the linac coordinates by comparing with the patient position defined in treatment plan. Both kV and MV beams have been utilized for this application (Chang *et al* 2006, Dietrich *et al* 2006, Hawkins *et al* 2006, Jaffray *et al* 2002, Langen *et al* 2005, Sorcini and Tilikidis 2006, Thilmann *et al* 2006, Yin *et al* 2005). The former typically consists of a kV-source and flat-panel combination mounted on the drum of a medical accelerator, with the kV imaging axis orthogonal to that of MV therapy beam. In addition to guide the patient setup process, CBCT data acquired prior to the treatment can, in principle, be used to recalculate or verify the treatment plan based on the patient anatomy of the treatment day. The recalculation starts with the intended fluence maps from the patient's treatment plan, whereas the verification is done by using the fluence maps measured at the exiting sides of the incident beams. If CBCT-based dose calculation is accurate enough (say, with an accuracy within $1 \sim 2\%$), this will provide a valuable option for us to predict/assess the patient dose routinely. In reality, because of the presence of organ

movement/deformation, it is conceivable that the dose distributions delivered to the patient are usually different from fraction to fraction. It is paramount to be able to monitor the actual patient dose for each fraction as well as the accumulated doses to the target and sensitive structures while the fractional treatment proceeding. This will not only give physicians more confidence about the treatment but may, in future, afford us an effective means to adaptively modify the patient's treatment plan during the course of a radiation therapy based on the dose that has already been delivered.

Different from conventional CT, kV CBCT covers a much larger field of view (FOV) in the longitudinal direction, and scatter poses a more severe problem in the resultant image. In addition, the gantry rotation speed is limited to ~ 1 min by IEC regulation, which makes the CBCT more prone to motion artefacts. The deteriorated image quality raises serious concerns about the dosimetric reliability of CBCT-based dose calculation. In this work we evaluate the dosimetric accuracy of kV CBCT-based dose calculation.

2. Method and materials

2.1. Data acquisition

The on-board imager (OBI) integrated in a TrilogyTM medical linear accelerator (Varian Medical Systems, Palo Alto, CA) is used in this work to acquire CBCT images. The kV OBI system is capable of obtaining low-dose, high-resolution radiography, fluoroscopy and CBCT. The system is mounted on the treatment machine via robotically controlled arms, which operate along three axes of motion. A 150 kV x-ray tube with maximum 32 ms pulse length for continuous irradiation and maximum 320 ms pulse length for single pulse is designed for generating high-resolution images from a moving gantry. The spot of the tube is located at 90° to the MV source and 100 cm from the radiation axis of the accelerator. A $39.7 \text{ cm} \times 29.8 \text{ cm}$ amorphous silicon flat-panel x-ray image detector (Varian PortalVisionTM aS1000) mounted opposite the kV tube is used to acquire digital images with a pixel matrix of 2048×1536 . Using the OBI system, the CBCT data can be acquired in two modes: a full-fan mode and half-fan mode. In the full-fan mode, the beam central axis passes through the detector centre and a full projection of the scanned patient is acquired for each acquirement angle. A total of 675 projections are taken during the whole 364° gantry rotation with a maximum field of view (FOV) about 25 cm in diameter and 17 cm in length. The data acquisition time is about 60 s and the reconstruction time for 340 slices of 512×512 CBCT images with a voxel size of 0.5 mm^3 is also about 1 min on a PC. The half-fan mode is designed to obtain a larger FOV. In this mode, the detector is shifted laterally to take only half of the projection of the scanned patient for each acquirement angle. A total of about 965 projections are taken during the 364° gantry rotation and a FOV of 50 cm in the axial plane and 15 cm in the longitudinal direction can be achieved. The data acquisition and reconstruction time for 512×512 CBCT images with a voxel size of 0.95 mm^3 using this mode is about double compared with the full-fan mode. The averaged dose for a head and neck CBCT scan is about 2 cGy, and 3 cGy for an abdominal scan.

2.2. Calibration of relative electron density

To use CT or CBCT for radiation dose calculation, it is required to relate the Hounsfield unit (HU) of the scanner with the actual electron density. A CT-phantom, Catphan-600 module CTP404 (Phantom Laboratory, NY), was used for the calibration of pCT (GE Discovery-ST PET/CT scanner, Milwaukee, WI) and CBCT. The gantry rotation speed of the 16-slice

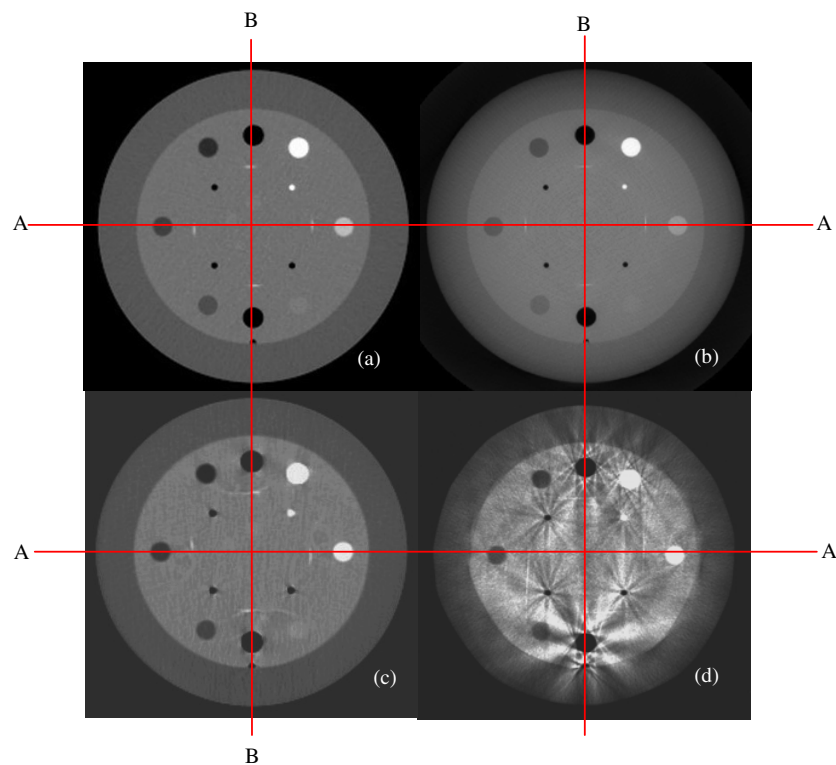


Figure 1. The CT and CBCT images with and without motion for the Catphan-600: (a) pCT in the absence of phantom motion; (b) CBCT in the absence of phantom motion; (c) pCT with moving phantom; and (d) CBCT with moving phantom.

Discovery-ST scanner is 0.5 sec/rotation. The CTP404 has a diameter of 150 mm (the longitudinal dimension of the phantom is 16 cm) and contains 17 different sizes of inserts with seven different tissue substitute materials, air, PMP, LDPE, polystyrene, acrylic, Delrin and Teflon, respectively. Their relative electron densities ranged from 0 to 1.866. A cross section of the phantom is shown in figure 1. The calibration of a CT scanner involves acquiring CT images, obtaining average HUs for each inserting materials, and plotting the HU as a function of the relative electron density. For CBCT calibration, the only difference from the conventional CT is that it is necessary to calibrate separately for full- and half-fan modes because the beam geometry and characteristics of the two types of scanning modes are different.

In order to test the stability of the CBCT calibration curve with time, the phantom was repeatedly scanned every week for 2 months. The obtained HU versus relative electron density curves were compared to assess the HU fluctuations with time.

2.3. Phantom study

CT and CBCT images of the Catphan-600 phantom were acquired using the procedure outlined in section 2.1. The phantom was placed on a platform that can be set to one-dimensional cyclic motion with a number of speeds. The axis of the cylindrically shaped phantom, along which

the phantom moves cyclically, was angled from the central axis of the CBCT gantry rotation by about 15° in order to study the motion influence on CT/CBCT. The movement of the phantom produces motion artefacts in the images and allows us to evaluate the performance of CBCT-based dose calculation in the presence of organ motion. The full-fan mode was used to scan the phantom. CT and CBCT images of the phantom were acquired with and without motion. In the former case, the peak-to-peak amplitude of the motion was 0.5 cm in the left–right direction and the period was 4 s. In addition, different sizes of homogeneity cylindrical phantoms, with a diameter of 10.8, 16 and 26.6 cm, respectively, were scanned to evaluate the scatter influence on image quality.

To quantify the difference in the image quality of the CT and CBCT images, we first analysed the HU distribution for all the acquired images. The influence of phantom motion and scatter radiation on the HU distribution was investigated. The CT and CBCT images were imported to a Varian Eclipse treatment planning system for dosimetric comparison study. For planning and evaluation purposes, a hypothetical spherical target with a diameter of 5 cm was created at the centre of the phantom and a single $5 \times 5 \text{ cm}^2$ 6 MV photon beam was used to irradiate the target. A simple beam configuration was used here because, in this way, the results are more intuitively interpretable. The pencil beam convolution dose calculation algorithm implemented in the Varian Eclipse treatment planning system was adopted for dose calculation. The resultant isodose curves, dose profiles and DVHs were compared.

A detailed study using a CIRS Model 002PRA pelvic IMRT phantom (CIRS Tissue Simulation & Phantom Technology, Norfolk, VA) was also performed to validate the on-board CBCT-based dose calculation. The specifications of the phantom can be found from http://www.cirsinc.com/002pra_rad.html. After CT and CBCT images were acquired, a five-field IMRT plan was generated with hypothetical target and sensitive structure at the centre of the phantom. The dose distributions and DVHs obtained using the two sets of images were then compared.

2.4. Patient study

Three prostate patients and a lung patient were selected for the evaluation study of CBCT-based dose calculation. For the prostate cases, the targets included the PTV, consisting of the prostate gland with a margin of 6 mm, and the seminal vesicles (SVs). The critical structures were rectum, bladder and femoral heads. IMRT plans using five 15 MV photon beams with gantry angles of 35° , 110° , 180° , 250° and 325° (in IEC convention) were adopted for the three cases. All the plans were normalized to deliver a prescription dose of 78 Gy to 99% the prostate PTV and no less than 50 Gy to the 98% of SVs in 39 fractions.

The patient was setup by using kV on-board imager (orthogonal projection images) under the guidance of implanted fiducials. After the kV AP/LAT images were acquired, the patient is shifted in such a way that the implanted gold seeds match with that on the DRRs. After the patients were setup using the current clinical procedure, CBCT images of the patients were acquired. The CBCT images were transferred to an Eclipse treatment planning system (Varian Medical Systems, Palo Alto, CA). For each case, the IMRT planning parameters generated for the patient's treatment, including beam configuration, MU settings and fluence maps, were employed to recalculate the dose based on the CBCT data. The CT- and CBCT-based treatment plans were then compared.

For the lung cancer case, the PTV consisted of the CTV with a margin of 10 mm. The critical structures involved were the right lung and the spinal cord. A conventional 3D conformal plan with three 15 MV photon beams (45° , 180° and 288° in IEC convention) was generated for this case. In this plan, the field shape of each beam was determined by

conforming the PTV projection in the corresponding beam direction. The plan was normalized to deliver a prescription dose of 70 Gy to 100% of the target volume in 35 fractions. The CBCT images of the patients were obtained using the half-fan mode.

2.5. Deformable electron density mapping (DEDM)

Unlike the phantom study, the pCT of a patient is generally acquired at the time of simulation and the anatomy may be different from that of CBCT acquired at the time of treatment delivery because of organ deformation. This makes it difficult to assess the accuracy of CBCT-based dose reconstruction. To tackle the problem, for each patient, we introduced a set of modified CBCT images (mCBCT) and the dose computed based on the mCBCT was used as a surrogate of the ‘ground truth’ in the evaluation of CBCT-based dose calculation. The mCBCT possesses the geometric information of the CBCT yet the electronic density distribution mapped from the pCT. The correspondence between the pCT and CBCT was accomplished by using an in-house BSpline deformable image registration software. The electron density mapping process is described as follows.

A free form spline (BSpline) deformable model (Li *et al* 2005, 2006a, 2006b, Paquin *et al* 2006, Schreiber *et al* 2006) was employed to register the pCT and CBCT. Briefly, a lattice of user-defined nodes is overlaid on the image. Each node contains a deformation vector, whose components are determined by optimizing a metric function that characterizes the goodness of the registration. In this work, a voxel-based normal cross correlation (NCC) metric was used and the node deformations were determined using the gradient-based optimization algorithm. The deformation at any point of the image is calculated by spline interpolation of closest nodes’ values. After registration, the HU in each voxel in pCT was mapped to the corresponding point in the CBCT to produce the mCBCT images.

3. Results

3.1. Calibration of CT and CBCT

The relationship between kV HU distribution of CBCT and relative electron density was established by using a Catphan-600 CT phantom following the procedure described in section 2.2. The calibration curves for pCT, half-fan and full-fan CBCT modes are shown in figure 2(a). Figure 2(b) shows the calibration data obtained with an interval of 1 week during a period of 2 months for full-fan CBCT. No significant variations were found in the calibration, which is similar to what has been observed for MV CBCT. The stability of the kV CBCT and electron density calibration is a good indicator of the HU number integrity and the overall performance of the CBCT system.

3.2. Phantom study

Figures 1(a)–(d) show the same transverse slices of the CT and CBCT images of the Catphan-600 phantom with and without motion. The first two panels are the CT and CBCT images of the phantom in the absence of motion, and the second two show the same with the phantom motion ‘switched on’. It is seen that the quality of CBCT images is worse than that of the conventional pCT, especially in the presence of motion. The HU profiles of the four images along the two orthogonal lines (lines A–A and B–B as marked in figure 1) are plotted in figure 3. It is found that the HU profiles of the pCT and CBCT normally agree to within 10% in the static situation. On the other hand, when the motion is ‘switched on’, CBCT shows a much

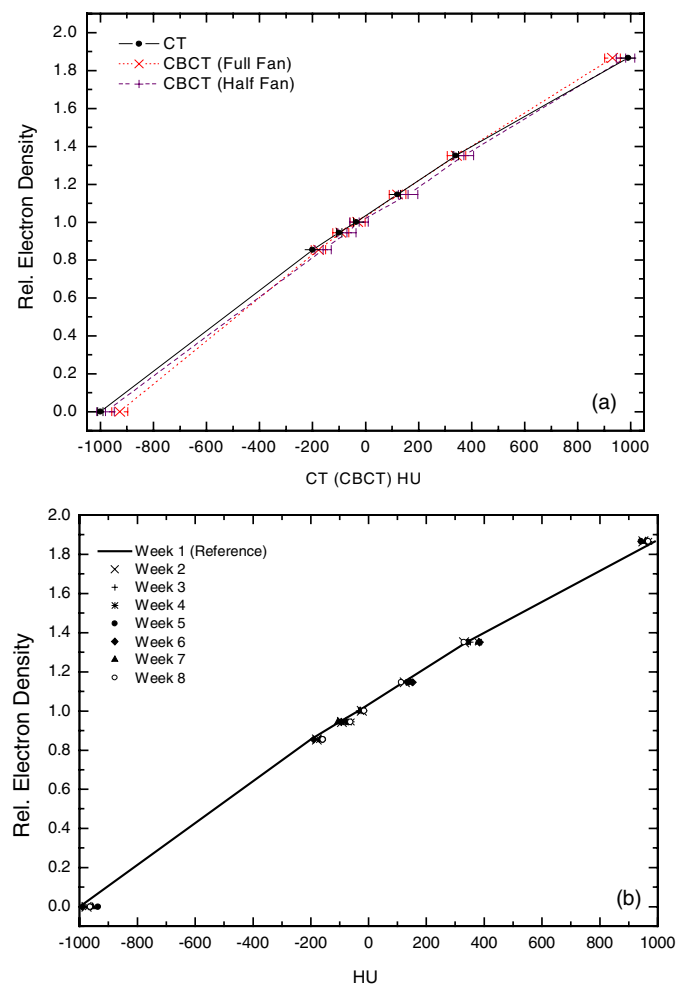


Figure 2. (a) The calibration curves (Hounsfield number versus relative electron density) for pCT, half-fan and full-fan mode CBCT; (b) the variation of calibration curves with time for the full-fan CBCT.

greater level of artefacts (figure 1(d)) and the HU difference between the conventional CT and CBCT is aggravated, with the maximum difference reaching several hundred HUs.

Because of the cone beam geometry, the influence of scatter radiation in CBCT is more severe as compared to that of a fan beam geometry. In general, x-ray scatter reduces image contrast, increases image noise and may introduce reconstruction error into CBCT. Figure 4 plots the HU profiles along a central axis of three different sized homogeneous cylindrical water phantoms. As expected, the fluctuation range of HU value increases with the phantom size, indicating the increased influence of scatter radiation.

Figures 5–7 present the dosimetric results calculated using a single 6 MV $5 \times 5 \text{ cm}^2$ photon beam. Figures 5(a)–(d) depict the dose distributions in a transverse slice calculated based on the four sets of images given in figure 1. Figures 6(a) and (b) compare the dose profiles along the two orthogonal lines (lines A–A and B–B in figure 1), and figure 7 compares

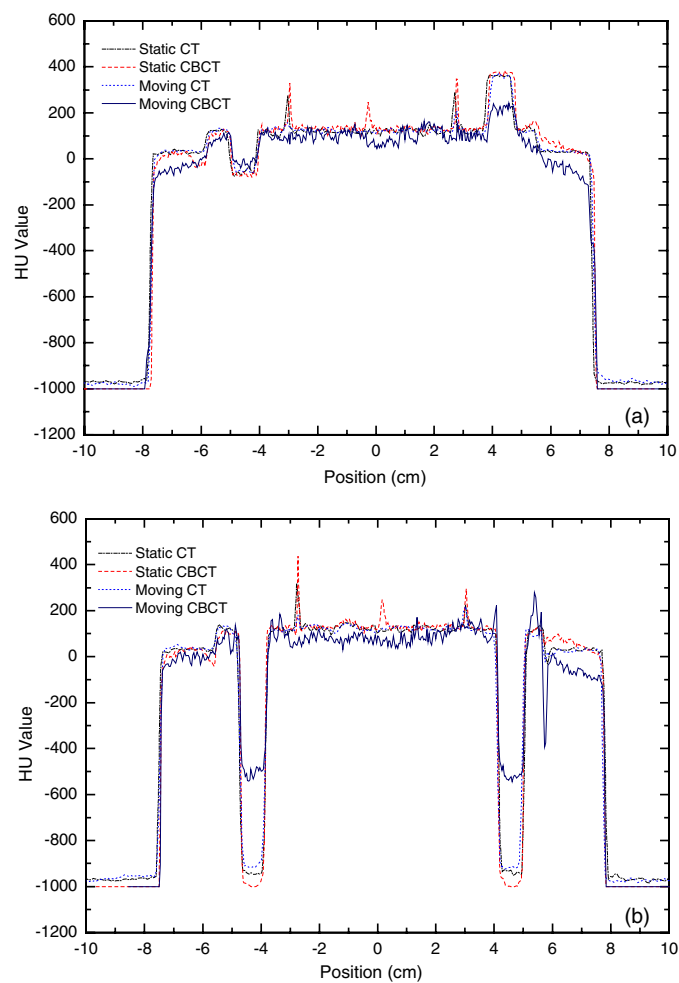


Figure 3. HU profiles of pCT and CBCT images (see figure 2) along the A–A line (panel (a)) and B–B line (panel (b)).

the DVHs of the target for the four different situations. From these results we see that the dose calculated using pCT agrees with that of CBCT-based calculation to within 1.0%, indicating that it is acceptable to use kV CBCT for dose calculation if no organ motion presents. However, when phantom motion is involved, the motion-induced artefacts significantly influence the HU distribution and thus the accuracy of CBCT-based dose calculation. For this simple phantom case, we find that the discrepancy between the pCT- and CBCT-based calculations is about 3%, which is clinically significant. Calculations using a few other field sizes ranging from 5 to 20 cm showed a similar level of agreement in the case of static phantom and the results are not presented here due to space limitation. The motion artefacts existing in the current CBCT limit the direct use of CBCT for dose calculation when intra-scanning organ motion is not negligible.

Figure 8 compares the IMRT dose calculations computed based on pCT and CBCT in the CIRS pelvic phantom. The DVHs of the target and sensitive structure are also presented

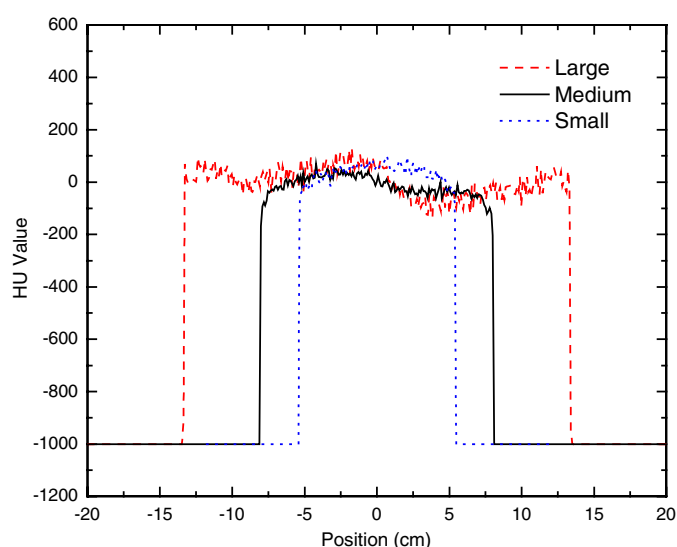


Figure 4. HU profiles for three different sized homogeneous cylindrical water phantoms. The diameters for large, medium and small phantoms are 26.6, 16.0 and 10.8 cm, respectively.

in figure 8. Once again, it is seen that the dose calculated using pCT agrees with that of CBCT-based calculation to within 1.0%, indicating that it is acceptable to use kV CBCT for dose calculation for a pelvic sized phantom.

3.3. Patient study

Figures 9(a)–(c) show the same transverse slices of the pCT, CBCT and checkerboard image resulting from the deformable registration of the two sets of images for one of the prostate cases. The mCBCT obtained by mapping the HUs from the pCT to CBCT is shown in figure 9(d). Our previous studies have indicated that an accuracy better than 3 mm is achievable by using the BSpline deformable model even in the presence of large deformations (Balter *et al* 2005, Schreiber *et al* 2006, Dietrich *et al* 2006, Kamath *et al* 2006). As can be seen from the checkerboard overlay, the registration between CT and CBCT is excellent. Figure 10 shows the isodose distributions for the three calculations based on pCT, CBCT and mCBCT for the same case. A comparison of DVHs of PTV, prostate, SVs, bladder and rectum is presented in the bottom of figure 10. Figures 11 and 12 present the DVHs of the targets and sensitive structures for the second and third cases. While there is significant dosimetric discrepancy between the pCT- and mCBCT-based plans, the results obtained using the CBCT or mCBCT are similar. The differences between the CBCT- and mCBCT-based calculations are generally less than 2%, suggesting that it is suitable to directly use CBCT for dose recalculation.

For all three prostate cases, we found that the CBCT-reconstructed prostate dose agrees with the planned one to within ~3%. In figure 10, the maximum prostate doses in the calculations based on planning CT, CBCT and modified CBCT are 105.3%, 107.2% and 106.4%, respectively. The maximum doses obtained with planning CT or CBCT differ from that obtained using modified CT by only 1%. In the absence of registration error, the dose difference between the planning CT and modified CBCT is due to daily anatomical change while the difference between the CBCT and modified CBCT is attributed to the HU value

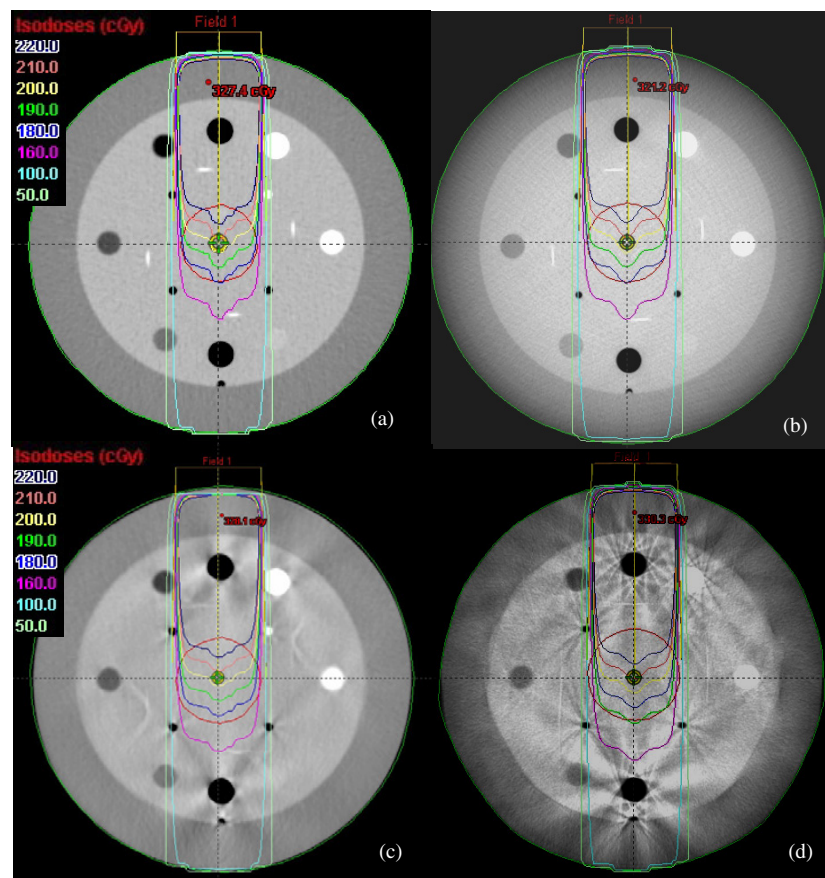


Figure 5. Dose distributions in a transverse slice calculated based on the four sets of CT data shown in figure 2: (a) pCT; (b) CBCT; (c) pCT with a motion; and (d) CBCT with a motion. In all four situations, a $5 \times 5 \text{ cm}^2$ single field plan was used to irradiate a spherical hypothetical target with a diameter of 5 cm located at the phantom centre.

change. We found the dosimetric difference in the PTV is quite significant, which could be greater than $6 \sim 10\%$. Similar observation was made in studies using daily CT on-rail (Court *et al* 2005, Paskalev *et al* 2004). For the rectum and bladder, the discrepancies between planned and reconstructed doses could be greater than 8%. We attribute the discrepancy between the planned and CBCT-reconstructed dose distribution to the inter-fractional organ movements.

Figures 13(a) to (d) show the same transverse slice from the planning CT, CBCT, checkerboard overlay of the planning CT and the mCBCT for the lung cancer case. Figure 14 compares the isodose distributions and the DVHs of the target and sensitive structures calculated based on the three sets of images for the 3D conformal treatment. In this case, the dosimetric discrepancy between the CBCT- and mCBCT-based calculations is larger than that in the prostate cases, especially for the right lung and PTV. The maximum dose difference is about 5%. However, the discrepancy between the results obtained using planning CT and mCBCT becomes much less. This study exemplifies that, unlike the prostate cases, the dosimetric inaccuracy arises from the inferior image quality of CBCT in the dose verification

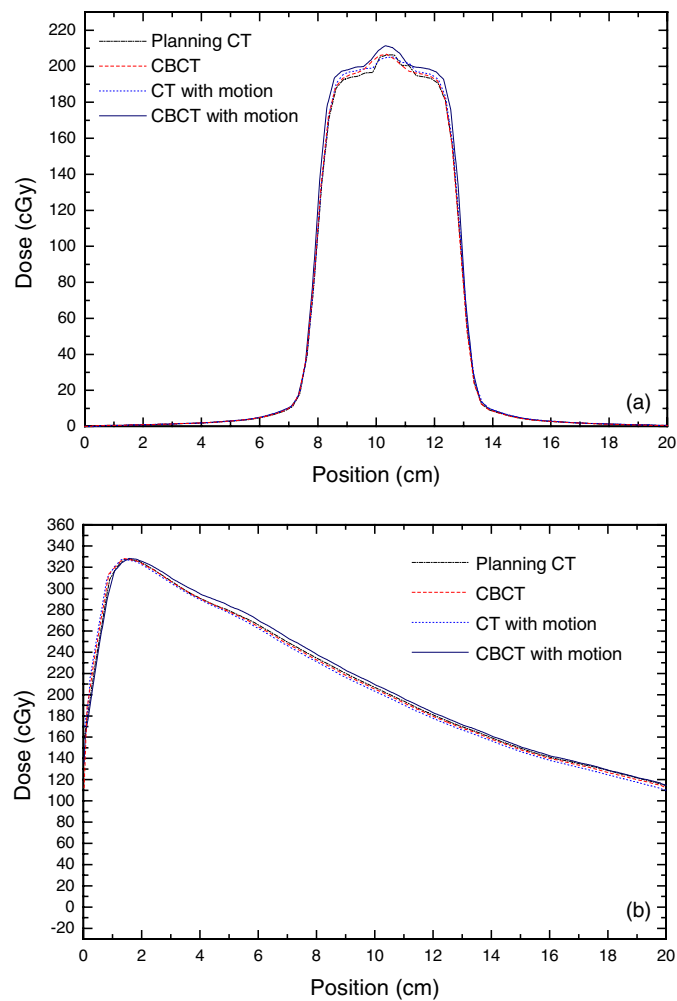


Figure 6. Comparison of the dose profiles along the two orthogonal lines shown in figure 2 for the Catphan-600 phantom: (a) profile along the A–A line; (a) profile along the B–B line.

calculation. The motion artefacts not only make it difficult to see the extent of the tumour, but also limit the direct use of CBCT for dose calculation in clinical practice.

4. Discussion

CBCT volumetric imaging integrated with a medical linear accelerator opens new avenues for improving current radiation oncology practice. CBCT has two important applications: patient setup and dose reconstruction/verification. By imaging the patient routinely during a course of radiation therapy, the accuracy of the patient setup can potentially be improved. Furthermore, the CBCT provides a pre-treatment patient model upon which the dose calculation can be performed using intended fluence maps from the planning system or other means. Both applications rely on quality of the volumetric images. In reality, the design of current on-board CBCT is far from optimal. Its quality is adversely influenced by many factors, such as

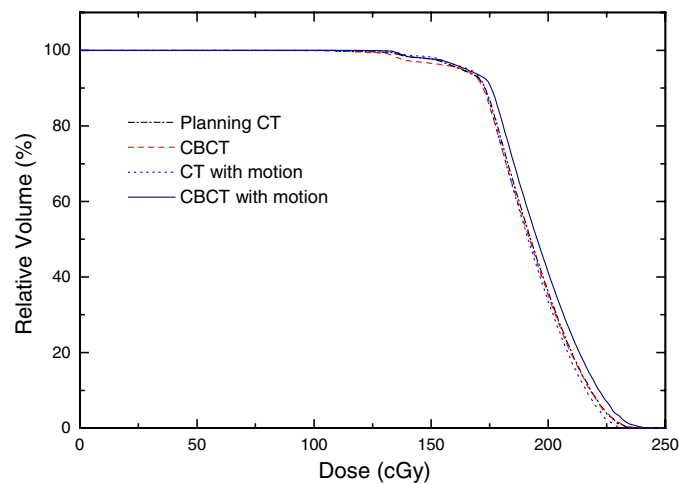


Figure 7. Comparison of the target DVHs calculated based on the four sets of CT data shown in figure 2 for the phantom case.

scatter, beam hardening and intra-scanning organ motion. This raises the question whether current CBCT images can be used directly for radiation dose calculation. In this work, the feasibility and accuracy of using a commercial kV CBCT to calculate dose are investigated with a CT phantom and three clinical prostate cases.

Dose distributions computed based on CBCT or mCBCT represent the dose to be delivered to the patient because the CBCT is usually acquired prior to the patient's treatment after repositioning under the standard patient setup procedure. In general, the difference between the planned and CBCT-reconstructed dose distributions arises from two factors: (i) patient positioning error and organ deformation/displacement; and (ii) relative electron density variation in CBCT images. The small discrepancy between the doses computed using CBCT and mCBCT (see the last section) suggests that, in the prostate cases, the second factor is small and it is acceptable to directly use CBCT for dose calculation. Our static phantom studies also support the notion. However, the dosimetric error caused by the inter-scanning organ motion/deformation is not insignificant, as suggested by the large discrepancies between the original plan and the dose distribution reconstructed based on CBCT or mCBCT. For example, in the first case, the SVs receive $\sim 50\%$ lower dose as compared to the planned delivery, whereas the second shows $\sim 10\%$ higher dose as compared to the planned one. In the third case, a clinically unacceptable SV underdosing is observed. The significant difference in SV DVHs of the original and to-be-delivered plans is caused by the relatively small volume and mobile nature of the SV. For the rectum and bladder, the discrepancies between planned and reconstructed doses are less yet clinically significant in all three cases.

While CBCT-based doses agree with mCBCT-based calculation to within $\sim 2\%$ in most situations and the CBCT images can be used directly for dosimetric validation for a disease site such as the prostate, it is not recommended to replace the conventional planning CT by CBCT for the purpose of radiation treatment planning. In addition to the inferior image quality, which may affect the physician's ability to delineate the tumour and sensitive structures, the limited FOV of CBCT (especially in the longitudinal direction) often renders the resultant images non-usable for treatment planning.

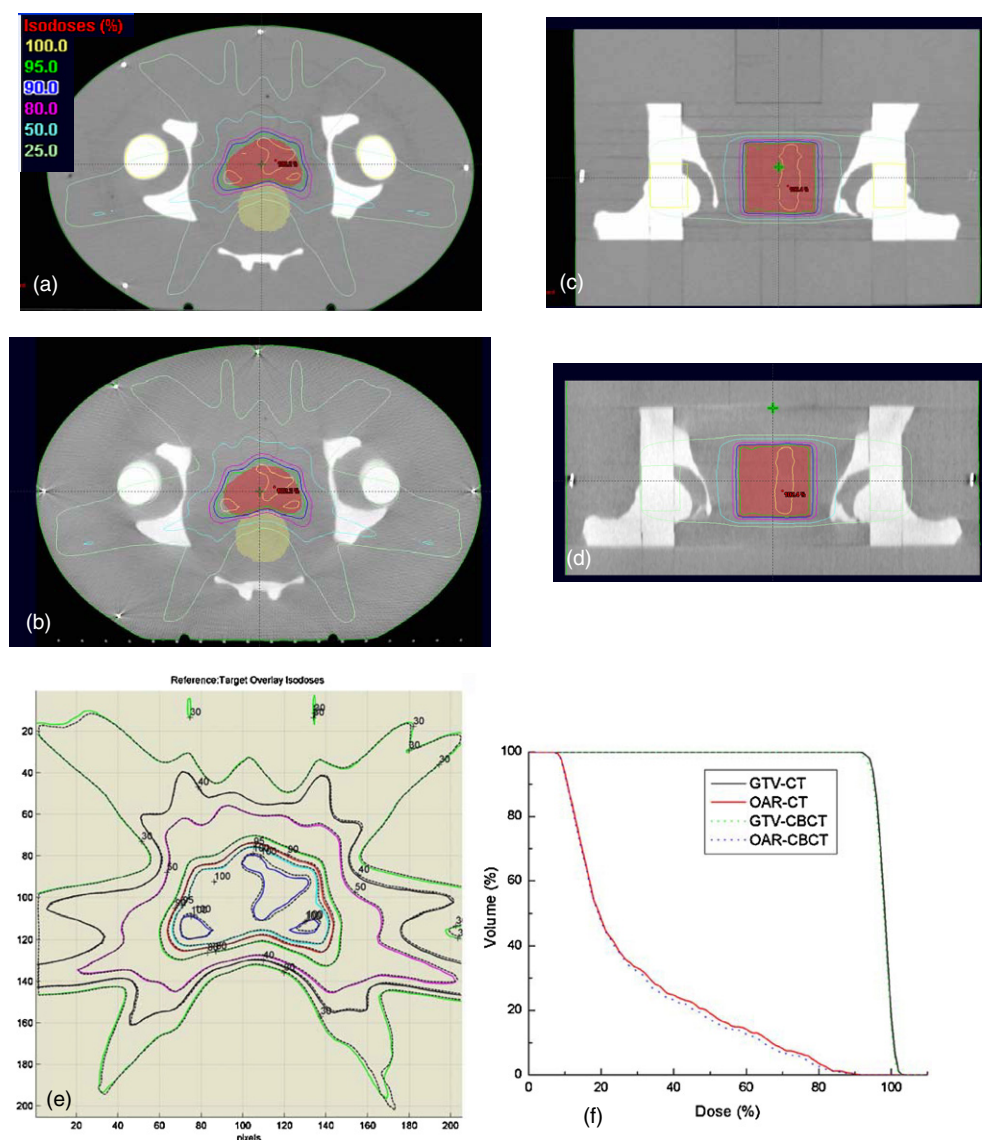


Figure 8. Dose distributions computed based on CT (top row) and CBCT (middle row) in the CIRS pelvic phantom. The overlay of CT- and CBCT-based doses in the target region on an axial slice is shown in the lower-left panel. The DVHs of the target and sensitive structure are shown in the lower-right panel. In the bottom row, the solid and dotted curves represent the results from CT and CBCT-based calculations, respectively.

A few groups are working on deformable model-based segmentation and patient setup procedures (Xing *et al* 2006). When a deformable model is used, one can go beyond simply aligning the 3D bony structures to achieve a registration based on the matching of soft-tissue organ(s). There are multiple ways to set up the patient depending on which structure to align during the patient positioning. Generally, the degree of freedom available for the patient setup is much less than the dimensionality of the patient deformation. Thus a deformable



Figure 9. CT, CBCT and mCBCT images for the first prostate case: (a) pCT; (b) daily CBCT; (c) checkerboard overlay of CT and CBCT after the deformation registration; and (d) mCBCT.

registration-based patient setup is not likely to be the ultimate solution to volumetric image-guided radiation therapy, even though it improves the current bony-structure-based patient alignment by partially taking into account organ deformation. A more attractive solution to accommodate various factors mentioned above is to reoptimize (or tweak) the IMRT plan based on the patient's setup CBCT. In order to fully utilize the volumetric imaging data, a new paradigm with a seamlessly integrated simulation, planning, verification and delivery procedure is needed. Until this is realized clinically, the volumetric image-based patient positioning is simply an expensive extension of the existing planar setup procedure.

In the DEDM technique described above, a pre-assumption is that the accurate registration between pCT and CBCT is achievable. In reality, an excellent registration is attainable in the case of rigid bodies through a variety of means, such as fiducials, manual, or automated registration method. The validity and advantage of the approach in this situation can, therefore, be easily envisaged. In the phantom case presented earlier, it is perceivable that the CBCT-phantom dose calculation can be trivially improved if the pCT imaging data (figure 5(b)) are mapped to CBCT (figure 5(a)). The existence of organ deformation in more general situations necessitates a deformable registration for electron density mapping. The BSpline method used in this work was employed for several IGRT-related projects involving intra- and inter-modality deformable registrations and its performance has been demonstrated (Balter *et al* 2005, Schreiber *et al* 2006, Dietrich *et al* 2006, Kamath *et al* 2006). The studies carried out by our group and others (Allen *et al* 2004, Brock *et al* 2003, Coselmon *et al* 2004, Xiong *et al* 2006) have suggested that a spatial accuracy better than 3 mm is readily achievable using various deformable image registration techniques. The accuracy can be further improved when more sophisticated methods are used (Kamath *et al* 2006). To assess the influence of registration accuracy on the mCBCT-based dose reconstruction, for the first prostate case, we intentionally introduced a number of 'wrong assignments' of the

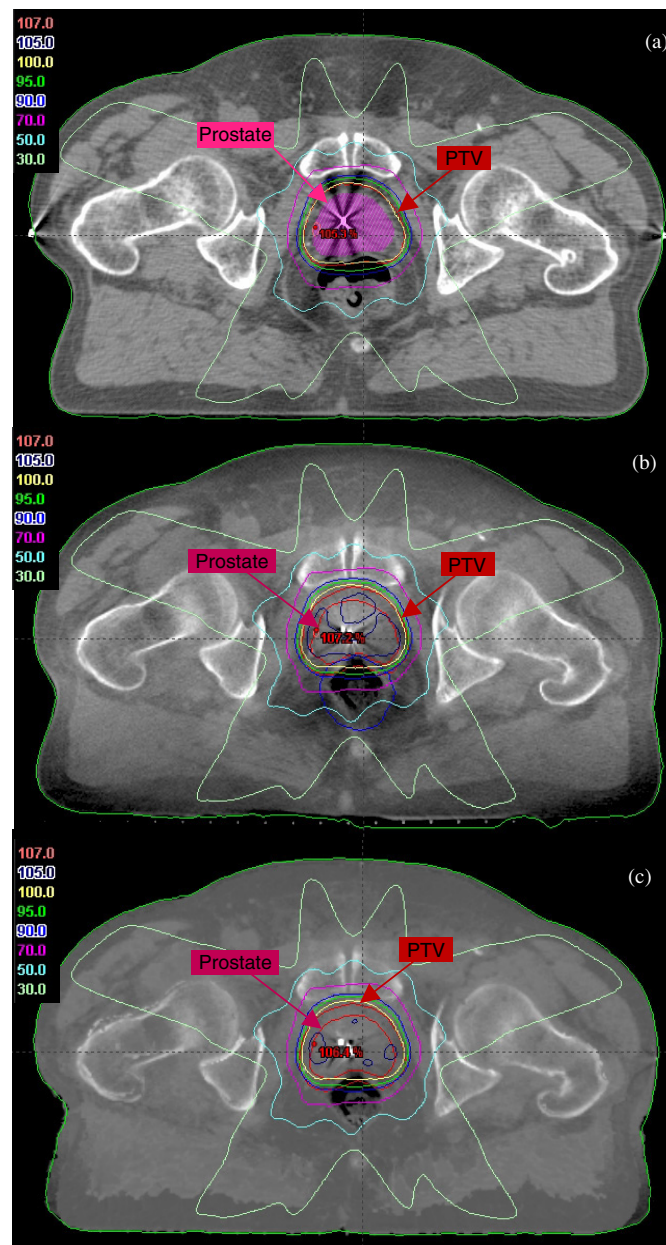


Figure 10. Dose distributions in a transverse slice calculated based on the: (a) pCT; (b) CBCT; (c) mCBCT for the first prostate case. DVHs of the prostate, PTV, rectum and bladder obtained based on the pCT, CBCT and mCBCT images for the case are plotted in (d).

electron density distribution when mapping the electron density from pCT to CBCT (the spatial inaccuracy of the ‘wrong assignments’ was restricted to within 3 mm in the soft-tissue regions in these digital experiments). The resultant dosimetric deviations from the presented mCBCT-based calculations were found negligible (all within 1.5%), which indicate that (i) the

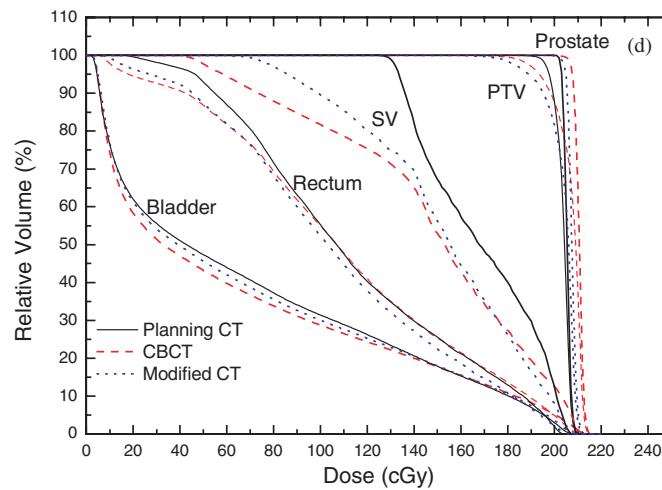


Figure 10. (Continued.)

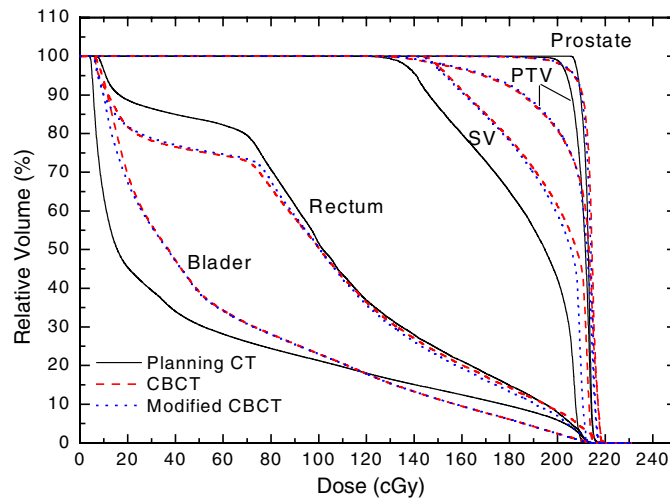


Figure 11. Comparison of DVHs of the prostate, PTV, rectum and bladder obtained based on the pCT, CBCT and mCBCT images for the second prostate case.

final dose distribution is not very sensitive to small regional variations in the registration; and (ii) the mCBCT-reconstructed dose represents a good ‘surrogate’ of the ‘ground truth’. The fact that the CBCT- and mCBCT-based dose calculations differ little also supports the above arguments. A more direct and perhaps the ultimate validation of the DEDM could be accomplished if the patient had undergone a CT on-rail scan (right before or after the CBCT acquisition) in addition to the pCT and CBCT. Before this type of data becomes available, we alert the readers that the DEDM approach remains heuristic in nature and one should bear its inherent limitation in mind when using it for dose calculation.

In the presence of intra-scan organ motion, our phantom study indicated that significant dosimetric errors could happen. The same conclusion can be drawn from the lung study.

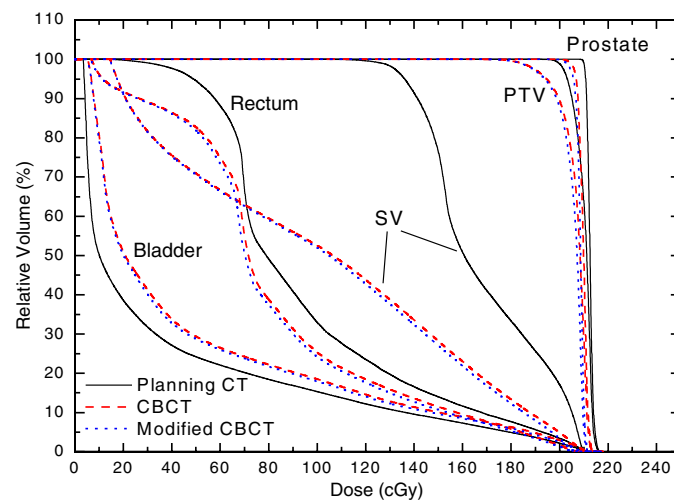


Figure 12. Comparison of DVHs of the prostate, PTV, rectum and bladder obtained based on the pCT, CBCT and mCBCT images for the third prostate case.

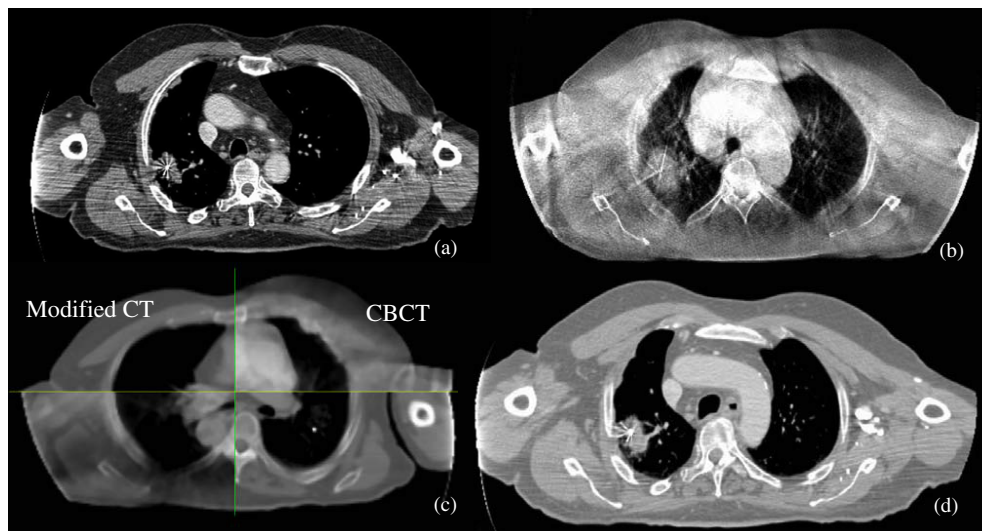


Figure 13. CT, CBCT and modified CT images for the lung case: (a) planning CT; (b) CBCT; (c) checkerboard image after the deformation registration; and (d) modified CBCT.

Recent developments of 4D CT (Allen *et al* 2004, Berbeco *et al* 2005, de Koste *et al* 2003, Vedam *et al* 2003, Wink *et al* 2005) and 4D CBCT (Dietrich *et al* 2006, Sonke *et al* 2005, Li *et al* 2006a, 2006b), in conjunction with the proposed DEDM method, may provide a valuable solution to the problem of CBCT-based dose calculation in the regions of thorax and upper abdomen. This is clearly a subject of future investigation.

It is worth mentioning that previous studies indicate that bulk CT density correction can be quite effective for heterogeneity corrections for all treatment sites. For a prostate case treated with high energy x-rays, the homogeneous dose calculation method will only introduce

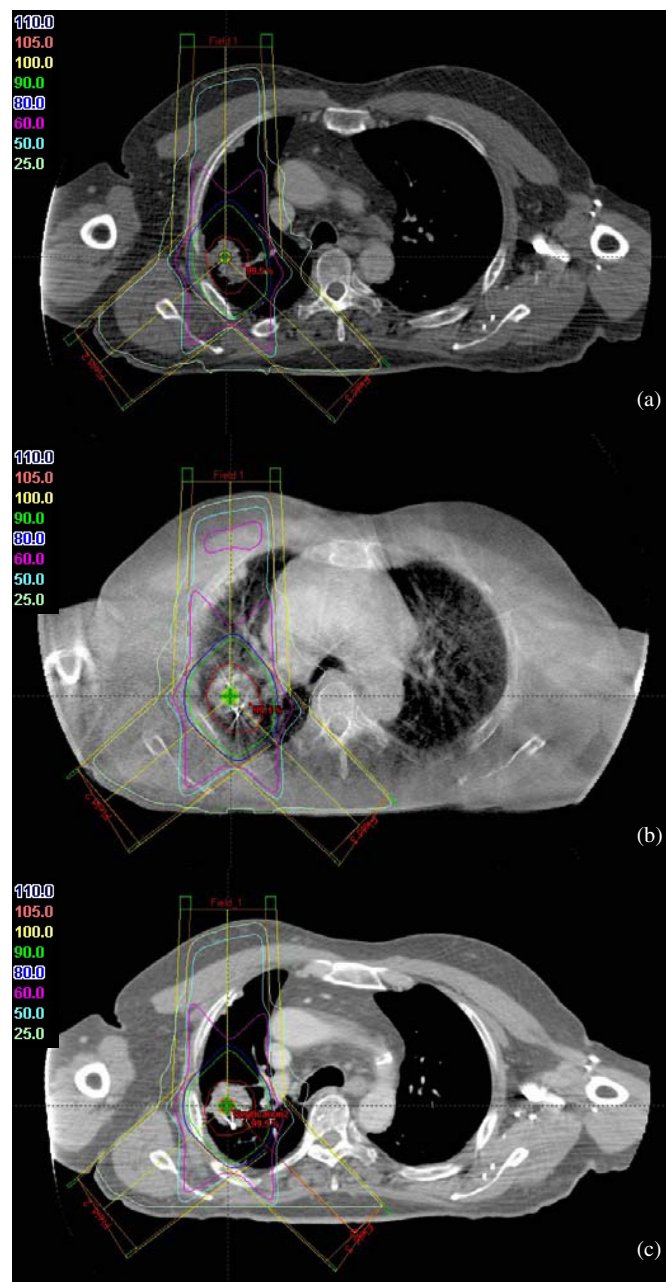


Figure 14. Dose distribution in a transverse slice calculated based on (a) planning CT; (b) CBCT; and (c) modified CBCT for the lung case. A comparison of the DVHs of GTV, PTV, right lung and spinal cord obtained based on planning CT, CBCT and the modified CBCT images is shown in (d).

2–4% error (depending on beam directions and relative weights). It may be acceptable to use the homogeneous dose calculation method for certain cases, as suggested by a study by Chen *et al* (2004). A detailed study along this line should be useful in the future.

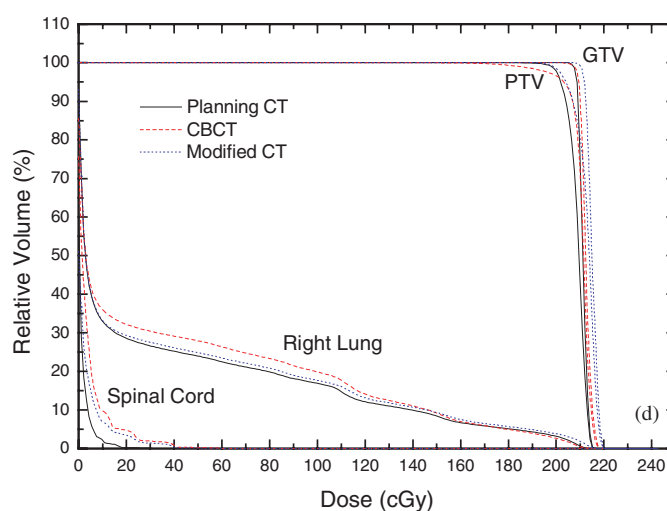


Figure 14. (Continued.)

5. Conclusion

On-board CBCT provides useful volumetric anatomy information for patient positioning verification. When used for dose verification calculation, a reliable relationship between the HU and relative electron density is needed. Our phantom and prostate patient studies have indicated that, in the absence of motion artefacts, the dosimetric accuracy of CBCT-based dose calculation is acceptable for the purpose of dosimetric checks. Our motion phantom and lung patient studies showed that the dosimetric errors become more pronounced when intra-scanning organ motion is present. In this situation, a direct use of CBCT for dose calculation is not recommended. Before an effective CBCT image quality improving technique is in place, DEDM may be a useful interim solution for improved dose calculation.

Acknowledgments

We wish to acknowledge Drs C King, S Hancock, T Pawlicki, P Maxim and G Luxton for useful discussions. The support from the National Cancer Institute (1 R01 CA98523-01), Department of Defense (PC040282) and Varian Medical Systems are also gratefully acknowledged.

References

- Allen A M, Siracuse K M, Hayman J A and Balter J M 2004 Evaluation of the influence of breathing on the movement and modeling of lung tumors *Int. J. Radiat. Oncol. Biol. Phys.* **58** 1251–7
- Balter J M, Wright J N, Newell L J, Friemel B, Dimmer S, Cheng Y, Wong J, Vertatschitsch E and Mate T P 2005 Accuracy of a wireless localization system for radiotherapy *Int. J. Radiat. Oncol. Biol. Phys.* **61** 933–7
- Berbeco R I, Neicu T, Rietzel E, Chen G T and Jiang S B 2005 A technique for respiratory-gated radiotherapy treatment verification with an EPID in cine mode *Phys. Med. Biol.* **50** 3669–79
- Brock K K, McShan D L, Ten Haken R K, Hollister S J, Dawson L A and Balter J M 2003 Inclusion of organ deformation in dose calculations *Med. Phys.* **30** 290–5
- Chang J, Sillanpaa J, Ling C C, Seppi E, Yorke E, Mageras G and Amols H 2006 Integrating respiratory gating into a megavoltage cone-beam CT system *Med. Phys.* **33** 2354–61

- Chen L, Price R A Jr, Wang L, Li J, Qin L, McNeeley S, Ma C M, Freedman G M and Pollack A 2004 MRI-based treatment planning for radiotherapy: dosimetric verification for prostate IMRT *Int. J. Radiat. Oncol. Biol. Phys.* **60** 636–47
- Coolens C, Evans P M, Seco J, Webb S, Blackall J M, Rietzel E and Chen G T 2006 The susceptibility of IMRT dose distributions to intrafraction organ motion: an investigation into smoothing filters derived from four dimensional computed tomography data *Med. Phys.* **33** 2809–18
- Coselmon M M, Balter J M, McShan D L and Kessler M L 2004 Mutual information based CT registration of the lung at exhale and inhale breathing states using thin-plate splines *Med. Phys.* **31** 2942
- Court L E, Dong L, Lee A K, Cheung R, Bonnen M D, O'Daniel J, Wang H, Mohan R and Kuban D 2005 An automatic CT-guided adaptive radiation therapy technique by online modification of multileaf collimator leaf positions for prostate cancer *Int. J. Radiat. Oncol. Biol. Phys.* **62** 154–63
- de Koste J R, Lagerwaard F J, de Boer H C, Nijssen-Visser M R and Senan S 2003 Are multiple CT scans required for planning curative radiotherapy in lung tumors of the lower lobe? *Int. J. Radiat. Oncol. Biol. Phys.* **55** 1394–9
- Dietrich L, Jetter S, Tucking T, Nill S and Oelfke U 2006 Linac-integrated 4D cone beam CT: first experimental results *Phys. Med. Biol.* **51** 2939–52
- Hawkins M A, Brock K K, Eccles C, Moseley D, Jaffray D and Dawson L A 2006 Assessment of residual error in liver position using kV cone-beam computed tomography for liver cancer high-precision radiation therapy *Int. J. Radiat. Oncol. Biol. Phys.* **66** 610–9
- Hector C L, Webb S and Evans P M 2000 The dosimetric consequences of inter-fractional patient movement on conventional and intensity-modulated breast radiotherapy treatments *Radiother. Oncol.* **54** 57–64
- Hugo G D, Agazaryan N and Solberg T D 2003 The effects of tumor motion on planning and delivery of respiratory-gated IMRT *Med. Phys.* **30** 1052–66
- Jaffray D A, Siewerdsen J H, Wong J W and Martinez A A 2002 Flat-panel cone-beam computed tomography for image-guided radiation therapy *Int. J. Radiat. Oncol. Biol. Phys.* **53** 1337–49
- Kamath S, Paquin D, Levy D, Schreibmann E and Xing L 2006 Incorporating priori knowledge into deformable image registration 2006 *Annual Meeting of ASTRO (Philadelphia, PA)*
- Langen K M, Meeks S L, Poole D O, Wagner T H, Willoughby T R, Kupelian P A, Ruchala K J, Haimeri J and Olivera G H 2005 The use of megavoltage CT (MVCT) images for dose recomputations *Phys. Med. Biol.* **50** 4259–76
- Li T, Schreibmann E, Thorndyke B, Tillman G, Boyer A, Koong A, Goodman K and Xing L 2005 Radiation dose reduction in four-dimensional computed tomography *Med. Phys.* **32** 3650–60
- Li T, Schreibmann E, Yang Y and Xing L 2006a Motion correction for improved target localization with on-board cone-beam computed tomography *Phys. Med. Biol.* **51** 253–67
- Li T, Xing L, Munro P, McGuinness C, Yang Y, Cao M, Loo B and Koong A 2006b Four-dimensional cone-beam computed tomography using an on-board imager *Med. Phys.* **33** 3825–33
- Litzenberg D W, Balter J M, Hadley S W, Sandler H M, Willoughby T R, Kupelian P A and Levine L 2006 Influence of intrafraction motion on margins for prostate radiotherapy *Int. J. Radiat. Oncol. Biol. Phys.* **65** 548–53
- Paquin D, Levy D and Xing L 2006 Hybrid multistage landmark and deformable image registration *IEEE Pattern Recognit. Mach. Intell.* submitted
- Paskalev K, Ma C M, Jacob R, Price R, McNeeley S, Wang L, Movsas B and Pollack A 2004 Daily target localization for prostate patients based on 3D image correlation *Phys. Med. Biol.* **49** 931–9
- Ruan D, Fessler J A, Balter J M and Sonke J J 2006 Exploring breathing pattern irregularity with projection-based method *Med. Phys.* **33** 2491–9
- Schreibmann E, Chen G T and Xing L 2006 Image interpolation in 4D CT using a BSpline deformable registration model *Int. J. Radiat. Oncol. Biol. Phys.* **64** 1537–50
- Sonke J J, Zijp L, Remeijer P and van Herk M 2005 Respiratory correlated cone beam CT *Med. Phys.* **32** 1176–86
- Sorcini B and Tilikidis A 2006 Clinical application of image-guided radiotherapy, IGRT (on the Varian OBI platform) *Cancer Radiother.* **10** 252–7
- Thilmann C *et al* 2006 Correction of patient positioning errors based on in-line cone beam CTs: clinical implementation and first experiences *Radiat. Oncol.* **1** 16
- Vedam S S, Keall P J, Kini V R, Mostafavi H, Shukla H P and Mohan R 2003 Acquiring a four-dimensional computed tomography dataset using an external respiratory signal *Phys. Med. Biol.* **48** 45
- Webb S 2006 Motion effects in (intensity modulated) radiation therapy: a review *Phys. Med. Biol.* **51** R403–25
- Wink N M, McNitt-Gray M F and Solberg T D 2005 Optimization of multi-slice helical respiration-correlated CT: the effects of table speed and rotation time *Phys. Med. Biol.* **50** 5717–29

- Xiong L, Viswanathan A, Stewardt A J, Haker S, Tempny C M, Chin L and Cormack R A 2006 Deformable structure registration of bladder through surface mapping *Med. Phys.* **33** 1848–56
- Xing L, Thorndyke B, Schreibmann E, Li T, Yang Y, Kim G, Luxton G and Koong A 2006 Overview of image guided radiation therapy (IGRT) *Med. Dosim.* **31** 91–122
- Yin F F, Guan H and Lu W 2005 A technique for on-board CT reconstruction using both kilovoltage and megavoltage beam projections for 3D treatment verification *Med. Phys.* **32** 2819–26



Formulating adaptive radiation therapy (ART) treatment planning into a closed-loop control framework*

Adam de la Zerda¹, Benjamin Armbruster² and Lei Xing³

¹ Department of Electrical Engineering, Stanford University, Stanford, CA 94305-9505, USA

² Department of Management Science and Engineering, Stanford University, Stanford, CA 94305-4026, USA

³ Department of Radiation Oncology, Stanford University, Stanford, CA 94305-5847, USA

E-mail: lei@reyes.stanford.edu

Received 17 January 2007, in final form 25 April 2007

Published 14 June 2007

Online at stacks.iop.org/PMB/52/4137

Abstract

While ART has been studied for years, the specific quantitative implementation details have not. In order for this new scheme of radiation therapy (RT) to reach its potential, an effective ART treatment planning strategy capable of taking into account the dose delivery history and the patient's on-treatment geometric model must be in place. This paper performs a theoretical study of dynamic closed-loop control algorithms for ART and compares their utility with data from phantom and clinical cases. We developed two classes of algorithms: those *Adapting to Changing Geometry* and those *Adapting to Geometry and Delivered Dose*. The former class takes into account organ deformations found just before treatment. The latter class optimizes the dose distribution accumulated over the entire course of treatment by adapting at each fraction, not only to the information just before treatment about organ deformations but also to the dose delivery history. We showcase two algorithms in the class of those *Adapting to Geometry and Delivered Dose*. A comparison of the approaches indicates that certain closed-loop ART algorithms may significantly improve the current practice. We anticipate that improvements in imaging, dose verification and reporting will further increase the importance of adaptive algorithms.

(Some figures in this article are in colour only in the electronic version)

1. Introduction

Current IMRT treatment plan optimization and dose delivery are two decoupled steps (AAPM IMRT Sub-committee 2003, Webb 2001). In each fraction, the patient geometry is hardly the

* Presented at ASTRO Annual Meeting, 2006, Philadelphia, PA.

same as in the pre-treatment CT simulation. A commonly used method to take the uncertainty into account is to add a safety margin, whose size is based on population statistics, to the target and sensitive structures (Balter *et al* 1995, van Herk 2006). This significantly compromises the success of radiation therapy.

Recently, cone-beam computed tomography (CBCT) integrated with a medical linear accelerator has become available and promises to improve the situation. CBCT provides a valuable 3D (or even possibly 4D) geometric model of the patient in the treatment position and allows for verification of the delivered dose distribution (Xing *et al* 2006). This not only affords an opportunity for on-line correction of patient setup error and inter-fraction rigid motion (Oldham *et al* 2005, Pouliot *et al* 2005), but also allows dose recalculation and adaptive radiation therapy (ART) (Langen *et al* 2005, Yang *et al* 2007), which uses the volumetric information to adjust the treatment plan each fraction to the updated patient anatomy and positioning. A significant promise of ART is the optimal compensation of uncertainties including organ deformation and inter-fraction organ motion as well as dosimetric errors incurred in previous fractions (Trofimov *et al* 2005, Wu *et al* 2006, Mohan *et al* 2005, de la Zerda *et al* 2006, Olivera *et al* 2006). To realize ART clinically and maximally exploit the potential of this new form of image guided radiation therapy (IGRT), a robust inverse planning strategy for ART must be in place.

The purpose of this work is to develop dynamic closed-loop control strategies for ART inverse planning and to demonstrate their utility with data from phantom and clinical cases. Closed-loop control algorithms are a general tool for dealing with time-dependent systems (Widrow and Stearns 1985, Widrow and Walach 1995) and are used to solve a variety of problems including automobile cruise control, supply chain optimization, computer chip design and spaceship navigation. The algorithms in all these applications share the same basic closed-loop control framework of repeated re-evaluation and re-planning. ART is a natural application for closed-loop control because CBCT provides frequently updated system information. To meet different clinical requirements, we investigate a few variants of these algorithms.

The next section starts with a brief review of the foundations of closed-loop control. Section 2 continues by presenting a formalism for ART planning, the intensity-modulated radiation therapy (IMRT) approach, and our new ART algorithms. In section 3, we demonstrate the significance of our new approach with phantom and patient case studies. Section 4 takes a broader perspective to discuss this work and directions for future research. We conclude in section 5.

2. Methods and materials

This section starts with an overview of closed-loop control and then later describes various closed-loop control algorithms for ART before summarizing these algorithms in table 2.

2.1. Foundations of closed-loop control

The use of feedback makes closed-loop control unique (Widrow and Stearns 1985, Widrow and Walach 1995, Yan *et al* 1997). In open-loop control, figure 1(a), some *input* is fed to the *controller* which then decides on an *action*. The controller then performs that action on the *system* (the system being the physical or biological system we want to control), effectively putting the system into a new state (which hopefully is ‘better’ in some sense). We could simulate an open-loop control context by connecting the output of the algorithm implemented

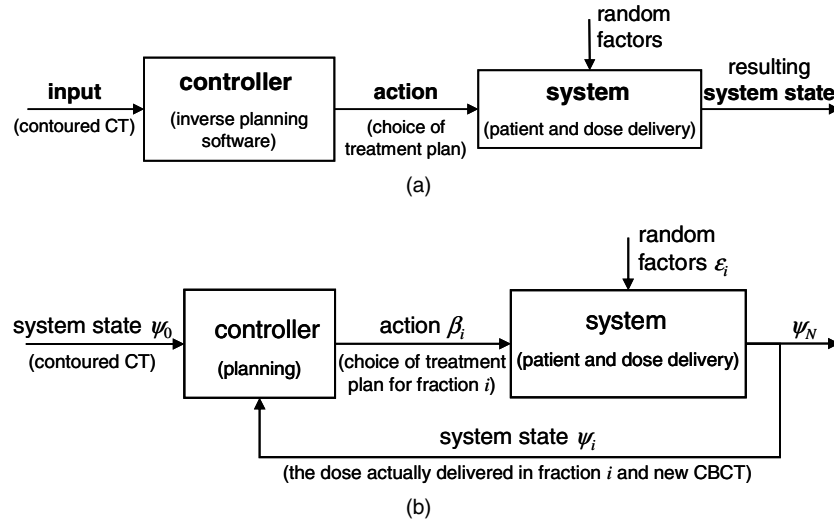


Figure 1. (a) Open-loop control (conventional treatment planning), (b) the closed-loop control framework.

by the controller to a simulation of the system: the input is fed to the algorithm which feeds an action to the system simulator which outputs the new state of the system.

Conventional inverse planning is a form of open-loop control. The *input* is a set of contoured CT images or the geometric model of the patient. The *controller* is the inverse planning software, and it outputs a treatment plan (the action). Finally, a simulator of the system (modeling the execution of the plan) uses the treatment plan and some random factors to output the resulting system state.

In closed-loop control, the controller is not run just once but repeatedly, each time receiving the current state of the system as its input (Widrow and Stearns 1985, Widrow and Walach 1995, Yan *et al* 1997). The term *feedback* is used because the effect of the current action (the new state of the system) is used by the controller to plan the next action. Suppose we have N time periods (treatment fractions), and we let β_i be the action in period i (treatment plan for fraction i) and ψ_i the resulting system state at the end of period i . Then a closed-loop controller is a function ξ_i producing an action for the current period from the state at the end of the last period $\beta_i = \xi_i(\psi_{i-1})$.

We propose to plan ART using closed-loop control, figure 1(b), where the controller is the inverse planning software and the state of the system after fraction i , $\psi_i = (\psi_i^{\text{geometry}}, \psi_i^{\text{cumdose}})$, has two parts: the patient's geometric model derived from contoured CBCT images, ψ_i^{geometry} , and the cumulative dose, ψ_i^{cumdose} , delivered in fractions 1 through i . (Clearly, $\psi_0^{\text{cumdose}} = 0$.) Unlike the open-loop control in conventional RT, in ART the controller outputs a plan (the action) for only the current treatment fraction. Table 1 summarizes the relationship between control theory and treatment planning.

Closed-loop control algorithms (which we propose for ART) are richer than static open-loop control algorithms (found for example in conventional RT). A static open-loop controller determines a treatment plan, $(\beta_1, \dots, \beta_N)$, and therefore the final state of the system ψ_N is based only on the initial state of the system ψ_0 , whereas dynamic closed-loop algorithms re-evaluate the state each time step and based on that, decide their current action. Because of that, the treatment plan, $(\beta_1, \dots, \beta_N)$, depends not only on the initial state ψ_0 , but also on the progress made during treatment, $(\psi_0, \dots, \psi_{N-1})$. Hence closed-loop control algorithms

Table 1. Relationship between control theory and treatment planning.

Closed-loop control	Radiation therapy
Time period (i)	Fraction
Input (ψ_0)	Contoured CT images (ψ_0^{geometry})
Action in period i , (β_i)	Treatment plan for fraction i
System state after period i , (ψ_i)	Contoured CBCT images (ψ_i^{geometry}), and cumulative delivered dose (ψ_i^{cumdose})
Controller	RT inverse planning software
System	Patient geometry and treatment delivery
Random factors/noise in period i , (ε_i)	Setup errors, delivery errors, and organ deformations in fraction i

are more likely to produce better results than static open-loop control algorithms for time-dependent systems.

Treatment planning is a critical step to realizing the potential of ART in clinical practice. Current IMRT inverse planning is designed for a conventional fractionated treatment scheme (Bortfeld 1999, Webb 2001, Censor 2003, Xing *et al* 2005, Xiao *et al* 2000, Yang and Xing 2004b) and is incapable of planning an adaptive treatment with consideration of the dose delivery history and updated patient geometry. However, anticipated improvements in imaging and verifying the dose and anatomy during dose delivery drive the need for sophisticated algorithms for ART planning. The purpose of this work is to establish a dynamic control framework for adaptive radiation therapy to explore the subtleties of possible planning algorithms. This planning framework allows us to individualize radiation therapy for each patient by taking advantage of newly available volumetric imaging information.

2.2. Formalization of ART plan optimization

Consider plans, $(\beta_1, \dots, \beta_N)$, for N fractions. Suppose at voxel v , the importance factor is $\alpha(v)$ (Xing *et al* 1999) and the prescribed dose is $D^{\text{prescribed}}(v)$. We define a dose delivery function $D(\cdot)$, such that under plan β and delivery error ε the cumulative dose after fraction i is $\psi_i^{\text{cumdose}}(v) = \psi_{i-1}^{\text{cumdose}}(v) + D(v; \beta, \varepsilon, \psi_{i-1}^{\text{geometry}})$ at voxel v . Without delivery errors (i.e., without any setup errors or deformations of organs), $\varepsilon = 0$. Let B be the set of deliverable (feasible) plans. Our ultimate goal is then to find the feasible plan $(\beta_1, \dots, \beta_N)$ optimizing

$$\begin{aligned} \min_{\beta_1 \in B, \dots, \beta_N \in B} \sum_v \alpha(v) (D^{\text{prescribed}}(v) - \psi_N^{\text{cumdose}}(v))^2 \\ = \min_{\beta_1 \in B, \dots, \beta_N \in B} \sum_v \alpha(v) \left(D^{\text{prescribed}}(v) - \sum_{i=1}^N D(v, \beta_i, \varepsilon_i, \psi_{i-1}^{\text{geometry}}) \right)^2. \end{aligned} \quad (1)$$

The objective function is the weighted quadratic deviation of the cumulative delivered dose from the prescribed dose. There is no way to find in advance the optimal solution to this problem because the actual delivery error in fraction i , ε_i , is unknown when we must decide on the plan β_i . In general, ART dose optimization is a degenerate problem as there exist numerous ways to take the delivery history and new patient geometry into consideration. Finding the optimal adaptation strategy is an important part of ART treatment planning. While the simplest idea is to optimize

$$\min_{\beta_1 \in B, \dots, \beta_N \in B} \sum_v \alpha(v) \left(D^{\text{prescribed}}(v) - \sum_{i=1}^N D(v, \beta_i, 0, \psi_0^{\text{geometry}}) \right)^2,$$

we suggest in the following sections some more sophisticated approximations to problem (1). These approaches provide valuable ART alternatives and, as demonstrated later, they often lead to improved accumulated dose distributions. For comparison purpose, the conventional planning strategy with population-based margin is also formalized and described.

2.3. Baseline algorithm 1: planning with population-based margins

A common approach adds large margins to structures to compensate for delivery errors and uses the same plan every fraction, $\beta_1 = \dots = \beta_N$ (i.e., a static plan). These margins lead to modified dose prescriptions, $\tilde{D}^{\text{prescribed}}(\cdot)$, and importance factors, $\tilde{\alpha}(\cdot)$. This yields the optimization problem:

$$\beta_1 = \dots = \beta_N = \arg \min_{\beta \in B} \sum_v \tilde{\alpha}(v) \left(\frac{\tilde{D}^{\text{prescribed}}(v)}{N} - D(v, \beta, 0, \psi_0^{\text{geometry}}) \right)^2.$$

While this approximation is simple, it exposes much healthy tissue to high dose.

2.4. Baseline algorithm 2: Adapting to Changing Geometry

Assume that a CBCT image is taken prior to every treatment fraction. Based on the current anatomy information, a new plan for the current fraction is formed. This means that we consider $\psi_{i-1}^{\text{geometry}}$ when determining β_i . In particular we choose for fraction i the feasible plan that minimizes the weighted quadratic deviation from the initial prescribed dose: for all fractions i ,

$$\beta_i = \arg \min_{\beta \in B} \sum_v \alpha(v) \left(\frac{D^{\text{prescribed}}(v)}{N} - D(v, \beta, 0, \psi_{i-1}^{\text{geometry}}) \right)^2.$$

In other words, the algorithm tries to deliver the same daily prescribed dose, $D^{\text{prescribed}}/N$, in each fraction.

2.5. Adapting to Geometry and Delivered Dose

We can do better than in section 2.4, by taking into account not only the up-to-date CBCT imaging information $\psi_{i-1}^{\text{geometry}}$, but also other factors such as the cumulative delivered dose $\psi_{i-1}^{\text{cumdose}}$. Here we present two algorithms that take into account both $\psi_{i-1}^{\text{geometry}}$ and $\psi_{i-1}^{\text{cumdose}}$ when choosing a feasible plan for fraction i which minimizes the weighted quadratic deviation from the adaptive dose goal for this fraction. In general this adaptive dose goal may depend on the dose delivery history, $\psi_{i-1}^{\text{cumdose}}$, and predictions of future geometry. We assume that there is a mechanism that can calculate $\psi_{i-1}^{\text{cumdose}}$. The two algorithms we investigate differ in how they choose this adaptive dose goal. The first compensates every fraction for delivery errors in previous fractions, and the second incorporates predictions of the future patient geometry. (For example, the tumor shrinkage in response to the radiation therapy can be modeled by a tissue-feature based deformable registration (Chao *et al* 2007).)

2.5.1. Immediately Correcting Algorithm (ICA). This algorithm, figure 2, takes into account the dose delivery history as well as the anatomy model derived from daily CBCT images. No prediction is attempted about the patient model in the subsequent fractions. This algorithm adjusts the originally prescribed dose to completely compensate voxels which were overdosed (or underdosed) in previous fractions by decreasing (or increasing) the dose goal at those voxels. Specifically, it adds in fraction i the accumulated error from the previous fractions,

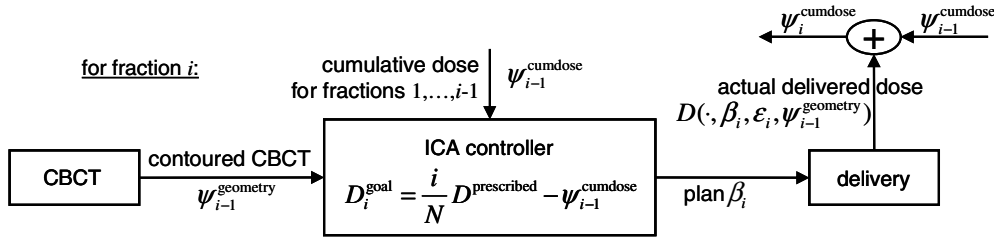


Figure 2. Block diagram for ICA.

$\frac{i-1}{N} D^{\text{prescribed}} - \psi_{i-1}^{\text{cumdose}}$, to the original daily prescription dose, $D^{\text{prescribed}}/N$, resulting in an adaptive dose goal of

$$D_i^{\text{goal}} = \frac{D^{\text{prescribed}}}{N} + \left(\frac{i-1}{N} D^{\text{prescribed}} - \psi_{i-1}^{\text{cumdose}} \right) = \frac{i}{N} D^{\text{prescribed}} - \psi_{i-1}^{\text{cumdose}}.$$

In the control theory literature, this is considered a form of proportional control. Note that the adaptive dose goal can be accurately calculated as long as the previous delivered doses, $\psi_{i-1}^{\text{cumdose}}$, are known. While this is currently not the case, the information is becoming increasingly available. This algorithm chooses the feasible plan $\beta_i \in B$ for fraction i that minimizes the weighted quadratic deviation of the planned dose, $D(\cdot, \beta_i, 0, \psi_{i-1}^{\text{geometry}})$ from the adaptive dose goal, D_i^{goal} :

$$\begin{aligned} \beta_i &= \arg \min_{\beta \in B} \sum_v \alpha(v) (D_i^{\text{goal}}(v) - D(v, \beta, 0, \psi_{i-1}^{\text{geometry}}))^2 \\ &= \arg \min_{\beta \in B} \sum_v \alpha(v) \left(\frac{i}{N} D^{\text{prescribed}}(v) - \psi_{i-1}^{\text{cumdose}}(v) - D(v, \beta, 0, \psi_{i-1}^{\text{geometry}}) \right)^2. \end{aligned} \quad (2)$$

2.5.2. Prudent Correcting Algorithm (PCA). Consider a treatment course of N fractions. Let i be the current fraction index and d be the number of fractions for which we forecast the patient's anatomy and position (e.g., $d = 2$ means predicting 2 days ahead of the current fraction). Note that d may be a function of the current fraction i . For instance, taking $d(i) = N - i$ means that we predict the anatomy and organ locations for the rest of the treatment course. In reality, we can interrupt a pre-designed re-planning schedule at any fraction and re-plan the subsequent fractions using a rolling horizon of d fractions: every time we re-plan we find the optimal plan for fractions $i, \dots, i + d$ (the current fraction and the subsequent d fractions) and then deliver the first part of the plan (i.e., until we re-plan again). In the control theory literature this is called finite horizon control. We then update the system when the next set of information becomes available (possibly before every fraction). Optimizing only for the current fraction ignores our (albeit imperfect) knowledge of the future and therefore misses the opportunity to compensate the dose in future fractions. To determine the plan chosen for fraction i we optimize

$$\begin{aligned} \min_{\beta'_1 \in B, \dots, \beta'_{i+d} \in B} \sum_v \alpha(v) & \left(\frac{i+1}{N} D^{\text{prescribed}}(v) - \psi_{i-1}^{\text{cumdose}}(v) \right. \\ & \left. - \sum_{j=i}^{i+d} D(v, \beta'_j, 0, \psi_j^{\text{predicted-geometry}}) \right)^2 \end{aligned} \quad (3)$$

where $\psi_i^{\text{predicted-geometry}}, \dots, \psi_{i+d}^{\text{predicted-geometry}}$ are the predicted anatomy locations for fractions i through $i + d$. The optimizers of problem (3) are a sequence of plans, $\beta_i, \dots, \beta_{i+d}$, the first of which is the plan, β_i , that we will implement in fraction i . Clinically, this scheme is useful when dealing with situations of tumor shrinkage after a re-planning CT/CBCT is done (see section 4 for more details).

We consider a simple prediction model in which the anatomy remains unchanged for the next d fractions to illustrate the approach (in practice one may use more sophisticated prediction models). That is, we assume $\psi_i^{\text{predicted-geometry}} = \psi_{i-1}^{\text{geometry}}$ for fractions i through $i + d$. For this prediction model, it can be shown that (3) reduces to

$$\beta_i = \arg \min_{\beta \in B} \sum_v \alpha(v) \left(\frac{i+d}{N} D_i^{\text{prescribed}}(v) - \psi_{i-1}^{\text{cumdose}}(v) - (1+d)D(v, \beta, 0, \psi_{i-1}^{\text{geometry}}) \right)^2.$$

We can also give this model the form of problem (2) by defining

$$D_i^{\text{goal}} = \frac{D^{\text{prescribed}}}{N} + \frac{1}{d+1} \left(\frac{i-d}{N} D^{\text{prescribed}} - \psi_{i-1}^{\text{cumdose}} \right). \quad (4)$$

If $d = 0$, then this algorithm coincides with the previous ICA algorithm. In equation (4), we see that this algorithm differs from the ICA algorithm because the correction to the accumulated error is divided among the subsequent $d + 1$ fractions of therapy to achieve better uniformity and robustness of therapy. Alternative schedules for compensating the accumulated error that accommodate specific clinical considerations should be easily implementable.

2.6. Evaluation and case study

We developed an in-house inverse planning platform to evaluate this closed-loop control framework and the novel *Adapting to Geometry and Delivered Dose* algorithms. This platform implements various RT planning strategies by optimizing fluence maps using the commercial nonlinear optimization code SNOPT (Gill *et al* 2005). The platform also evaluates the effectiveness of these plans by simulating the dose delivery function $D(\cdot)$.

Using this platform we compare the following algorithms: *Adapting to Changing Geometry* (our baseline), *Immediately Correcting Algorithm* (ICA), *Prudent Correcting Algorithm* (PCA) and *Perfect Foresight*. Results of the population-based margins planning algorithm are not shown since the selection of margin size varies with institution and, in general, it performs much worse than our baseline. *Perfect Foresight* is an algorithm that plans the entire course of treatment using accurate predictions of the future errors and motions during the course of treatment (see table 2). Note that in the *Perfect Foresight* algorithm, the entire treatment course is planned as a whole (i.e., the fractions and their corresponding anatomies are taken into account all in one optimization problem). In contrast to PCA with $d = N$, the *Perfect Foresight* algorithm ‘knows’ *exactly* what the anatomy will be in each fraction. When the prediction model is perfect, then PCA with $d = N$ is the same as the *Perfect Foresight*. It is worth stressing the purpose of the *Perfect Foresight* algorithm: it is not an algorithm in the usual sense (because we assume that it knows the future) but only a bound on normal algorithms. It is also worth noting that not even *Perfect Foresight* can achieve complete conformity. We include *Perfect Foresight* in our comparisons to have a more realistic standard against which to compare our algorithms. Further, as our ability of predicting the future becomes better, the performance of our algorithms (and most other reasonable algorithms) should approach that of *Perfect Foresight*. Thus, even though the performance of this algorithm may not actually be attainable, it sets a valuable theoretical upper bound on the performance of any ART planning algorithm. It is critically important for

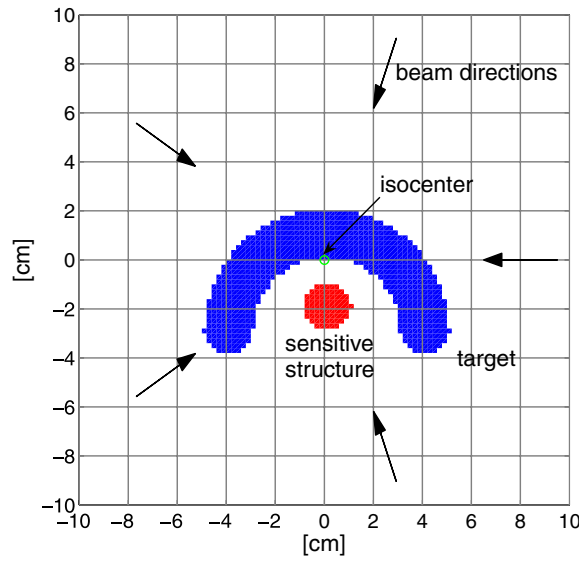


Figure 3. Phantom anatomy.

Table 2. Summary of various ART optimization schemes.

Algorithm	Objective functions for different schemes of dose optimization
Perfect Foresight	$\min_{\beta_1 \in B, \dots, \beta_N \in B} \sum_v \alpha(v) \left(D^{\text{prescribed}}(v) - \sum_{i=1}^N D(v, \beta_i, \varepsilon_i, \psi_{i-1}^{\text{geometry}}) \right)^2$ <p>Minimize the difference between the prescription and the delivered dose accumulated over <i>all</i> treatment fractions with knowledge of the dose delivery errors ε_i.</p>
Baseline 1: population-based margins	$\beta_1 = \dots = \beta_N = \arg \min_{\beta \in B} \sum_v \tilde{\alpha}(v) \left(\frac{\bar{D}^{\text{prescribed}}(v)}{N} - D(v, \beta, 0, \psi_0^{\text{geometry}}) \right)^2$ <p>Add margins to the prescription and then minimize the difference between the prescription and the daily planned dose.</p>
Baseline 2: Adapting to Changing Geometry	$\beta_i = \arg \min_{\beta \in B} \sum_v \alpha(v) \left(\frac{D^{\text{prescribed}}(v)}{N} - D(v, \beta, 0, \psi_{i-1}^{\text{geometry}}) \right)^2$ <p>Update the patient's geometric model every fraction using CBCT and plan a dose for that geometry that minimizes the difference to the daily prescription.</p>
Adapting to Geometry and Delivered Dose	
Immediately Correcting Algorithm (ICA)	$\beta_i = \arg \min_{\beta \in B} \sum_v \alpha(v) \left(\frac{i}{N} D^{\text{prescribed}}(v) - \psi_{i-1}^{\text{cumdose}}(v) - D(v, \beta, 0, \psi_{i-1}^{\text{geometry}}) \right)^2$ <p>Update the patient's geometric model every fraction using CBCT and plan a dose for that geometry that minimizes the difference to the prescribed dose plus the accumulated error.</p>
Prudent Correcting Algorithm (PCA)	$\beta_i = \arg \min_{\beta \in B} \sum_v \alpha(v) \left(\frac{i+d}{N} D^{\text{prescribed}}(v) - \psi_{i-1}^{\text{cumdose}}(v) - (1+d)D(v, \beta, 0, \psi_{i-1}^{\text{geometry}}) \right)^2$ <p>Update the patient's geometric model every fraction using CBCT and using that geometry plan a dose for remaining $(d+1)$ fractions that minimizes the difference to the prescribed dose plus the accumulated error.</p>

the algorithmic development of ART planning and provides an important measure helping the algorithm designer judge the potential for further improvement.

We compared the algorithms on a cubic phantom case and a prostate patient case. Phantom study is valuable for algorithm development, simply because the results are more intuitively

Table 3. Cumulative dose delivered to phantom for various algorithms relative to the baseline algorithm, *Adapting to Changing Geometry*.

Algorithm	Tumor		Sensitive structure		Normal tissue	
	Avg dose (%)	Std dev (%)	Avg dose (%)	Std dev (%)	Avg dose (%)	Std dev (%)
ICA	+9	+48	−48	−12	+18	+47
PCA	+8	−13	−18	−9	+7	+14
Perfect foresight	+9	−30	−89	−65	−8	+13

predictable/understandable and the ‘ground truth’ is readily attainable. A number of new tools/steps are involved in ART planning, such as deformable registration (Court and Dong 2003), CBCT-based dose calculation (Yang *et al* 2007) and dose optimization, each of them needs to be evaluated independently before they can be assembled together. Given the developmental status of these ‘enabling’ tools for ART, it seems logical to illustrate the methodology using some intuitive examples. The phantom, figure 3, is 20 cm in size and at its center has a C-shaped target enclosing a round sensitive structure. In the prostate case, the target volume was the prostate and the sensitive structures involved were rectum, femoral heads and bladder. In both cases, we asked the algorithms to generate an IMRT plan with 15 fractions and using five equally spaced beam directions. The tumor, sensitive structures and normal tissue were assigned importance factors of $\alpha = 10$, $\alpha = 3$ and $\alpha = 0.7$ respectively. The PCA parameter, d , was always set to the number of fractions left in the treatment $d = N - i$. We simulated setup errors by introducing, independently for every fraction, a random translation chosen uniformly at random from $[-1, 1]$ cm and a random rotation chosen uniformly at random from $[-2^\circ, 2^\circ]$. Other types of motion were not simulated in this study as a change in the motion model does not change the nature of the closed-loop control. Since the intentionally introduced motion has no systematic component, the prediction model for PCA assumes that the anatomy remains unchanged for the remainder of the treatment course (as described in section 2.5.2). In section 3, we compare the results visually in terms of the cumulative DVH and numerically for each organ in terms of the average dose and standard deviation of the dose.

3. Results

3.1. Phantom study

The results are shown graphically in figure 4 and statistically in table 3. Each row of table 3 compares an algorithm to our baseline, *Adapting to Changing Geometry*.

Figure 4(a) shows three benefits the *Adapting to Geometry and Delivered Dose* algorithms (and of course the *Perfect Foresight* algorithm) have over baseline 2, *Adapting to Changing Geometry*. For the first benefit, note how the 25% contour in our baseline is shifted slightly down from the sensitive structure. All the other algorithms do not show this shift. This shift is most likely due to some setup error (that is not corrected for in our baseline). The second benefit (also seen in the DVHs and table 3) is dose escalation to the tumor while keeping the sensitive structure close to 25% (unlike the baseline, these algorithms achieve tumor doses close to 100%). The third benefit is steeper gradients around the tumor (because dose correcting algorithms will not let errors accumulate).

Aside from these benefits, the dose distributions in figure 4(a) also show how much worse ICA is than PCA. As discussed above, ICA is able to escalate dose to the tumor while keeping the dose to the sensitive structure low, but along the way it overdoses normal tissue and decreases dose uniformity (see table 3). ICA may have fractions with higher doses than PCA

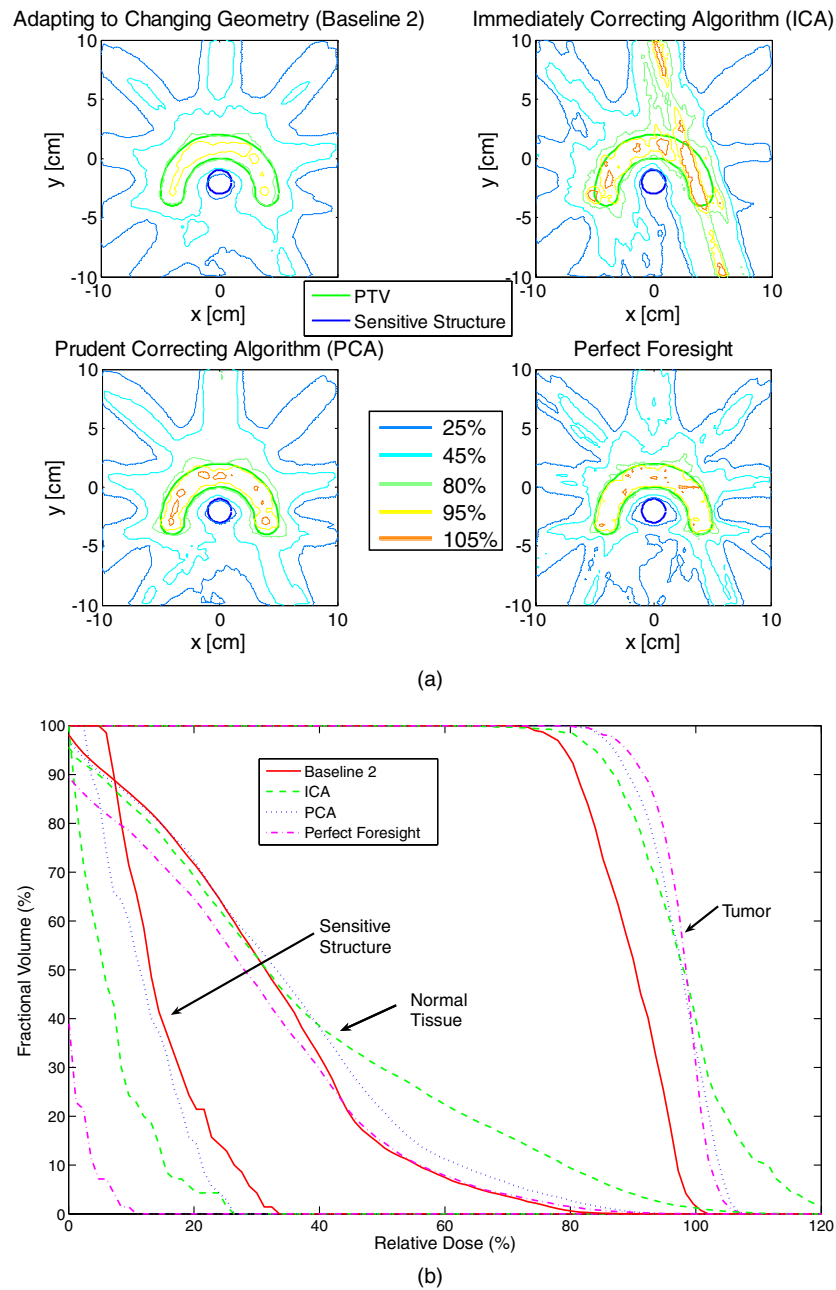


Figure 4. (a) Cumulative dose delivered to phantom as per cent of prescription. (b) DVHs of cumulative dose delivered to phantom as per cent of prescription.

since it tries to completely correct for dose delivery errors in the next fraction. We believe this makes ICA less robust than PCA because when combined with organ deformation or setup error these higher doses lead to bigger errors. The differing performance of the two *Adapting to Geometry and Delivered Dose* algorithms shows that the algorithmic details matter.

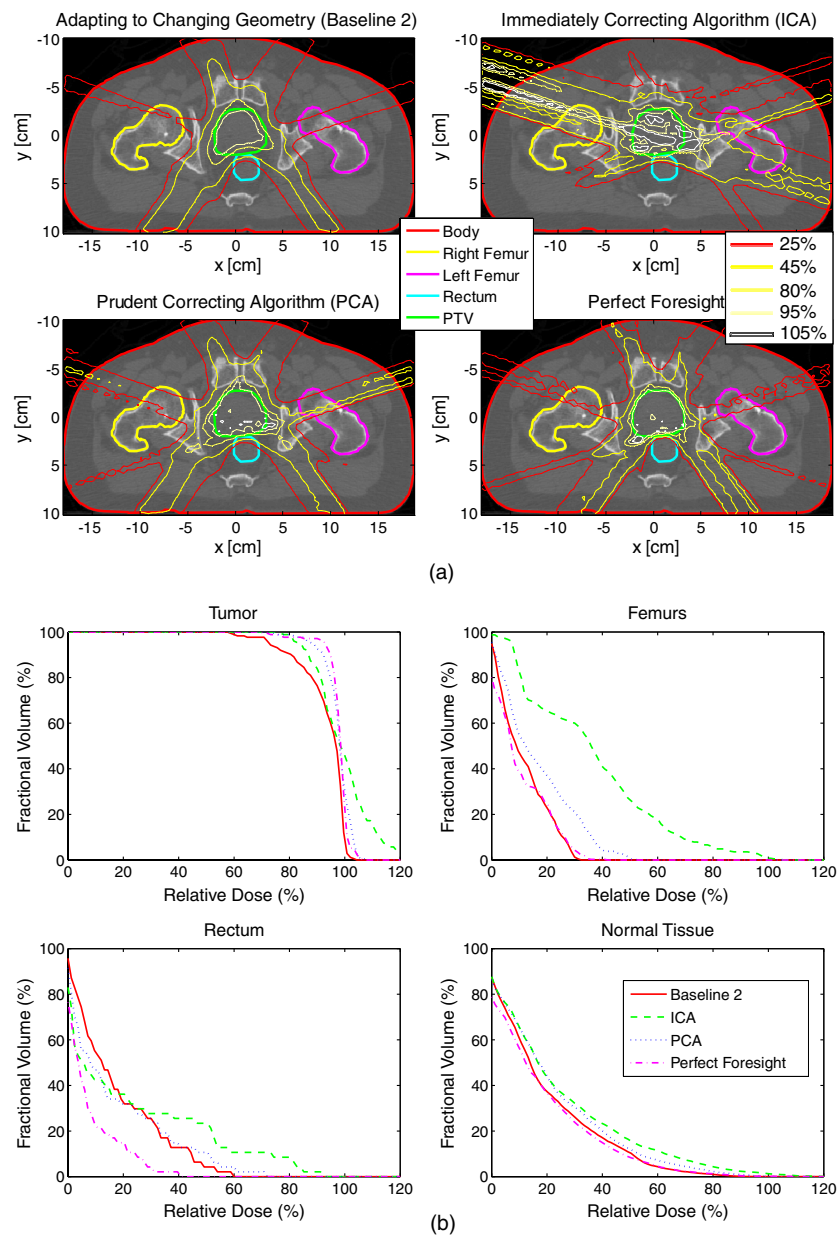


Figure 5. (a) Cumulative dose delivered in prostate study as per cent of prescription. (b) DVHs of cumulative dose delivered in prostate study as per cent of prescription.

Looking at the DVH in figure 4(b), we see that the *Perfect Foresight* algorithm achieves significantly better results than the adaptive algorithms (e.g., PCA). *Perfect Foresight* is superior not only in terms of tumor target coverage, but also in the sparing of sensitive structures. This is explained by the obvious fact that the *Perfect Foresight* algorithm has the fundamental advantage of accurately ‘knowing’ the future. The *Perfect Foresight* algorithm gives an upper limit on the potential of any closed-loop control algorithm. As treatment

Table 4. Cumulative dose delivered in a prostate study for various algorithms relative to the baseline algorithm, *Adapting to Changing Geometry*.

Algorithm	Tumor		Femurs		Rectum		Normal tissue	
	Avg dose (%)	Std dev (%)	Avg dose (%)	Std dev (%)	Avg dose (%)	Std dev (%)	Avg dose (%)	Std dev (%)
ICA	+6	+14	+196	+165	+21	+73	+24	+28
PCA	+5	−44	+40	+45	−5	+18	+13	+11
Perfect Foresight	+5	−49	−8	+12	−54	−40	−7	+2

imaging, planning and delivery techniques become more sophisticated, the performance of treatment will become closer and closer to the *Perfect Foresight* algorithm.

3.2. Prostate study

The resulting dose distributions and their DVHs are in figures 5(a) and (b). Each row of table 4 compares an algorithm to our baseline, *Adapting to Changing Geometry*.

As in the phantom case, the dose distributions (80% and 95% contour lines of figure 5(a)) show that PCA improves upon the baseline by being able to achieve dose escalation and increased uniformity to the tumor while keeping the dose to the rectum (the sensitive structure) low. Interestingly, ICA performs even worse than in the phantom case (it delivers more dose to the femurs and normal tissue). At the same time, even more than in the phantom case, the *Perfect Foresight* DVH shows how much the *Adapting to Geometry and Delivered Dose* algorithms can still improve. In particular, the dose could be lower to the femurs and to a lesser extent to normal tissue and the rectum. We believe that the difference between ICA and PCA arises from the fact that ICA achieves the adaptive goal by sequentially optimizing each fraction, whereas the PCA collectively optimizes a number of fractions with the goal of producing the best possible cumulative dose. ICA may not be optimal in producing the best possible cumulative dose because, when optimizing the treatment of a fraction, no knowledge about the subsequent fractions is taken into account. Thus it is not surprising that the performance of the PCA generally surpasses that of the ICA. Effectively, PCA benefits from the partial cancellation of random delivery errors caused by fractionation (Bortfeld *et al* 2002, Chui *et al* 2003).

4. Discussion

In current clinical practice, patient setup relies primarily on information from simulation and treatment planning (Balter 2003). During the whole course of treatment, usually the same treatment plan and setup DRRs (digitally reconstructed radiographs) are employed. Clinically, effort is focused on reproducing, with the aid of orthogonal planar images, the patient's geometry at the simulation stage using translations (and occasionally rotations). While this approach is justifiable for treatment of certain types of diseases such as brain tumors, it generally compromises the treatment because inter-fraction variations in volumes and shapes of the target and sensitive structures are not taken into account. Generally, these inter-fraction changes are multi-dimensional because organs can move relative to each other, and in an extreme situation, each voxel within a soft organ can move relative to other voxels in a complicated manner. Deformable image registration (Court and Dong 2003, Court *et al* 2005) helps by making these inter-fraction changes visible. But even then, compromised treatment is inevitable because the few degrees of freedom in patient setup (translation and

rotation) cannot completely correct for the multi-dimensional changes in the patient geometry: patient setup cannot simultaneously align all the involved structures.

ART solves the problems described in the previous paragraph by adjusting every fraction, not only the setup but also the treatment plan. We treat ART as a closed-loop control system where every fraction we re-optimize the radiation beams based on the latest information (e.g., coming from CBCT). The hope is that the many degrees of freedom available in selecting a plan allow us to compensate for the multi-dimensional changes in the patient geometry. In ART the plan is updated routinely, and the fraction-to-fraction variations of anatomy/physiology and dose delivery lead to modifications of the voxel-specific dose prescription.

ART can be implemented at different levels where the beams can be made to accommodate (i) the new patient setup and the deformed target shape; (ii) positional/anatomic/physiological changes of all involved organs; or (iii) deformable changes of organs and accumulated dose delivery errors. In conventional 3D conformal radiation therapy, it is not uncommon for a physician to modify a beam portal under the guidance of portal films while the patient is on the treatment couch. In a sense, this is an example of the first kind of ART listed above. However to adapt well to multi-dimensional organ deformations, the number of variables in the beam should be large. Thus the modality of choice for the treatments of type (ii) or (iii) is IMRT or alike. The information available in a particular treatment setup (e.g., whether information is captured about the delivered dose) restricts the types of ART possible in that setup. Our results show that correcting for dose delivery errors (i.e., type (iii) ART) incurred in previous treatment fractions is important. In conventional radiation therapy (and types (i) and (ii) ART) dose errors accumulate because they lack such a compensating mechanism. As technology improves, more sophisticated versions of ART with increased feedback can be implemented and our closed-loop control algorithms gain in relevance.

ART is a new strategy and its implementation entails the development of a number of ‘enabling’ tools, such as deformable image registration, automated contour mapping from planning CT to the CBCT just before treatment, and effective dose optimization algorithms. This paper tackles the dose optimization problem in ART by developing suitable dynamic control algorithms. These algorithms try to rapidly optimize the treatment plan each time a new set of input data is available. We propose two types of closed-loop control algorithms (*Adapting to Changing Geometry* and *Adapting to Geometry and Delivered Dose*, see table 2 for details) for different clinical applications. *Adapting to Changing Geometry* is useful when the accumulated dose is not known accurately. At this point, the deformable registration, which is essential for the calculation of accumulative dose, is still not robust enough for clinical use. *Adapting to Changing Geometry* is particularly helpful in this situation as it affords a currently implementable technique to cope with the nuisance caused by organ deformation. The ‘manual’ approach described by Mohan *et al* (2005) represents a special example of geometric adaptation. The algorithms *Adapting to Geometry and Delivered Dose* are designed to optimize the radiation treatment when both geometric and dosimetric updates are available from time to time. The two algorithms *Adapting to Geometry and Delivered Dose* (ICA and PCA) differ in how they use the update data to direct the treatment. First, ICA is proposed for the situation where the dose compensation needs to be performed right after each update of the system parameters. Clinically, ICA may be useful in dealing with unpredictable daily changes resulting from random and fraction-specific organ deformation such as rectum or bladder filling. Disease sites that are likely to benefit from the treatment include, but are not limited to, prostate, rectum and cervical cancers. In PCA, the task of dose compensation is accomplished by spreading the previous dosimetric errors over a number of subsequent fractions. For practical or clinical reason, the volumetric images just before treatment may not be available on a daily basis. In this case, PCA becomes a viable option for certain types of

diseases since it distributes the task of compensating a dosimetric error among a number of fractions instead of all-in-one. Indeed, there are clinical situations where the variation of the anatomy may not be notable from day to day but over a larger time span. Tumor shrinkage and weight loss in some head and neck cases represents a model example, where the CBCT and re-planning do not need to be performed on daily basis. Re-planning using PCA would allow us in this case to maximally benefit from state-of-the-art imaging information. In a way, PCA is similar to the off-line ‘dumped’ correction scheme proposed by Mackie *et al* (2003), Keller *et al* (2003), in which the correction is done at a certain point(s) of the treatment course and then applied to several subsequent fractions.

There is a point worth emphasizing here about the PCA algorithm. Even though the re-evaluation/re-planning are performed for a series of fractions, the specific plan used in PCA may vary from fraction to fraction as a result of PCA optimization. This may happen even if the anatomy/geometry does not change throughout the d fractions or the whole course of the treatment. In general, the deviation from the prescription consists of two factors: (i) the inherent difference between the prescription and the physically achievable dose distribution and (ii) the dose delivery error due to changes in the patient’s anatomy and/or actual dose delivery. Indeed, voxels within a target or a sensitive structure volume are generally not equivalent in achieving their dosimetric goals in IMRT planning (unless non-attenuating beams are used). Depending on the patient’s geometry, beam modality and field configuration, some regions may have a better chance to meet the prescription than others, and vice versa. Thus even when there is no geometric change at each fraction and the delivery can faithfully reproduce what is planned without any error, the dose goal will likely need to be modified to compensate for the inherent difference between the planned and prescribed doses in previous fraction(s). Dosimetrically, it is advantageous to optimally vary the plan for each fraction to accomplish the best possible cumulative dose distribution. A virtue of the PCA algorithm is that it is capable of incorporating our prediction about the patient’s anatomy. A simple prediction would be that the anatomy does not change in the following d fractions. A more sophisticated prediction would be, for example, a model predicting the tumor shrinkage for each of the following fractions (Chao *et al* 2007). In the special case where there is no geometric change in the whole course and no delivery error, the difference between ICA and PCA becomes how to better utilize the following fractional deliveries to make up the inherent dosimetric difference of previous fractions.

Although showing significant improvement, we note that the algorithms described in this paper are still far from the maximum theoretical performance limit. We encourage the development of more sophisticated closed-loop control algorithms that come closer to this limit. Better predictive schemes for future patient geometry should improve the PCA algorithm greatly. Our use of a weighted quadratic objective function for plan optimization (specifically the selection of beamlet weights) is probably suboptimal (Yang and Xing 2004a, 2004b, Wu *et al* 2002, Thieke *et al* 2003, Bedford and Webb 2006, Popple *et al* 2005, Oelfke and Bortfeld 1999, Choi and Deasy 2002). However, all the algorithms discussed in this paper would work with other objective functions. One could probably construct an optimal algorithm using the theory of optimal stochastic control. One hurdle to applying this theory is the fact that after delivering the treatment plan for some fraction, we must specify the probability of every possible system state. We are researching these ideas.

Finally, we emphasize that the proposed ART is purely dose based and does not consider any radiobiological effects. In principle treatment plan optimization should be based on biological models as they are clinically the most relevant. In practice, however, there is much controversy to this approach: the dose–response function linking the biological effect to the radiation dose is not sufficiently understood for various structures. Yang and Xing (2005)

have recently proposed a general time–dose–fractionation optimization strategy. This idea combined with our ART framework could potentially handle biologically adaptive radiation therapy. This is clearly a subject for future research.

5. Conclusion

The level of sophistication of adaptive therapy depends on the technology used to provide feedback data. In the last decade, the electronic portal imaging device (EPID) and the standalone CT scanner were the only technologies available for acquiring feedback information and the focus was on adaptively defining the margin for delineating the planning tumor target (PTV) (Yan *et al* 1997). In the era of onboard volumetric imaging, the meaning of ART is obviously different from previous studies. The feedback from onboard CBCT makes it possible for the first time to adaptively modify not only the margin but also the spatial dose distribution to best accommodate the geometric changes of the patient as well as the dosimetric deviations from the ideal prescription. The technical tools for implementing this new type of geometry- and dosimetry-based ART are still not available yet, and an effective treatment planning strategy capable of taking into account the dose delivery history and the patient's on-treatment geometric model must be in place in order for this new scheme of ART to reach its potential. We have formulated ART treatment planning into the framework of closed-loop control and developed three closed-loop ART algorithms: one *Adapting to Changing Geometry* and two *Adapting to Geometry and Delivered Dose* (ICA and PCA). The new formalism is useful in answering questions such as 'how to effectively utilize information about the current state and past delivery errors?', 'can we benefit from including the patient's future treatment(s) into today's adaptation strategy?', and 'what is the best achievable scenario of ART in an ideal situation?' All three algorithms are capable of incorporating volumetric imaging information acquired just before treatment and the latter two can also incorporate information on the accumulated dose. Application of the proposed algorithms to the phantom and clinical cases indicates that the algorithms utilizing the accumulated dose data (ICA and PCA) allow an escalation of the dose to the tumor target. For a patient positioning procedure with random setup errors, we found that the PCA performed best and significantly better than ICA even though the implemented algorithms differ only slightly. The over-correcting tendency of the ICA is not a desirable feature and should be avoided in the design of a practical ART planning algorithm. Generally, the performance of a closed-loop algorithm may depend on the motion model and other case-related issues. An important point here is that the details of closed-loop adaptation play a critical role in the success of ART. Clearly, much research remains to be done in developing more sophisticated closed-loop algorithms and searching for the best possible ART strategy to maximally utilize the geometric and dosimetric information that become or will soon become available. Given the complex interaction among errors, motion and the doses delivered to the patient, a sophisticated disease-site specific adaptation scheme may be useful.

Acknowledgments

We wish to thank Sachin Adlakha, Joseph Deasy, Yong Yang and Bernard Widrow for useful discussions. This work was supported in part by grants from the Department of Defense (PC040282), the National Cancer Institute (1R01 CA104205 and 5R01 CA98523), the Komen Breast Cancer Foundation (BCTR0504071) and a Graduate Research Fellowship from the

National Science Foundation. We also thank two anonymous referees for many helpful comments.

References

- AAPM IMRT Sub-committee 2003 Guidance document on delivery, treatment planning, and clinical implementation of IMRT: Report of the IMRT Sub-committee of the AAPM Radiation Therapy Committee *Med. Phys.* **30** 2089–115
- Balter J 2003 Target and critical structure definitions, dose prescription and reporting for IMRT *Intensity-Modulated Radiation Therapy: The State of the Art* ed J Palta and T Mackie (Colorado Springs, CO: Medical Physics Publishing) pp 183–98
- Balter J M, Sandler H M, Lam K, Bree R L, Lichter A S and ten Haken R K 1995 Measurement of prostate movement over the course of routine radiotherapy using implanted markers *Int. J. Radiat. Oncol. Biol. Phys.* **31** 113–8
- Bedford J L and Webb S 2006 Constrained segment shapes in direct-aperture optimization for step-and-shoot IMRT *Med. Phys.* **33** 944–58
- Bortfeld T 1999 Optimized planning using physical objectives and constraints *Semin. Radiat. Oncol.* **9** 20–34
- Bortfeld T, Jokivarsi K, Goitein M, Kung J and Jiang S 2002 Effects of intra-fraction motion on IMRT dose delivery: statistical analysis and simulation *Phys. Med. Biol.* **47** 2203–20
- Cao D, Earl M A, Luan S and Shepard D M 2006 Continuous intensity map optimization (CIMO): a novel approach to leaf sequencing in step and shoot IMRT *Med. Phys.* **33** 859–67
- Censor Y 2003 Mathematical optimization for the inverse problem of intensity-modulated radiation therapy *Intensity-Modulated Radiation Therapy: The State of the Art* ed J Palta and T Mackie (Colorado Springs, CO: Medical Physics Publishing) pp 25–50
- Chao M, Xie Y, Le Q and Xing L 2007 Modeling the volumetric change of head-and-neck tumor in response to radiation therapy 2007 *Annual Meeting of ASTRO (Los Angeles, CA)* (Abstract)
- Choi B and Deasy J O 2002 The generalized equivalent uniform dose function as a basis for intensity-modulated treatment planning *Phys. Med. Biol.* **47** 3579–89
- Court L E and Dong L 2003 Automatic registration of the prostate for computed-tomography-guided radiotherapy *Med. Phys.* **30** 2750–7
- Court L E, Dong L, Lee A K, Cheung R, Bonnen M D, O'Daniel J, Wang H, Mohan R and Kuban D 2005 An automatic CT-guided adaptive radiation therapy technique by online modification of multileaf collimator leaf positions for prostate cancer *Int. J. Radiat. Oncol. Biol. Phys.* **62** 154–63
- Chui C, Yorke E and Hong L 2003 The effects of intra-fraction organ motion on the delivery of intensity modulated field with a MLC *Med. Phys.* **30** 1736–46
- de la Zerda A, Armbruster B and Xing L 2006 Inverse planning for adaptive radiation therapy using dynamic programming *Annual Meeting of ASTRO (Philadelphia, PA)*
- Gill P E, Murray W and Saunders M A 2005 SNOPT: an SQP algorithm for large-scale constrained optimization *SIAM Rev.* **47** 99–131
- Keller H, Ritter M A and Mackie T R 2003 Optimal stochastic correction strategies for rigid-body target motion *Int. J. Radiat. Oncol. Biol. Phys.* **55** 261–70
- Langen K M, Meeks S L, Poole D O, Wagner T H, Willoughby T R, Kupelian P A, Ruchala K J, Haimeri J and Olivera G H 2005 The use of megavoltage CT (MVCT) images for dose recomputations *Phys. Med. Biol.* **50** 4259–76
- Mackie T R *et al* 2003 Image guidance for precise conformal radiotherapy *Int. J. Radiat. Oncol. Biol. Phys.* **56** 89–105
- Mohan R, Zhang X, Wang H, Kang Y, Wang X, Liu H, Ang K K, Kuban D and Dong L 2005 Use of deformed intensity distributions for on-line modification of image-guided IMRT to account for interfractional anatomic changes *Int. J. Radiat. Oncol. Biol. Phys.* **61** 1258–66
- Oelfke U and Bortfeld T 1999 Inverse planning for x-ray rotation therapy: a general solution of the inverse problem *Phys. Med. Biol.* **44** 1089–104
- Oldham M, Letourneau D, Watt L, Hugo G, Yan D, Lockman D, Kim L H, Chen P Y, Martinez A and Wong J W 2005 Cone-beam-CT guided radiation therapy: a model for on-line application *Radiother. Oncol.* **75** 271E1–8
- Olivera G H, Mackie T R, Ruchala K, Lu W and Kapatoes J 2006 Adaptive radiation therapy (art) strategies using helical tomotherapy *Image-Guided IMRT* ed T Bortfeld, R Schmidt-Ullrich, W De Deve and D E Wazer (Berlin: Springer) pp 235–246
- Popple R A, Prellow P B, Spencer S A, De Los Santos J F, Duan J, Fiveash J B and Brezovich I A 2005 Simultaneous optimization of sequential IMRT plans *Med. Phys.* **32** 3257–66
- Pouliot J *et al* 2005 Low-dose megavoltage cone-beam CT for radiation therapy *Int. J. Radiat. Oncol. Biol. Phys.* **61** 552–60

- Thieke C, Bortfeld T, Niemierko A and Nill S 2003 From physical dose constraints to equivalent uniform dose constraints in inverse radiotherapy planning *Med. Phys.* **30** 2332–9
- Trofimov A, Reitzel E, Lu H M, Martin B, Jiang S, Chen G and Bortfeld T 2005 Temporo-spatial IMRT optimization: concepts, implementation and initial results *Phys. Med. Biol.* **50** 2779–98
- van Herk M 2006 Errors and margins in radiotherapy *Semin. Radiat. Oncol.* **14** 52–64
- Webb S 2001 *Intensity-Modulated Radiation Therapy* (Bristol: Institute of Physics Publishing)
- Widrow B and Stearns S 1985 *Adaptive Signal Processing* (Upper Saddle River, NJ: Prentice-Hall)
- Widrow B and Walach E 1995 *Adaptive Inverse Control* (Upper Saddle River, NJ: Prentice-Hall)
- Wu Q, Liang J and Yan D 2006 Application of dose compensation in image-guided radiotherapy of prostate cancer *Phys. Med. Biol.* **51** 1405–19
- Wu Q, Mohan R, Niemierko A and Schmidt-Ullrich R 2002 Optimization of intensity-modulated radiotherapy plans based on the equivalent uniform dose *Int. J. Radiat. Oncol. Biol. Phys.* **52** 224–35
- Xiao Y, Galvin J, Hossain M and Valicenti R 2000 An optimized forward-planning technique for intensity modulated radiation therapy *Med. Phys.* **27** 2093–9
- Xing L, Li J G, Donaldson S, Le Q T and Boyer A L 1999 Optimization of importance factors in inverse planning *Phys. Med. Biol.* **44** 2525–36
- Xing L, Thorndyke B, Schreiber E, Yang Y, Li T F, Kim G Y, Luxton G and Koong A 2006 Overview of image-guided radiation therapy *Med. Dosim.* **31** 91–112
- Xing L, Wu Q, Yang Y and Boyer A 2005 Physics of IMRT *Intensity-Modulated Radiation Therapy: A Clinical Perspective* ed A Mundt and J Roeske (Hamilton: BC Decker) pp 20–52
- Yan D, Vicini F, Wong J and Martinez A 1997 Adaptive radiation therapy *Phys. Med. Biol.* **42** 123–132
- Yang Y, Schreiber E, Li T and Xing L 2007 Dosimetric evaluation of kV cone-beam CT (CBCT) based dose calculation *Phys. Med. Biol.* **52** 685–705
- Yang Y and Xing L 2004a Clinical knowledge-based inverse treatment planning *Phys. Med. Biol.* **49** 5101–17
- Yang Y and Xing L 2004b Inverse treatment planning with adaptively evolving voxel-dependent penalty scheme *Med. Phys.* **31** 2839–44
- Yang Y and Xing L 2005 Optimization of radiation dose–time–fractionation scheme with consideration of tumor specific biology *Med. Phys.* **32** 3666–77

Automated contour mapping using sparse volume sampling for 4D radiation therapy



Ming Chao, Eduard Schreibmann, Tianfang Li, Nicole Wink, and Lei Xing^{a)}

Department of Radiation Oncology, Stanford University School of Medicine, Stanford, California 94305-5847

(Received 26 November 2006; revised 16 July 2007; accepted for publication 16 August 2007; published 26 September 2007)

The purpose of this work is to develop a novel strategy to automatically map organ contours from one phase of respiration to all other phases on a four-dimensional computed tomography (4D CT). A region of interest (ROI) was manually delineated by a physician on one phase specific image set of a 4D CT. A number of cubic control volumes of the size of ~ 1 cm were automatically placed along the contours. The control volumes were then collectively mapped to the next phase using a rigid transformation. To accommodate organ deformation, a model-based adaptation of the control volume positions was followed after the rigid mapping procedure. This further adjustment of control volume positions was performed by minimizing an energy function which balances the tendency for the control volumes to move to their correspondences with the desire to maintain similar image features and shape integrity of the contour. The mapped ROI surface was then constructed based on the central positions of the control volumes using a triangulated surface construction technique. The proposed technique was assessed using a digital phantom and 4D CT images of three lung patients. Our digital phantom study data indicated that a spatial accuracy better than 2.5 mm is achievable using the proposed technique. The patient study showed a similar level of accuracy. In addition, the computational speed of our algorithm was significantly improved as compared with a conventional deformable registration-based contour mapping technique. The robustness and accuracy of this approach make it a valuable tool for the efficient use of the available spatial-tempo information for 4D simulation and treatment. © 2007 American Association of Physicists in Medicine. [DOI: [10.1118/1.2780105](https://doi.org/10.1118/1.2780105)]

Key words: CT, image registration, contour mapping, IGRT

I. INTRODUCTION

A longstanding question in radiation therapy is how to accurately and efficiently segment a region of interest (ROI) such as a tumor target volume or a critical structure.¹⁻⁶ In spite of intense research efforts in the past few decades, ROI segmentation remains a time consuming task in treatment planning. In most cases, the segmentation is performed manually in a slice-by-slice fashion, creating a strong need for automated segmentation tools in the clinics. The introduction of four-dimensional computed tomography (4D CT) in radiation oncology practice further amplifies this need as the number of images to be segmented is increased dramatically.⁷⁻¹⁵ Generally, a 4D CT scan consists of 5–10 sets of three-dimensional (3D) CT images, each representing the patient anatomy at a specific phase of respiration. For 4D radiation therapy applications, it is labor intensive to follow the 3D approach of manual segmentation due to the immense workload associated with this process.

A natural way to deal with the 4D segmentation problem is to start with a known set of contours for a selected phase and map these contours onto all other phases. ROIs for the selected phase are first manually contoured, similar to that done in treatment planning based on 3D CT image data sets. The mapping procedure can be accomplished with the aid of a computer algorithm that registers an arbitrary point on the selected phase to the corresponding points on all other

phases. While conceptually simple, the implementation of this idea is not straightforward. An intelligent algorithm capable of providing accurate point-to-point correspondence between the phased images, or at least between points within the ROIs, is the key to the success of this approach. Various studies have investigated algorithms to automatically map contours using deformable image registration and surface mapping techniques. One method is based on a deformable registration model.¹⁶⁻¹⁸ This method has limited accuracy, especially in the regions proximate to the interfaces of different organs, and is brute-force in nature, which entails a large amount of computations. In reality, contour mapping is a regional problem and a global association of the phase-based images is neither necessary nor efficient. Surface mapping achieves the stated goal of contour transformation by iteratively deforming the ROI contour-extended surface until the optimal match with the reference is reached.^{2,19-22} Numerous surface mapping techniques, such as spatial partitioning, principal component analysis, conformal mapping, rigid affine transformation, deformable contours, and warping based on the thin-plate spline (TPS), have been developed over the years and the end point of all of these techniques is a mapping between topological components of the input surfaces that allow for transfer of annotations. This type of computation is inherently more efficient in comparison with the deformable model-based approaches, but it suf-

fers from the fact that the resultant mapping heavily depends on the model used and the fact that the model parameters in the calculations are not physically transparent.

In this work, we combine the useful features of the two different types of techniques for contour mapping. Our working hypothesis is that information contained in the boundary region is often sufficient to guide the contour mapping process without relying on the use of an *ad hoc* surface deforming model. In the proposed technique, the neighborhood information of the contour surface is captured by a series of small cubic (or other shaped) control volumes placed around the surface.²³ The collection of the centers of the control volumes is a representation of the contour surface. The ROI contour mapping proceeds iteratively under the guidance of the information contained in the control volumes. The proposed method is illustrated by a digital phantom experiment and three clinical lung case studies. The results suggest that the technique is capable of automatically mapping contours among the 4D CT phases with clinically acceptable accuracy.

II. MATERIALS AND METHOD

II.A. Software platform

The Insight Toolkit²⁴ (ITK) and the Visualization Toolkit²⁵ (VTK), which are open source cross-platform C++ software toolkits and are freely available for research purposes, were used in this study. A variety of methods have been programmed into the ITK platform for image registration and segmentation. ITK was used for automatic mapping while VTK was mainly used for 3D visualization and contour construction.

II.B. Image acquisition

The 4D CT image data sets for three lung cancer patients were acquired with a multislice helical CT scanner (Discovery ST, GE Medical System, Milwaukee, WI). The collected data were sorted into ten phase bins.¹⁰ The 4D CT image sets for all patient studies were reconstructed with a 2.5 mm slice thickness. The size and pixel resolution of each CT slice was 512×512 and 0.98×0.98 mm², respectively. The 4D CT images were transferred through DICOM to a personal computer with a Pentium IV (2.66 GHz) processor for image processing. One of the phases, which is referred to as the template phase, was selected for manual segmentation of the ROIs. We refer to the other phases in the 4D CT image set as the target phases with corresponding target contours. The enrolled patients in this study were under an Institutional Review Board approved protocol.

II.C. Placement of control volumes along the ROI contour surface

The task of mapping a contour is to find its corresponding location on the target phase for an arbitrary point on the contour drawn on the template image. In general, the image feature surrounding a contour point can be used as a signature of the point to aid the search for its corresponding position on the target phase. In this study, the image feature at

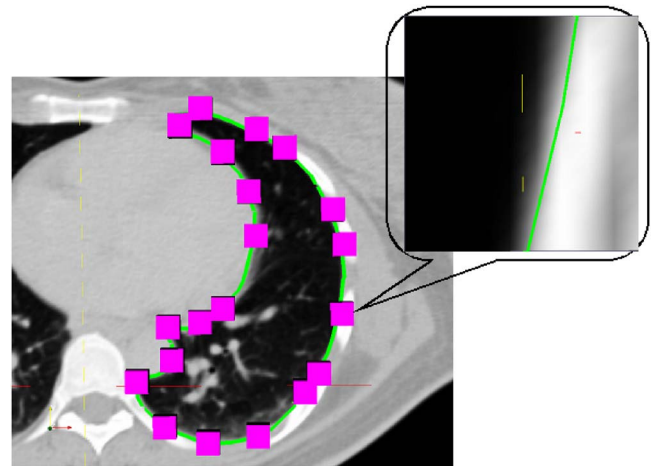


FIG. 1. A schematic drawing of the placement of control volumes (shown as squares) on the manually segmented contour (depicted curve). Each control volume is typically ~ 1 cm in cubic shape as shown in the zoomed image. No interpolated volumes are displayed.

each point was captured by introducing a cubic control volume (~ 1 cm in size) centered at the point. The manual ROI delineation was first performed on the template phase using the Varian Eclipse TPS (Varian Medical Systems, Palo Alto, CA). Afterwards, the contours were exported from the TPS to a local computer for contour propagation. The exported contours are polygons on individual slices, and the vertices of the polygons were used as the locations of control volumes. This is depicted in Fig. 1, where the curve represents the contour and the squares represent the control volumes. The center of each control volume was set at a contour point, typically 0.5–1 cm from the next point. More control volumes are placed through interpolation if the spacing between two consecutive control volumes is greater than 1 cm. The collection of these points represents the ROI contour surface.

The contour mapping was carried out in three steps: (i) mapping the introduced control volumes collectively using a rigid image registration algorithm; (ii) iteratively fine-tuning the 3D positions of the control volumes to determine the deformed ROI contour surface; and (iii) reconstructing the new contours by cutting the deformed surface slice-by-slice along the transversal, sagittal, or coronal direction. This procedure is shown in Fig. 2 and described in detail below.

II.D. Collective mapping of control volumes

After a series of control volumes were placed along the segmented contours on the template phase, we mapped them onto the target phase collectively (i.e., all the control volumes were treated as an entity) using a rigid image registration algorithm.²⁴ A feature of the rigid collective mapping is that the relative distances and orientations of the control volumes remain the same during the course of mapping, resulting in an approximate ROI contour surface in the target phase and providing a good start for further adjustment of the contour shape to accommodate the organ deformations. We note that using a rigid mapping is not a necessary step

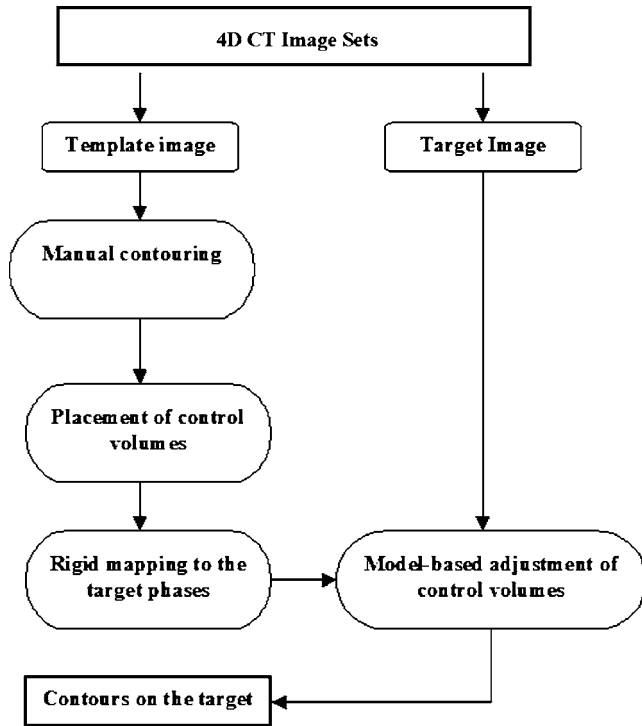


FIG. 2. Flow chart of the automatic contour mapping process for 4D CT images.

and other methods capable of providing a reasonable initial estimate of the ROI surface may also be used.

The collective mapping of the control volumes was performed under the guidance of a normal cross correlation (NCC) metric²⁴ defined by

$$f = - \frac{\sum_{\alpha} \sum_{\beta} \sum_{i=1} I_{\alpha}(\mathbf{x}_i) I_{\beta}(\mathbf{x}'_i)}{\sqrt{\sum_{\alpha} \sum_{i=1} I_{\alpha}^2(\mathbf{x}_i) \sum_{\beta} \sum_{j=1} I_{\beta}^2(\mathbf{x}'_j)}}, \quad (1)$$

where $I_{\alpha}(\mathbf{x}_i)$ is the intensity at a point \mathbf{x}_i in a control volume indexed by α in the target phase and $I_{\beta}(\mathbf{x}'_j)$ represents the intensity at a point \mathbf{x}'_j in a control volume indexed by β in the template phase. In Eq. (1), \mathbf{x} and \mathbf{x}' are related by a rigid transformation \mathbf{T} , where $\mathbf{T}\mathbf{x}' = \mathbf{x}$. We calculated the transformation matrix \mathbf{T} , which maps the ensemble of control volumes from the template phase to the target phase. The limited memory Broyden–Fletcher–Goldfarb–Shannon algorithm (L-BFGS) algorithm^{26–30} was used to optimize the metric in Eq. (1) with respect to the transform parameters. The details of this algorithm have been described elsewhere^{18,31} and will not be repeated here. During the course of the control volume mapping, an iterative calculation based on the L-BFGS algorithm was carried out until a preset maximum number of iterations were met or until the NCC function stopped improving.

II.E. Fine tuning of the mapped control volumes

In the absence of deformation, the ROI contour of the target phase is obtained by connecting the centers of the

rigidly mapped control volumes. In a more general case where deformation does exist, the contour from the rigid mapping serves as an initial estimate of the ROI contour in the target phase. Further positional adjustment of the control volumes is needed to accommodate the deformation of the ROI. The final positions of the control volumes, which define the ROI surface, are determined by balancing the self-energy and the interaction energy, which drive the control volumes to their corresponding locations while maintaining similar shape integrity of the contour.

Mathematically, the above adaptation process is modeled by two “energy terms.” The first term is referred to as “self-energy” and the second term describes the “interaction” among the control volumes. Self-energy tends to drive a control volume toward a position where the neighborhood environment resembles itself most. For each control volume in the template image, this process was driven by the NCC between the volume and its corresponding locations in the target image. The interaction term among the control volumes intends to maintain the integrity of the control volume cluster as a whole and prevents any unrealistic control volume configuration from happening. The interaction energy term is described by

$$E_{\text{interaction}} = M_{\text{template}} - M_{\text{target}}, \quad (2)$$

where M_{template} is defined as the correlation between a control volume in the template phase and the neighboring control volumes in the target phase, M_{target} represents the correlation between the control volume in the target phase and the neighboring volumes in the template phase. These two terms take into account the neighborhood environment of the control volume being adjusted and apply a constraint on the possible form of the control volume configuration. In a sense, the interaction energy in Eq. (2) exerts a restoring force when the position of a control volume is varied with respect to its neighbors. The interaction force is important in preventing the control volumes from moving to unrealistic positions simply driven by the self-energy and in retaining the shape integrity of the ROI surface. For simplicity, only the adjacent control volumes were considered when computing the interaction energies. The final position of each control volume was determined by minimizing the sum of the self-energy and interaction energy terms.

A simple searching algorithm was implemented to find the minimum of Eq. (2) and thus the final configuration of the control volumes. The algorithm was realized using an exhaustive search in the defined local region around the control volume and was based on three dimensional basis. For each rigidly mapped control volume on the target phase, we defined a small region of ~ 3 cm around the central point in the volume. The search region of 3 cm was chosen primarily to accommodate maximum deformation of tissue. 3 cm is a very conservative value because the tissue deformation in two adjacent phases barely exceeds this value (the maximum deformation occurring between the inhale and exhale phases may reach ~ 3 cm). Equation (2) was then minimized to determine the optimal control volume location within this region. This process was repeated for each separate control

volume. Due to the fact that the interaction energy term demands the information from the neighboring volumes, adjusting the location of each control volume changes the position of the previously fine-tuned volume. Therefore, several cycles of this process were needed to obtain the truly optimal positions of all the control volumes. We found (see digital phantom study in results section) that 2–3 complete adjustment cycles were adequate to find the optimal control volume configuration.

II.F. Reconstruction of target contours

Upon completion of the control volume mapping and adaptation, the centers of each control volume were identified. A ROI surface was constructed with these central points using a triangulated surface construction technique which uses marching cubes³² method and triangular surface decimation of VTK.^{25,33} The intersection of the surface with each CT slice was superimposed on top of the image in order to visualize the contour in a conventional fashion. These contours can be exported as ASCII or DICOM-RT format for treatment planning.

II.G. Evaluation of the algorithm and case study

Evaluation of a contour mapping algorithm is a difficult task because of the general lack of a gold standard for comparison. The proposed control volume based 4D contouring technique was first evaluated with a digital phantom experiment. In this study, a thoracic CT image was deformed intentionally using a known deformation matrix which was introduced by drifting the positions of each control volume along the contour with known sizes. Specifically, for a control volume i , we assign the following displacements:

$$D(x,y) = i * 0.01 \text{ and } D(z) = i * 0.001 \text{ if } i = 0, 1, \dots, N/2 \quad (3)$$

or

$$D(x,y) = (N - i) * 0.01 \text{ and } D(z) = (N - i) * 0.001 \text{ if } i = N/2 + 1, N/2 + 2, \dots, N, \quad (4)$$

where N is the total number of control volumes on the ROI contour. The artificially deformed image serves as a “new breathing phase” relative to the original image. The “ground truth” lung surface in the target phase was attainable by transforming the original contours with the same deformation matrix. The manually delineated lung contours in the original image were also mapped using the proposed novel control volume based approach. A comparison of the mapped lung surface with the ground truth allowed us to quantitatively assess the success of the proposed approach.

The control volume based contour mapping technique was also applied to three 4D CT patient scans. A physician manually delineated the lungs and GTV for each scan on a selected phase (for example, the exhale phase). These contours were then mapped onto all other phases using the proposed technique. Visual inspection was used to evaluate the three patient studies. Although it is less quantitative, visual

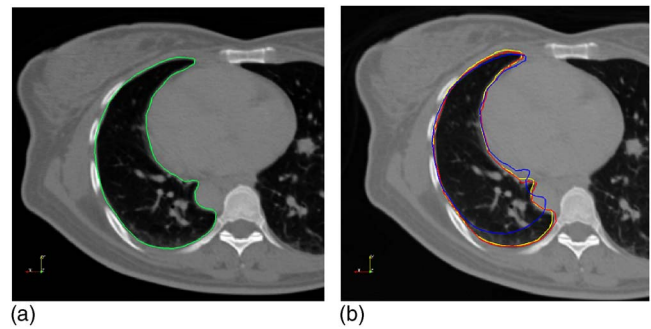


FIG. 3. Validation process of proposed algorithm using a digital phantom. (a) Original image and contour; (b) Artificially deformed image and contour (ground truth contour) together with contour after fine tuning. These two contours are almost indistinguishable. The contour after rigid mapping is also shown.

inspection is a convenient way for rapid assessment of a segmentation calculation, especially in a case where the ground truth contours do not exist.

III. RESULTS

III.A. Digital phantom study

The thoracic CT images before and after the intentionally introduced deformation are shown in Fig. 3. The manually delineated lung contour is shown in Fig. 3(a), while the ground truth contour obtained by transforming the manual contour with the known transformation matrix is plotted in Fig. 3(b). The contour from the proposed approach is shown in the same figure. To be comprehensive, the rigidly mapped contour, which served as the start of the model-based refinement, is also plotted in Fig. 3(b). Clearly, it is significantly deviated from the lung boundary. Visual inspection of the ground truth contour and contour after refinement in Fig. 3(b) indicated that the gold standard and the mapped contours are similar, despite the fact that the intentionally introduced deformation field is quite large (the displacement of some of the voxels is as large as 2.0 cm). The mean and maximum separations between the two sets of contours were found to be 1.5 and 2.5 mm, respectively.

To better understand the mapping process, we examined the behavior of each energy term (metrics) during the course of the contour mapping. In Fig. 4(a) we plotted the values of self-energy, interactive energy, and total energy of one of the control volumes in the process of positional adjustment in the surrounding area of the control volume in the deformed image. For this particular control volume, the minimum of Eq. (2) was reached after searching the first 30 points. For control volumes located in regions where the deformation is large, more searching points may be required to reach the minimum. It is also interesting to show how the average metric value of all the control volumes evolved. In Fig. 4(b) the metric value is depicted as a function of the calculation process. The first point, corresponding to step 0, is the metric before mapping. Step 1 refers to the system after rigid mapping. The metric at this point is decreased but does not reach the minimum. The third point shows the metric after each of

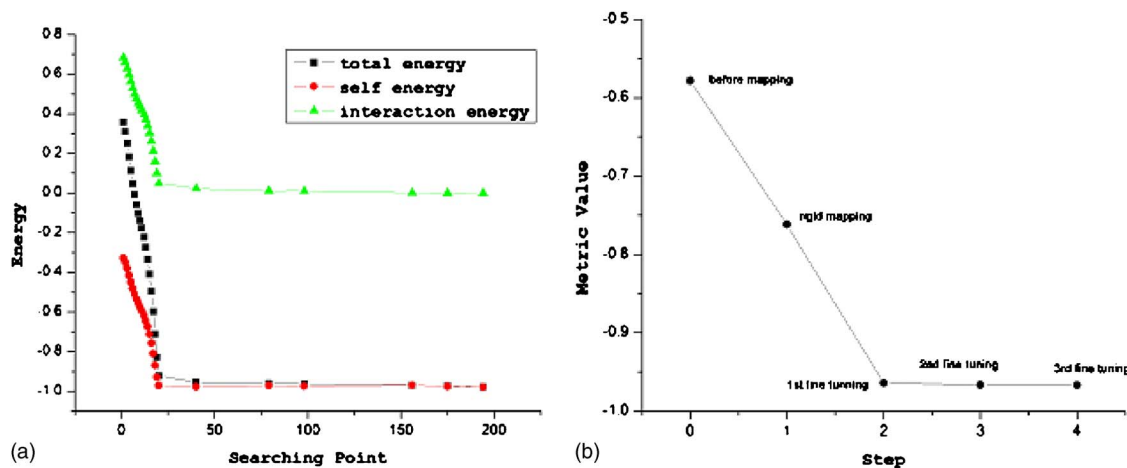


FIG. 4. (a) Energies (self, interaction, and total energy) as a function of the searching points in the surrounding area of a randomly selected control volume in the target image (see text for details). (b) The metric value versus step during the course of the contour mapping. The metric values are the average NCC of all the involved control volumes.

the control volumes is fine tuned sequentially. To obtain the optimal contours two more cycles of fine tuning were performed; however, the improvement with further iterations was not significant.

III.B. Patient studies

The proposed technique was assessed using 4D CT images of three lung cancer patients. Figure 5 shows the manually delineated contours on the 4D CT scans of two lung cancer patients for lung and GTV, respectively. The CT images and contours are displayed in axial, coronal, and sagittal views. Contours were drawn on the exhale phases (phase 1) for patient 1 (top row in Fig. 5). The GTV contour for patient 3 was delineated on the inhale phase (phase 5) as shown in Fig. 5 bottom row. For patients 1 and 2 the mapping of the lung contours was studied. For the third patient, GTV contour mapping was investigated.

The lung contours before and after the control volume-based mapping for the first patient are presented in Fig. 6. To

better visually evaluate the results, the CT images and contours for this patient are displayed in axial, coronal, and sagittal views as in left, middle, and right columns, respectively. Target phases 4, 7, and 10 are selected to demonstrate the results as in the top, middle, and bottom rows in Fig. 6. The template contours and rigidly mapped contours were shown and significantly deviated from the ROI boundary. The final contours after the model-based adaption are presented as well.

When the lung deformation is small, for example, in phase 10 of patient 1 [see Figs. 6(g)–6(i)], the rigidly mapped contours closely resemble the target contours. Fine tuning merely provides limited adjustment of the contours. For phases with large deformations (e.g., phases of 4 and 7

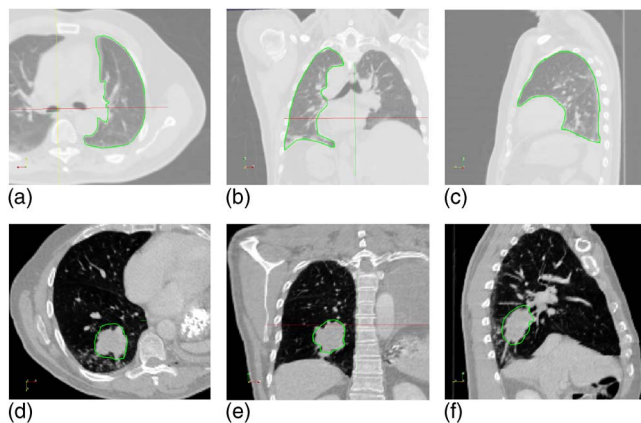


FIG. 5. The template CT images and manually segmented contours for two lung cancer patients (top row: patient 1; bottom row: patient 3) on axial, coronal, and sagittal views. Right lung of patient 1 and GTV of patient 3 were manually delineated, respectively.

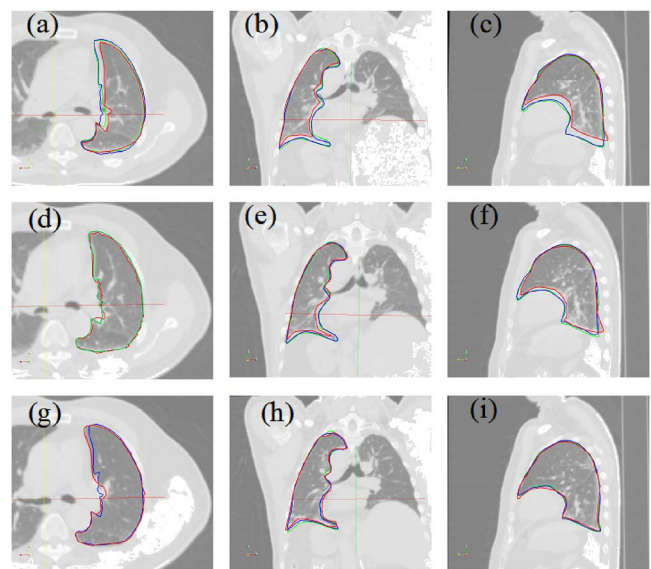


FIG. 6. Axial, coronal, and sagittal views of CT images along with lung contours for the first patient. Top row: phase 4; middle row: phase 7; bottom row: phase 10. Rigidly mapped and target contours are displayed. Template contour is also overlaid on displayed phases.

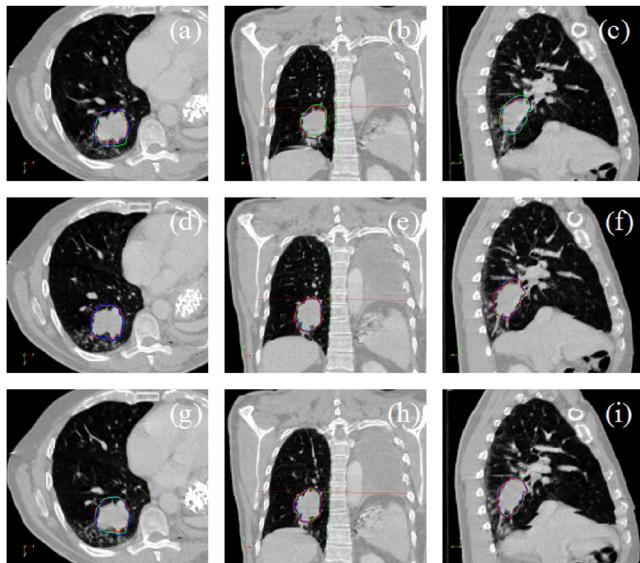


FIG. 7. Axial, coronal, and sagittal views of CT images along with GTV contours for the third patient. Top row: phase 2; middle row: phase 4; bottom row: phase 7. Rigidly mapped and target contours are displayed. Template contour is also overlaid on displayed phases.

of this patient), the model-based adjustment after the rigid contour mapping plays an important role in obtaining optimal contour arrangement. In case of the lung contours, our analyses of the patient data indicate that the accuracy of our contour mapping technique is within one pixel in the superior part of the lung, where respiration induced deformation is small. In other parts, the average error on the target contours is estimated to be less than 2.5 mm.

The mapped GTV contours for phases 2, 4, and 7 in the study of patient 3 are shown in Fig. 7. The representation of the contours is the same as in Fig. 6. For phases 4 and 7 the deformation was relatively small and our contour mapping algorithm performed reliably. For phase 2, which corresponded to the exhale phases, significant deformation in the ROIs was observed. Despite this less ideal case, our algorithm still worked well in these phases.

IV. DISCUSSION

As in 3D radiation therapy, delineation of ROIs in 4D CT images is a necessary step for treatment planning.³⁴ 4D segmentation is required for constructing a 4D patient model and for computing the accumulated dose of moving or deformed organs. One way to proceed is to draw all contours on one of the phases of respiration and map or propagate these contours onto the remaining phases. Various deformable models have been used for ROI contour mapping as discussed in the introduction. In this work, we take a regional approach based on the mapping and adaptation of the sparsely sampled control volumes. Our approach takes advantage of the imaging features surrounding the ROI and uses them as guidance in searching for the optimal mapped contours while considering the shape integrity of the ROI surface.

The mapping of a point in one image to another is easily achievable if a unique identifier or signature can be tagged to the point. Here the image feature contained in a control volume is employed as a signature of the point to facilitate the process of finding its corresponding location in the target phases. The concept of control volume was first introduced by Schreiber and Xing²³ and its advantages for both intra- and intermodality image registration have been demonstrated. This study represents a novel application of the concept to 4D image segmentation. After a rigid mapping of the contours from the template phase to the target phase, a model-based adaptation is performed to establish a reliable association between the ROIs in two phase specific image sets. This adaptation takes into account the deformation of an object and ensures the overall integrity of the resultant ROI surface. The calculation is local in nature, which improves both computational efficiency and convergence behavior.

A quantitative comparison of different deformable registration algorithms is a difficult task because of the multifaceted and even subjective nature of the problem. An unbiased and meaningful comparison may entail the efforts from multiple institutions.³⁵ Thus we defer the detailed comparative study to the future. However, we wish to emphasize that the chief advantage of the proposed technique is its computational efficiency. Because of the regional nature of the calculation, our general finding is that the new algorithm is at least an order of magnitude faster than the whole image based approach.^{17,18} Enormous saving in the memory usage in the proposed approach is also self-explanatory and highly desirable feature in practice.

A common problem in image segmentation and contour mapping studies is the lack of quantitative validation. In the study of Lu *et al.*,³⁶ for example, the accuracy of a deformable model-based contour mapping technique was evaluated purely based on visual inspection. The same approach was employed in many other previous investigations.^{4,6,16,18} In our study, in addition to the visual evaluation, a set of digital phantom experiments was introduced to evaluate the success of the proposed technique. By applying a prespecified deformation matrix to the original image, the ground truth of the contour propagation is readily known. Therefore, the experiments provide a quantitative test of the proposed algorithm. In general, we found that a spatial accuracy better than 2.5 mm is achievable using our technique.

V. CONCLUSION

The development of 4D radiation therapy involves the use of a large number of images acquired at different times and/or with different modalities. Clinical implementation of the new IGRT paradigm is, to a large extent, bottlenecked by the inability to accurately and efficiently register images and segment the ROIs. In this work, a mathematical framework for control volume-based contour mapping has been proposed for 4D radiation therapy. We demonstrated that the information contained in the boundary region is sufficient to guide the contour mapping process without registering the whole image or relying on the use of an *ad hoc* surface

deforming model. The results showed that the control volume-based contour mapping algorithm is capable of robustly and accurately mapping contours from one phase of a 4D CT to the remaining phases. Our technique decreases the workload involved in 4D CT ROI segmentation and provides a valuable tool for the efficient use of available spatial-tempo information for 4D simulation and treatment.

ACKNOWLEDGMENTS

This work was supported in part by grants from the Department of Defense (W81XWH-06-1-0235 and W81XWH-05-1-0041), Komen Breast Cancer Foundation (BCTR0504071), and National Cancer Institute (5R01 CA98523 and 1R01 CA98523).

- ^{a)} Author to whom correspondence should be addressed. Present address: Stanford University School of Medicine, Department of Radiation Oncology, 875 Blake Wilbur Drive, Stanford, CA 94305-5847; Telephone: (650)498-7896; Fax: (650)498-4015; Electronic mail: lei@reyes.stanford.edu
- ¹ M. R. Kass, A. Witkin, and D. Terzopoulos, "Snakes: Active contour models," *Int. J. Comput. Vis.* **1**, 321–331 (1988).
 - ² T. Cootes, A. Hill, C. Taylor, and J. Haslam, "The use of active shape models for locating structures in medical images," *J. Image. Vis. Comput.* **12**, 355–366 (1994).
 - ³ C. Xu and J. L. Prince, "Snakes, shapes, and gradient vector flow," *IEEE Trans. Image Process.* **7**, 359–369 (1998).
 - ⁴ F. Liu, B. Zhao, P. K. Kijewski, L. Wang, and L. H. Schwartz, "Liver segmentation for CT images using GVF snake," *Med. Phys.* **32**, 3699–3706 (2005).
 - ⁵ J. Weese *et al.*, "Shape constrained deformable models for 3D medical image segmentation," *Information Processing in Medical Imaging: 17th International Conference, IPMI 2001, Davis, CA, June 18–22, 2001, Vol. 2082*, pp. 380–387 (2001).
 - ⁶ V. Pekar, T. R. McNutt, and M. R. Kaus, "Automated model-based organ delineation for radiotherapy planning in prostatic region," *Int. J. Radiat. Oncol. Biol. Phys.* **60**, 973–980 (2004).
 - ⁷ C. J. Ritchie, J. Hsieh, M. F. Gard, J. D. Godwin, Y. Kim, and C. R. Crawford, "Predictive respiratory gating: A new method to reduce motion artifacts on CT scans," *Radiology* **190**, 847–852 (1994).
 - ⁸ S. S. Vedam, P. J. Keall, V. R. Kini, H. Mostafavi, H. P. Shukla, and R. Mohan, "Acquiring a four-dimensional computed tomography dataset using an external respiratory signal," *Phys. Med. Biol.* **48**, 45–62 (2003).
 - ⁹ L. Xing, B. Thorndyke, E. Schreibmann, Y. Yang, T. F. Li, G. Y. Kim, G. Luxton, and A. Koong, "Overview of image-guided radiation therapy," *Med. Dosim.* **31**, 91–112 (2006).
 - ¹⁰ T. Pan, T. Y. Lee, E. Rietzel, and G. T. Chen, "4D-CT imaging of a volume influenced by respiratory motion on multi-slice CT," *Med. Phys.* **31**, 333–340 (2004).
 - ¹¹ L. Dietrich, S. Jetter, T. Tucking, S. Nill, and U. Oelfke, "Linac-integrated 4D cone beam CT: First experimental results," *Phys. Med. Biol.* **51**, 2939–2952 (2006).
 - ¹² T. Li, E. Schreibmann, B. Thorndyke, G. Tillman, A. Boyer, A. Koong, K. Goodman, and L. Xing, "Radiation dose reduction in four-dimensional computed tomography," *Med. Phys.* **32**, 3650–3660 (2005).
 - ¹³ W. Lu and T. R. Mackie, "Tomographic motion detection and correction directly in sonogram space," *Phys. Med. Biol.* **47**, 1267–1284 (2002).
 - ¹⁴ T. Li, L. Xing, P. Munro, C. McGuinness, M. Chao, Y. Yang, B. Loo, and A. Koong, "Four-dimensional cone-beam computed tomography using an on-board imager," *Med. Phys.* **33**, 3825–3833 (2006).
 - ¹⁵ J. J. Sonke, L. Zijp, P. Remeijer, and M. van Herk, "Respiratory correlated cone beam CT," *Med. Phys.* **32**, 1176–1186 (2005).
 - ¹⁶ T. M. Guerrero, G. Zhang, T. C. Huang, K. P. Lin, P. Giraud, Y. De Rycke, B. Dubray, S. Helfre, D. Voican, L. Guo, J. C. Rosenwald, K. Keraudy, M. Housset, E. Touboul, and J. M. Cosset, "Intrathoracic tumour motion estimation from CT imaging using the 3D optical flow method," *Phys. Med. Biol.* **49**, 4147–4161 (2004).
 - ¹⁷ D. Ragan, G. Starkschall, T. McNutt, M. Kaus, T. Guerrero, and C. W. Stevens, "Semiautomated four-dimensional computed tomography segmentation using deformable models," *Med. Phys.* **32**, 2254–2261 (2005).
 - ¹⁸ E. Schreibmann, G. T. Chen, and L. Xing, "Image interpolation in 4D CT using a B Spline deformable registration model," *Int. J. Radiat. Oncol. Biol. Phys.* **64**, 1537–1550 (2006).
 - ¹⁹ T. McInerney and D. Terzopoulos, "Deformable models in medical image analysis," *Med. Image Anal.* **1**, 91–108 (1996).
 - ²⁰ A. Chakraborty, L. H. Staib, and J. S. Duncan, "An integrated approach for surface finding in medical images" *IEEE Workshop Mathematical Methods in Biomedical Image Analysis*, 1996, pp. 253–262.
 - ²¹ J. Montagnat, H. Delingette, and N. Ayache, "A review of deformable surfaces: Topology, geometry and deformation," *Image Vis. Comput.* **19**, 1023–1040 (2001).
 - ²² J. Montagnat and H. Delingette, "4D deformable models with temporal constraints: Application to 4D cardiac image segmentation," *Med. Image Anal.* **9**, 87–100 (2005).
 - ²³ E. Schreibmann and L. Xing, "Image registration with auto-mapped control volumes," *Med. Phys.* **33**, 1165–1179 (2006).
 - ²⁴ L. Ibanez, W. Schroeder, L. Ng, ITK Software Guide, Kitware Inc., 2003, <http://www.itk.org>.
 - ²⁵ W. Schroeder, K. Martin, B. Lorensen, *The Visualization Toolkit: An Objective-Oriented Approach To 3D Graphics*, <http://public.kitware.com/VTK/>.
 - ²⁶ C. G. Broyden, "The convergence of a class of double-rank minimization algorithms 2, the new algorithm," *J. Inst. Math. Appl.* **6**, 222–231 (1970).
 - ²⁷ R. Fletcher, "A new approach to variable-metric algorithms," *Comput. J.* **13**, 317–322 (1970).
 - ²⁸ D. Goldfarb, "A family of variable-metric algorithms derived by variational means," *Math. Comput.* **24**, 23–26 (1970).
 - ²⁹ D. F. Shanno, "Conditioning of quasi-Newton methods for function minimization," *Math. Comput.* **24**, 647–656 (1970).
 - ³⁰ D. C. Liu and J. Nocedal, "On the limited memory BFGS method for large scale optimization," *Math. Program.* **45**, 503–528 (1989).
 - ³¹ E. Schreibmann and L. Xing, "Narrow band deformable registration of prostate magnetic resonance imaging, magnetic resonance spectroscopic imaging, and computed tomography studies," *Int. J. Radiat. Oncol. Biol. Phys.* **62**, 595–605 (2005).
 - ³² W. E. Lorensen and H. E. Cline, "Marching cubes: A high resolution 3D surface construction algorithm," *ACM Comput. Graph.* **21**, 163–169 (1987).
 - ³³ W. Schroeder, J. Zarge, and W. E. Lorensen, "Decimation of triangle meshes," *Comput. Graph.* **26**, 65–70 (1992).
 - ³⁴ E. Rietzel, G. T. Chen, N. C. Choi, and C. G. Willet, "Four-dimensional image-based treatment planning: Target volume segmentation and dose calculation in the presence of respiratory motion," *Int. J. Radiat. Oncol. Biol. Phys.* **61**, 1535–1550 (2005).
 - ³⁵ J. West *et al.*, "Comparison and evaluation of retrospective intermodality image registration techniques," *Proc. SPIE* **2710**, 332–347 (1996).
 - ³⁶ W. Lu, G. H. Olivera, Q. Chen, M. Chen, and K. J. Ruchala, "Automatic re-contouring in 4D radiotherapy," *Phys. Med. Biol.* **51**, 1077–1099 (2006).

CT image registration in sinogram space

Weihua Mao, Tianfang Li, Nicole Wink, and Lei Xing

Department of Radiation Oncology, Stanford University School of Medicine, Stanford, California 94305-5847



(Received 5 December 2006; revised 5 July 2007; accepted for publication 5 July 2007; published 22 August 2007)

Object displacement in a CT scan is generally reflected in CT projection data or sinogram. In this work, the direct relationship between object motion and the change of CT projection data (sinogram) is investigated and this knowledge is applied to create a novel algorithm for sinogram registration. Calculated and experimental results demonstrate that the registration technique works well for registering rigid 2D or 3D motion in parallel and fan beam samplings. Problem and solution for 3D sinogram-based registration of metallic fiducials are also addressed. Since the motion is registered before image reconstruction, the presented algorithm is particularly useful when registering images with metal or truncation artifacts. In addition, this algorithm is valuable for dealing with situations where only limited projection data are available, making it appealing for various applications in image guided radiation therapy. © 2007 American Association of Physicists in Medicine. [DOI: [10.1118/1.2767402](https://doi.org/10.1118/1.2767402)]

Key words: CT, registration, IGRT, sinogram

I. INTRODUCTION

Registration of computed tomography (CT) images plays an important role in image guided interventions. Usually, the registration is performed on reconstructed images due to their prominent spatial and anatomical details.¹⁻⁴ In reality, this type of registration can be difficult if artifacts exist.⁵⁻⁸ When patients with prostheses, dental fillings, metal markers, or surgical clips are studied with CT, the metallic objects can lead to severe streaking artifacts. Artifacts in a reconstructed image not only deteriorate the image quality, but also hinder image registration for treatment planning or patient localization. A loss of detail usually occurs around the metal-tissue interface.⁹⁻¹³ Many techniques have been devoted to reduce or suppress metal artifacts, but a complete solution remains illusive. Because streak artifacts most often rise from inaccurate beam hardening corrections used in filtered backprojection (FBP) reconstruction, image registration before the reconstruction has the potential to attain more accurate and reliable results.

Previously, registrations in projection data space have been investigated using Radon and Fourier transforms.¹⁴⁻¹⁸ While this method is general, the inherent mathematical complexity makes it conceptually less intuitive and difficult to implement. Particularly, continuous and smooth images functions were assumed in order to perform the Fourier transformations and this made it problematic to register the case with metal implants. In order to be mathematically manageable, assumptions such as small rotation angles,¹⁷ are often introduced, which further limits the inverse based approach.

In this work, we study a relationship between the body motion and projection data (sinogram) and demonstrate that the relation can be used for image registration directly in sinogram space. Chief advantages of the proposed technique are that it is comprehensive and relatively simple in imple-

mentation. Applications of the approach to a number of beam geometries, including parallel, fan, and cone beam geometries, indicated that the algorithm is valuable for image registration. This technique is particularly useful in the presence of metal or other types of reconstruction artifacts. The approach sheds some insight into the image registration problem and provides valuable perspective for future development along the direction.

II. METHOD

II.A. 2D motion in parallel beam scan

A rigid body motion can be represented as a rotation around a fixed center plus a translation of the point. In a 2D case (motion in the axial plane), after a rotation $[R_z(\alpha), \alpha$ is the rotation angle around the z axis, central axis, or superior-inferior direction] and a translation $[M(r, \beta),$ where r is the translation amplitude and β is the polar angle of the translation vector] operation, a point on a reference x-ray path (defined as the reference position with a subscript of r), (x_r, y_r) , becomes a point on the same physical x-ray path, (x_f, y_f) , at the floating position (with a subscript of f). The transformation between the two positions is given by

$$\begin{aligned}x_f &= x_r \cos \alpha + y_r \sin \alpha + r \cos \beta, \\y_f &= -x_r \sin \alpha + y_r \cos \alpha + r \sin \beta.\end{aligned}\quad (1)$$

During parallel beam sampling, the projection for the floating position (x_f, y_f) is

$$\begin{aligned}R[f](\theta_f, s_f) &= \int_{-\infty}^{\infty} \int_{-\infty}^{\infty} f(x_f, y_f) \delta(x_f \sin \theta_f - y_f \cos \theta_f \\&\quad - s_f) dx_f dy_f,\end{aligned}\quad (2)$$

where $f(x_f, y_f)$ represents the decay efficiency (attenuation

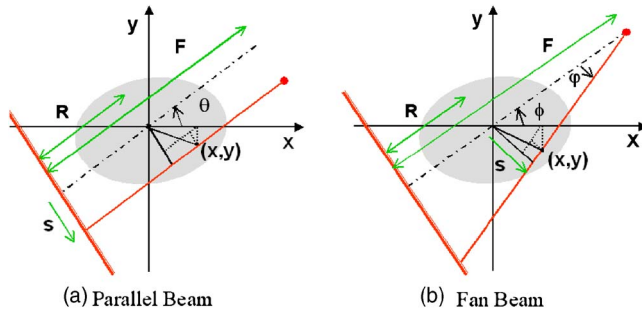


FIG. 1. Schematic diagrams for the parallel and fan beam projection geometries: (a) parallel beam and (b) fan beam.

coefficient) and (θ_f, s_f) is the projection angle and the radial distance of (x_f, y_f) at the floating position [see Fig. 1(a) for a schematic diagram].

Using the transformation [Eq. (1)], we have

$$x_f \sin \theta_f - y_f \cos \theta_f - s_f = x_r \sin (\theta_f + \alpha) - y_r \cos (\theta_f + \alpha) + r \sin (\theta_f - \beta) - s_r. \quad (3)$$

The projection data for the floating position become

$$R[f](\theta_f, s_f) = \int_{-\infty}^{\infty} \int_{-\infty}^{\infty} f'(x_r, y_r) \delta(x_r \sin \theta_r - y_r \cos \theta_r - s_r) dx_r dy_r = R[f](\theta_r, s_r), \quad (4)$$

where the projection angle (θ_r) and radial distance (s_r) for the reference position are defined as

$$\begin{aligned} \theta_r &= \theta_f + \alpha, \\ s_r &= s_f - r \sin (\theta_f - \beta). \end{aligned} \quad (5)$$

At the same time, $f'(x_r, y_r) = f(x_f, y_f)$, since they are the decay efficiency for the same physical point on the object.

It is evident in Eq. (4) that the projection ray paths are repeated, but the projection angle and radial distance might be modified by the motion as indicated in Eq. (5). This demonstrates that any rigid motion in the axial plane only relocates the projection data on the sinogram without changing projection intensities. Equation (5) gives the relationship between the motion and the projection angle and radial distance.

II.B. 2D motion in fan beam scan

A similar relationship exists for fan beam sampling with a focus length of F and radial length R , where $FR = F - R$. Figure 1(b) illustrates the fan beam geometry. After a rotation $[R_z(\alpha)]$ and a translation $[M(r, \beta)]$, any original reference point (x_r, y_r) becomes a point on the floating trace (x_f, y_f) . The sinogram transformations are

$$\phi_r + \varphi_r = \phi_f + \varphi_f + \alpha,$$

$$\sin \varphi_r = \sin \varphi_f - \frac{r}{FR} \sin (\phi_f + \varphi_f - \beta), \quad (6)$$

where ϕ_r and ϕ_f are the angles of the source, and φ_r and φ_f are the fan angles [$\tan (\varphi) = s/F$, s is the radial distance]. Subscripts r and f are denoted for the reference and floating positions, respectively.

II.C. 3D motion registration

Similar to that studied by Lu *et al.*,¹⁷ the sinogram-based registration can be extended to 3D motion with six degrees of freedom under the assumption of small angle rotations (pitch or yaw) on a direction perpendicular to the central axis. Because of the limited practical usage of the approximation scheme, the details are presented in the Appendix . The derivation is essentially the same as that of Lu *et al.*,¹⁷ except that here it is done in the real space instead of the Fourier space.

Obtaining sinogram transformation for an arbitrary object motion is a mathematically challenging task. For practical purpose, here we apply the sinogram-based registration to an important special situation of interest, that is, the registration in the presence of metal implants. The study not only provides the solution to a clinically relevant issue but also sheds valuable insight into the problem of registration in sinogram space.

Theoretically, registering a 3D motion of a rigid body is equivalent to registering the motion of three or more points in the object provided that those points are not on a straight line. For a patient with three or more metallic implants or fiducial markers, the registration can be simplified to register these fiducials. As is well known, a metallic fiducial appears in the tomographic sinogram as a bright sinusoidal curve and can be easily identified. Simplification of registering metallic fiducials arises from the fact that one can simply relate the fiducial coordinates geometrically before and after object motion without worrying about their intensity change in the projections. Geometrically, the transformation of a spatial point on different planes is readily attainable, and the relation can be employed to guide the optimal match of the sinusoidal curves of the implanted fiducials.

A radiation-opaque fiducial at (x_B, y_B, z_B) or (r_B, θ_B, z_B) in Fig. 1(b) is reflected by a bright curve on the sinogram of the slice z_B . For a fan beam geometry as sketched in Fig. 1(b), the gantry angle (ϕ) and the fan angle (φ) are related by

$$\tan \varphi = \frac{r_B \sin (\phi - \theta_B)}{FR - r_B \cos (\phi - \theta_B)}. \quad (7)$$

Similar projection trace for metallic fiducials can be derived for cone beam scanning. The location of the fiducial on a projection depends on its position (r_B, θ_B, z_B) and gantry angle ϕ as defined in Fig. 1(b). Generally, the portal imager has two orthogonal axes, s and z , while the z is along the longitudinal direction and coincident to the patient coordinate z and s is perpendicular to z direction. Assuming that the origin of the s - z coordinate system is at the imager center, we have

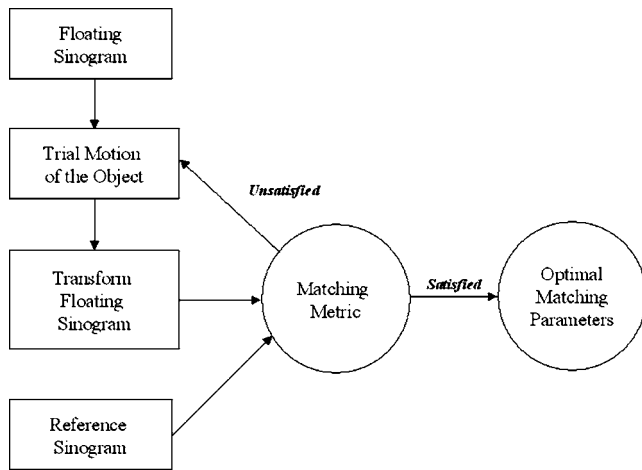


FIG. 2. Flow chart of sinogram registration procedure.

$$s = \frac{Fr_B \sin(\phi - \theta_B)}{FR - r_B \cos(\phi - \theta_B)},$$

$$z = \frac{Fz_B}{FR - r_B \cos(\phi - \theta_B)}. \quad (8)$$

II.D. Registration procedure

The flow chart of the sinogram-based registration procedure is shown in Fig. 2. The calculation starts from a trial association of the two input sinograms and is followed by iterative tests of sequential trial motions under the guidance of a search algorithm. For each trial motion, the corresponding sinogram was generated from the floating sinogram according to the transformation given in Eqs. (5)–(8). The trial sinogram was then compared with the reference sinogram. After the iterative trial and comparison, the optimal motion transformation is found. To examine the performance of the iterative search algorithm, an exhaustive search was also implemented for the 2D studies.

For the 3D fiducial registration, the fiducials were represented by the coordinates of their centers of mass, and their locations on the projection planes were presented as functions of gantry angle. The locations of the fiducials on the projection planes were detected by an intensity-based fiducial search algorithm. The 3D coordinates of a fiducial were calculated based on Eq. (7) or (8). At last, six transformation parameters relating the two sets of fiducial position 3D coordinates were calculated by a simple six degree of freedom rigid transformation.¹⁹

Both exhaustive search method and iterative algorithm were used for optimization. The former algorithm searches the multi-dimensional space within a prespecified region of interest to find the shifts. A normalized cross correlation (NCC) between the two sinograms was used to rank different matching.⁸ To be computationally efficient, the search step was set to a large value initially and then gradually reduced. A typical capture range includes an axial rotation in all directions (360 deg) and translations up to 100 pixels or rel-

evant length in two orthogonal directions. The final resolution is up to 0.2 deg in rotation and one pixel in translation. The iterative algorithm, simulated annealing, was also investigated for optimization of the metric function. Each step of the simulated annealing algorithm replaces the current solution by a random “nearby” solution, chosen with a probability that depends on the difference between the corresponding function values and on a global parameter (called the annealing temperature), which is gradually decreased during the process.^{20,21} Generally, a registration could be completed on a PC (DELL Precision 470, CPU 3.40 GHz, and 3.0 GB of RAM) in a few minutes.

II.E. Digital phantom study

A simulated 2D Shepp-Logan head phantom model (512 pixels × 512 pixels) (Matlab, MathWorks, Inc., Natick, MA) was adopted to test the algorithm for 2D registration. After rotational and translational operations, floating images were created and the corresponding sinograms were simulated for different projection geometry including parallel beam, fan beam with equal angle sampling, and fan beam with equal distance sampling. Radon transform and inverse radon transform functions from Matlab were used for parallel beam simulation and reconstruction. In-house software was used for fan beam simulation and reconstruction. A 3 pixel by 3 pixel metal filling was added to the phantom model in order to test the effects of metal artifacts on registration. After a rotation and a translation, a floating position was generated. Fan beam sinograms with equal distance sampling were simulated for the modified phantom. To show the advantage of sinogram-based registration, the results were compared with that obtained by traditional NCC-based registration after image reconstruction.⁸

II.F. Physical phantom study

A physical head phantom was scanned using an onboard kV cone beam scanner (Trilogy, Varian Medical Systems, Palo Alto, CA). The phantom was installed on a platform that allows 3D translational and 2D rotational (around the z axis and/or y axis) motion. For the 2D study, fan beam sinograms were generated for the central axial plane because the central axial plane projection of cone beam CT is identical to a fan beam scan.

This phantom was also used to test the fiducial based 3D registration. Four CT BBs with a diameter of 1.57 mm were placed on the surface of the phantom. After a reference scan was done, five motions were introduced, each corresponding to one of the five permissible motions of the phantom platform. Combinational motions of the five degrees of freedom of the phantom platform were also introduced and the ability of the algorithm to identify the introduced errors was evaluated.

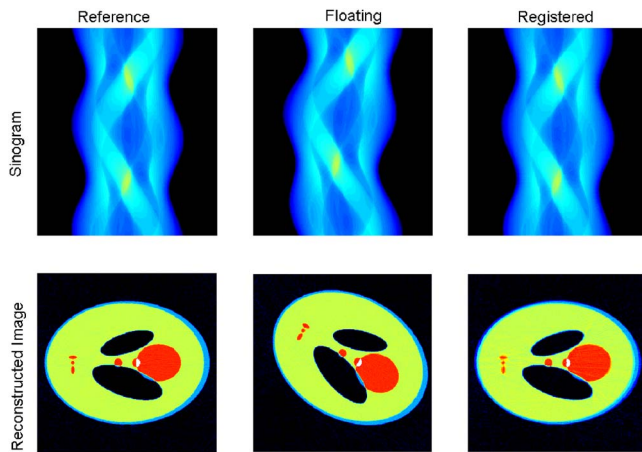


FIG. 3. Sinograms and reconstructed images for the reference case, the floating case, and the registered results of a phantom model using a fan beam with equal angle sampling.

III. RESULTS

III.A. 2D registration of digital phantom

The presented algorithm was found to work well in both simulated and physical phantom experiments. Rotations, translations, and the combinations of rotations and translations were registered correctly for various CT sampling methods and geometries. Figure 3 shows the results of the simulated fan beam with equal distance sampling. Along with the sinograms of the reference position, the floating position, and the registered position, the reconstructed images are shown on the bottom row for clarity. The registered position is obtained by transforming the floating position sinogram to match the reference position sinogram. It is evident that the registered sinogram and reconstructed image are indistinguishable from those of the reference. The registration accuracy has been evaluated by subtracting the reconstructed images based on the registered sinograms from the reconstructed images based on the reference sinograms. The maximum error was then obtained from the differences. The spatial accuracy of registration illustrated in Fig. 3 is better than 2 pixels in all directions.

For comparison, registration was performed in image space based on the reconstructed reference and floating images. The two methods of registration yield the similar registration accuracy in the absence of metal artifacts. As will be seen later, this is, however, not the case in the presence of metal artifacts.

III.B. 2D registration of digital phantom with metal filling

When the metal artifacts are “switched on,” the image based registration failed to yield accurate motion values. On the other hand, the presence of metal imposed little influence on the sinogram-based registration and the registration result remained essentially unchanged. The first row of Fig. 4 compares the registered sinogram with the reference sinogram of the simulation phantom with metal filling. The reconstructed

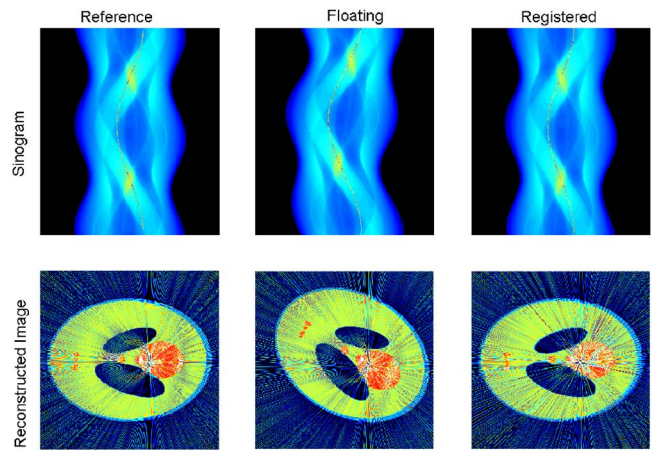


FIG. 4. Sinograms and reconstructed images for the reference case, the floating case, and the registered results of a phantom model with a metal filling using a fan beam with equal angle sampling.

images based on the sinogram data are shown in the second row. The metal fillings lead to obvious streak artifacts on the reconstructed images but no effect on the sinogram data. The conventional image-based registration behaves poorly in this case. Spatial accuracy of the registration was found to be greater than 4 pixels in the best scenarios. After an image-based registration, the NCC value was improved from -0.45 to -0.87 (the NCC for the perfect matching is -1). For Fig. 3 without metal artifacts, the value of NCC in the image-based registration is -0.98 . It is interesting to note that the ground truth solution of system does not yield the best metric. When we manually put the two images together according to the known shifts, the NCC value was only -0.83 due to the existence of the streak artifacts that are not affiliated to the motion. This suggests that the artifacts seriously disturb the search space and introduce nonphysical minima in the metric function space. In contrast, the metal fillings led to bright thin lines on the sinogram, which facilitate the sinogram registration. A spatial accuracy better than 2 pixels was readily achievable by the sinogram-based registration.

III.C. 2D registration of physical phantom

The registration results for the physical phantom experiments are shown in Fig. 5. After the reference scan was performed, the phantom was moved with a known amount to generate the sinogram. The new position of the phantom was set by rotating the phantom by 15 deg around the central axis and translating it by 3 cm on the axial plane. The reference and floating scans were performed in different gantry rotation directions (clockwise and counter-clockwise) and they had different projection numbers (640 projections for the reference scan and 639 projections for the floating scan) and different projection angle lists. In addition, a small portion of the nose of the phantom was outside of the scan range in the reference scan. The sinogram-based registration was able to find the correct solution in this less than ideal case with all of these differences in the two sinogram data sets. After registration, the motion trace and the original sinogram were re-

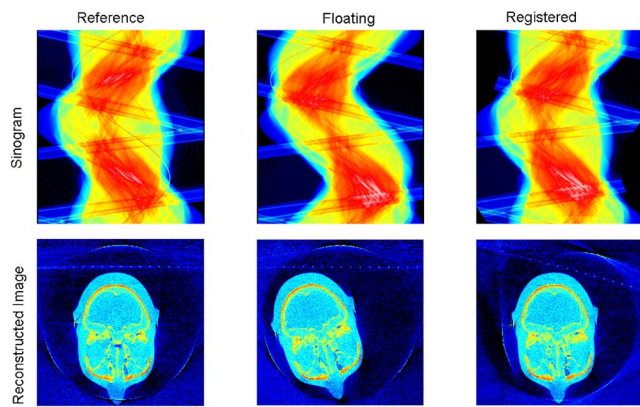


FIG. 5. Central axial plane sinograms and reconstructed images for the reference case, the floating case, and the registered results of a phantom scanned using a cone beam CT.

covered, shown as a registered sinogram. The spatial accuracy was found to be better than 1 mm in this case.

III.D. 3D registration of physical phantom with metal fiducials

Figure 6 illustrates four projections acquired during a typical cone beam CT scan. Projected positions of the four fiducials (BBs) vary with gantry angle and they are plotted in Fig. 7. In few cases, a BB was hardly detectable when it is close to the projection of the edge of a bony structure. However, the missing portion of the projections (see Fig. 7) does not affect our registration because its projections from other directions provide sufficient information to guide the registration. After the fiducial coordinates were calculated from reference and floating data, the 3D transformation parameters were calculated and compared against the known phantom 3D motion. Table I summarizes the calculated results for the five independent motions of the phantom. Additionally, it is found that the proposed algorithm was able to resolve any intentionally introduced combinational object motion of the

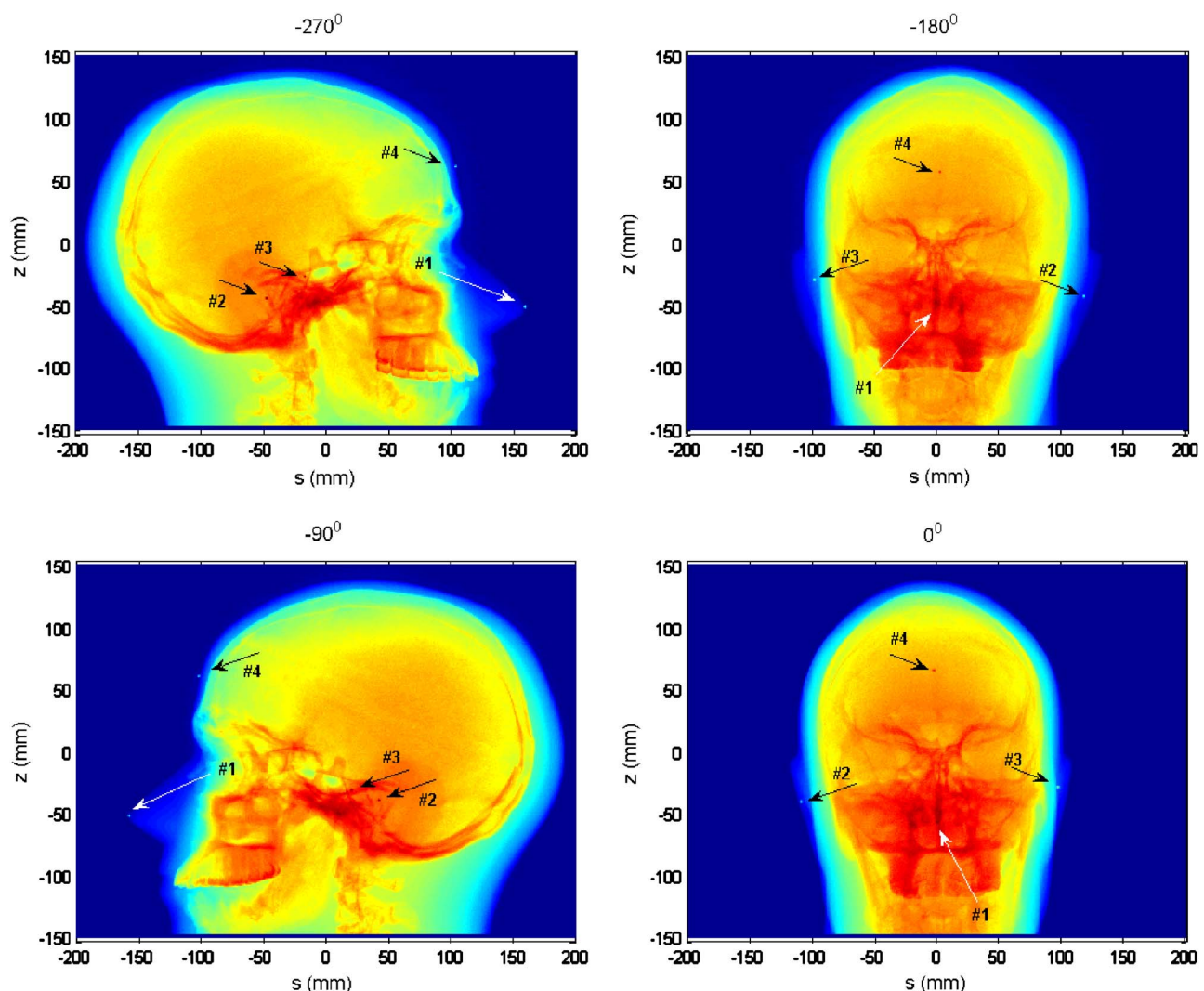


FIG. 6. Four projections of the cone beam CT scan of the head phantom. Gantry angle is labeled on each plot.

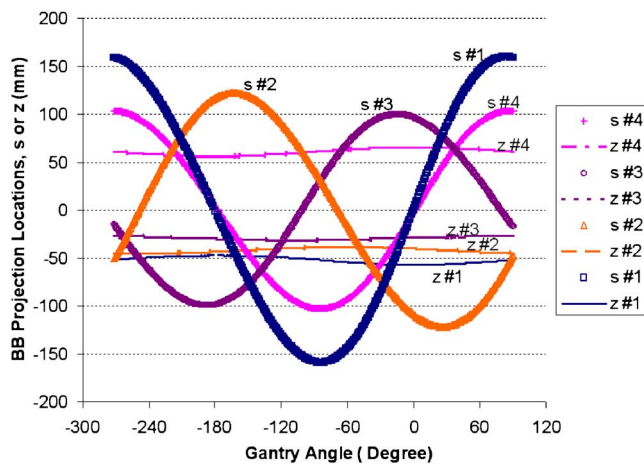


FIG. 7. Fiducial projections in a cone beam CT scan.

five degrees of freedom and yield registration better than 0.4 deg for angular variables or 0.4 mm for spatial translations.

IV. DISCUSSION

In this work, the relationship between an object motion and the resulted sinogram change was employed to facilitate the registration of two sinograms. A salient feature of the sinogram-based registration is that it allows us to avoid any adverse influence of image reconstruction and thus register the motion more accurately and reliably. The application of this algorithm is not limited to metal artifact evasion. Generally speaking, the method is valuable wherever the image reconstruction is incapable of reconstructing the image with high fidelity. In this case, a direct registration in the image space is often adversely influenced by the reconstruction-induced artifacts, and sinogram-based registration provides a complementary alternative. Another useful application of the proposed algorithm is to register two objects with incomplete projection data. This is of practical importance; as in many circumstances in IGRT, the available data is limited due to various clinical constraints. For example, in respiration-gated radiation therapy guided by fluoroscopic imaging, the only data available from time to time are the two stereotactic projection data.^{22–24}

Three-dimensional motion registration in sinogram space is generally limited to small angle rotation due to a general lack of a direct mathematical relation between sinograms

corresponding to different object positions. One way to proceed is to derive the transformation by going through the inverse image reconstruction process. In CyberKnife stereotactic x-ray guidance system (Accuray Inc., Sunnyvale, CA), for example, this is achieved by prestoring a large number of digitally reconstructed radiograms (DRRs), each corresponding to a possible object motion. During an actual treatment session, the acquired projection images at a time point are compared with the prestored DRRs to determine the actual patient anatomy in the treatment machine coordinates. Another alternative to obtain the transformation is to use Fourier transform. Unfortunately, this approach assumes a smooth density function of the object and thus also can cause metal artifacts (except for MV tomographic application). While the formalism is general, the actual implementation cannot easily proceed without approximation of small angle limitation.¹⁷

In lieu of attempting to provide a complete 3D solution, which seems to be mathematically intractable, we focused on developing a formalism of 3D metallic fiducial registration in sinogram space. After all, this is where the image-based registration encounters difficulty and this is where the sinogram registration complements the conventional approach. Our results suggest that the technique provides a viable solution for fiducial matching of image guided radiation therapy.

In the above only rigid registration is discussed. In the presence of organ deformation, the 3D registration in sinogram space may be difficult because of the lack of aforementioned sinogram transformation that links two object positions. Conceptually, there seems to be no obstacle impeding the extension of any image-feature-based deformable model (such as the basis spline or thin plate spline method) to deal with the problem in sinogram space if the sinogram transformation is available either analytically or numerically. However, one may encounter difficulty when attempting to develop a physical-model-based registration (such as elastic-model-based registration) in sinogram space without invoking the inverse image reconstruction process because a physics model is usually developed in image space. The fact that our formalism is established in the real space instead of the Fourier space makes it potentially useful in the development of deformable registration in sinogram space in the future. This is clearly a subject of future study.

V. CONCLUSION

We have investigated the relationship between object displacement and CT projection data relocation and applied this relation for sinogram-based image registration. Problem and solution for 3D sinogram-based registration of metallic implants were also addressed. Simulated and experimental results demonstrated that the new registration technique worked well for registration of 2D rigid axial motion in parallel beam sampling and fan beam sampling CT scans. Three-dimensional fiducial matching experiments in sinogram space were also carried out. The main advantages of the proposed technique in comparison to conventional ap-

TABLE I. Calculated transformation parameters versus phantom setup. Each column presents a one-dimensional motion in one of the five degree of freedom of the phantom platform. R_y and R_z are rotations around y and z axes, respectively. D_x , D_y , and D_z are translations along x , y , and z axes, respectively.

	R_y (deg)	R_z (deg)	D_x (mm)	D_y (mm)	D_z (mm)
Phantom motion	5.0	5.0	5.0	5.0	5.0
Calculated	5.0	4.8	5.0	5.0	5.0

proach lies in that it allows us to avoid any possible adverse effect of image reconstruction (such as the metal artifact or other types of reconstruction artifacts). A direct 3D sinogram transformation relating two arbitrary object motions is desirable to provide a complete solution for sinogram-based registration.

ACKNOWLEDGMENTS

This work was supported in part by grants from the Department of Defense (Grant No. PC040282), the National Cancer Institute (Grant No. 1R01 CA104205), and the Komen Breast Cancer Foundation (Grant No. BCTR0504071).

APPENDIX: 3D SINOGRAM TRANSFORMATION FOR SMALL PITCH AND YAW MOTION

An arbitrary 3D motion includes independent 3D rotations and translations. The 3D rotations can be expressed as roll about the axial/longitudinal axis (z) for angle α [$R_z(\alpha)$], pitch around the x axis for angle ε [$R_x(\varepsilon)$], and yaw around the y axis for angle γ [$R_y(\gamma)$]. 3D translation becomes $M(r, \beta, \Delta z)$.

Similar to the approximations made by Lu *et al.*,¹⁷ for a small pitch and yaw angle (<10 deg), the 3D motion moves a point (x_r, y_r, z_r) to (x_f, y_f, z_f) :

$$R_x(\varepsilon)R_y(\gamma)R_z(\alpha)\begin{pmatrix} x_r \\ y_r \\ z_r \end{pmatrix} \cong R_z(\alpha)\begin{pmatrix} x_r \\ y_r \\ z_r \end{pmatrix} + \begin{pmatrix} z_r \tan \varepsilon \\ z_r \tan \gamma \\ 0 \end{pmatrix}; \quad (\text{A1})$$

$$\begin{pmatrix} x_t \\ y_t \\ z_t \end{pmatrix} \cong R_z(\alpha)\begin{pmatrix} x_r \\ y_r \\ z_r \end{pmatrix} + \begin{pmatrix} z_r \tan \varepsilon \\ z_r \tan \gamma \\ 0 \end{pmatrix} + M(r, \beta, \Delta z); \quad (\text{A2a})$$

$$\begin{aligned} x_t &= x_r \cos \alpha + y_r \sin \alpha + z_r \tan \varepsilon + r \cos \beta, \\ y_t &= -x_r \sin \alpha + y_r \cos \alpha + z_r \tan \gamma + r \sin \beta, \\ z_t &= z_r + \Delta z. \end{aligned} \quad (\text{A2b})$$

For a parallel beam sampling geometry, we have

$$\begin{aligned} R[f](\theta_f, s_f, \zeta_f) &= \int_{-\infty}^{\infty} \int_{-\infty}^{\infty} \int_{-\infty}^{\infty} f(x_f, y_f, z_f) \delta(x_f \sin \theta_f \\ &\quad - y_f \cos \theta_f - s_f) \delta(z_f - \zeta_f) dx_f dy_f dz_f. \end{aligned} \quad (\text{A3})$$

The x-ray path will be the same for two projections satisfying the following equations:

$$\begin{aligned} \theta_r &= \theta_f + \alpha, \\ s_r &= s_f - r \sin(\theta_f - \beta) + z_r \tan \varepsilon \sin \theta_f + z_r \tan \gamma \cos \theta_f, \\ z_r &= z_f - \Delta z. \end{aligned} \quad (\text{A4})$$

For a fan beam scan, similar sinogram transformation for 3D motion could be deduced:

$$\phi_r + \varphi_r = \phi_f + \varphi_f + \alpha,$$

$$\begin{aligned} \sin \varphi_r &= \sin \varphi_f - \frac{r}{FR} \sin(\phi_f + \varphi_f - \beta) + \frac{z_r}{FR} \tan \varepsilon \sin(\phi_f \\ &\quad + \varphi_f) + \frac{z_r}{FR} \tan \gamma \cos(\phi_f + \varphi_f), \end{aligned} \quad (\text{A5})$$

¹B. Fei *et al.*, "Deformable and rigid registration of MRI and microPET images for photodynamic therapy of cancer in mice," *Med. Phys.* **33**, 753–760 (2006).

²W. Lu *et al.*, "Deformable registration of the planning image (kVCT) and the daily images (MVCT) for adaptive radiation therapy," *Phys. Med. Biol.* **51**, 4357–4374 (2006).

³H. Wang *et al.*, "Implementation and validation of a three-dimensional deformable registration algorithm for targeted prostate cancer radiotherapy," *Int. J. Radiat. Oncol., Biol., Phys.* **61**, 725–735 (2005).

⁴L. Xiong *et al.*, "Deformable structure registration of bladder through surface mapping," *Med. Phys.* **33**, 1848–1856 (2006).

⁵D. J. Hawkes, "Algorithms for radiological image registration and their clinical application," *J. Anat.* **193** (Pt. 3), 347–361 (1998).

⁶J. B. Maintz and M. A. Viergever, "A survey of medical image registration," *Med. Image Anal.* **2**, 1–36 (1998).

⁷B. F. Hutton *et al.*, "Image registration: An essential tool for nuclear medicine," *Eur. J. Nucl. Med. Mol. Imaging* **29**, 559–577 (2002).

⁸E. Schreibmann and L. Xing, "Image registration with auto-mapped control volumes," *Med. Phys.* **33**, 1165–1179 (2006).

⁹J. F. Barrett and N. Keat, "Artifacts in CT: Recognition and avoidance," *Radiographics* **24**, 1679–1691 (2004).

¹⁰D. A. Sennst *et al.*, "An extensible software-based platform for reconstruction and evaluation of CT images," *Radiographics* **24**, 601–613 (2004).

¹¹K. M. Horton, "CT imaging of patients with metallic hardware," *Crit. Rev. Comput. Tomogr.* **44**, 305–313 (2003).

¹²A. H. Mahnen *et al.*, "A new algorithm for metal artifact reduction in computed tomography: In vitro and in vivo evaluation after total hip replacement," *Invest. Radiol.* **38**, 769–775 (2003).

¹³J. Wei *et al.*, "X-ray CT high-density artefact suppression in the presence of bones," *Phys. Med. Biol.* **49**, 5407–5418 (2004).

¹⁴K. R. Hoffmann and J. Esthappan, "Determination of three-dimensional positions of known sparse objects from a single projection," *Med. Phys.* **24**, 555–564 (1997).

¹⁵E. E. Fitchard *et al.*, "Registration of synthetic tomographic projection data sets using cross-correlation," *Phys. Med. Biol.* **43**, 1645–1657 (1998).

¹⁶E. E. Fitchard *et al.*, "Registration using tomographic projection files," *Phys. Med. Biol.* **44**, 495–507 (1999).

¹⁷W. Lu *et al.*, "Image/patient registration from (partial) projection data by the Fourier phase matching method," *Phys. Med. Biol.* **44**, 2029–2048 (1999).

¹⁸Y. Xie and B. Bao, "Image registration by the Diagonal Mutual Information Method for the Projection Data," *International Conference on Sensing, Computing and Automation (ICSCA 2006)*, Chongqin, China, 2006. Vol. 2006, pp. 3921–3923.

¹⁹Lipps VCCaR, "ISAR imaging of small craft with roll, pitch and yaw analysis," *IEEE International Radar Conference 2000*, pp. 493–498.

²⁰Wikipedia, <http://en.wikipedia.org/wiki/Simulated-annealing>.

²¹A. Pugachev and L. Xing, "Incorporating prior knowledge into beam orientation optimization in IMRT," *Int. J. Radiat. Oncol., Biol., Phys.* **54**, 1565–1574 (2002).

²²J. Kim *et al.*, "Effects of x-ray and CT image enhancements on the robustness and accuracy of a rigid 3D/2D image registration," *Med. Phys.* **32**, 866–873 (2005).

²³H. Livyatan, Z. Yaniv, and L. Joskowicz, "Gradient-based 2-D/3-D rigid registration of fluoroscopic X-ray to CT," *IEEE Trans. Med. Imaging* **22**, 1395–1406 (2003).

²⁴L. Xing *et al.*, "Overview of image-guided radiation therapy," *Med. Dosim.* **31**, 91–112 (2006).

HYBRID MULTISCALE LANDMARK AND DEFORMABLE IMAGE REGISTRATION

DANA PAQUIN

Department of Mathematics, Stanford University
Stanford, CA 94305-2125

DORON LEVY

Department of Mathematics, Stanford University
Stanford, CA 94305-2125



LEI XING

Department of Radiation Oncology, Stanford University
Stanford, CA 94305-5947

(Communicated by Yang Kuang)

ABSTRACT. An image registration technique is presented for the registration of medical images using a hybrid combination of coarse-scale landmark and B-splines deformable registration techniques. The technique is particularly effective for registration problems in which the images to be registered contain large localized deformations. A brief overview of landmark and deformable registration techniques is presented. The hierarchical multiscale image decomposition of E. Tadmor, S. Nezzar, and L. Vese, *A multiscale image representation using hierarchical (BV, L^2) decompositions*, Multiscale Modeling and Simulations, vol. 2, no. 4, pp. 554–579, 2004, is reviewed, and an image registration algorithm is developed based on combining the multiscale decomposition with landmark and deformable techniques. Successful registration of medical images is achieved by first obtaining a hierarchical multiscale decomposition of the images and then using landmark-based registration to register the resulting coarse scales. Corresponding bony structure landmarks are easily identified in the coarse scales, which contain only the large shapes and main features of the image. This registration is then fine tuned by using the resulting transformation as the starting point to deformably register the original images with each other using an iterated multiscale B-splines deformable registration technique. The accuracy and efficiency of the hybrid technique is demonstrated with several image registration case studies in two and three dimensions. Additionally, the hybrid technique is shown to be very robust with respect to the location of landmarks and presence of noise.

1. Introduction. Image registration is the process of determining the optimal spatial transformation that brings two images into alignment with each other. Image registration is necessary, for example, when images of the same object are taken at different times, from different imaging devices, or from different perspectives. The two images to be registered, called the fixed and moving images, are the input to

2000 *Mathematics Subject Classification.* Primary: 68U10; Secondary: 92C55, 62P10, 94A08.

Key words and phrases. deformable image registration, multiscale analysis, CT, 4DCT, landmark registration, noise.

Development of a QA phantom and automated analysis tool for geometric quality assurance of on-board MV and kV x-ray imaging systems

Weihua Mao, Louis Lee, and Lei Xing^{a)}

Department of Radiation Oncology, Stanford University School of Medicine, Stanford, California 94305

(Received 27 September 2007; revised 15 January 2008; accepted for publication 17 January 2008; published 19 March 2008)



The medical linear accelerator (linac) integrated with a kilovoltage (kV) flat-panel imager has been emerging as an important piece of equipment for image-guided radiation therapy. Due to the sagging of the linac head and the flexing of the robotic arms that mount the x-ray tube and flat-panel detector, geometric nonidealities generally exist in the imaging geometry no matter whether it is for the two-dimensional projection image or three-dimensional cone-beam computed tomography. Normally, the geometric parameters are established during the commissioning and incorporated in correction software in respective image formation or reconstruction. A prudent use of an on-board imaging system necessitates a routine surveillance of the geometric accuracy of the system like the position of the x-ray source, imager position and orientation, isocenter, rotation trajectory, and source-to-imager distance. Here we describe a purposely built phantom and a data analysis software for monitoring these important parameters of the system in an efficient and automated way. The developed tool works equally well for the megavoltage (MV) electronic portal imaging device and hence allows us to measure the coincidence of the isocenters of the MV and kV beams of the linac. This QA tool can detect an angular uncertainty of 0.1° of the x-ray source. For spatial uncertainties, such as the source position, the imager position, or the kV/MV isocenter misalignment, the demonstrated accuracy of this tool was better than 1.6 mm. The developed tool provides us with a simple, robust, and objective way to probe and monitor the geometric status of an imaging system in a fully automatic process and facilitate routine QA workflow in a clinic. © 2008 American Association of Physicists in Medicine. [DOI: [10.1118/1.2885719](https://doi.org/10.1118/1.2885719)]

I. INTRODUCTION

The integration of on-board kilovoltage (kV) flat-panel imager to a medical linear accelerator has recently been realized by linac vendors¹⁻⁴ for image-guided radiation therapy (IGRT). These on-board imagers are mounted on robotic arms with an axis orthogonal to the megavoltage beam.⁵ An on-board imager offers three modes of acquisitions namely: (1) Two-dimensional (2D) planar projection image (radiographic acquisition); (2) 2D planar fluoroscopic image (fluoroscopic acquisition); and (3) three-dimensional (3D) cone-beam computed tomography (CBCT). The radiographic acquisition is used for 2D-2D matching with the digital reconstructed radiograph (DRR) for setup verification based on the bony landmarks or implanted fiducials.^{1,6} The fluoroscopic acquisition is employed for verifying the gating threshold or target position prior to a respiratory-gated treatment.⁷ The CBCT is used for 3D-3D matching with the planning CT for setup verification.⁸⁻¹¹ The geometric information of a patient derived from any of these modes relies on the configuration of the imager geometry, such as the position of the x-ray source, imager position and orientation, isocenter, and focus-to-imager distance. The functionality of the system depends heavily on the mechanical integrity and stability of the imaging device (the x-ray tube, imager and robotic arms) and the linac (on which the imaging system is mounted) at various gantry angles. This is particularly crucial for the flat-panel based CBCT that is mounted on an already laden gantry of a linac. The gantry sagging, together

with the flexing of the imaging system, results in geometric nonidealities during the gantry rotation in CBCT acquisition.^{10,12} The accurate reconstruction of transaxial slices of a 3D object from a set of 2D projections requires the x-ray source position and the detector orientation to be known precisely in 3D space in the rotation trajectory during the CBCT reconstruction.^{10,13-15} These geometric parameters are generally established through a geometrical calibration process done during the commissioning of the new machine and incorporated in image formation or reconstruction for correction.^{10,16} A prudent use of an on-board imaging system necessitates a routine surveillance of geometric accuracy of the system. This echoes to what Yoo *et al.*¹⁷ have pointed out that the most crucial part of a comprehensive QA program on an on-board imager would be those tests monitoring the geometric accuracy and stability of the imaging system. The recommendation by Yoo *et al.*¹⁷ on these tests is based on imaging a small cube phantom embedded with a central fiducial at orthogonal gantry angles and manually measuring the discrepancy between the recorded position of the fiducial and the digital graticule. This method is straightforward yet subjective due to the manual measurement. Furthermore, it is unable to give a full picture of the geometric status of the imaging system.

In research involving micro-CBCT, several geometric phantoms and associated analysis software have been developed for the geometric calibration and QA.^{14,18} A modification and an extension of its methodology might be warranted for the geometric QA of the on-board imaging system. Stud-

ies have also reported on the use of projection images of simple phantoms embedded with multiple fiducials to estimate the geometric parameters of the on-board imaging system,^{12,19} however the geometric parameters that can be estimated implicitly from the projection images have not been fully extracted due to the limitations in the design of the phantoms or associated data analysis software.

The purpose of the present work is to design a geometric QA phantom and develop an automated data analysis software to assess the geometric accuracy of an on-board imager, including the x-ray source position, the detector position and orientation, the isocenter, the rotation trajectory, and the source-to-imager distance (SID), from the projection images of the phantom. The developed phantom and analysis software apply equally well to the geometric QA of the MV electronic portal imaging device (EPID), and allow us to measure the coincidence of the isocenters of the MV and kV beams, which is an important parameter in ensuring that the treatment beam is targeting to where the imaging is guiding. The geometric QA procedure using this phantom, together with the automation of the data analysis, greatly facilitates the QA workflow and eliminates the subjectivity incurred in the manual measurement and result interpretation.

II. METHODS AND MATERIALS

II.A. Phantom design

An in-house software developed with the MatLab (MathWorks, Inc., Natick, MA) was used to simulate the projection image of an object with designated imaging geometry defined by the position of the source, position and orientation of the imager, and source-to-imager distance at any gantry angle. Virtual cubic phantoms (instead of physical phantoms) of various dimensions from 10 to 25 cm with 9, 13, 17 fiducials arranged in a helical trajectory at the surfaces were designed. These virtual phantoms served as inputs into the simulation program to simulate the projection images obtained at different gantry angles. The helical arrangement of the fiducials was chosen because it gave a good distribution of the fiducials in 3D space and offered the least superposition of the fiducials in the projection images obtained from different gantry angles for easy detection and identification. Nonuniform helical increments (itches) along the helical axis were used to further spare the fiducial projections.

Simulated projection images were created for each virtual phantom at every 30° of gantry angles. The phantom design, including the size and fiducial locations, was determined by maximizing the detection efficiency and sensitivity of fiducials to a change in imaging geometry. Based on the findings from the simulation, a cubic phantom measuring 18 × 18 × 18 cm³ with 13 steel ball bearings (BBs) of diameter 4.76 mm was fabricated. The BBs were embedded in the surface of the phantom in a skewed helical trajectory as shown in Fig. 1. The outside surface of every BB was tangential to the surface of the phantom ensuring that all BBs were protected from possible displacement or wearing during setup or handling. Orthogonal lines were scribed on the sur-

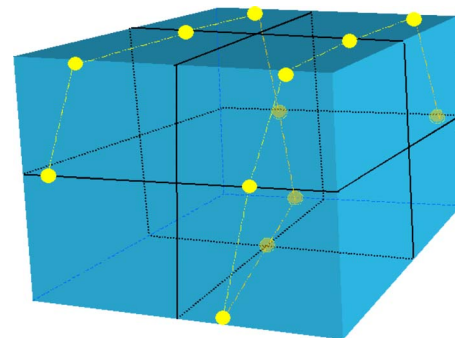


FIG. 1. The *gQA* phantom with 13 steel ball bearings (BBs) mounted on the surfaces in a skewed helical trajectory.

faces of the phantom to indicate the center of the cube at the intersection of these lines. This phantom was termed as *gQA* phantom hereafter for easy reference.

II.B. Reference coordinate system

To describe the geometry of the imaging system, a Cartesian phantom coordinate system was introduced. This coordinate system is attached to the phantom and aligned in space to an ideal linac with a rotating gantry. The *z* axis is along the rotation axis of the gantry, the *x* axis is horizontal, and *y* axis is vertical [Fig. 2(a)]. The origin is referred to the intersection of the laser alignments.

For a gantry angle ϕ (which also indicates the x-ray source angle), the position of the x-ray source (R, ϕ, z) is conveniently defined in a phantom fixed cylindrical coordinate which has the same origin and *z* axis of the phantom coordinate system, where *R* is the radius of the source rotation circle or the source-to-axis distance (SAD). A fiducial at (r, θ, z_B) is projected on the imager (*u, v*) [Fig. 2(b)] with

$$u = \frac{-Fr \cos(\theta - \phi)}{R + r \sin(\theta - \phi)}, \quad (1)$$

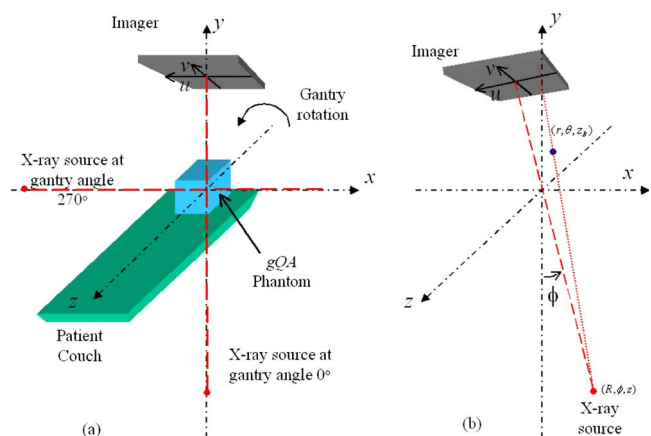


FIG. 2. Schematic representation of the phantom coordinate system (a), and the position of the x-ray source and a fiducial in the cylindrical coordinate system (b).

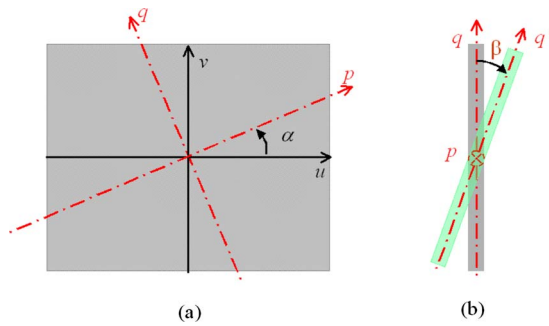


FIG. 3. Schematic diagram showing the tilting of the imager. The imager (uv plane) tilts along an imaginary axis p (a) and the tilting angle is defined as β (b).

$$v = \frac{F(z_B - z)}{R + r \sin(\theta - \phi)} + z, \quad (2)$$

where (u, v) defines an imager fixed coordinate system which rotates with the gantry. The imager center is the origin of the uv plane. The focal distance (F) is the SID. Details on how to derive Eqs. (1) and (2) are summarized in Appendix A. Considering the variations ($\Delta\phi$, ΔR , ΔF , Δu , and Δv) of the geometric parameters (ϕ , R , F , u , and v), the projections become

$$u + \Delta u = \frac{-(F + \Delta F)r \cos[\theta - (\phi + \Delta\phi)]}{(R + \Delta R) + r \sin[\theta - (\phi + \Delta\phi)]}, \quad (3)$$

$$v + \Delta v = \frac{(F + \Delta F)(z_B - z)}{(R + \Delta R) + r \sin[\theta - (\phi + \Delta\phi)]} + z. \quad (4)$$

Assuming that the imager might be tilted along an imaginary axis p , which is at an angle α with u axis, the imaginary axes are defined as p and q , respectively, on the uv plane as shown in Fig. 3(a). The transformation between coordinates (p, q) and (u, v) is

$$\begin{pmatrix} p \\ q \end{pmatrix} = \begin{pmatrix} \cos(\alpha) & \sin(\alpha) \\ -\sin(\alpha) & \cos(\alpha) \end{pmatrix} \begin{pmatrix} u \\ v \end{pmatrix}. \quad (5)$$

Further taking the tilted angle β into consideration [Fig. 3(b)], a new axis q' is defined accordingly with

$$q' = \left(1 + \frac{q}{F}\beta + \frac{1}{2}\beta^2\right)q. \quad (6)$$

In obtaining the above equation, it was assumed that the tilting angle is small ($<15^\circ$). Please refer to Appendix B for the derivation of Eq. (6).

It follows that the new projected coordinates (u_I, v_I) of the fiducial on a tilted imager are

$$\begin{aligned} \begin{pmatrix} u_I \\ v_I \end{pmatrix} &= \begin{pmatrix} \cos(\alpha) & -\sin(\alpha) \\ \sin(\alpha) & \cos(\alpha) \end{pmatrix} \begin{pmatrix} p \\ q' \end{pmatrix} \\ &= \begin{pmatrix} u \\ v \end{pmatrix} + \left(\frac{q}{F} + \frac{\beta}{2}\right)q\beta \begin{pmatrix} -\sin(\alpha) \\ \cos(\alpha) \end{pmatrix}. \end{aligned} \quad (7)$$

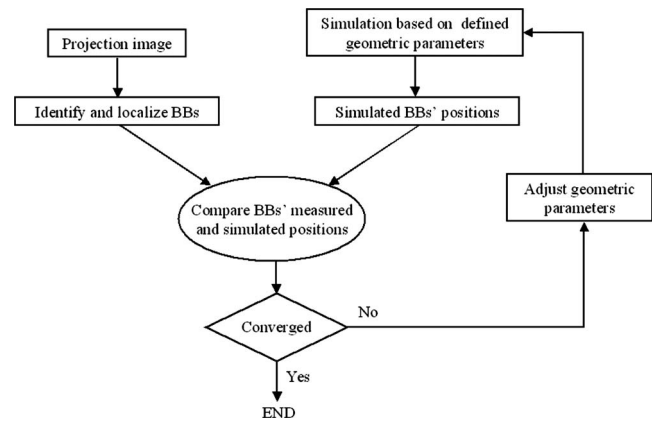


FIG. 4. Flow chart showing the algorithm of the analysis software.

II.C. Automated analysis software

From a projected image of the fiducials at a given gantry angle, eight geometric parameters could be quantitatively evaluated. These are: (1) Three parameters for the x-ray source position, namely the deviation of the gantry angle ($\Delta\phi$), the deviation of rotation radius (ΔR), and the deviation from the rotation plane (Δz); (2) three parameters for the position of the imager center, namely the deviation of the focal distance (ΔF), and the two translational offsets (Δu and Δv) in the uv plane; (3) two angular parameters (α and β) for the imager orientation.

An analysis software in C language was developed to estimate the eight parameters at any given gantry angle by comparing the measured and simulated BB locations in an iterative manner. The newly adjusted geometric parameters for the simulated BB location served as the inputs for the iteration (Fig. 4). The analysis software first identified and measured the BB locations (\bar{u}, \bar{v}) from the projection image in the presence of random background noise by intensity weighted averaging using

$$\begin{cases} \bar{u} = \frac{\sum_i u_i I_i}{\sum_i I_i} \\ \bar{v} = \frac{\sum_i v_i I_i}{\sum_i I_i} \end{cases}, \quad (8)$$

where I_i was the signal intensity of the pixel number i .²⁰ The software then determined the geometric parameters by minimizing the difference between the BBs measured and simulated locations from the simulation results based on Eqs. (3)–(7). For this purpose, the distance between the positions of the measured BB and its corresponding simulated BB was computed. The summation of these distances for all the BBs was used as the converging criterion for the optimization process. A hybrid optimization algorithm was adopted for this eight-parameter nonlinear optimization problem. Exhaustive search was applied first and possible solutions were compared in order to find the best 1000 seeds of parameter combinations for the simulated annealing algorithm to start with. Each step of the simulated annealing algorithm replaced the current solution by a random “nearby” solution

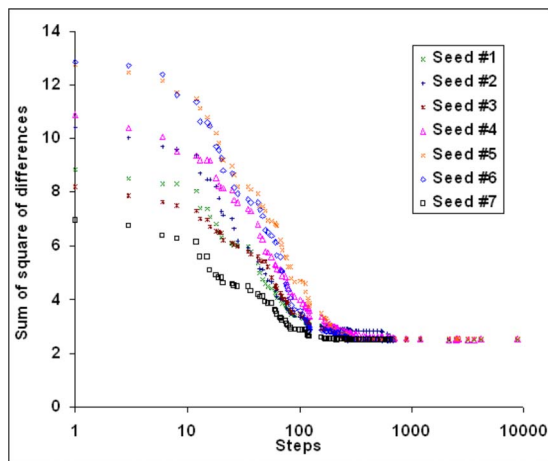


FIG. 5. Typical optimization converging curves.

chosen with a probability that depends on the difference between the corresponding function value and a global parameter (called the annealing temperature).^{21–24} The annealing temperature gradually decreased during the process. Finally the progress converged to the best estimate of the geometric parameters. Figure 5 illustrates several converging curves during the simulated annealing processes in analyzing a typical projection. This tool took about half a minute to analyze one projection image on a personal computer (DELL Precision 470 Workstation, 3.4 GHz CPU and 4 GB RAM). Typically, the sum of square distance differences converged to about 2.5 mm^2 . The average discrepancy for one fiducial was about 0.44 mm ($=\sqrt{2.5/13}$), which was around the size of an imager pixel.

II.D. Experimental evaluation

The developed *gQA* phantom and the automated analysis software (collectively called the *gQA* tool) were tested on a Varian Trilogy linac (Varian Medical Systems, Palo Alto, CA). The Trilogy is equipped with two image acquisition systems (IAS3): (1) MV EPID and (2) kV on-board imaging system (OBI). Both systems have a flat-panel detector with a matrix dimension of 1024×768 . The physical pixel sizes of the MV and kV imagers are 0.392 and 0.388 mm, respectively. The Trilogy is routinely maintained, and all the operating parameters are monitored and assured through a comprehensive QA program as suggested by TG 40.²⁵ The center of the *gQA* phantom was positioned at the nominal treatment isocenter as indicated by the room lasers. The relationship between the intersection of the room lasers and the mechanic isocenter of the linac was assumed to be maintained and calibrated in accordance with the routine QA practice.²⁵

II.D.1. Reproducibility of the analysis results

Projection images were acquired for MV EPID at a gantry angle of 0° (Varian convention) and at a SID of 1500 mm, the values were nominal. To ensure the *gQA* tool functions

properly in the worst-case scenario, the MV EPID was chosen here because the image quality of the MV acquisition was relatively inferior compared to that of the kV OBI. A 6 MV beam and 25 monitor units were used. The field size was $26 \times 20 \text{ cm}^2$. Twenty-one projections, 1 min apart, were made with the same imaging geometry and fed into the analysis software tool to estimate the geometric parameters of the imaging system. Although the 21 projection images were acquired under the same condition, they were associated with different random background noise. The purpose of this evaluation was to assess the reproducibility of the analysis results under different noisy environments.

II.D.2. Minimum detectable change in gantry angle

With the same setup, four projection images at nominal gantry angles of 0° , 0.1° , 0.2° , and 0.5° were taken. The projection images at nominal gantry angles of 0.1° , 0.2° , and 0.5° were subtracted from the one of 0° gantry angle to show the difference between the projection images made at slightly different angles. The purpose of this evaluation was to demonstrate the minimum change in gantry angle that could be detected from the projection image of the BBs.

II.D.3. Gantry angle offset

Further projection images were taken at nominal gantry angles of 0° , $\pm 0.1^\circ$, $\pm 0.2^\circ$, $\pm 0.3^\circ$, $\pm 0.5^\circ$, and $\pm 1.0^\circ$. This narrow range of gantry angle was chosen because an offset would affect a small gantry angle more than a large one. These images were then analyzed. The discrepancies between the nominal and estimated gantry angles were then compared in order to determine the gantry angle offset.

II.D.4. SID offset

Projection images were further acquired for MV EPID at a gantry angle of 180° but at different nominal SID of 1300, 1400, 1500, 1550, and 1600 mm. The best estimate of the SID was found by the analysis software. The discrepancies between the nominal and estimated SID were then compared in order to determine the SID offset.

II.D.5. Imager center offset

With the SID reset to 1500 mm, projection images were acquired with the imager center at (0, 0) and offset to (20, 20), (20, -20), (-20, -20), and (-20, 20) mm in the *uv* plane. The best estimate of the detector shift was found by the analysis software. The discrepancies between the actual and estimated offsets with and without systematic drift correction were then compared in order to determine the imager center offset.

II.D.6. Phantom positional shift

With the imager center reset to the origin, the *gQA* phantom was displaced -5.0 mm in each of the *x*, *y*, and *z* directions simultaneously. This was to mimic a condition where there were spatial drifts in the imaging geometry ($\Delta R, \Delta z, \Delta F, \Delta u, \Delta v$) in 3D space. When the phantom posi-

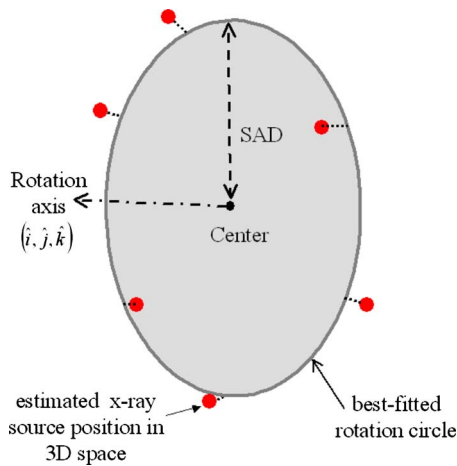


FIG. 6. Schematic diagram showing a best fitted rotation circle that has the shortest distances (the least sum distance square) from all the estimated x-ray sources in 3D space. The center of this circle is taken as the isocenter of the gantry rotation.

tion was shifted, the whole imaging system, including the source and imager position, was shifted in the opposite direction from the phantom's point of view. Projection images were then acquired at a SID of 1500 mm with gantry angles at 0° , 90° , 180° , and 270° . The same set of projection images was repeated with the phantom displaced 5.0 mm in the x, y, z direction and 10.0 mm in the same direction as well. The geometric parameters corresponding to these changes were estimated by the analysis software. The purpose of this evaluation was to demonstrate the accuracy of the *gQA* tool in detecting the variations in the imaging geometry.

II.D.7. Coincidence of the isocenters for the MV and kV beams

The center of the *gQA* phantom was repositioned at the nominal treatment isocenter as indicated by the room lasers. Projection images were acquired for MV EPID at every 10° of gantry angle for 360° and at a SID of 1500 mm resulting in 36 projection images in total. Projection images were also acquired for the OBI at every 0.56° of gantry angle for 360° and at a SID of 1500 mm resulting in 640 projection images in total (i.e. CBCT acquisition mode). The exposure factors were 125 kVp, 2 mAs, and the field size was $26 \times 20 \text{ cm}^2$ for the OBI projection image. The eight geometric parameters for each series of projected images were estimated and the

variation of each parameter for the full gantry rotation was examined. For each series of data, a best-fitted rotation circle was found such that it had the shortest distances (the least sum distance square) from all estimated x-ray sources in 3D space. The direction of the rotation circle was denoted by the unit vectors $(\hat{i}, \hat{j}, \hat{k})$, and its radius (SAD) was calculated. The rotation circle was taken as the rotation trajectory of the imaging system and its center as the isocenter (Fig. 6). The isocenters for the MV and kV beams were then found and compared.

II.D.8. Relationship among various geometric parameters

A change in one geometric parameter, for instance, the gantry angle, might affect other parameters of the imaging system as the whole imaging assembly is mounted on a laden gantry and robotic arms. There might be a subtle relationship between these parameters depending on the actual configuration and position of the imaging system. We studied this issue by scrutinizing the data obtained in Sec. II D 7 in which the projection images were acquired at different gantry angles. The aim was to see the changes in other parameters brought by the change in the gantry angle. We limited the studied range to be in $\pm 45^\circ$ because, beyond this range, the sagging of the gantry might overwhelm the subtle relationship amongst the different parameters. Furthermore, we studied the changes in parameters brought about by the specific parameter we varied in other evaluations such as in SID offset and imager off center (Secs. II D 4 and II D 5). All the results were compiled in a table to show the changes.

III. RESULTS

III.A. Reproducibility of the analysis results

Table I shows the variations of each of the eight geometric parameters of the MV imaging system for the 21 projection images with different background noise. The small standard deviation of each estimated geometric parameter indicated a good agreement of the data and the analysis results were highly reproducible. The imager center offset ($\Delta u, \Delta v$) was up to $(-0.63 \text{ mm}, 1.67 \text{ mm})$, which was due to a systematic drift of the MV imager.

TABLE I. The variations of each of the eight geometric parameters of the imaging system for the 21 projection images with different background noise. $\Delta\phi$, ΔR , and Δz are the deviations of the gantry angle, rotation radius and deviation from the rotation plane, respectively. ΔF , Δu , and Δv are the deviations of the source-to-detector distance, and the two translational offsets of the detector in the uv plane, respectively; α and β describe the orientation of the imager.

	$\Delta\phi$ ($^\circ$)	ΔR (mm)	Δz (mm)	ΔF (mm)	Δu (mm)	Δv (mm)	α ($^\circ$)	β ($^\circ$)
Min.	-0.39	-0.69	0.03	-0.48	-0.65	1.63	-0.28	-1.00
Max.	-0.35	-0.52	0.10	-0.24	-0.61	1.71	-0.11	-0.92
Mean	-0.37	-0.59	0.06	-0.37	-0.63	1.67	-0.22	-0.98
SD	0.01	0.04	0.02	0.06	0.01	0.02	0.05	0.02

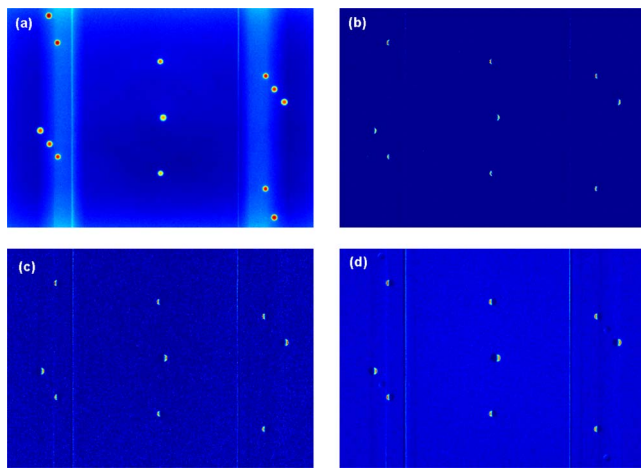


FIG. 7. (a) The projection image of the *gQA* phantom at gantry angle 0° . (b)–(d) show the image subtractions of the projection images at gantry angles 0.1° , 0.2° , and 0.5° from that at gantry angle 0° , respectively.

III.B. Minimum detectable change in gantry angle

Figure 7(a) shows the projection image at gantry angle 0° . Figures 7(b)–7(d) show the image subtractions of the projection images at the gantry angles 0.1° , 0.2° , and 0.5° from that at 0° , respectively. From the subtraction images, 9 out of 13 BBs' locations showed residual values indicating that 4 BBs were not differentiated by the projections made with small gantry angle changes and were totally subtracted out. In other words, there still remained 9 BBs that were “sensitive” enough to show the gantry change down to 0.1° .

III.C. Gantry angle offset

Figure 8 depicts the correlation of the nominal and estimated gantry angles in the range of $\pm 1^\circ$. The coefficient of determination (R^2) of 1.00 shows a very good correlation

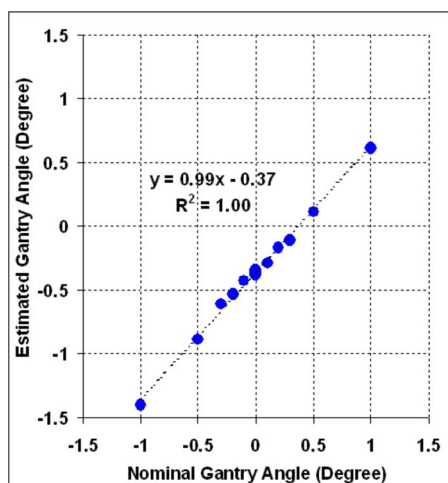


FIG. 8. The correlation of the nominal and estimated gantry angles in the range of $\pm 1^\circ$.

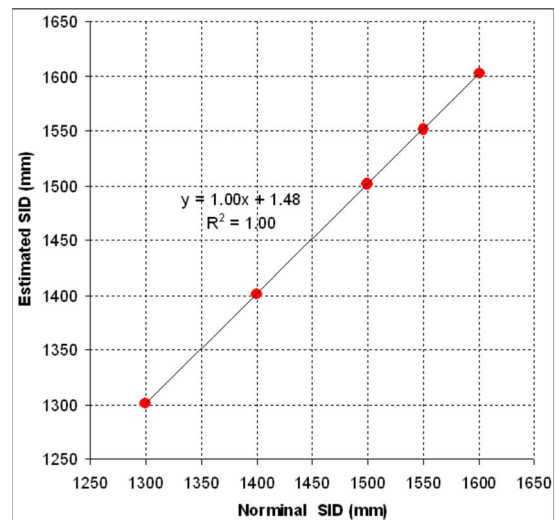


FIG. 9. The correlation of the nominal and estimated source-to-imager distance (SID) at a gantry angle of 180° .

between the two angles. From the regression line, a residual angle offset of 0.37° is evident for the nominal value of the gantry angle in the range studied.

III.D. SID offset

Figure 9 shows the correlation of the nominal and estimated SID in the range of 1300–1600 mm. The R^2 of 1.00 shows an almost perfect linearity between nominal and estimated SID. The regression line indicates that there is a consistent offset of 1.48 mm to the nominal SID in the range studied.

III.E. Imager center offset

Figure 10 shows the actual and estimated offset positions of the MV imager center on the (u, v) imager coordinate plane. A systematic drift of the detector was noted as observed in the previous evaluation II.D.1. If this systematic drift was corrected, the net estimated offset positions of the imager were close to the actual offsets within ± 1 mm.

III.F. Phantom positional shift

Table II lists the estimated relative shifts of the imaging geometry for the displaced phantoms with different magnitudes of displacement at the four principal orthogonal gantry angles. Depending on the gantry angle, ΔR , Δz , ΔF , Δu , and Δv reflected the displacement of the phantom in each of the x, y, z directions. The signs of the variations depend on the relative position between the phantom and the imaging system governed by the gantry angle. The maximum discrepancy between the actual and estimated shift was less than 1.6 mm ($1.6 = |10 - 8.4|$), which came from the differences between phantom shift of 10 mm and the estimated ΔR .

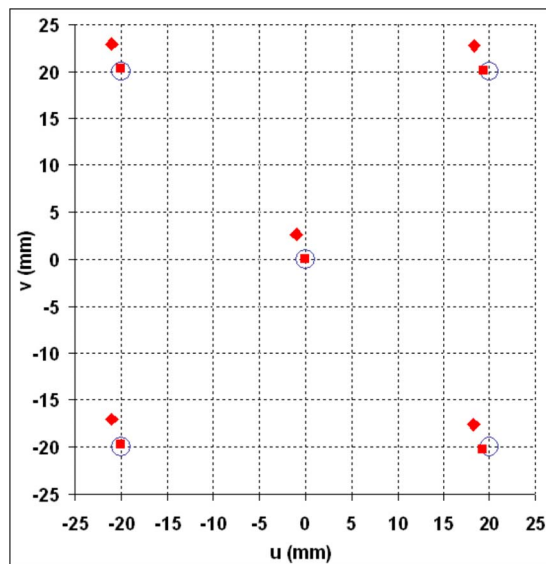


FIG. 10. The estimated shift (\blacklozenge) and estimated shift after the correction of the systematic drift (\blacksquare) compared to the actual offset of imager center (\circ) on the (u, v) imager coordinate plane.

III.G. Coincidence of the isocenters for the MV and kV beams

Table III lists the variation of each of the eight geometric parameters estimated for the MV EPID and kV OBI for a complete gantry rotation. The standard deviation of each estimated geometric parameter for the MV EPID and kV OBI were small indicating a good agreement of the same geometric parameter at different gantry angles. The orientations of the MV and kV rotation plane were found to be (0.00010, 0.00006, 1.00000) and (0.00030, 0.00001, 1.00000), respectively. The estimated isocenters for the MV and kV beams were at $(-0.95, -0.84, -0.25)$ mm and $(-0.97, -1.21, -0.13)$ mm in the reference coordinate. The coincidence of the two isocenters was well within 0.5 mm.

III.H. Relationship among various geometric parameters

Table IV lists the changes of geometric parameters of the imaging system brought about by the specific parameters varied in different evaluations. A change in one specific parameter could, to a certain extent, cause changes in other parameters depending on the actual configuration or the position of the imaging system, however, these changes were small and assumed not to affect the results of the experimental evaluations.

IV. DISCUSSION

We have designed a geometric QA phantom tailoring to an automated analysis to successfully estimate the geometric parameters of an on-board imaging system with a reasonable accuracy. The size of the phantom and the helical arrangement of the fiducials on the surface ensure the projected positions of the fiducials are well spaced on a detector area at any gantry angle for easy detection and identification. In principle, the more the number of the fiducials is, the more information that can be extracted for estimating the geometric parameters, but there will be higher chances of superposition among the fiducial projections. There is a trade-off between the number of fiducials and the minimum distance between the fiducial projections. Based on the result from the evaluation II.D.2, we concluded that 13 BBs were adequate for the present application and this *gQA* tool can detect an angular uncertainty of 0.1° .

Concerning the analysis software, the direct relationship between the 2D projected position of a fiducial and the idealized geometric parameters of an imaging system was used in an optimal manner for determining the geometric parameters. Theoretically, eight equations (from four fiducials' 2D projections) might be enough to solve this type of eight-parameter problem in a perfect mathematical model. In reality, the system is not perfect and several imperfect factors might occur: (1) The x-ray source is not a real geometry

TABLE II. The estimated relative drifts of the imaging geometry for the displaced phantoms with different magnitudes of displacement at four principal orthogonal gantry angles. ΔR , Δz , and ΔF are the deviation of the rotation radius, deviation from the rotation plane and deviations of the source-to-detector distance, respectively. Δu and Δv are the two translational offsets of the detector in the uv plane, respectively.

Phantom shift (mm)	Gantry angle ($^\circ$)	ΔR (mm)	Δz (mm)	ΔF (mm)	Δu (mm)	Δv (mm)
$\Delta x = -5.0$	0	3.7	-5.4	-0.2	4.6	5.3
$\Delta y = -5.0$	90	4.5	-5.1	0.0	-3.9	5.4
$\Delta z = -5.0$	180	-4.2	-5.4	-0.2	-4.5	5.3
	270	-4.6	-5.6	0.1	4.0	5.2
$\Delta x = 5.0$	0	-5.6	4.6	0.0	-4.6	-4.8
$\Delta y = 5.0$	90	-4.5	4.8	0.0	5.6	-4.8
$\Delta z = 5.0$	180	5.4	4.8	-0.2	4.7	-4.8
	270	4.9	4.7	0.2	-5.5	-4.8
$\Delta x = 10.0$	0	-8.4	9.7	0.0	-9.7	-9.9
$\Delta y = 10.0$	90	-9.2	10.2	0.2	8.6	-9.8
$\Delta z = 10.0$	180	8.4	10.4	-0.3	9.5	-9.6
	270	9.9	8.9	-0.4	-8.4	-10.4

TABLE III. The variations of each of the eight geometric parameters of the MV/kV imaging systems from projections acquired through a complete gantry rotation. $\Delta\phi$, ΔR , and Δz are the deviations of the gantry angle, rotation radius and deviation from the rotation plane, respectively. ΔF , Δu , and Δv are the deviations of the focal distance, and the two translational offsets of the detector in the uv plane, respectively.

		$\Delta\phi$ (°)	ΔR (mm)	Δz (mm)	ΔF (mm)	Δu (mm)	Δv (mm)	α (°)	β (°)
MV	Min.	-0.4	-1.2	-0.8	-2.3	-1.0	1.3	-0.3	-1.4
	Max.	0.0	2.7	0.1	2.5	-0.5	2.2	0.3	-0.6
	Mean	-0.2	0.5	-0.3	0.2	-0.8	1.7	0.0	-1.0
	SD	0.1	1.4	0.3	1.8	0.2	0.3	0.2	0.2
kV	Min.	-0.3	0.2	-0.8	-2.2	-1.2	1.3	-0.3	-2.4
	Max.	0.1	4.9	0.2	2.3	0.9	2.5	0.4	-0.7
	Mean	-0.1	2.2	-0.2	-0.1	-0.1	1.9	0.0	-1.3
	SD	0.1	1.5	0.3	1.6	0.7	0.4	0.2	0.5

point and has a finite size, which leads to geometric penumbra; (2) the accuracy of the spatial location of the fiducial is limited by measurement; and (3) the imager pixel has a finite size and is associated with noise. These imperfections render us to summon more equations in solving the problem. This proposed analysis tool takes all fiducial projections into account in the optimization. In addition, Eqs. (3)–(7) indicate that this is a nonlinear problem and multiple local minima might possibly coexist with the global minimum. While it is not clear whether the estimation results from some image-based optimization approaches¹⁹ would be trapped in the local minimum, we adopted to use a global optimization algorithm of simulated annealing for our software to ensure a global minimum is always achievable. Moreover, the exhaustive search at the beginning of the process warrants well-distributed seeds for the simulated annealing and, in turn, saves optimization time significantly.

We have evaluated the *gQA* tool by estimating the geometric parameters of the imaging system under various imaging geometries. The results were highly reproducible and showed that the developed tool was responsive to all the changes introduced in the evaluation such as SID, detector offset, and phantom shift. The best estimates of these spatial parameters in different situations were well within 1.6 mm.

The estimation of the rotation plane and the isocenter by a series of projection images of the *gQA* phantom through a full gantry rotation is extremely useful in monitoring the geometric parameters pertinent to the flat-panel based CBCT and the coincidence of the MV and kV beams. We found that the coincidence of the MV/kV beam isocenters were 0.5 mm

comparable to the value of 0.8 mm which was obtained by the routine OBI QA exercise on the Trilogy. Comparing to the existing OBI QA exercise, our tool is more comprehensive giving a full picture of the geometric status and details on the rotation trajectories of both the x-ray sources (MV/kV) and their orientation of the rotation planes. Yoo *et al.*¹⁷ pointed out that their recommendation did not include a separate geometric QA measurement for the OBI CBCT, the developed tool would be a good choice to fill it this gap because of its simplicity, easy implementation and full automation of the analysis.

Just like any other phantom-based QA studies,^{13–15,19} one limitation of the present work lies on the mechanical imprecision in the positions of the BBs since the simulation of the BBs position assumes a perfect alignment of the BBs in the designated skewed helical trajectory. The BBs in the present *gQA* phantom are accurate to within 0.5 mm in their designated position and is considered adequate for the current application.

A simple guideline is recommended here on how to use this *gQA* tool in a clinic. First, set up the phantom to the room lasers, which is used to provide a reference to the room coordinates. A level can be used or even embedded in the phantom to assure its geometric setup. Second, kV and/or MV projection images are acquired at a designated angle. Each (kV or MV) imaging system is described by the eight geometric parameters. To obtain the eight parameters of the imaging system (kV or MV) at a designated angle, in principle, a single projection measurement at that angle is sufficient. Last, the projection image is fed to the analysis soft-

TABLE IV. The changes of geometric parameters of the imaging system brought about by the specific parameters varied in different evaluations. $\Delta\phi$, ΔR , and Δz are the changes in the gantry angle, rotation radius and distance from the rotation plane, respectively. ΔF , Δu , and Δv are the changes of the focal distance, and the two translational offsets of the imager in the uv plane, respectively; α and β describe the changes in the tilting of the imager.

Evaluation	Parameter varied	Range varied	$\Delta\phi$ (°)	ΔR (mm)	Δz (mm)	ΔF (mm)	Δu (mm)	Δv (mm)	α (°)	β (°)
II.D.4	SID	1300–1600 mm	0.01	1.06	0.08	...	0.23	0.75	0.34	0.13
II.D.5	Imager off center	± 20 mm	0.00	0.27	0.08	0.12	0.61	0.25
II.D.7	Gantry angle	$\pm 45^\circ$...	0.28	0.05	0.50	0.02	0.06	0.13	0.05

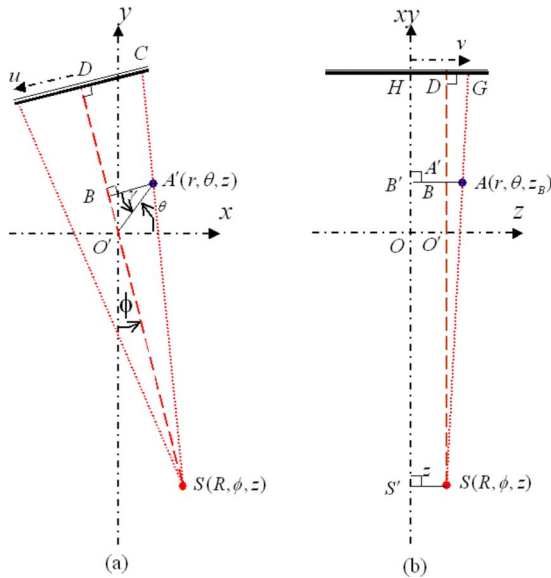


FIG. 11. Geometric relationship between a fiducial's 3D position and its projection on the imager.

ware to calculate the geometric parameters. A more comprehensive approach would be acquiring the projections during a continuous gantry rotation (kV CBCT/MV arc mode delivery). In that case, the geometric parameters at different gantry angles could be evaluated. Furthermore, the isocenters of the imaging system could also be calculated by the software if three or more projections are available.

V. CONCLUSIONS

A new geometric QA phantom and an automated analysis software have been developed to estimate the geometric status of a MV or kV on-board imager. This provides us a simple, robust and objective way to probe and monitor the geometric status of an imaging system in a fully automatic process, and facilitate routine QA workflow in a clinic.

ACKNOWLEDGMENTS

This work was supported in part by grants from the Department of Defense (PC040282), the National Cancer Institute (1R01 CA104205), and the Komen Breast Cancer Foundation (BCTR0504071). Support from the Sir Robert Black Postdoctoral Fellowship and the Hong Kong Hospital Authority Overseas Training Allowance for the second author are also gratefully acknowledged.

APPENDIX A: DERIVATION OF THE FIDUCIAL LOCATION (U, V)

When the x-ray source $S(R, \phi, z)$ is at a gantry angle of ϕ , an arbitrary object $A(r, \theta, z_B)$ is projected to C on imager u axis centering at D . Figure 11(a) provides a 2D view on an xy plane where the source S locates (z). $A'(r, \theta, z)$ is the projection of A on this plane. Using the similar triangle relationship between the triangles $SA'B$ and SCD , we have Eq. (A1)

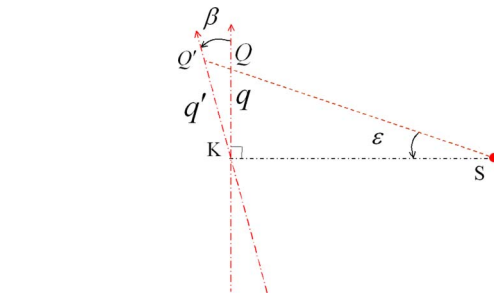


FIG. 12. Schematic diagram showing the tilting of the imager upon the p axis.

$$\frac{|CD|}{|A'B|} = \frac{|SD|}{|SB|}, \quad (\text{A1})$$

while $|A'B| = r \cos \gamma$ is the distance from A' to the projection central line (SO') and SD is the source-to-imager distance (F). SB is the distance from source to the projection on the central line. It is calculated by Eq. (A2)

$$|SB| = R + r \sin \gamma, \quad (\text{A2})$$

given

$$\begin{aligned} \gamma &= \angle BA'O' = \angle A'O'S - \angle A'BO' \\ &= \left[\left(\theta + \frac{\pi}{2} \right) - \phi \right] - \frac{\pi}{2} = \theta - \phi. \end{aligned} \quad (\text{A3})$$

So we have

$$|CD| = F \frac{|A'B|}{R + r \sin \gamma} = \frac{Fr \cos(\theta - \phi)}{R + r \sin(\theta - \phi)}$$

or

$$u = \frac{-Fr \cos(\theta - \phi)}{R + r \sin(\theta - \phi)}.$$

The negative sign was added due to the definition of u axis.

A side view perpendicular to the beam axis is shown in Fig. 11(b). Now A' and B are overlapped on this view. Based on the similarity between triangles SAB and SGD , the magnification factor is

$$\frac{|DG|}{|AB|} = \frac{|SD|}{|SB|}$$

while $|AB| = |AB'| - |SS'| = z_B - z$, $|SD| = F$, $|SB| = R + r \sin \gamma$.

So the projection on the v axis is

$$v = |GH| = |DG| + z = \frac{F(z_B - z)}{R + r \sin(\theta - \phi)} + z.$$

APPENDIX B: DERIVATION OF THE TILTED AXIS q'

After a tilting of β , the projection at Q moved to Q' , and the coordinate on q axis becomes a coordinate on q' axis. As shown in Fig. 12, from the triangle KQQ' , we have

$$\frac{|KQ|}{\sin(\angle Q'QK)} = \frac{|KQ'|}{\sin(\angle QQ'K)}.$$

Because

$$\angle Q'QK = \pi - \left(\beta + \frac{\pi}{2} \right) - \varepsilon = \frac{\pi}{2} - (\beta + \varepsilon)$$

and

$$\angle QQ'K = \frac{\pi}{2} + \varepsilon,$$

so

$$\frac{q'}{q} = \frac{|KQ'|}{|KQ|} = \frac{\sin\left(\frac{\pi}{2} + \varepsilon\right)}{\sin\left(\frac{\pi}{2} - (\beta + \varepsilon)\right)} = \frac{\cos(\varepsilon)}{\cos(\beta + \varepsilon)}.$$

Use small angle approximation, $\cos(\varepsilon) \approx 1 - 1/2\varepsilon^2$ and $\cos(\beta + \varepsilon) \approx 1 - 1/2(\beta + \varepsilon)^2$,

$$\begin{aligned} \frac{q'}{q} &\approx \frac{1 - \frac{1}{2}\varepsilon^2}{1 - \frac{1}{2}(\beta + \varepsilon)^2} \approx \left[1 - \frac{1}{2}\varepsilon^2 \right] \left[1 + \frac{1}{2}(\beta + \varepsilon)^2 \right] \\ &\approx 1 + \beta\varepsilon + \frac{1}{2}\beta^2. \end{aligned}$$

Approximately, $\varepsilon \approx q/F$.

So

$$q' \approx \left(1 + \beta\varepsilon + \frac{1}{2}\beta^2 \right) q.$$

^{a)} Author to whom correspondence should be addressed. Electronic mail: lei@reyes.stanford.edu

¹ B. Sorcini and A. Tilikidis, "Clinical application of image-guided radiotherapy, IGRT (on the Varian OBI platform)," *Cancer Radiother* **10**, 252–257 (2006).

² C. A. McBain, A. M. Henry, J. Sykes, A. Amer, T. Marchant, C. M. Moore, J. Davies, J. Stratford, C. McCarthy, B. Porritt, P. Williams, V. S. Khoo, and P. Price, "X-ray volumetric imaging in image-guided radiotherapy: The new standard in on-treatment imaging," *Int. J. Radiat. Oncol., Biol., Phys.* **64**, 625–634 (2006).

³ L. Xing, B. Thorndyke, E. Schreibmann, Y. Yang, T. F. Li, G. Y. Kim, G. Luxton, and A. Koong, "Overview of image-guided radiation therapy," *Med. Dosim.* **31**, 91–112 (2006).

⁴ Y. Yang, E. Schreibmann, T. Li, C. Wang, and L. Xing, "Evaluation of on-board kV cone beam CT (CBCT)-based dose calculation," *Phys. Med. Biol.* **52**, 685–705 (2007).

⁵ D. Letourneau, J. W. Wong, M. Oldham, M. Gulam, L. Watt, D. A. Jaffray, J. H. Siewerdsen, and A. A. Martinez, "Cone-beam-CT guided radiation therapy: Technical implementation," *Radiother. Oncol.* **75**, 279–

286 (2005).

⁶ W. Mao, T. Li, N. Wink, and L. Xing, "CT image registration in sinogram space," *Med. Phys.* **34**, 3596–3602 (2007).

⁷ C. Huntzinger, P. Munro, S. Johnson, M. Miettinen, C. Zankowski, G. Ahlstrom, R. Glettig, R. Filliberti, W. Kaissl, M. Kamber, M. Amstutz, L. Bouchet, D. Klebanov, H. Mostafavi, and R. Stark, "Dynamic targeting image-guided radiotherapy," *Med. Dosim.* **31**, 113–125 (2006).

⁸ T. Li, L. Xing, P. Munro, C. McGuinness, M. Chao, Y. Yang, B. Loo, and A. Koong, "Four-dimensional cone-beam computed tomography using an on-board imager," *Med. Phys.* **33**, 3825–3833 (2006).

⁹ M. Oldham, D. Letourneau, L. Watt, G. Hugo, D. Yan, D. Lockman, L. H. Kim, P. Y. Chen, A. Martinez, and J. W. Wong, "Cone-beam-CT guided radiation therapy: A model for on-line application," *Radiother. Oncol.* **75**, 271–278 (2005).

¹⁰ D. A. Jaffray, J. H. Siewerdsen, J. W. Wong, and A. A. Martinez, "Flat-panel cone-beam computed tomography for image-guided radiation therapy," *Int. J. Radiat. Oncol., Biol., Phys.* **53**, 1337–1349 (2002).

¹¹ J. Lu, T. M. Guerrero, P. Munro, A. Jeung, P.-C. M. Chi, P. Balter, X. R. Zhu, R. Mohan, and T. Pan, "Four-dimensional cone beam CT with adaptive gantry rotation and adaptive data sampling," *Med. Phys.* **34**, 3520–3529 (2007).

¹² M. B. Sharpe, D. J. Moseley, T. G. Purdie, M. Islam, J. H. Siewerdsen, and D. A. Jaffray, "The stability of mechanical calibration for a kV cone beam computed tomography system integrated with linear accelerator," *Med. Phys.* **33**, 136–144 (2006).

¹³ B. E. H. Claus, presented at the *Proceedings of SPIE*, 2006 (unpublished).

¹⁴ Y. Cho, D. J. Moseley, J. H. Siewerdsen, and D. A. Jaffray, "Accurate technique for complete geometric calibration of cone-beam computed tomography systems," *Med. Phys.* **32**, 968–983 (2005).

¹⁵ A. Rougee, C. Picard, C. Ponchut, and Y. Troussset, "Geometrical calibration of x-ray imaging chains for three-dimensional reconstruction," *Comput. Med. Imaging Graph.* **17**, 295–300 (1993).

¹⁶ R. Fahrig and D. W. Holdsworth, "Three-dimensional computed tomographic reconstruction using a C-arm mounted XRRI: Image-based correction of gantry motion nonidealities," *Med. Phys.* **27**, 30–38 (2000).

¹⁷ S. Yoo, G. Y. Kim, R. Hammoud, E. Elder, T. Pawlicki, H. Guan, T. Fox, G. Luxton, F. F. Yin, and P. Munro, "A quality assurance program for the on-board imagers," *Med. Phys.* **33**, 4431–4447 (2006).

¹⁸ K. Yang, A. L. Kwan, D. F. Miller, and J. M. Boone, "A geometric calibration method for cone beam CT systems," *Med. Phys.* **33**, 1695–1706 (2006).

¹⁹ M. Mamalui-Hunter, H. Li, and D. A. Low, presented at the *AAPM 49th Annual Meeting*, Minneapolis, MN, 2007 (unpublished).

²⁰ L. Dong, A. Shiu, S. Tung, and A. Boyer, "Verification of radiosurgery target point alignment with an electronic portal imaging device (EPID)," *Med. Phys.* **24**, 263–267 (1997).

²¹ S. Webb, "Optimization of conformal radiotherapy dose distributions by simulated annealing," *Phys. Med. Biol.* **34**, 1349–1370 (1989).

²² A. Pugachev and L. Xing, "Incorporating prior knowledge into beam orientation optimization in IMRT," *Int. J. Radiat. Oncol., Biol., Phys.* **54**, 1565–1574 (2002).

²³ I. I. Rosen, K. S. Lam, R. G. Lane, M. Langer, and S. M. Morrill, "Comparison of simulated annealing algorithms for conformal therapy treatment planning," *Int. J. Radiat. Oncol., Biol., Phys.* **33**, 1091–1099 (1995).

²⁴ J. G. Li, A. L. Boyer, and L. Xing, "Clinical implementation of wedge filter optimization in three-dimensional radiotherapy treatment planning," *Radiother. Oncol.* **53**, 257–264 (1999).

²⁵ G. J. Kutcher *et al.*, "Comprehensive QA for radiation oncology: Report of AAPM Radiation Therapy Committee Task Group 40," *Med. Phys.* **21**, 581–618 (1994).

PHYSICS CONTRIBUTION

RETROSPECTIVE IMRT DOSE RECONSTRUCTION BASED ON
CONE-BEAM CT AND MLC LOG-FILE

LOUIS LEE, PH.D., QUYNH-THU LE, M.D., AND LEI XING, PH.D.

Department of Radiation Oncology, Stanford University School of Medicine, Stanford, CA

Purpose: Head-and-neck (HN) cone-beam computed tomography (CBCT) can be exploited to probe the IMRT dose delivered to a patient taking into account the interfraction anatomic variation and any potential inaccuracy in the IMRT delivery. The aim of this work is to reconstruct the intensity-modulated radiation therapy dose delivered to an HN patient using the CBCT and multileaf collimator (MLC) log-files.

Methods and Materials: A cylindrical CT phantom was used for calibrating the electron density and validating the procedures of the dose reconstruction. Five HN patients were chosen, and for each patient, CBCTs were performed on three separate fractions spaced every 2 weeks starting from the first fraction. The respective MLC log-files were retrieved and converted into fluence maps. The dose was then reconstructed on the corresponding CBCT with the regenerated fluence maps. The reconstructed dose distribution, dosimetric endpoints, and DVHs were compared with that of the treatment plan.

Results: Phantom study showed that HN CBCT can be directly used for dose reconstruction. For most treatment sessions, the CBCT-based dose reconstructions yielded DVHs of the targets close (within 3%) to that of the original treatment plans. However, dosimetric changes (within 10%) due to anatomic variations caused by setup inaccuracy, organ deformation, tumour shrinkage, or weight loss (or a combination of these) were observed for the critical organs.

Conclusions: The methodology we established affords an objective dosimetric basis for the clinical decision on whether a replanning is necessary during the course of treatment and provides a valuable platform for adaptive therapy in future. © 2008 Elsevier Inc.

Cone-beam CT, Head and neck IMRT, MLC log-file, Dose reconstruction, Adaptive radiation therapy.

INTRODUCTION

Two implicit assumptions are made in the current multileaf collimator (MLC)-based intensity modulated radiotherapy (IMRT) process. First, the geometric sizes, shapes, and locations of the targets and organs (internal anatomy) and the geometric topography of the patient are the same as at the time of computed tomography (CT) simulation throughout the treatment course. Second, the delivered fluence maps are the same as the planned ones and delivered by the MLC in an idealized manner. In reality, neither of these assumptions is guaranteed in clinical situations.

Many patients, especially those with head and neck (HN) cancers who undergo fractionated RT course, have marked geometric changes in their internal anatomy and topography during the treatment course, which are attributable to organ deformation, tumor shrinkage, weight loss or a combination

of these (1, 2). These geometric changes might cause undesirable underdosage of the targets and potential overdosage of the critical organs in the vicinity of the targets and lead to a suboptimal treatment outcome. This issue poses a particular concern in HN IMRT cases because of the steep dose gradient that often exists between the boundary of the target and critical organs in an IMRT plan. The use of the three-dimensional (3D) patient model derived from a single planning CT (pCT) set to guide the fractionated RT course is a major hurdle to further advancing the radiation therapy (3). Recently, many in-room imaging modalities including CT-on-rail (4), kilovoltage-CBCT (5, 6), megavoltage cone-beam CT (7), and tomotherapy system (8) have been developed to monitor the geometric changes on a temporal basis. These new imaging modalities are primarily designed to verify and correct the patient's setup in a 3D space with respect to the pCT on the basis of bony landmarks, as well as soft tissue structures,

Reprint requests to: Lei Xing, Ph.D., Department of Radiation Oncology, Stanford University School of Medicine, 875 Blake Wilbur Drive, Room G-204, Stanford, CA 94305-5847. Tel: (650) 498-7896; Fax: (650) 498-4015; E-mail: lei@reyes.stanford.edu

This work was supported by the National Cancer Institute (Grant Nos. 1R01 CA98523 and CA104205), the Komen Breast Cancer Foundation (BCTR0504071), and the Department of Defense (PC040282). Support from the Sir Robert Black Postdoctoral Fel-

lowship and the Hong Kong Hospital Authority Overseas Training Allowance for the first author are also gratefully acknowledged.

Conflict of interest: none.

Acknowledgements—We thank Drs. Sam Brain, Gary Luxton, and Peter Maxim for the Perl program that allowed us to merge the two sets of CBCTs and for useful discussion.

Received June 27, 2007, and in revised form Sept 27, 2007. Accepted for publication Sept 28, 2007.

before dose delivery. In principle, the CBCT can be further exploited to derive a 3D patient model for dose reconstruction to reflect the dosimetric impact resulting from the residual setup errors and geometric changes occurring over time.

Feasibility studies have been carried out by several research groups to reconstruct the IMRT dose distribution using CBCT and the planned fluence maps from the treatment planning system (TPS) (9–11). This maneuver is based on the second assumption mentioned earlier that the planned fluence maps can be faithfully realized by the delivery system (11). However, in a MLC-based IMRT using the step-and-shoot method, there may be errors associated with the control of leaf motion and fractional monitor unit (MU) delivery such as overshoot, undershoot segmental MU, dropped segments, and beam delivery during leaf motion (12–15). These factors might affect the dose delivery and result in a delivered fluence map different from the planned one. A more pragmatic approach in reconstructing the delivered dose is to use the fluence maps actually delivered for the treatment; therefore, we propose retrieving the MLC log-file that records the leaf position of each individual leaf and the fractional MU status during the delivery of IMRT from the MLC workstation and deriving the delivered fluence map from it.

The objective of this study is twofold: (1) to establish a methodology and procedures to reconstruct the dose delivered to a patient on a series of kV-CBCTs taken during a treatment course using the delivered fluence maps derived from the corresponding MLC log-files and (2) to study the potential dosimetric impact on the intended treatment plan taking into account the patient's geometric changes over time, residual setup errors, and the inherent delivery errors associated with the MLC. This work can serve as a platform for implementing a workflow in reconstructing the IMRT delivered dose and providing the necessary dosimetric information needed to modify the treatment plan, if indicated, on the basis of the accumulated dose given to the patient.

METHODS AND MATERIALS

CBCT image acquisition

The CBCT images in this study were acquired by the onboard imager (OBI) integrated in a Trilogy medical linear accelerator (Varian Medical Systems, Palo Alto, CA). The OBI system is mounted on the gantry of the linear accelerator perpendicular to the beam axis of the MV beam by robotic arms. The OBI system consists of a kV X-ray tube assembly at one end and an amorphous silicon flat-panel image receptor (39.7 cm × 29.8 cm) (Varian 4030CB flat panel) facing the X-ray tube at the other end in the full-extended configuration. The focus of the X-ray tube and the center of the image receptor are at 100 cm and 50 cm from the isocenter, respectively, resulting in a source-to-imager distance of 150 cm. The OBI isocenter coincides with the MV treatment isocenter within ± 1.5 mm and is routinely checked in the weekly quality assurance procedure (16). The CBCT can be acquired in two modes, the “half-fan” mode and “full-fan” mode. The half-fan mode is designed to increase the field-of-view (FOV) beyond 24 cm and was used exclusively in this study. In the half-fan mode, the image receptor is displaced laterally by 14.8 cm, and the blades of the X-ray tube are offset to cover the detector area. A half-bowtie filter is used in this

mode. A half-fan projection image is acquired for each acquirement angle for the 364° gantry rotation in about 60 s, resulting in a total of 640–700 projections (16). Only part of the object is viewed in one half-fan projection; the other part of the object is viewed in the half-fan projection from the opposite position. The entire object is reconstructed by using the projections acquired 180° apart. The FOV and longitudinal coverage in this mode are 45 cm in diameter and 15 cm in length, respectively. A total of 640 projections are acquired and reconstructed into CBCT images of 512 × 512 matrix.

Electron density calibration

Electron density calibration was performed by scanning a phantom with inserts of known relative electron densities with respect to water (ρ_e^w) and calibrating the ρ_e^w against the Hounsfield units (HU) of the inserts. A 20-cm cylindrical CT phantom, Catphan-600 with CTP404 module (Phantom Laboratory, NY), was used for the electron density calibration for the pCT (GE Discovery-ST PET/CT scanner, Milwaukee, WI) and CBCT. This phantom was chosen because it has a size and shape comparable to a patient's HN region. Designated scanning parameters for HN patients were chosen for the pCT and similar scanning parameters were applied as far as possible for the CBCT; the slice thickness used was 2.5 mm. The half-fan CBCT mode (half-bowtie mounted) was used to give a FOV of 45 cm, comparable to that of 45–50 cm used in pCT to include the lower neck region. Both CT sets had a pixel size of about 1 mm in a 512 × 512 matrix image. The techniques for the CBCT used were 125 kVp, 80 mA, and 25-ms pulse, which are precalibrated for clinical use. The HUs of the inserts for both the pCT and CBCT were measured from the acquired images and plotted against the known ρ_e^w . The vertical and horizontal HU profiles of the same images were also plotted and compared. The temporal CBCT HU stability has been investigated by our group, and there is no significant fluctuation observed over a period of 8 weeks (10).

MLC log-file retrieval and processing

The Trilogy is equipped with the Millennium 120-leaf MLC (Varian Medical Systems) capable of IMRT delivery. During a step-and-shoot IMRT delivery, the MLC workstation logs the position of each individual leaf and the fractional MUs delivered every 50 ms; it also produces two separate log-files for each leaf bank (A and B sides). A split IMRT field results in four such MLC log-files. These automatically generated MLC log-files have been validated to represent accurately the actual IMRT delivery (17, 18). For this study, the MLC log-files were retrieved from the MLC workstation after the treatment session in which the CBCT was performed; the leaf positions and delivered fractional MUs were extracted and converted to leaf sequence files by software developed in-house, written in Visual Basic 6.0 code (Microsoft, Bellevue, WA). The leaf sequence files were then imported back into the TPS to regenerate the delivered fluence maps, which were used in the dose reconstruction on the CBCT-derived 3D patient model (Fig. 1). To access the practicability of the retrieval and conversion procedures, the MLC log-files of a HN IMRT patient were retrieved, and the subsequently regenerated fluence maps were attached to the original treatment fields in the IMRT plan. The dose was reconstructed using the original set of pCT; the resultant dose distribution and dose volume histograms (DVH) of the target and organs were then compared with those from the original plan to see the discrepancy due solely to the difference in the fluence maps used.

Phantom study

Planning CT and CBCT were acquired for the Catphan-600 phantom using the techniques previously described. Both sets of images

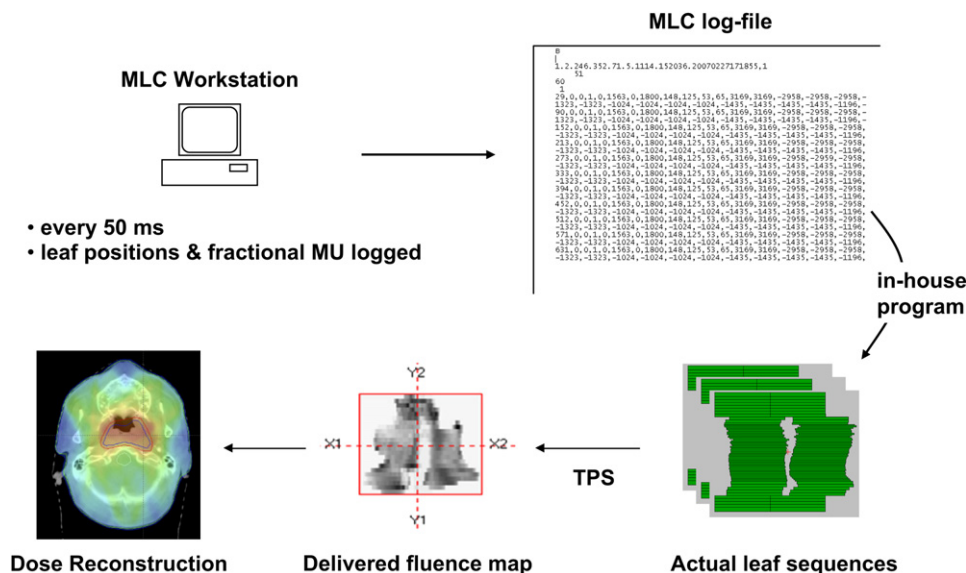


Fig. 1. The workflow from the retrieval of the multileaf collimator (MLC) log-file to the regeneration of the delivered fluence map and dose reconstruction. MU = monitor unit; TPS = treatment planning system.

were imported into the Eclipse TPS (Varian Medical Systems) for feasibility study. A hypothetical identical target in a shape of cuboid ($4 \times 4 \times 2$ cm) was created in the center of the phantom for the two image sets. An isocentric plan with two orthogonal 6-MV fields (Varian scale 180° and 90° gantry angle) each measuring 10×10 cm was applied to the center of the phantom in each image set. The Anisotropic Analytical Algorithm (AAA) implemented in the Eclipse TPS was adopted for dose calculation. The electron calibration curve of the pCT, which had been commissioned for the use of dose calculation in TPS, was applied to both image sets for dose calculation; this is based on the findings from the electron density calibration scans performed on the pCT and CBCT earlier. A five-field IMRT plan from an HN patient was also applied to two image sets of the phantom to validate further the use of CBCT for dose calculation. The resultant dose distributions, orthogonal dose profiles, and DVHs of the hypothetical target from the pCT- and CBCT-based calculations were compared.

Patient CBCT scheduling and acquisition

Five HN IMRT patients were chosen for this work. The patient was setup under the guidance of kV orthogonal planar imaging routinely using the OBI. The CBCT was then acquired using the techniques previously described. There was no attempt to use the CBCT for 3D-3D setup correction because 3D-3D setup verification has not yet been adopted as a routine clinical procedure at our clinic. Because of the limited coverage of the CBCT in the longitudinal direction, two sets of CBCT 10 cm apart in this direction were taken for each patient. The two CBCT image sets were merged together

before they were imported into the TPS. Three CBCTs at 2-week intervals starting from the first or second fraction in a 30-fraction treatment course (Fig. 2) were taken for the patients. There is usually a 2-week gap from the pCT to the first treatment; the first CBCT not only serves as a starting time point to see the temporal geometric changes but also shows the geometric changes that might have occurred during the 2-week gap before the treatment commences. The number of CBCTs taken and the time interval between them are a compromise based on the consideration of imparted CBCT dose, workload, and the progress of anatomic changes that manifest on the CBCT. The acquired CBCTs and the retrospective dose reconstructions were used only for research purposes and not for altering the original treatment or clinical practice.

Procedures for dose reconstruction

After each treatment, the MLC log-files and the CBCT image sets were retrieved. The merged HN CBCT was imported into the Eclipse TPS; a 3D patient model was generated from the CBCT and fused to the pCT 3D patient model using a rigid-body image registration technique based on mutual information of the whole CT volumes. This image registration was used only for mapping the targets and organ contours from the pCT image set onto the CBCT image set. These initial mapped contours were edited by the same physician who did the contouring for the original plan, if necessary, to adapt to changes in the patient's anatomy due to tumour shrinkage, organ deformation, or weight loss. After the CBCT image set had been finalized with the corrected contours, it was decoupled from the registration to retain its own geometric status, including

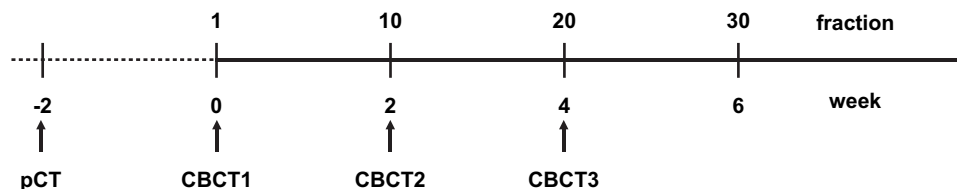


Fig. 2. Timeline showing the scheduling of the cone-beam computed tomography (CBCT) and the time of planning computed tomography (pCT).

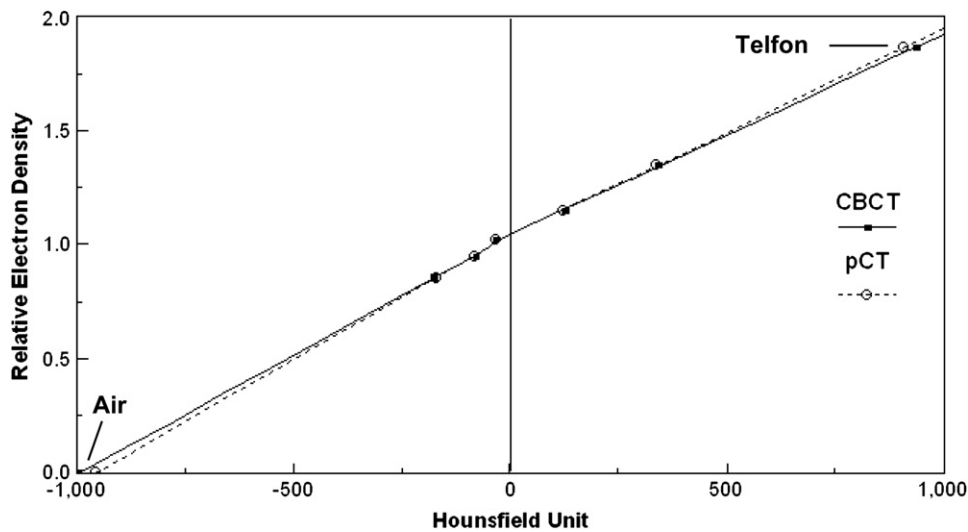


Fig. 3. The electron density calibration curves for the planning computed tomography (pCT) and cone-beam computed tomography (CBCT).

the residual setup errors for the subsequent dose reconstruction. The configuration including the beam angulations and field sizes of the original treatment plan were copied to the CBCT and placed at the same isocenter of the pCT. Because the MLC log-files are logged for each independent delivery, a split IMRT field would have to be considered as two independent subfields, each with its own derived fluence map when copied to the CBCT plan. A typical HN

IMRT plan with seven split-fields would result in 14 individual subfields each with its corresponding derived fluence maps. The delivered MUs for each subfield were entered when the fluence map was regenerated. The dose reconstruction was then calculated on the CBCT-derived patient model. The resultant dose distributions, dosimetric endpoints, and DVHs of the target and critical organs were compared with those of the original plan and the other two CBCTs.

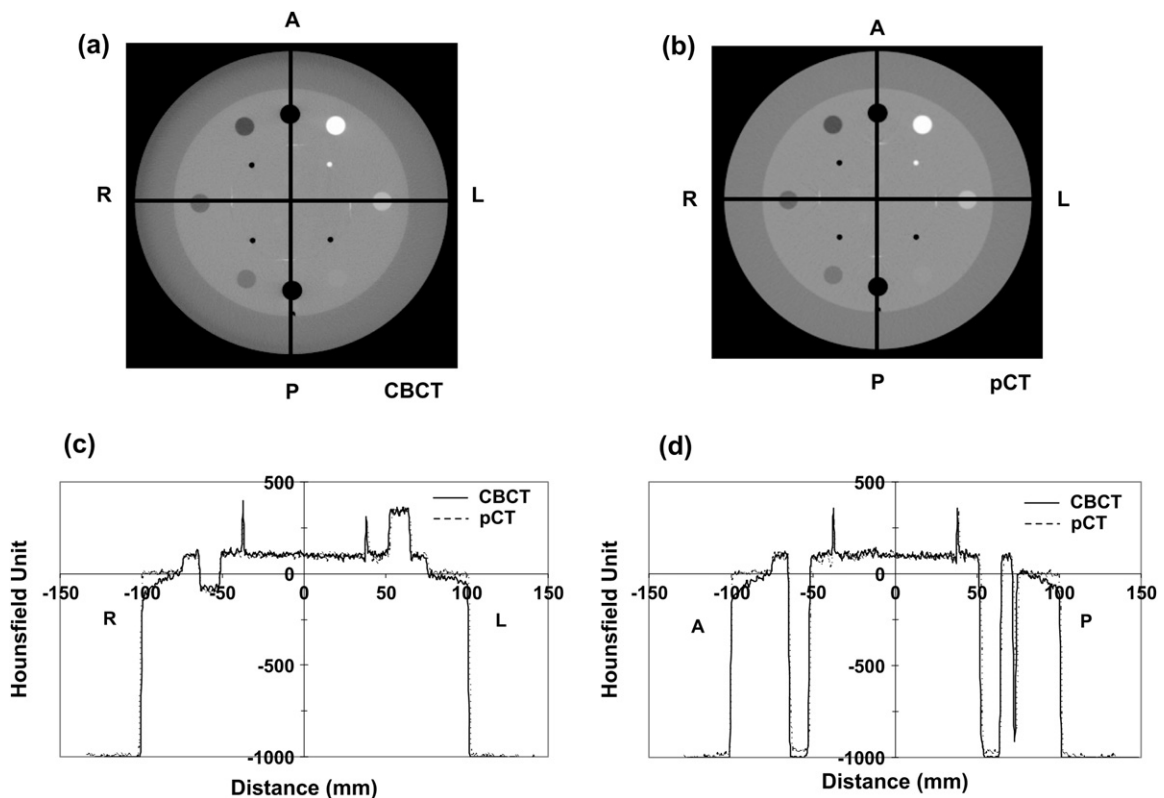


Fig. 4. An axial slice through the inserts from (a) the cone-beam computed tomography (CBCT) and (b) the planning computed tomography (pCT). (c) The horizontal Hounsfield unit (HU) profiles along the lines right-to-left (RL) for the CBCT and pCT. (d) The vertical HU profiles along the lines anteroposterior (AP) for the CBCT and pCT.

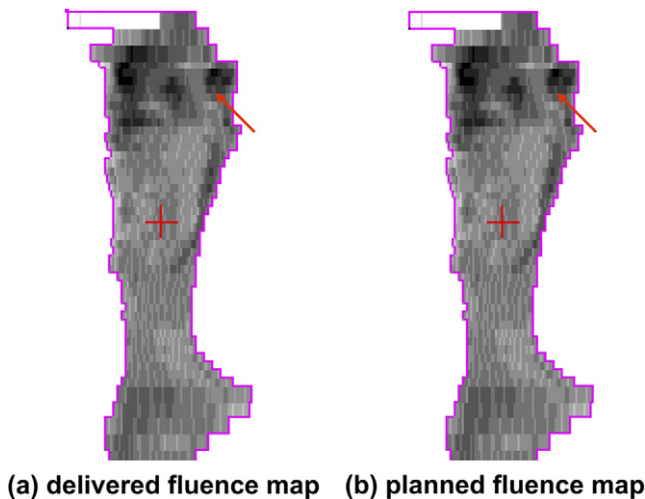


Fig. 5. No discernible difference was seen between the two fluence maps except at the region indicated by the arrow.

RESULTS

Electron density calibration

Figure 3 shows the relative electron density calibration curves for the pCT and CBCT. No significant difference in the calibrations was noted over the range of HUs. The differences in the HUs of the inserts for the two modes of CT were less than 10 HUs, except for the air and Teflon inserts; however, the maximum relative difference was only 5% and 3% for the air and Teflon, respectively.

Figures 4a and 4b show the axial images of the phantom through the inserts from the CBCT and pCT, respectively.

The horizontal and vertical HU profiles along the lines right-to-left (RL) and anteroposterior (AP) for the CBCT and pCT are compared in Figs. 4c and 4d. The CBCT and pCT HU profiles were in agreement to within 10% except that the CBCT showed a larger fluctuation of HU and reduced HUs at the periphery of the phantom.

Derivation of fluence maps from the MLC log-files

Figures 5a and 5b show a delivered fluence map derived from the MLC log-files and the corresponding planned fluence map from the TPS, respectively. There was essentially no discernible difference in the intensity levels between the two maps except at the region indicated by the arrow. Figures 6a and 6b depict the dose distribution on an axial slice calculated on the same pCT set using the delivered and planned fluence maps; their corresponding DVHs of the targets and critical organs are shown in Figs. 6c and 6d. There was essentially no discernible difference in the dose distributions on the axial slice. The DVHs of the planning tumour volumes (PTV), gross tumour volumes (GTV), and critical organs of the plan based on delivered fluence maps overlapped with the ones from the plan based on planned fluence maps.

Phantom study

For the open beam dose calculation, the dose distributions on the same axial slice from the CBCT- and pCT-based dose calculations were essentially identical; the difference in dose maximum was less than 0.5% (Figs. 7a and 7b). The horizontal and vertical dose profiles for the CBCT- and pCT-based calculations were in agreement to within 1% except at the field

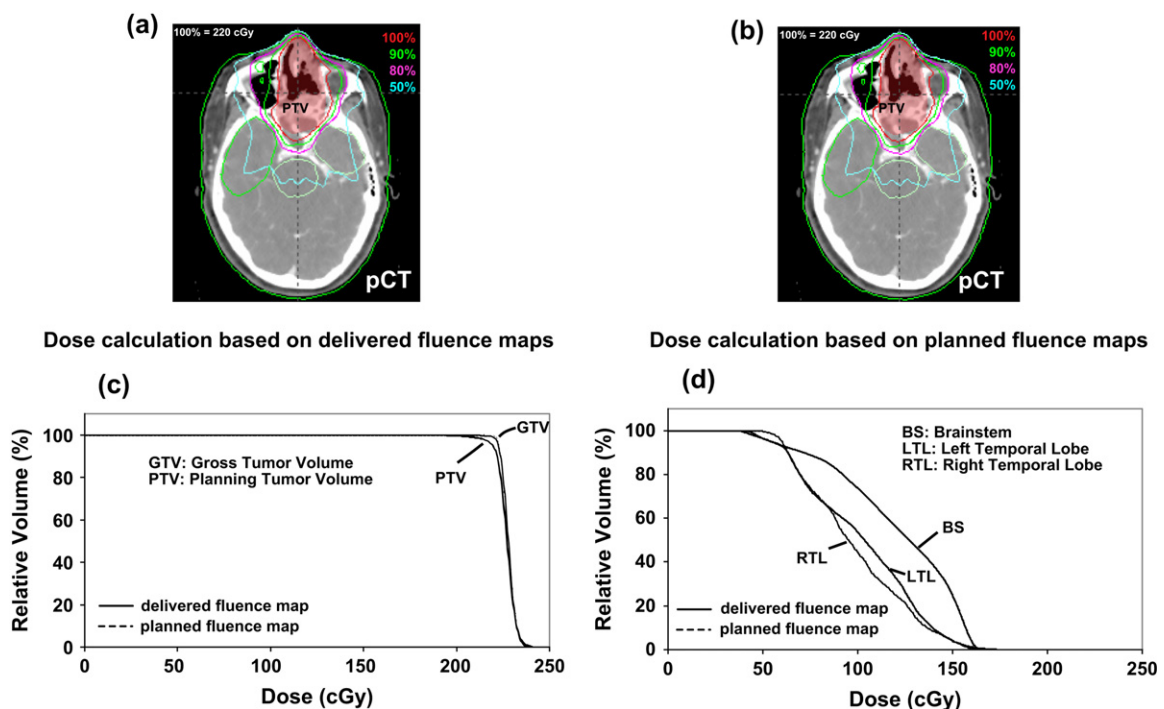


Fig. 6. Intensity-modulated radiation therapy dose distribution on an axial slice from the planning computed tomography for the dose calculations based on (a) the delivered and (b) the planned fluence maps. Dose volume histograms of the gross tumor volume (GTV), planning tumor volume (PTV) (c), and the critical organs (d) for the two calculations.

edges, where there was a maximum difference of 3%. (Fig. 7c). The DVHs of the hypothetical target from the two calculations essentially overlapped (Fig. 7d). The same comparisons were performed for the IMRT dose calculation. There was also no significant difference in the dose distributions on the axial slices shown and in the dose maximum points (Figs. 8a and 8b). Both the dose profiles and the DVHs from the two calculations were in agreement to within 2% (Figs. 8c and 8d).

Patient study

Patients with PTV in the head region. Of the three patients (A, B, and C) in the study, two had nasopharyngeal carcinoma (NPC), the other one had esthesioneuroblastoma surgically debulked, with residual tumour at the base of skull to be treated. The PTVs of these patients received 6,600 cGy in 30 fractions at 220 cGy per fraction. For the patients studied here, we observed that the change in the shape of the targets had already occurred during the 2-week waiting period. These were then followed by a progressive change in the shape and size of the targets during the treatment. The dosimetric comparisons of the pCT- with CBCT-based plans per fraction for the three patients are shown in Table 1. For the PTV, the dose to 95% of the volume (D_{95}) and the volume receiving at least 93% of the prescribed dose (V_{93}) of the pCT were in agreement to within 3% with those of the CBCTs. For the GTV, the dose to 99% of the volume (D_{99}) also showed the same agreement between the pCT and CBCTs. The differences in the dosimetric endpoints of the critical organs for the pCT and CBCTs were generally in

the range of 10%; however, the difference could be as high as 15%–20% in some individual treatment sessions for the parotid gland, optic track, and the temporal lobe when they were in extreme proximity with the PTV. The comparisons of the dose distributions and the DVHs between the pCT- and CBCT-based plans for one of the patients are shown in Fig. 9 for illustrative purposes.

Patients with PTV in the neck region. The two other patients (D and E) we selected had primary tumors in the hypopharynx and the lacrimal gland; both had undergone surgery. There were two PTVs defined for these patients: PTV1 for the tumor bed and PTV2 for the involved neck. PTV1 and PTV2 received 6,000 cGy and 5,400 cGy, respectively, in 30 fractions at 200 cGy per fraction. Because of the limited coverage of the CBCT, the PTV1 of one of the patients (E) was not completely included and was not compared. The main emphasis here was to study the dosimetric impact of the change of the neck contour on the PTV2. From the first CBCT, the neck contours of these patients had a marked change from the pCT, and the change was slight throughout the progression of the treatment up to the third CBCT (Fig. 10). For the PTV1 of the patient D, D_{95} and V_{93} of the pCT-based plan agreed well with those of the CBCT-based plans (Table 2). For the PTV2 of both patients, D_{95} and V_{93} showed agreement to within 3% between the pCT- and CBCT-based plans. The differences in the dosimetric endpoints of the critical organs for the pCT- and CBCT-based plans were generally in the range of 5% (Table 2). The comparisons of the dose distributions and the DVHs between the pCT- and CBCT-based plans for one of these patients are shown in Fig. 10.

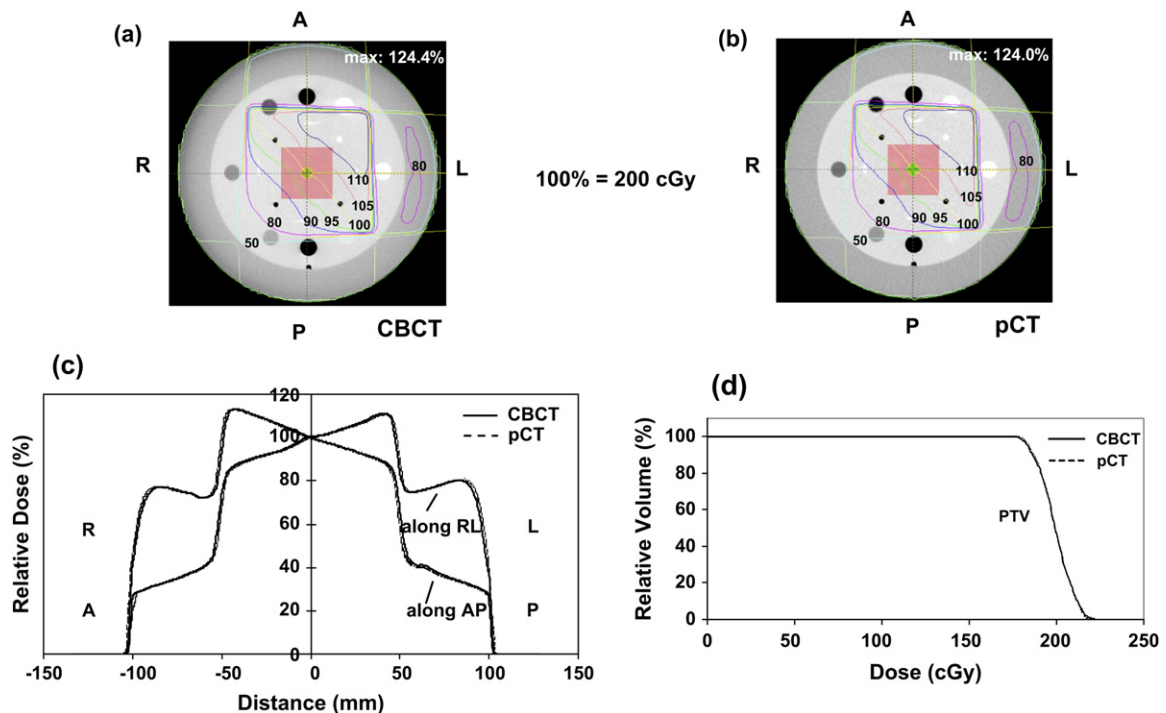


Fig. 7. Dose distribution from two orthogonal 10×10 cm open fields on the axial slice with (a) the cone-beam computed tomography (CBCT)-based and (b) the planning computed tomography (pCT)-based dose calculations. (c) Dose profiles along lines right-to-left (RL) and anteroposterior (AP) for CBCT- and pCT-based calculations. (d) Dose volume histograms of the hypothetical target for the CBCT-based and pCT-based calculations.

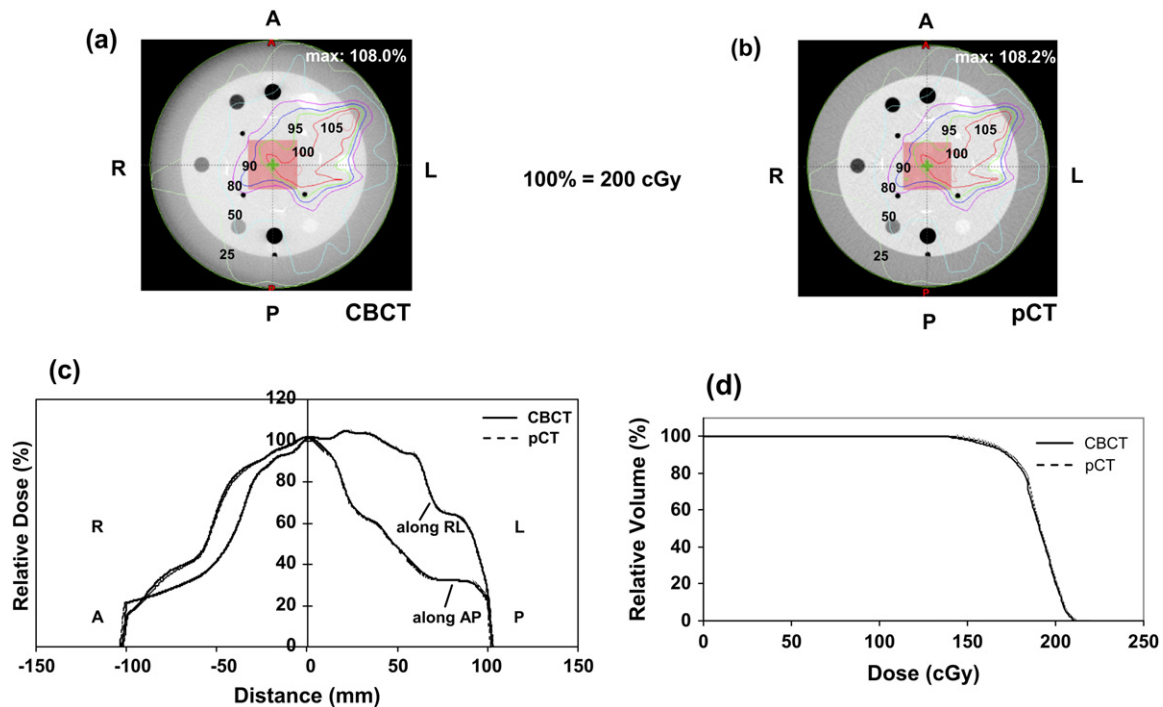


Fig. 8. Intensity modulated radiation therapy (IMRT) dose distribution on the axial slice with (a) the cone-beam computed tomography (CBCT)-based and (b) the planning computed tomography (pCT)-based dose calculations. (c) Dose profiles along lines right-to-left (RL) and anteroposterior (AP) for CBCT-based and pCT-based calculations. (d) Dose volume histograms of the hypothetical target for the CBCT-based and pCT-based calculations.

DISCUSSION

The advent of onboard CBCT expands our horizon in correcting the daily setup errors and probing the geometric change of a patient's anatomy in his or her treatment position during the course of radiation treatment. We have shown that

the CBCT could be further exploited for dose reconstruction to provide the dosimetric information necessary for replanning or reoptimization should there be significant deviations in the delivered dose from the intended plan. The main hurdle in preventing us from using the CBCT for dose reconstruction

Table 1. Comparison of dosimetric endpoints of the targets and critical organs between the pCT- and the serial CBCT-based plans for the patients A, B, and C (Prescription: 6600 cGy to PTV in 30 fractions at 220 cGy per fraction; values shown below are for one fraction)

Dosimetric end point	Patient A				Patient B				Patient C			
	pCT	CBCT1 pCT	CBCT2 pCT	CBCT3 pCT	pCT	CBCT1 pCT	CBCT2 pCT	CBCT3 pCT	pCT	CBCT1 pCT	CBCT2 pCT	CBCT3 pCT
PTV, D ₉₅ (cGy)	220	0.98	0.99	0.98	220	0.97	0.97	0.99	220	1.01	1.00	1.01
PTV, V ₉₃ (%)	99	0.99	1.00	0.99	100	0.99	0.98	1.00	100	1.00	1.00	1.00
GTV, D ₉₉ (cGy)	220	0.97	0.99	0.98	219	1.00	1.00	0.99	219	1.01	1.00	1.01
BS, D _{max} (cGy)	165	1.06	1.04	1.04	156	1.02	1.09	1.03	153	1.08	1.02	1.03
SC, D _{max} (cGy)	—	—	—	—	139	0.97	0.97	0.99	150	1.01	1.00	1.01
OC, D _{max} (cGy)	164	1.01	1.13	1.06	—	—	—	—	156	1.08	0.97	1.01
R ON, D _{max} (cGy)	164	0.93	0.97	0.92	—	—	—	—	152	1.04	0.93	1.00
L ON, D _{max} (cGy)	170	1.08	0.84	1.10	—	—	—	—	156	1.01	0.98	0.98
R PARO, D _{mean} (cGy)	—	—	—	—	113	1.05	0.85	1.07	90	0.97	0.99	1.19
L PARO, D _{mean} (cGy)	—	—	—	—	141	1.07	1.12	1.03	108	0.97	1.08	1.03
R TL, D _{max} (cGy)	175	1.00	1.00	0.98	160	0.95	0.92	0.97	—	—	—	—
L TL, D _{max} (cGy)	175	1.09	1.19	1.23	158	1.03	1.06	0.98	—	—	—	—

Abbreviations: BS = brainstem; CBCT = cone-beam computed tomography; D₉₅ = dose to 95% of the volume; D₉₉ = dose to 99% of the volume; D_{max} = maximum dose; D_{mean} = mean dose; GTV = gross target volume; L = left; OC = optic chiasm; ON = optic nerve; PARO = parotid gland; pCT = planning computed tomography; PTV = planning target volume; R = right; SC = spinal cord; TL = temporal lobe; V₉₃ = volume receiving at least 93% of the prescribed dose.

Note: For each patient, the first column lists the value for the pCT-based plan, and the second to fourth columns show the ratio of the values of the subsequent CBCT- to pCT-based plan for easier comparison. Blank cells indicate that the organ is not included in the CBCT coverage because of PTV site.

is that the CBCT does not always warrant an image quality comparable to conventional CT because of the scatter environment encountered in CBCT (19). Another issue is the provision of an appropriate electron density calibration; large variations of HU were observed for the same material under different scanning conditions and parameters used in CBCT (9, 10). We mitigated these problems by restricting the electron density calibration to designated scanning parameters and using a cylindrical phantom with a caliber close to a patient's HN region. By scanning the Catphan in the similar scanning parameters in pCT and in CBCT, we found that the electron density calibration curves had no significant difference except for that of the air and Teflon; however, these 3%–5% HU difference will not transform into clinically significant difference in doses (<1%) (20, 21). This explained why the fluctuating HUs and peripheral reduced HUs seen in the CBCT phantom images (Figs. 4c and 4d) did not lead to any significant difference in the dose profiles (Figs. 7c and 8c) when we validated the CBCT for dose calculation. Therefore, we adopted to use the commissioned pCT electron density calibration for the CBCT dose calculation; this has also been proposed by Yoo and Yin on the basis of the same argument (9). The good agreement of the DVHs of the hypothetical targets for the pCT- and CBCT-based dose calculations (Figs. 7d and 8d) further justifies our method. However, the ultimate solution is the continual improvement in the image reconstruction algorithm for the CBCT making it more

consistent and reliable under different scanning conditions and parameters (19). The results from the phantom study strongly supported that the CBCT obtained under the proposed scanning condition could be directly used for dose reconstruction.

The MLC log-files have been validated to faithfully reflect the actual delivery process of a MLC-based IMRT (17, 18); this serves to be a powerful tool in verifying or reconstructing the IMRT dose delivered to the patients. The use of the MLC sequence files from the original plan instead of the MLC log-files in dose reconstruction, which most other research groups did (9, 11, 22, 23), rests on the assumption the treatment was indeed delivered as intended. Our approach of using MLC log-file is more realistic and has the potential to take MLC delivery errors into account. This approach is straightforward and easy to implement in a clinic.

From the serial CBCTs performed on the patients, we noticed that the first CBCT provided valuable geometric information about the target and the patient's topography at the start of the treatment. The other two CBCTs monitored the geometric change of the internal anatomy and the dose reconstruction of these provided us the necessary dosimetric information necessary for the decision of replanning or reoptimizing. From the patient study, we found that there was no significant compromise (<3%) on the target coverage even though there was evidence of geometric changes during the course of treatment. The impact of these geometric changes,

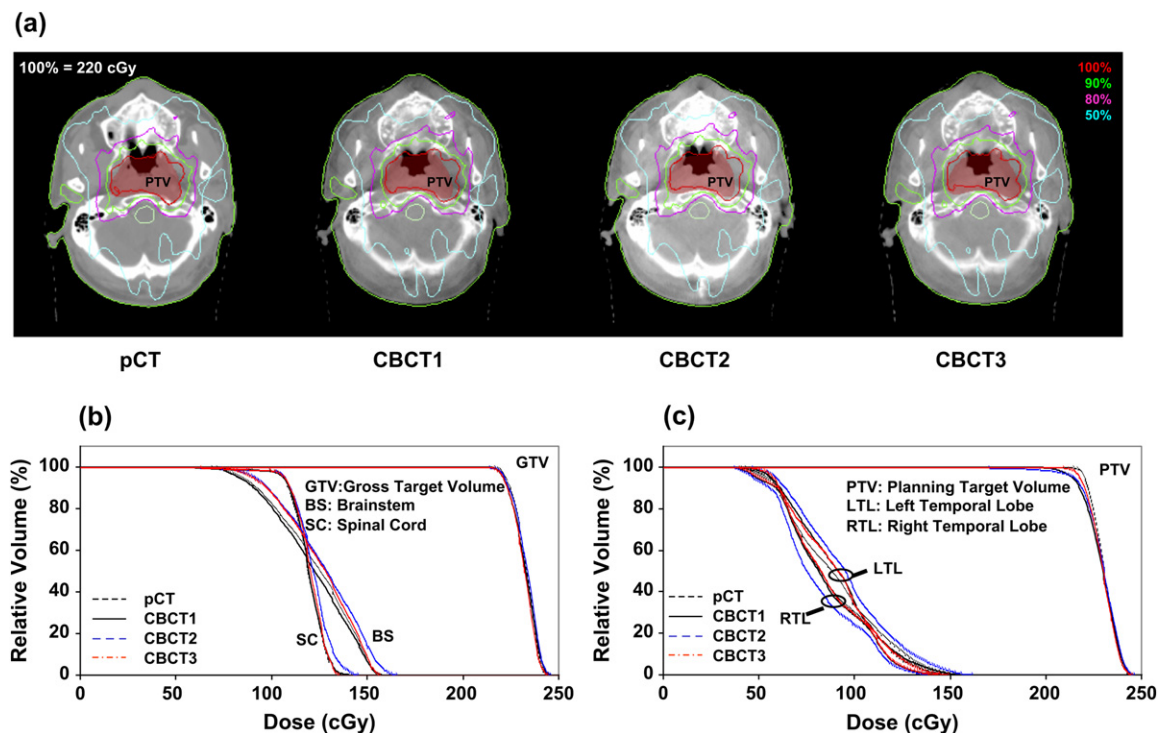


Fig. 9. (a) Geometric change of the target of patient B was noted in the first cone-beam computed tomography (CBCT). The CBCT dose reconstructions yielded dose distributions close to that of the original plan. (b) The dose volume histograms (DVHs) of the gross tumor volume (GTV) for the planning computed tomography (pCT)-based and cone-beam computed tomography (CBCT)-based plans essentially overlapped. (c) The coverage of the planning tumor volume (PTVs) in the CBCTs were slightly compromised when compared with that of the pCT. The dose volume histograms of the critical organs of the CBCT-based plans deviated from those of the original plan in various degrees (b) and (c).

however, largely affected the dose deposited to the critical organs in the vicinity of the target. This might be due to the steep dose gradient that commonly exists between the target and the critical organs in an IMRT plan, and any deviated geometric change, whether due to the residual setup error, tumor shrinkage, organ deformation or patient weight loss, would result in a considerable change (up to 20%) in the dose received by these critical organs. Another less subtle reason is the inaccuracy in contouring these organs in the CBCT that was not supplemented by the contrast enhancement or magnetic resonance imaging (MRI) fusion as the pCT had been. This is particularly crucial when one comes to an organ of small volume such as the optic nerve or optic chiasm, for which a slight error in contouring would cause a drastic change of the dose received (Table 1). In the patients with targets in the neck region, despite the fact that there were marked changes of the neck contour on the CBCTs compared with the pCT, the coverage of the neck target (PTV2) was not significantly compromised, probably because these patients' original PTV2 had been markedly modified to be confined to the neck and still received adequate dose coverage. Because of the small number of patients in this work, it is not recommended that these findings be generalized to the dosimetric impact of geometric changes. Nevertheless, this work gives us some insight how important and useful the on-treatment serial CBCTs could be in adapting the radiation treatment in future.

Although we have set up a methodology and procedures to reconstruct the IMRT dose on CBCT, we still face some practical issues in implementing it into clinical practice. First, we must determine how many CBCTs should be taken, and how often, so that a clinically meaningful intervention can rely on. The contouring of the targets and organs in all the CBCTs is another practical problem we encounter; until we have a reliable deformable image registration that can directly propagate the contours from the pCT to CBCTs (24, 25), it is difficult to handle contouring in a large number of CBCT sets. Furthermore, it has always been technically challenging to interpret dose distributions and DVHs and infer from them the cumulative doses from various sets of 3D patient models with changing internal anatomy (26, 27). The DVH definition may need to be redefined to handle the changing target (28). We must identify predictive indices on the basis of all the dosimetric information gained from the CBCTs to guide us in making a clinical decision regarding when and how a treatment can be adapted appropriately and efficaciously should the need arise. All these factors need to be addressed in future research. An ideal paradigm that integrates a seamless workflow from simulation to planning, verification, offline or on-line replanning (15), and finally delivery is essential for the success of adaptive radiation therapy (26). This study has demonstrated the fundamental steps required for the full implementation of using CBCT for this ideal paradigm.

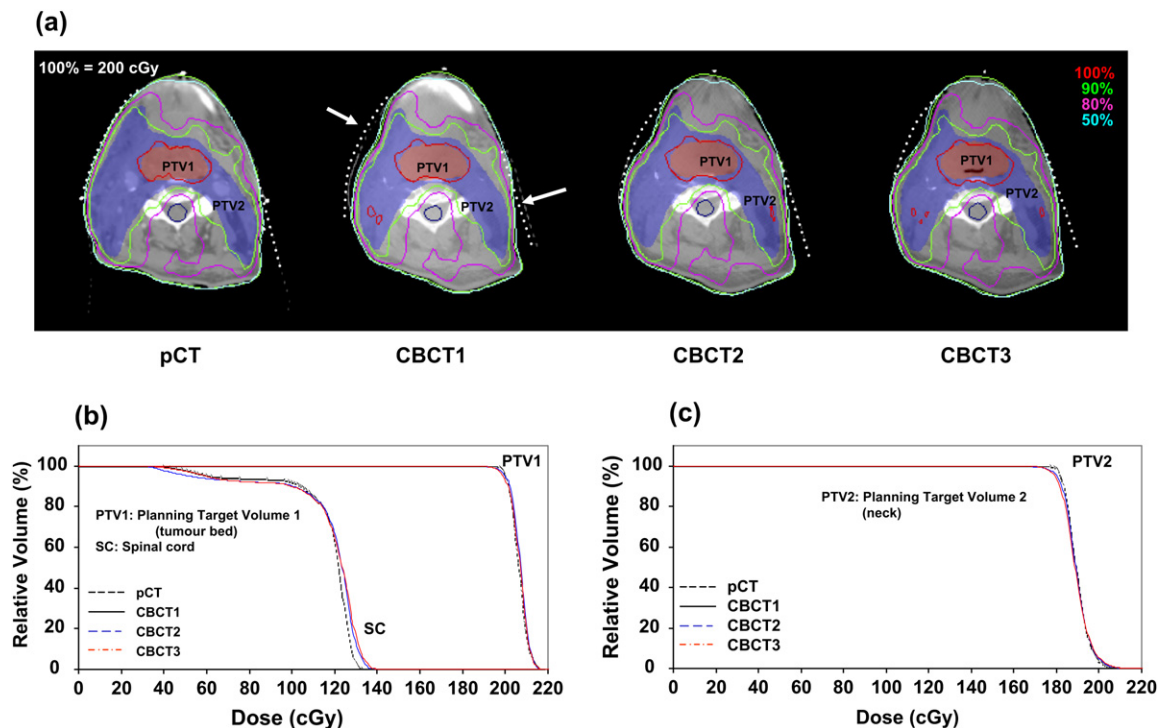


Fig. 10. (a) Marked changes of the neck contour (white arrows) and planning tumor volume 2 (PTV2) were noted in the first cone-beam computed tomography (CBCT) of patient D. The CBCT dose reconstructions otherwise yielded dose distributions close to that of the original plan when geometric changes were taken into account. (b) The dose volume histograms (DVHs) of the PTV1 for the planning computed tomography (pCT)- and CBCT-based plans essentially overlapped. (c) The coverage of the PTV2s in the CBCT-based plans were slightly compromised compared with that of the pCT-based plan. The DVHs of the spinal cord of the CBCT-based plans deviated from those of the original plan (b).

Table 2. Comparison of dosimetric endpoints of the targets and critical organs between the pCT- and the serial CBCT-based plans for patients D and E (prescription: 6,000 cGy to PTV1 and 5,400 cGy to PTV2 in 30 fractions at 200 cGy per fraction; values shown are for one fraction)

Dosimetric end point	Patient D				Patient E			
	pCT	$\frac{CBCT1}{pCT}$	$\frac{CBCT2}{pCT}$	$\frac{CBCT3}{pCT}$	pCT	$\frac{CBCT1}{pCT}$	$\frac{CBCT2}{pCT}$	$\frac{CBCT3}{pCT}$
PTV1, D ₉₅ (cGy)	200	1.00	1.00	1.00	—	—	—	—
PTV1, V ₉₃ (%)	100	1.00	1.00	1.00	—	—	—	—
PTV2, D ₉₅ (cGy)	182	0.99	0.99	0.99	179	0.98	0.98	0.97
PTV2, V ₉₃ (%)	100	1.00	1.00	1.00	100	0.99	1.00	0.99
BS, D _{max} (cGy)	—	—	—	—	124	0.96	0.97	0.92
SC, D _{max} (cGy)	135	1.05	1.04	1.05	109	1.05	1.04	1.00

Abbreviations: BS = brainstem; CBCT = cone-beam computed tomography; D₉₅ = dose to 95% of the volume; D_{max} = maximum dose; pCT = planning computed tomography; PTV1 = planning target volume 1 (tumour bed); PTV2 = planning target volume 2 (neck); SC = spinal cord; V₉₃ = volume receiving at least 93% of the prescribed dose.

Note: For each patient, the first column lists the value for the pCT-based plan, and the second to fourth columns show the ratio of the values of the subsequent CBCT- to pCT-based plans for easier comparison. Blank cells indicate that the target or organ is not included in the CBCT coverage.

CONCLUSIONS

In this study, we established methodology and procedures to reconstruct the IMRT dose delivered on the basis of a series of on-treatment CBCTs and the MLC log-files, pragmatically taking into account geometric changes of patients' anatomy over time and the potential inaccuracy in the IMRT delivery.

Dose reconstruction is valuable for examining the actual dose delivered to a patient at a particular fraction. This maneuver affords an objective dosimetric basis for clinical decision making on whether replanning or reoptimization is necessary during the course of treatment. It also provides a valuable platform for adaptive radiation therapy in future.

REFERENCES

- Barker JL Jr., Garden AS, Ang KK, *et al.* Quantification of volumetric and geometric changes occurring during fractionated radiotherapy for head-and-neck cancer using an integrated CT/linear accelerator system. *Int J Radiat Oncol Biol Phys* 2004;59:960–970.
- Sobel S, Rubin P, Keller B, *et al.* Tumor persistence as a predictor of outcome after radiation therapy of head and neck cancers. *Int J Radiat Oncol Biol Phys* 1976;1:873–880.
- Yan D, Lockman D, Martinez A, *et al.* Computed tomography guided management of interfractional patient variation. *Semin Radiat Oncol* 2005;15:168–179.
- Ma CM, Paskalev K. In-room CT techniques for image-guided radiation therapy. *Med Dosim* 2006;31:30–39.
- Oldham M, Letourneau D, Watt L, *et al.* Cone-beam-CT guided radiation therapy: A model for on-line application. *Radiother Oncol* 2005;75:271–278.
- Jaffray DA, Siewerdsen JH, Wong JW, *et al.* Flat-panel cone-beam computed tomography for image-guided radiation therapy. *Int J Radiat Oncol Biol Phys* 2002;53:1337–1349.
- Pouliot J, Bani-Hashemi A, Chen J, *et al.* Low-dose megavoltage cone-beam CT for radiation therapy. *Int J Radiat Oncol Biol Phys* 2005;61:552–560.
- Mackie TR, Kapatoes J, Ruchala K, *et al.* Image guidance for precise conformal radiotherapy. *Int J Radiat Oncol Biol Phys* 2003;56:89–105.
- Yoo S, Yin FF. Dosimetric feasibility of cone-beam CT-based treatment planning compared to CT-based treatment planning. *Int J Radiat Oncol Biol Phys* 2006;66:1553–1561.
- Yang Y, Schreiber E, Li T, *et al.* Evaluation of on-board kV cone beam CT (CBCT)-based dose calculation. *Phys Med Biol* 2007;52:685–705.
- Langen KM, Meeks SL, Poole DO, *et al.* The use of megavoltage CT (MVCT) images for dose recomputations. *Phys Med Biol* 2005;50:4259–4276.
- Ezzell GA, Chungbin S. The overshoot phenomenon in step-and-shoot IMRT delivery. *J Appl Clin Med Phys* 2001;2:138–148.
- Xia P, Chuang CF, Verhey LJ. Communication and sampling rate limitations in IMRT delivery with a dynamic multileaf collimator system. *Med Phys* 2002;29:412–423.
- Wiersma R, Xing L. Examination of geometric and dosimetric accuracies of gated step-and-shoot IMRT. *Med Phys* 2007;34:3962–3970.
- Litzenberg DW, Hadley SW, Tyagi N, *et al.* Synchronized dynamic dose reconstruction. *Med Phys* 2007;34:91–102.
- Yoo S, Kim GY, Hammoud R, *et al.* A quality assurance program for the on-board imagers. *Med Phys* 2006;33:4431–4447.
- Li JG, Dempsey JF, Ding L, *et al.* Validation of dynamic MLC-controller log files using a two-dimensional diode array. *Med Phys* 2003;30:799–805.
- Stell AM, Li JG, Zeidan OA, *et al.* An extensive log-file analysis of step-and-shoot intensity modulated radiation therapy segment delivery errors. *Med Phys* 2004;31:1593–1602.
- Zhu L, Starlack J, Bennett NR, Li T, Xing L, Fahrig R. Improved scatter correction for x-ray conebeam CT using primary modulation. In: Hsieh J, Flynn M, editors. *Proceedings of SPIE: Medical Imaging 2007: Physics of Medical Imaging*, San Diego, CA; 2007.
- Cozzi L, Fogliata A, Buffa F, *et al.* Dosimetric impact of computed tomography calibration on a commercial treatment planning system for external radiation therapy. *Radiother Oncol* 1998;48:335–338.

21. Guan H, Yin FF, Kim JH. Accuracy of inhomogeneity correction in photon radiotherapy from CT scans with different settings. *Phys Med Biol* 2002;47:N223–N231.
22. Hansen EK, Bucci MK, Quivey JM, *et al.* Repeat CT imaging and replanning during the course of IMRT for head-and-neck cancer. *Int J Radiat Oncol Biol Phys* 2006;64:355–362.
23. Morin O, Chen J, Aubin M, *et al.* Dose calculation using megavoltage cone-beam CT. *Int J Radiat Oncol Biol Phys* 2007;67:1201–1210.
24. Xing L, Thorndyke B, Schreibmann E, *et al.* Overview of image-guided radiation therapy. *Med Dosim* 2006;31:91–112.
25. Schreibmann E, Chen GT, Xing L. Image interpolation in 4D CT using a BSpline deformable registration model. *Int J Radiat Oncol Biol Phys* 2006;64:1537–1550.
26. Zerda Adl, Armbruster B, Xing L. Formulating adaptive radiation therapy (ART) treatment planning into a closed-loop control framework. *Phys Med Biol* 2007;52:4137–4153.
27. Yan D, Jaffray DA, Wong JW. A model to accumulate fractionated dose in a deforming organ. *Int J Radiat Oncol Biol Phys* 1999;44:665–675.
28. Nioutsikou E, Webb S, Panakis N, *et al.* Reconsidering the definition of a dose-volume histogram. *Phys Med Biol* 2005;50:L17–L19.

PHYSICS CONTRIBUTION

AUTOMATED CONTOUR MAPPING WITH A REGIONAL DEFORMABLE MODEL

MING CHAO, PH.D., TIANFANG LI, PH.D., EDUARD SCHREIBMANN, PH.D.,
ALBERT KOONG, M.D., AND LEI XING, PH.D.

Department of Radiation Oncology, Stanford University School of Medicine, Stanford, CA

Purpose: To develop a regional narrow-band algorithm to auto-propagate the contour surface of a region of interest (ROI) from one phase to other phases of four-dimensional computed tomography (4D-CT).

Methods and Materials: The ROI contours were manually delineated on a selected phase of 4D-CT. A narrow band encompassing the ROI boundary was created on the image and used as a compact representation of the ROI surface. A BSpline deformable registration was performed to map the band to other phases. A Mattes mutual information was used as the metric function, and the limited memory Broyden-Fletcher-Goldfarb-Shanno algorithm was used to optimize the function. After registration the deformation field was extracted and used to transform the manual contours to other phases. Bidirectional contour mapping was introduced to evaluate the proposed technique. The new algorithm was tested on synthetic images and applied to 4D-CT images of 4 thoracic patients and a head-and-neck Cone-beam CT case.

Results: Application of the algorithm to synthetic images and Cone-beam CT images indicates that an accuracy of 1.0 mm is achievable and that 4D-CT images show a spatial accuracy better than 1.5 mm for ROI mappings between adjacent phases, and 3 mm in opposite-phase mapping. Compared with whole image-based calculations, the computation was an order of magnitude more efficient, in addition to the much-reduced computer memory consumption.

Conclusions: A narrow-band model is an efficient way for contour mapping and should find widespread application in future 4D treatment planning. © 2008 Elsevier Inc.

Deformable model, Image registration, Contour mapping, IGRT.

INTRODUCTION

Segmentation of a region of interest (ROI), such as a tumor target volume or a sensitive structure, is an important but time-consuming task in radiotherapy (1–6). With the emergence of four-dimensional (4D) imaging and adaptive radiotherapy, the need for efficient and robust segmentation tools is even increasing (7–11). Because of dramatically increased numbers of images, it becomes impractical to manually segment the ROIs slice by slice as in current three-dimensional radiotherapy practice. A natural solution to the 4D computed tomography (4D-CT) segmentation problem is to delineate the ROIs on a selected phase and then propagate the contours onto other phases using a mathematical model. Along this line, deformable model-based contour mapping has been implemented by a few groups (12–14). Although feasible, the calculation is global in nature and thus computationally intensive. In addition, the accuracy of the mapped contours may be compromised because the registration may be

influenced unnecessarily by the image content distant from the ROIs, which would otherwise be irrelevant to the contour mapping process. This is especially problematic when non-local deformable models, such as thin plate spline and elastic model, are used. In general, contour mapping is a regional problem, and a global association of the phase-based images is neither necessary nor efficient.

Surface mapping techniques (15–17) represent a competitive alternative to the deformable model-based approach. The idea of surface mapping is to obtain contour transformation by iteratively deforming the ROI contour-extended surface until the optimal match with the reference is found. The calculation involves only the surface region and is thus computationally efficient. Numerous surface mapping techniques have been developed in the past, which include, to name a few, spatial partitioning, principal component analysis, conformal mapping, rigid affine transformation, deformable contours, and warping based on the thin-plate spline. All of

Reprint requests to: Lei Xing, Ph.D., Department of Radiation Oncology, Stanford University School of Medicine, 875 Blake Wilbur Drive, Stanford, CA 94305-5847. Tel: (650) 498-7896; Fax: (650) 498-4015; E-mail: lei@reyes.stanford.edu

Supported in part by grants from the Department of Defense (W81XWH-06-1-0235 and W81XWH-05-1-0041), Komen Breast Cancer Foundation (BCTR0504071), and National Cancer Institute

(5R01 CA98523 and 1 R01 CA98523).

Conflict of interest: none.

Acknowledgment—The authors thank Dr. B. Loo from Stanford University for useful discussions.

Received March 12, 2007, and in revised form Sept 18, 2007.

Accepted for publication Sept 27, 2007.

these techniques are a mapping between topologic components of the input surfaces that allow for transfer of annotations. Although the calculations are inherently efficient, the results depend heavily on the model used, which may not be generally applicable for all clinical situations because the ROI surface is multidimensional and hardly modeled by only a few parameters.

In this work, we present a novel regional algorithm for ROI propagation among different 4D-CT phases. The deformation of an ROI contour-extended surface in our algorithm is not driven by an *ad hoc* surface-based model but instead by the image features in the neighborhood of the surface. The underlying hypothesis here is that information contained in the ROI boundary region is sufficient to guide the contour mapping process. In the proposed algorithm the neighborhood image features of an ROI are captured by a narrow band, which is composed of all points within two surfaces with the signed distances of $\pm d$ from the ROI boundary. The algorithm is a hybrid of the regional surface-based model and the global deformable registration-based approach. The combination takes advantage of the desirable features of each of these two techniques and provides a robust and computationally efficient contour propagation tool for 4D radiotherapy.

METHODS AND MATERIALS

Software platform

The proposed contour mapping algorithm was implemented using the Insight Toolkit (18) and the Visualization Toolkit (19), which are open source cross-platform C++ software toolkits sponsored by the National Library of Medicine.

Overview of the mapping process

Figure 1 depicts the overall contour mapping process. For a given 4D-CT image set, a selected phase, named the template phase, was selected, and the ROIs were manually delineated by a physician. The manually outlined contour was referred to as the template contour. A narrow band encompassing the template contour was created (see next section for details). A deformable mapping was then carried out to propagate the band from the template phase to other phases, referred to as target phases. Upon successful mapping of the band, the deformation field was used to transform the template contour to the target images.

Narrow-band representation of ROI contour

The contour manually segmented on an axial slice of the template image has a polygon shape, and the vertices of the polygon form the basis for constructing the narrow band. As schematically shown in Fig. 2, a band with signed distances $\pm d$ was placed along the template contour. The regional image features contained in the band function serve as a “signature” of the contour and drive the contour mapping process. The distance between the neighboring vertices on the contour is typically 2–10 mm, depending on the shape of the contour. In generating the narrow band, we first created cubes with a side length of $2d$ around all the vertices, as depicted by points A and B in Fig. 2. To obtain a smooth band, between A and B three more cubes, centered at points C, D, and E, were inserted. Point C was chosen to be the middle point between A and B, point D the middle between A and C, and point E the middle between C and

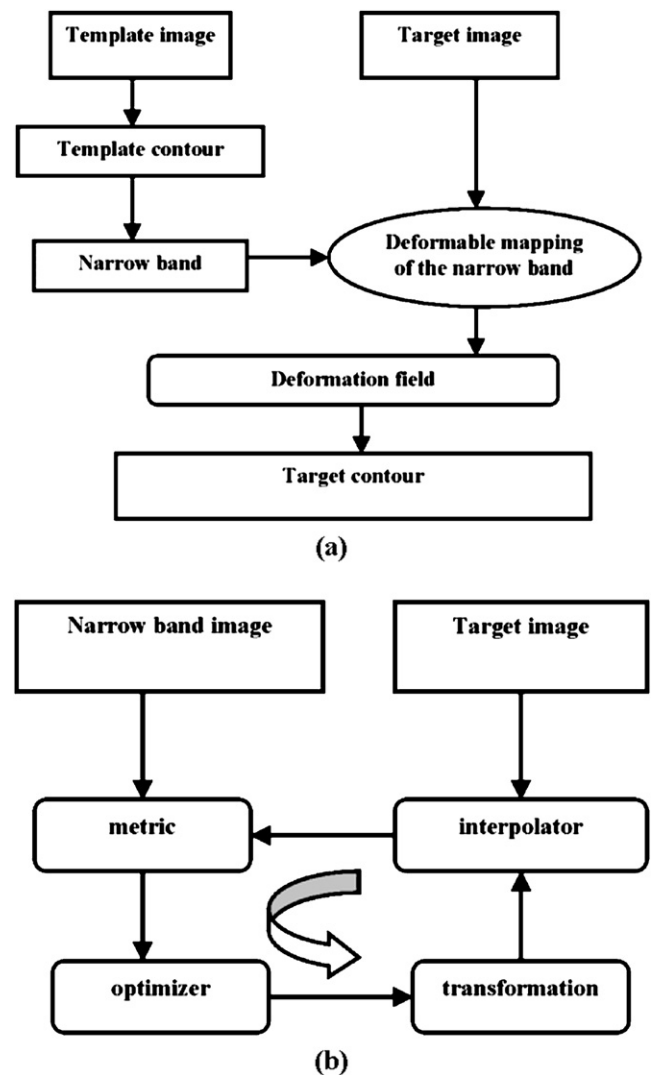


Fig. 1. Flow chart of narrow band-based contour mapping procedure. (a) Overall calculation process. (b) Deformable mapping process of the narrow band.

B. More interpolated vertex points can be introduced similarly when needed. Figure 3 illustrates a narrow band surrounding the lung boundary on the template phase CT image. The light green area stands for the narrow band, and the green curve is the manual contour. The width of the narrow band was set to be $2d = 15$ mm in our calculations. To examine the robustness of the proposed mapping algorithm, a variety of other bandwidths, ranging from 4 mm through 30 mm, were also tested for one of the clinical cases.

Contour propagation

As illustrated in Fig. 1, the process of contour mapping is essentially to warp the narrow band constructed above in such a way that its best match in the target image is found. Mathematically, the mapping process of the narrow band constitutes an optimization problem, in which a group of transformation parameters that transform the points within the band in the template phase to their homologous points in the target image. The warping of the narrow band is quantified by a metric function, which ranks a trial matching based on the “accordance” level of the image content of the band and its correspondence in the target image. The calculation process is detailed below.

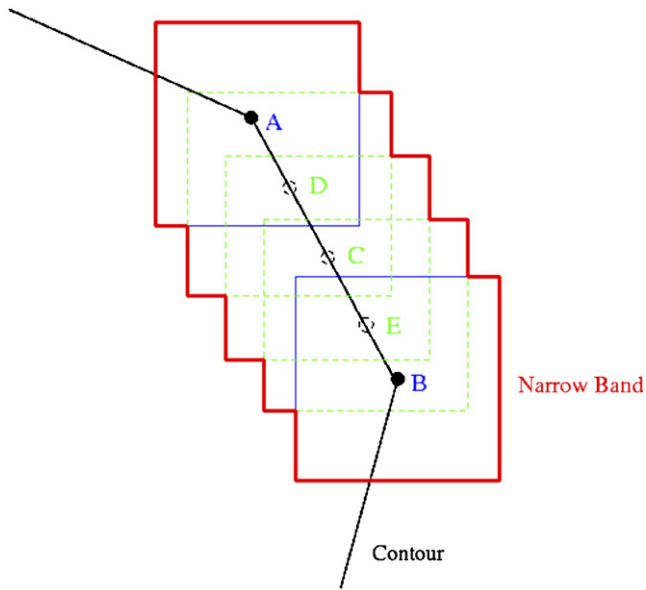


Fig. 2. A schematic drawing of narrow-band construction.

The input to the contour mapping software includes the narrow band and the whole target image, which are described by the image intensity distributions $I_a(\mathbf{x})$ and $I_b(\mathbf{x})$, respectively. It is worth emphasizing that, even though the whole target image was used, only fractional voxels in the target image (the voxels encompassed by the band) are involved in each iteration (a subregion surrounding the ROI on the target image could be created and used in the calculation, but the algorithm converged so fast that after two to three iterations the searching was quickly confined in the neighborhood of the optimal solution). The narrow band acts as a representation of the ROI contour. The task is to find the transformation matrix, $T(\mathbf{x})$, that maps an arbitrary point in the band to the corresponding point on the target image (or *vice versa*) so that the best possible correspondence, as measured by the metric function, is achieved. The calculation proceeds iteratively. A BSpline deformable model is used to model the deformation of the band, but other models should also be applicable. The spacing between the BSpline nodes was chosen to be approximately 0.5 cm (smaller spacing was tested, but no significant difference was found in the final registration results). The displacement of a node i is specified by a vector \mathbf{x}_i , and the displacement vectors (20) of a collection of nodes characterize the tissue deformation. The displacement at a location \mathbf{x} on the image is deduced by a BSpline polynomial fitting.

The Mattes Mutual Information (MMI) (21) was used as the metric function for narrow-band mapping (22–25). The central concept

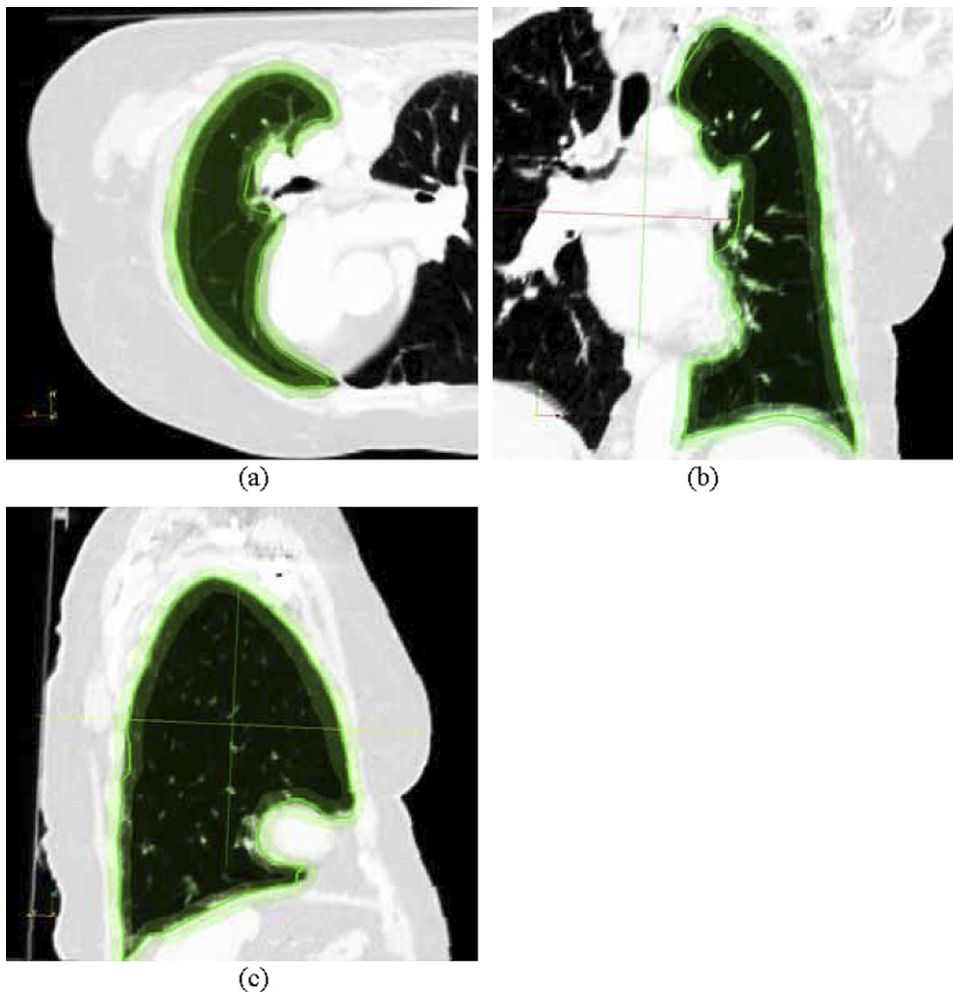


Fig. 3. Computed tomographic images with manual contours and the narrow bands for patient 1. The narrow bands are shown in light green and the contours are green curves. (a) Transverse view; (b) coronal view; (c) sagittal view.

of mutual information (MI) is the calculation of entropy. For an image A, the entropy is defined as

$$H(A) = - \int p_A(a) \log p_A(a) da,$$

where $p_A(a)$ (also called the marginal probability density function [PDF]) is the probability distribution of grey values (image intensities), which is estimated by counting the number of times each grey value occurs in the image and dividing those numbers by the total number of occurrences. Given two images, A and B, their joint entropy is

$$H(A, B) = - \iint p_{AB}(a, b) \log p_{AB}(a, b) dadb,$$

where $p_{AB}(a, b)$ is the joint PDF defined by a ratio between the number of grey values in the joint histogram (feature space) of two images and the total entries (26). The mutual information is generally expressed as

$$MI(A, B) = H(A) + H(B) - H(A, B).$$

Mutual information measures the level of information that a random variable (e.g., $\mathbf{I}_a(\mathbf{x})$) can predict about another random variable (e.g., $\mathbf{I}_b(\mathbf{x})$). Different from the conventional MI, whereby two separate intensity samples are drawn from the image, the Mattes implementation, MMI, uses only one set of intensity to evaluate both the marginal and joint PDFs at discrete positions or bins that uniformly spread within the dynamic range of the images. Entropy values were computed by summing over all the bins. The number of bins used to compute the entropy in MMI metric evaluation was chosen to be 30, and the number of spatial samples used was 20,000. Details of MMI implementation can be found in Mattes *et al.* (21).

The limited memory Broyden-Fletcher-Goldfarb-Shanno algorithm (L-BFGS) (27–29) was used to optimize the MMI metric function with respect to the displacement parameters of the nodes, $\{\mathbf{x}_i\}$, to find the transformation matrix $\mathbf{T}(\mathbf{x})$ that relates the points on image A and image B. Here we just briefly show the algorithm. Starting from a positive definitive approximation of the inverse Hessian \mathbf{H}_0 at \mathbf{x}_0 , L-BFGS derives the optimization variables by iteratively searching through the solution space. At an iteration k , the calculation proceeds as follows: [1] determine the descent direction $\mathbf{p}_k = -\mathbf{H}_k \nabla f(\mathbf{x}_k)$; [2] line search with a step size $\alpha_k = \arg \min_{\alpha \geq 0} f(\mathbf{x}_k + \alpha \mathbf{p}_k)$, where α is the step size defined in the L-BFGS software package; [3] update $\mathbf{x}_{k+1} = \mathbf{x}_k + \alpha_k \mathbf{p}_k$; and [4] compute \mathbf{H}_{k+1} with the updated \mathbf{H}_k .

At each iteration a backtracking line search is used in L-BFGS to determine the step size of movement to reach the minimum of f along the ray $\mathbf{x}_k + \alpha \mathbf{p}_k$. For convergence α has to be chosen such that a sufficient decrease criterion is satisfied, which depends on the local gradient and function value and is specified in L-BFGS by the Wolfe conditions (27). During the course of optimization, the above iterative calculation based on L-BFGS algorithm continues until the following stopping criterion is fulfilled:

$$\frac{\|\nabla f(\mathbf{x}_k)\|_2}{\max(1, \|\mathbf{x}_k\|_2)} < \varepsilon$$

or a pre-set maximum number of iterations is reached. In this study we set $\varepsilon = 10^6$ and the iteration number to 200, but no more than 100 iterations were exceeded in all our calculations for the algorithm to converge.

Evaluation of algorithm performance

Evaluation of a contour mapping algorithm is a difficult task because of the lack of the ground truth for comparison. A straightforward means of evaluation is the visual inspection of the mapped contours. In addition to this, evaluation based on synthetic images (digital phantoms) is also commonly used. The images and existing contours are distorted with preset deformation fields. Because the gold standard is known, a direct comparison with the mapped contour is made so as to assess the propagation algorithm quantitatively. Beside these two methods, we further performed a bidirectional mapping to evaluate the proposed algorithm. In this test, the reverse of the original contour mapping was performed: the mapped contours on the target phase were treated as the template contours and mapped back to the original template phase. The contours so obtained were then compared with the original manual contours, and the difference between the two sets of contours was quantified. The difference between the resultant and template contours was measured in terms of the displacements of the vertex points on the two contours. The last yet pragmatic evaluation of the algorithm performance on patient's study was based on the physician's manual contours.

Case study

Four thoracic cancer patients, named as patient 1, 2, 3, and 4, were first used to test the proposed algorithm. These patients underwent 4D-CT scans. The 4D-CT images were acquired with a GE Discovery-ST CT scanner (GE Medical System, Milwaukee, WI). The collected data were sorted into 10 phase bins. The ROIs on the template phase were manually segmented by a physician. Specifically, for patients 1 and 2, the inhale phase was chosen for manual segmentation, and for patients 3 and 4, the exhale phase. Different ROIs were used to better evaluate the algorithm. Lungs were selected from patients 1, 2, and 3 and gross tumor volume (GTV) from patient 4. Figure 3 illustrates the manual contour and narrow band representation for the lung from patient 1. Contour is shown in the green curve together with the regional narrow bands (light green area) on the transverse, coronal, and sagittal views (Figs. 3a, 3b, and 3c, respectively).

To further assess the robustness of the proposed algorithm, we also carried out the contour propagation calculation from planning CT to Cone-beam CT (CBCT) for a head-and-neck case. The CBCT images were acquired using the Varian Trilogy system (Varian Medical Systems, Palo Alto, CA).

RESULTS

Convergence analysis

To better illustrate the iterative process of the contour propagation, in Fig. 4 the MMI metric as a function of iteration step is plotted for the narrow band mapping from the first phase (inhale phase) to the other nine phases for the first thoracic patient. In all nine calculations it is seen that the metric value decreases monotonically as the iteration proceeds. However, the number of iterations needed for the algorithm to find the optimal solution varies. It is interesting to observe that, for an “easier” mapping whereby the deformation between the two phases is small, the number of iterations required is less, whereas for “tougher” ones with larger differences in ROI shapes, the required number of iterations increases drastically. Indeed, from Fig. 4 it is seen that the minimum number of iterations required for the metric to saturate occurs when mapping the phase 1 to the adjacent

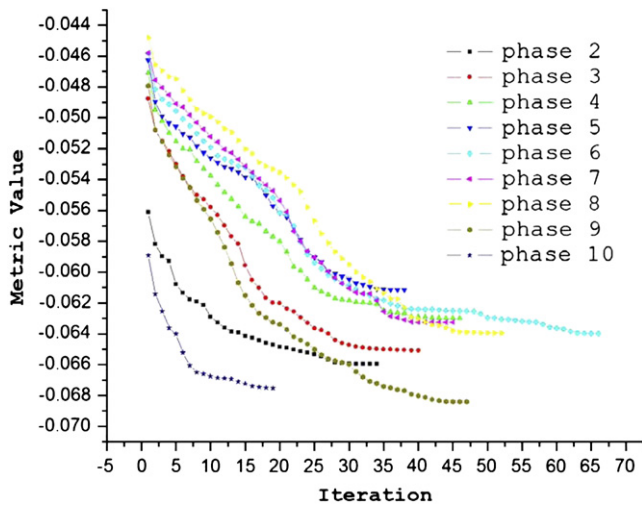


Fig. 4. Narrow-band metric values as a function of iteration step when mapping the narrow band from phase 1 to the other nine phases of the four-dimensional computed tomography.

phases, 2 and 10. For other mapping, the required iteration increases and reaches its largest value for the “toughest” mapping between inhale and exhale (phase 5) phases.

In the above analysis, the bandwidth was set to be 15 mm. The performance of the proposed algorithm was also evaluated by varying the width in the range of 4 mm and 30 mm. Specifically, we tried the widths of 4 mm, 8 mm, 10 mm, 15 mm, 20 mm, and 30 mm. Our results revealed that, when the band was too narrow (e.g., 4 mm), the mapping may fail locally at a place not containing sufficient neighborhood image features. The situation is improved dramatically as the bandwidth increases. For all the clinical cases studied here, no single failure was observed for a width of 15 mm. When the width is too large, the whole ROI will be included in the band. In this situation, the mapping becomes equivalent to registering the whole image and the advantage of the narrow band will be overshadowed by the dramatically increased memory and computing costs. Our experience indicates that a width of 10–15 mm provides a fine balance between the computational accuracy and the associated cost.

We found that the overall computing time was increased by roughly an order of magnitude when going from the narrow band approach to the conventional deformable model-based contour mapping, say, approximately 3 min for narrow band-based mapping vs. approximately 25 min for whole image-based mapping. The dramatically increased computer memory requirement in the latter case also posts a serious problem when developing a clinically practical contour propagation method for 4D radiotherapy.

Algorithm performance evaluation

In addition to visual inspect, the proposed algorithm was assessed by a series of synthetic images or digital phantoms. Typically, a thoracic CT image together with the contour was distorted with the intentionally introduced deformation, and then the contour was propagated onto the distorted image.

A quantitative comparison was carried out. The mean and maximum separation between the gold standard and the mapped contours were found to be 1.0 mm and 1.5 mm, respectively. Figure 5 shows one example of digital phantom experiments.

The performance of the proposed algorithm was further evaluated by the bidirectional mapping calculation outlined in Methods and Materials. A template contour at phase 1 was first mapped to phases 3 and 6. The mapped contours were then treated as the “starting contours” and mapped back to phase 1. The two back-mapped contours were compared with the original template contour. The displacement of each back-mapped vertex point relative to its original locations was computed, and a mean value of 0.8 mm was found for the bidirectional mapping between phases 1 and 3 and 1.8 mm between phases 1 and 6. The larger displacement in the latter situation was due to the fact that, computationally, it is more difficult to map between two opposite phases, such as inhale and exhale phases, owing to larger organ deformations. Overall, the observed displacement is comparable to the pixel size, indicating that the mapping is accurate and robust.

Thoracic patient study results

Figure 6 shows the contour mapping results for the first clinical case. The results are presented in axial, coronal, and sagittal planes for phases 2 (Fig. 6a–c), 6 (Fig. 6d–f), 8 (Fig. 6g–i), and 10 (Fig. 6j–l). For phases 2 and 10, which are immediately adjacent to the inhale phase, the deformation is relatively small and the mapped contours conform to the ROI boundary very well. This represents the “easy” mapping situation and is consistent with the analysis presented above. The average error was less than 1.5 mm. For a “remote” phase, such as phase 6 shown in Fig. 6d–f, more

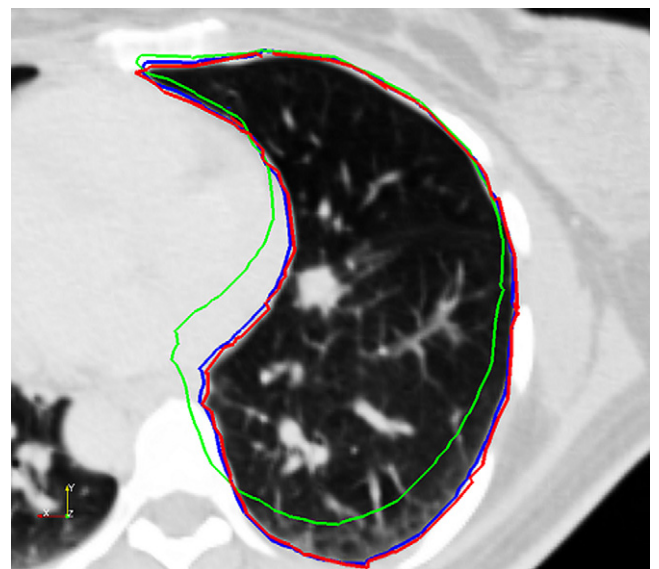


Fig. 5. Synthetic image and overlaid contours. The original contour is depicted in green, gold standard contour in blue, and the mapped contour in red.

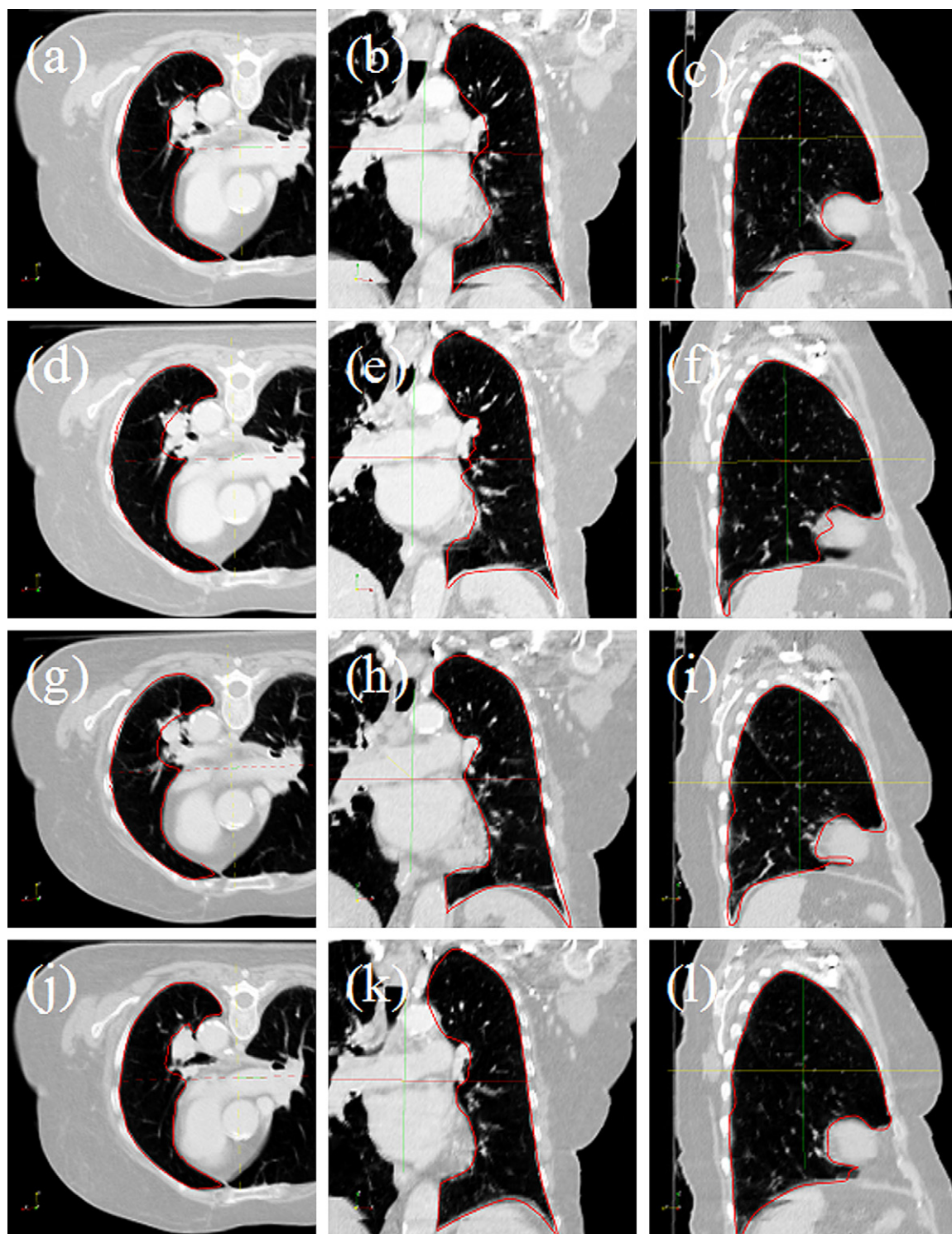


Fig. 6. Computed tomographic images and mapped contours for thoracic patient 1. Displayed are selected phases. From the top row to bottom, phases 2, 6, 8, and 10 are presented, respectively. For each phase, transverse, coronal, and sagittal views are shown from left to right.

iterations were entailed to find the optimal solution, and the resultant contours tend to be worse as compared with those phases adjacent to phase 1. According to the bidirectional mapping, the average mapping error for phase 6 was estimated to be less than 3 mm. The mapped GTV contours (in red) together with manual contours (in blue) by a physician

for phases 1, 4, 8, and 10 in the study of patient 4 are shown in Fig. 7 (parts a, b, d, and e, respectively). The template phase (phase 6) with the template manual contour (in green) is shown in Fig. 7c. In addition, the template manual contour from this phase was overlaid on all the displayed phases. For phases 4 and 8 the deformation was relatively

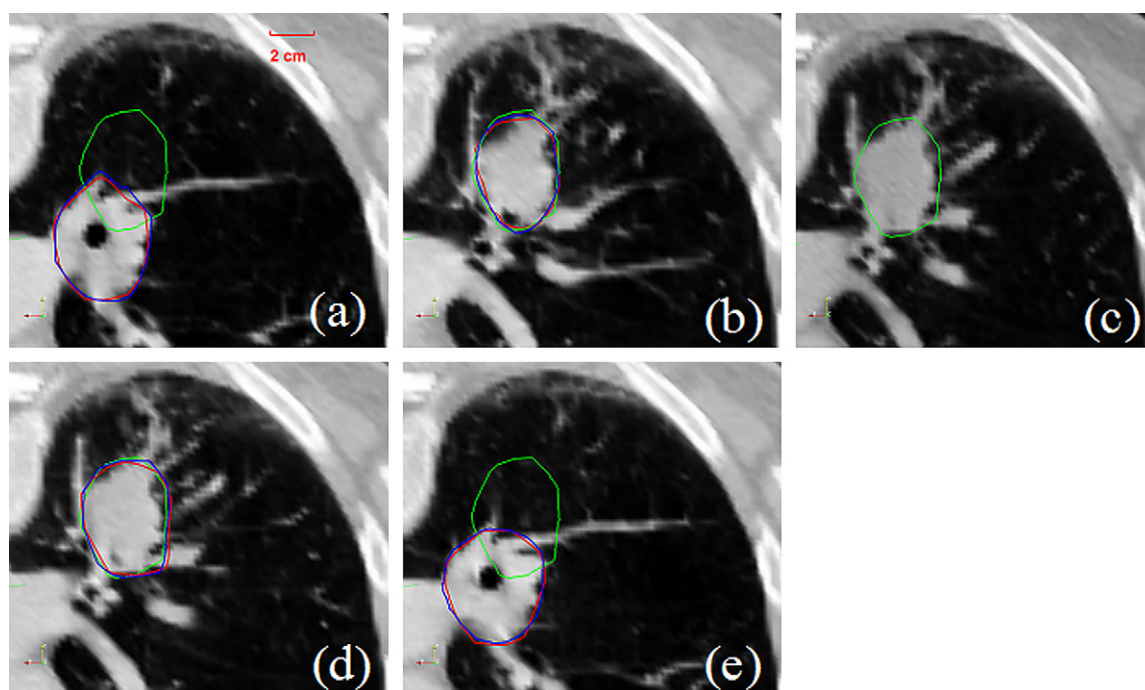


Fig. 7. Axial view of computed tomographic images with gross tumor volume contours for the fourth thoracic patient. (a), (b), (c), (d), and (e) correspond to phases 1, 4, 6 (template phase), 8, and 10, respectively. The green curves are the manually outlined template contour from phase 6, and the red curves represent the contours after warping. The manual contours (in blue) by a physician on individual phases were also displayed.

small (the manual contour was delineated on phase 6), and fewer iterations were needed to find the optimal bands on the target images. For phases 1 and 10, whereby deformation was significant in the ROIs although more computing load was necessary, a good result was still achieved with our narrow-band technique. Comparisons between the mapped contours and the manually segmented contours by physicians for these patients were also performed, and results revealed a similar level of accuracy (maximum and mean values of the discrepancy between the two sets of contours are 2.8 mm and -0.9 mm, respectively).

As a useful application of the proposed technique, in Fig. 8 we present the mean and maximum lung displacements of contour vortices for each breathing phase relative to their locations on the template phase. As seen in Fig. 8, the overall behavior of the mean and maximum displacements is consistent with our intuitive expectation. For cases 1 and 2, the inhale phase (phase 1) was manually segmented, thus the displacement for that phase is zero. For other phases, both mean and maximum displacement values vary with the breathing phase and reach their maxima at the opposite phase. For case 3 the exhale phase was manually segmented, and the behavior was thus opposite to cases 1 and 2. In general, an average displacement of approximately 3 mm was found for inhale and exhale phases. A slight digression is noticed in phase 7 of patient 1, which may be caused by 4D-CT binning artifacts. This type of data is particularly useful in determining the patient-specific tumor margin to account for breathing motion of the tumor target.

Contour propagation in a head-and-neck case

The results of contour mapping for the head-and-neck case are summarized in Fig. 9. Figure 9a shows the planning CT along with manually delineated contours, and Fig. 9b displays the mapped contours of the body, mandible, and GTV on CBCT. For body and mandible a simple rigid mapping is enough to achieve high accuracy. For the GTV, however, the proposed deformable registration model was necessary to adequately propagate the contour. A visual inspection of the propagated contours suggests that the mapping is clinically acceptable.

DISCUSSION

Four-dimensional CT image segmentation represents a necessary step in constructing a 4D patient model and computing the accumulated dose in 4D radiotherapy. A natural way to tackle the problem is to auto-map the manually delineated contours on one of the phases to the remaining phases. In this work, a regional computing algorithm was introduced to deal with the issue. The approach relies on the assumption that a narrow band surrounding the manually segmented contour can capture sufficient information to drive the finding of its counterparts in other phases of the 4D-CT. Obviously, this assumption is valid when the band is sufficiently wide so that a large number of voxels are involved in the registration calculation. As demonstrated by the presented data, the registration and the mapping are reliable when the bandwidth is larger than 4 mm. Computationally, the proposed approach

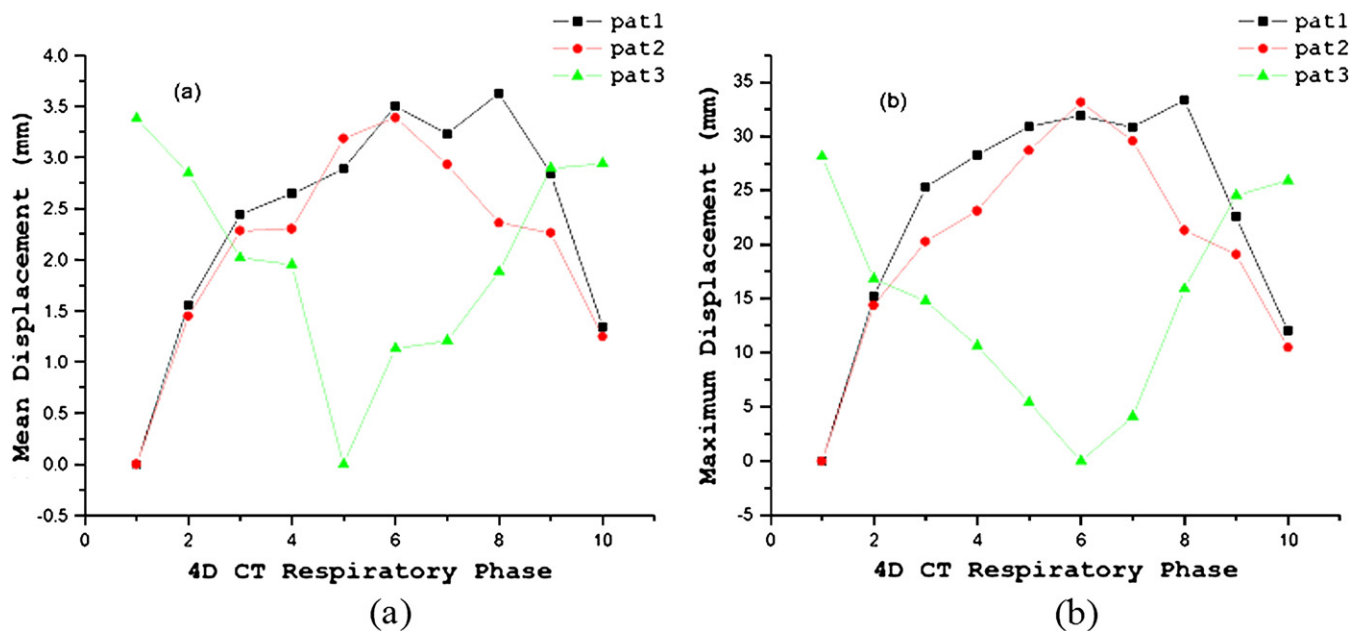


Fig. 8. Displacement of region of interest boundary points as a function of respiration phase for three thoracic patients. (a) Mean displacement vs. phase. (b) Maximum displacement vs. phase. 4D CT = four-dimensional computed tomography.

resides between a deformable model-based mapping and a surface model-based ROI contour mapping.

The success of the image content-based approaches, such as the proposed narrow-band approach or conventional deformable image registration, arises from the fact that they fully utilize the inherent image features of the two input images. The narrow band-based technique is particularly attractive because it takes advantages of the useful features of both image content-based technique and the regional surface-based model. In a sense, it is a hybrid approach of the two distinct types of algorithms. The narrow-band approach utilizes the imaging features surrounding the ROI to guide the search of the optimal mapped contours while considering the shape integrity of the ROI surface. It eliminates the need for a global

registration of the input images and thus greatly increases the computational efficiency.

Application of the proposed contour mapping technique to five clinical cases indicates that the technique is accurate and computationally efficient. A common problem in image segmentation and contour mapping studies is the lack of quantitative validation. In the studies of Lu *et al.* (13) and Schrieblmann *et al.* (14), for example, the accuracy of a deformable model-based contour mapping technique was evaluated purely on the basis of visual inspection. Although it is a convenient way for rapid assessment of a segmentation calculation, especially in a case in which the “ground truth” contours do not exist, the method falls short in quantization. The same approach was used in many other previous

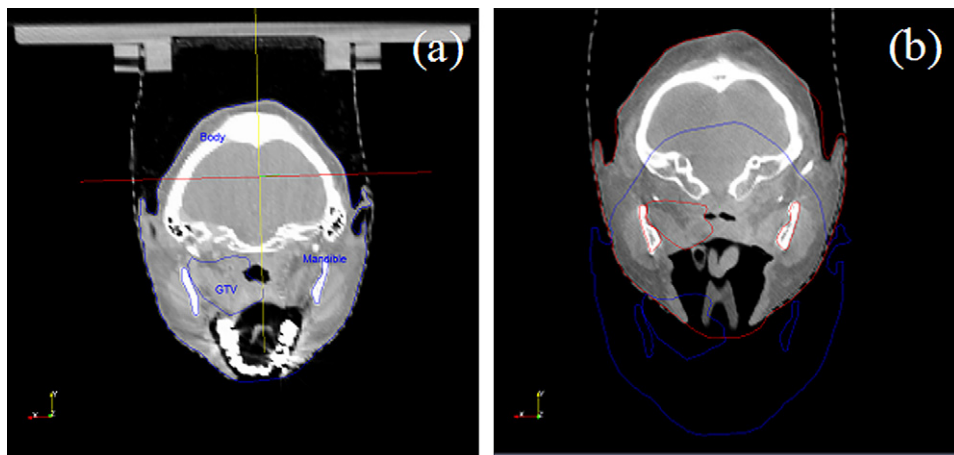


Fig. 9. Contour propagation in a head-and-neck case. (a) Planning computed tomography with manually outlined template contours (in blue) for body, mandible, and gross tumor volume. (b) Cone-beam computed tomography along with contours after warping (in red) for the corresponding structures.

investigations (1, 5, 14, 30). In this study, a bidirectional contour mapping was proposed to examine the reliability and robustness of a contour mapping technique. This method provides a useful test in assessing the success of a contour propagation algorithm. We would like to point out that the bidirectional mapping technique introduced in this work is a necessary (but not sufficient) test. In a rare but possible situation, the bidirectional mapping may not be able to find that an error occurred in the narrow-band mapping process. A visual inspection of the mapped result may help in this situation. On the basis of the bidirectional mapping experiments and visual inspection for the patient studies, we conclude that the proposed approach can perform very well even in the presence of significant deformations.

In our calculation, we observed that the regular grid of BSpline control points could be mapped to a region outside the narrow band. Although it seems that this does not directly affect the accuracy of the method, it may prolong the calculation by computing the displacements in regions where metric information is irrelevant. Setups have been proposed to adapt the splines control mesh to regions where deformation is found to be significant (31), and the extension of the method would allow us to use the BSpline control points defined only in the regions within the narrow band. Implementation of this type of technique should further reduce the computation time required to find the optimal solution.

Although there are numerous deformable algorithms, including, for example, the elastic model (32–34), viscous fluid model (35), optical flow model (5,30,36), finite element model (33, 37), and radial basis function models such as the basis spline model (28, 38, 39) and thin plate spline model (40–43), a truly robust tool suitable for routine clinical appli-

cations is yet to be developed. Each of these approaches has its pros and cons. The deformable calculation can be greatly facilitated if some *a priori* system information can be incorporated. Along this line, the homologous correspondence of the bony structure in two input images has been incorporated in thin plate spline method, and remarkable improvement has resulted (44). The narrow band-generated ROI contour correspondence could also be used as prior knowledge to improve a deformable registration. This work is still in progress and will be reported in the future.

CONCLUSIONS

In this work we have developed a regional deformable registration-based method to auto-propagate contours for 4D radiotherapy. The central idea is that a narrow band encompassing an ROI surface carries the neighborhood information of the ROI surface and can be used to establish a reliable association between the ROIs in two phase-specific image sets. Different from other type of regional algorithms, such as surface mapping, the method uses the image features captured in a band to guide the search for the optimal contour mapping. Compared with conventional deformable image registration-based approaches, a great reduction in computational burden and a large capture radius in optimization space result. Our study demonstrated that the information contained in the boundary region can be used to guide the contour mapping in all the testing cases presented in this article. The proposed regional model decreases the workload involved in 4D-CT ROI segmentation and provides a valuable tool for the efficient use of available spatial-temporal information for 4D simulation and treatment planning.

REFERENCES

1. Pekar V, McNutt TR, Kaus MR. Automated model-based organ delineation for radiotherapy planning in prostatic region. *Int J Radiat Oncol Biol Phys* 2005;60:973–980.
2. Kass MR, WitKen A, Terzopoulos D. Snakes: Active contour models. *Int J Comput Vis* 1988;4:321–331.
3. Coote T, Hill A, Taylor C, *et al.* The use of active shape models for locating structures in medical images. *J Image Vis Comput* 1994;12:355–366.
4. Xu C, Prince JL. Snakes, shapes, and gradient vector flow. *IEEE Trans Image Process* 1998;7:359–369.
5. Liu F, Zhao B, Kijewski PK, *et al.* Liver segmentation for CT images using GVF snake. *Med Phys* 2005;32:3699–3706.
6. Weese J, Kaus MR, Lorenz C, *et al.* Shape constrained deformable models for 3D medical image segmentation. In: Insana MF, Leahy RM. Information processing in medical imaging: 17th International Conference, IPMI 2001, Davis, CA, USA, June 18–22, 2001. *Lecture Notes in Computer Science* 2001; 2082:380–387.
7. Li T, Schreiber E, Thorndyke B, *et al.* Radiation dose reduction in four-dimensional computed tomography. *Med Phys* 2005;32:3650–3660.
8. Vedam SS, Keall PJ, Kini VR, *et al.* Acquiring a four-dimensional computed tomography dataset using an external respiratory signal. *Phys Med Biol* 2003;48:45–62.
9. Dietrich L, Jetter S, Tucking T, *et al.* Linac-integrated 4D cone beam CT: First experimental results. *Phys Med Biol* 2006;51: 2939–2952.
10. Li T, Xing L, Munro P, *et al.* Four-dimensional cone-beam computed tomography using an on-board imager. *Med Phys* 2006;33:3825–3833.
11. Rietzel E, Chen GT, Choi NC, *et al.* Four-dimensional image-based treatment planning: Target volume segmentation and dose calculation in the presence of respiratory motion. *Int J Radiat Oncol Biol Phys* 2005;61:1535–1550.
12. Gao S, Zhang L, Wang H, *et al.* A deformable image registration method to handle distended rectums in prostate cancer radiotherapy. *Med Phys* 2006;33:3304–3312.
13. Lu W, Olivera GH, Chen Q, *et al.* Automatic re-contouring in 4D radiotherapy. *Phys Med Biol* 2006;51:1077–1099.
14. Schreiber E, Chen GT, Xing L. Image interpolation in 4D CT using a BSpline deformable registration model. *Int J Radiat Oncol Biol Phys* 2006;64:1537–1550.
15. Chakraborty A, Staib LH, Duncan JS. An integrated approach for surface finding in medical images. In: IEEE workshop mathematical methods in biomedical image analysis. Los Alamitos, CA: IEEE Computer Society Press; 1996. p. 253–262.
16. McNerney T, Terzopoulos D. Deformable models in medical image analysis. *Med Image Anal* 1996;1:91–108.

17. Montagnat J, Delingette H, Ayache N. A review of deformable surfaces: Topology, geometry and deformation. *Image Vis Comput* 2001;19:1023–1040.
18. Ibanez L, Schroeder W, Ng L. ITK software guide. Clifton Park, NY: Kitware; 2003.
19. Schroeder W, Martin K, Lorensen B. The visualization toolkit: An object-oriented approach to 3D graphics. 4th edition. Kitware: Clifton Park, NY; 2006.
20. Chao M, Schreibmann E, Li T, *et al.* Knowledge-based auto-contouring in 4D radiation therapy. *Med Phys* 2006;33:2171.
21. Mattes D, Haynor DR, Vesselle H, *et al.* Non-rigid multi-modality image registration. In: Sonka M, Hanson KM, editors. *Medical imaging 2001: Image processing. Proceedings of SPIE* 2001;4322:1609–1620.
22. Woods RP, Cherry SR, Mazziotta JC. Rapid automated algorithm for aligning and reslicing PET image. *J Comput Assist Tomogr* 1992;16:620–633.
23. Woods RP, Mazziotta JC, Cherry SR. MRI-PET registration with automated algorithm. *J Comput Assist Tomogr* 1993;17:536–546.
24. Collingnon A, Maes F, Delaere D, *et al.* Automated multi-modality image registration based on information theory. In: Bizais Y, Barillot C, Paola RD, editors. *Information processing in medical imaging*. Dordrecht, The Netherlands: Kluwer; 1995. p. 263–274.
25. Wells WM III, Viola P, Kikinis R. Multi-modal volume registration by maximization of mutual information. *Med Image Anal* 1996;1:35–51.
26. Pluim JP, Maintz JB, Viergever MA. Mutual-information-based registration of medical images: A survey. *IEEE Trans Med Imaging* 2003;22:986–1004.
27. Liu DC, Nocedal J. On the limited memory BFGS method for large scale optimization. *Math Program* 1989;45:503–528.
28. Schreibmann E, Yang Y, Boyer A, *et al.* Image interpolation in 4D CT using a BSpline deformable registration model. *Med Phys* 2005;32:1924.
29. Schreibmann E, Xing L. Narrow band deformable registration of prostate magnetic resonance imaging, magnetic resonance spectroscopic imaging, and computed tomography studies. *Int J Radiat Oncol Biol Phys* 2005;62:595–605.
30. Guerrero TM, Zhang G, Huang TC, *et al.* Intrathoracic tumour motion estimation from CT imaging using the 3D optical flow method. *Phys Med Biol* 2004;49:4147–4161.
31. Camara O, Colliot O, Delso G, *et al.* 3D nonlinear PET-CT image registration algorithm with constrained free-form deformations. In: Hamza MH, editor. *Proceedings of the 3rd IASTED International Conference on Visualization, Imaging, and Image Processing*. Calgary: ACTA Press; 2003. p. 516–521.
32. Bajcsy R, Kovacic S. Multiresolution elastic matching. *Comput Vis Graphics Image Processing* 1989;46:1–21.
33. Gee JC, Haynor DR, Reivich M, *et al.* Finite element approach to warping of brain images. *Proc SPIE Med Imaging* 1994;2167:18–27.
34. Gee JC, Reivich M, Bajcsy R. Elastically deforming 3D atlas to match anatomical brain images. *J Comput Assist Tomogr* 1993;17:225–236.
35. Christensen GE, Rabitt RD, Miller MI. Deformable templates using large deformable kinematics. *IEEE Trans Med Imaging* 1996;5:1435–1447.
36. Thirion JP. Image matching as the diffusion process: An analogy with Maxwell's demons. *Med Image Anal* 1998;2:243–260.
37. Brock KM, Balter JM, Dawson LA, *et al.* Automated generation of a four-dimensional model of the liver using warping and mutual information. *Med Phys* 2003;30:1128–1133.
38. Schreibmann E, Xing L. Image registration with auto-mapped control volumes. *Med Phys* 2006;33:1165–1179.
39. Coselmon MM, Balter JM, McShan DL, *et al.* Mutual information based CT registration of the lung at exhale and inhale breathing states using thin-plate splines. *Med Phys* 2004;31:2942.
40. Lian J, Xing L, Hunjan S, *et al.* Mapping of the prostate in endorectal coil-based MRI/MRSI and CT: A deformable registration and validation study. *Med Phys* 2004;31:3087–3094.
41. Brock KK, Hollister SJ, Dawson LA, *et al.* Technical note: creating a four-dimensional model of the liver using finite element analysis. *Med Phys* 2002;29:1403–1405.
42. Fei B, Kemper C, Wilson DL. A comparative study of warping and rigid body registration for the prostate and pelvic MR volumes. *Comput Med Imaging Graph* 2003;4:267–281.
43. Bookstein FL. Principal warping: Thin plate splines and the decomposition of deformations. *IEEE Trans Pattern Anal Machine Intelligence* 1989;11:567–585.
44. Xie Y, Xing L. Incorporating a priori knowledge into deformable registration model [Abstract]. *Med Phys* 2007;34:2333–2334.

Computational Challenges for Image-Guided Radiation Therapy: Framework and Current Research

Lei Xing,* Jeffrey Siebers,[†] and Paul Keall*



It is arguable that the imaging and delivery hardware necessary for delivering real-time adaptive image-guided radiotherapy is available on high-end linear accelerators. Robust and computationally efficient software is the limiting factor in achieving highly accurate and precise radiotherapy to the constantly changing anatomy of a cancer patient. The limitations are not caused by the availability of algorithms but rather issues of reliability, integration, and calculation time. However, each of the software components is an active area of research and development at academic and commercial centers. This article describes the software solutions in 4 broad areas: deformable image registration, adaptive replanning, real-time image guidance, and dose calculation and accumulation. Given the pace of technological advancement, the integration of these software solutions to develop real-time adaptive image-guided radiotherapy and the associated challenges they bring will be implemented to varying degrees by all major manufacturers over the coming years.

Semin Radiat Oncol 17:245-257 © 2007 Elsevier Inc. All rights reserved.

There are 3 main stages in the radiotherapy process in which technology and the patient interact: the imaging, planning, and delivery stages. Figure 1 schematically shows these stages and how the basic radiotherapy process changes with the addition of image guidance and treatment adaptation. Although the timescales change and feedback loops are added with image guidance and/or treatment adaptation, the basic processes do not change. Currently available imaging, planning, and treatment systems are capable of executing the tasks required for image-guided adaptive radiotherapy. In the simplest form of image-guided radiotherapy, the most recent set of patient images is used for patient alignment, replacing the original image used for planning with a better estimate of the current anatomy for target localization. In the simplest form of adaptive radiotherapy, the most recently acquired images are used to replan the remaining treatment. Thus, the processes have not changed; what has changed is the timescale on which to perform these processes and the number of times these processes need to be repeated. Given the demands on time and resources to repeat processes, soft-

ware solutions to automate procedures such as structure segmentation, deformable registration, adaptive replanning and treatment device adaptation are needed.

This article describes software solutions for real-time adaptive image-guided radiotherapy (RAIR) about a common framework. In radiotherapy planning based on anatomic space \mathbf{x} given the imaged anatomy $I(\mathbf{x})$, the estimated prescribed dose, D_{Rx} is that computed for a given beam fluence Ψ is

$$D_{Rx} = d(\mathbf{x} | \Psi, I(\mathbf{x})), \quad (1)$$

(ie, the prescribed dose to the patient is the dose computed for a planned delivery sequence on the computed tomography [CT] image of the patient anatomy). When accounting for anatomic changes over time t (including inter- and intrafraction motion), the estimated delivered dose is computed on a changing anatomy, $I(\mathbf{x}, t)$. (Note the addition of the dependence on t .) The beam fluence $\Psi(t)$ can in general be time dependent and will be for both adaptive radiotherapy (ART) and strategies in which the radiation beam is adjusted in real-time based on the estimated anatomic motion and thus for RAIR. To correctly integrate the dose for a given voxel, the time-dependent displacement vector field from the deformable image registration algorithm, $\mathbf{u}(\mathbf{x}, t)$, is also needed. Thus, the estimated delivered total dose D from the treatment initiation to the end of the final treatment from a sequence of dose deliveries $d[\mathbf{x} | \Psi(t), I(\mathbf{x}, t)]$, noting that $\Psi(t)$ will obviously be zero when the beam is off, is as follows:

*Department of Radiation Oncology, Stanford University, Stanford, CA.

[†]Department of Radiation Oncology, Virginia Commonwealth University, Richmond, VA.

Supported by the National Cancer Institute (R01 CA 93,626, 98,524 and 104,205) and the Department of Defense (PC040282).

Address reprint requests to Paul Keall, Department of Radiation Oncology, Stanford University, 300 Pasteur Drive, A0-40, Stanford, CA 94305-5304. E-mail: Paul.Keall@stanford.edu



Intrafraction Motion of the Prostate in Cyberknife Hypofractionated Radiotherapy

Yaoqin Xie Ph.D.,* David Djajaputra Ph.D.,* Christopher R. King Ph.D., M.D.,* Sabbir Hossain, Ph.D.,[†] Lijun Ma, Ph.D.,[†] Lei Xing Ph.D.*^{a)}

*Department of Radiation Oncology, Stanford University School of Medicine, Stanford, CA; [†]Department of Radiation Oncology, University of California San Francisco, San Francisco, CA

a) Author to whom correspondence should be addressed.

Stanford University School of Medicine

Department of Radiation Oncology

875 Blake Wilbur Drive

Stanford, CA 94305-5847

E-mail: lei@reyes.stanford.edu

Phone: (650)498-7896

Fax: (650)498-4015

Conflicts of Interest Notification

No actual or potential conflicts of interest exist.

ABSTRACT

Purpose: To report the characteristics of prostate motion as tracked using implanted fiducials during hypotractionated radiotherapy treatments with CyberKnife.

Methods and Materials: Twenty-one patients from Jan. 10, 2005 to Sep. 10, 2007 with prostate cancer treated using CyberKnife system were retrospectively selected for this study. They were treated with a hypofractionated protocol, consisting of five fractions of 6.25 Gy delivered over 1.5 weeks to a total dose of 31.25 Gy. The CyberKnife uses a stereoscopic X-ray system to obtain the position of the prostate target through the monitoring of implanted gold fiducial markers. In pre-treatment patient positioning, the deviation of the target relative to the planning position is corrected by moving the treatment couch. During the treatment, the deviation is examined every 3-4 nodes (~40 s interval) and compensated by the robot. If there is significant deviation from the original step, the treatment is paused while the patient is repositioned by moving the couch. The prostate displacement calculated from X-ray images acquired within the time interval between two consecutive couch motions constitute a data set.

Results: A total of 427 data sets and 4439 time stamps of X-ray images were analyzed in this study. The average duration for each data set is 697 s. Almost all these cases show a certain degree of prostate movement. The spread of prostate position increases as the time elapses. At 30 s, a motion larger than 2mm exists in about ~5% of data sets. The percentage is increased to 8%, 11%, and 14% at 60s, 90 s, and 120 s, respectively. Similar trend happens for other values of prostate motion. For example, a motion larger

than 4mm occur in ~2%, 3%, 3.5%, and 5% of the data sets at 30s, 60 s, 90s, and 120 s, respectively.

Conclusions: The prostate target moves significantly and unpredictably during the hypofractionated treatment. Effective means of compensating the intra-fractional movement is critical to ensure adequate dose coverage of the tumor target.

Key words: CyberKnife, Prostate cancer, Fiducial markers, Localization, Real-time tracking

INTRODUCTION

Prostate cancer is the most common cancer among American men, with an estimated 232,000 new cases diagnosed in the United States each year. The condition claims the lives of 30,000 men annually, making it the second leading cause of cancer death among American men. Radiotherapy is an established standard modality for the treatment of localized prostate cancer. Recent randomized studies for patients with localized prostate cancer confirm that improved biochemical failure-free survival was achieved by using higher doses of external beam radiotherapy (RT)(1-3). Although higher dose is good for eradicating the tumor, it also carries higher risk of complications to bladder and rectum(4). Margin is required when planning a radiotherapy plan for prostate because prostate moves both intrafractionally and interfractionally. Knowing the extent of prostate movement during a fractionated or hypofractionated treatment is necessary to reduce the treatment margin to facilitate prostate dose escalation (5, 6). A number of techniques have been developed for measuring set-up variations and internal organ motions for individual patients from day-to-day and during a fractional treatment (7).

Ultrasound has been a useful tool for prostate target localization (8-10). Fung et al. (8) analyzed the data of 7825 daily fractions of 234 prostate patients and indicated average 3D inter-fractional displacement of about 7.8 mm. EPID and/or on-board kV X-ray imaging of implanted fiducials is also widely used for initial setup of the prostate patients (11-19). A recent development is the electromagnetic positioning and continuous monitoring system from Calypso Medical Technologies (Seattle, WA) (20-

22). The difference between skin mark vs. the Calypso System alignment was found to be >5 mm in vector length in more than 75% of fractions. Displacements >3 and >5 mm for cumulative durations of at least 30 s were observed during 41% and 15% of sessions. In individual patients, the number of fractions with displacements >3 mm ranged from 3% to 87%; whereas the number of fractions with displacements >5 mm ranged from 0% to 56%.

At our institution, CyberKnife has been employed for a phase 1 hypofractionated treatment of prostate cancer. By frequent stereoscopic X-ray imaging of implanted fiducials, the system provides an effective way to monitor the position of the prostate target during a hypofractionated treatment and adaptively adjust the radiation beam (23, 24). The system records the position of the center of the mass of the implanted fiducials as estimated from each pair of stereoscopic images during treatment, thus providing a valuable set of data for us to better understand the intrafractional movement of the prostate. In this study, we analyze 4439 time stamps recorded by CyberKnife for 21 prostate patients. In addition to the technical difference in monitoring the implanted fiducials, a major feature here is that the time span of tumor motion monitoring is significantly longer as compared to the Calypso data (2000 s for current study vs 600 s for Calypso tracking). The study sheds useful insight into the feature of intra-fractional prostate motion and re-emphasizes the need for an effective means of compensating the intra-fractional prostate movement to ensure adequate dose coverage of the tumor target.

MATERIALS AND METHODS

Accuray CyberKnife can track using 4 modes: 6D skull tracking for brain, X-sight tracking for spine, fiducial tracking for extracranial (such as prostate and lung), and Synchrony to account for respiratory motion. Fiducials must be rigidly fixed no more than 5 - 6 cm relative to a known reference or relative to the tumor. Any fiducial migration will degrade the accuracy of fiducial based targeting. Commonly, three fiducials are used for prostate cancer treatment. They are 5.0 mm gold seeds, at least 2 - 3 cm apart from each other to minimize uncertainty in measuring rotations.

The patient setup and treatment delivery process is illustrated in Fig. 1. First, x-ray images are acquired before treatment. The system determines the absolute position of the target volume via image-to-DRR (digitally reconstructed radiograph) registration. The three-dimensional translation and rotation deviation of the target from the planned position is calculated. The treatment starts if the computed shift is less than a pre-set threshold. In this case, the incident beam automatically adjusts itself to compensate for the deviation. The CyberKnife system can perform up to 10 mm translational correction, 1 degree rotational correction in pitch and roll, and 3 degrees in yaw. However, the larger the deviation, the larger is the uncertainty in the accuracy of the robot correction. Therefore it is recommended that the deviation during treatment be kept to minimum. At Stanford a threshold of 1 mm and 1 degree is normally used. If this threshold is not met, therapist moves the couch and acquires the x-ray images again until the shift is less than the threshold. During the beam delivery, x-ray images are acquired every 3 nodes about 40 s interval. The shift of x-ray images from the planning CT is monitored in real-time.

If the shift is more than the hardware limitation, which is 10 mm, the treatment will be stopped and the couch is moved until the shift is below the limit.

The patients were treated with hypofractionated protocol consisting of five fractions of 6.25 Gy per fraction delivered every other day. Totally 21 prostate cancer patients data who were treated under the protocol from Jan. 10, 2005 to Sep. 10, 2007 are used for the study. The prostate movement is defined as the displacement of the center of mass of the fiducials from the planned position. One fraction can have more than one data set, because during the treatment, if the prostate movement is out of the hardware limitation, the patient is repositioned manually.

RESULTS

Duration of data sets

For the 21 patients, a total of 427 data sets and 4439 time stamps were recorded. For each patient, the duration of each data set is an indicator of the stability of the tumor target position. Figure 2 shows the histogram of the duration of the 427 data sets. The x-axis and y-axis represent the duration and the number of data sets for a given time length, respectively. The time bin size is 200 s and the average duration of the 427 data sets is 697 s. The duration of a data set represents the time for the prostate to move to the limit of 1 cm. Thus the shorter the duration, the more “violent” the prostate moves. The data here suggest that, on average, it takes 697 s for the prostate to move to 1 cm relative to its planned position.

Intra-fractional movement of the prostate target

The movement of the center of mass of the three implanted fiducials is used as a surrogate of prostate movement. This quantity was recorded continuously over time and analyzed for the 427 data sets (on average, 20 data sets per patient). For convenience, a selection of observed motion behaviors are shown in Fig. 3. The x -axis represents the time stamp, and the y -axis is the prostate displacement (mm). The red, green and blue lines represent the movement in superior-inferior (SI), left-right (LR), and anterior-posterior (AP) directions, respectively. The black lines represent the total displacement of the prostate.

Similar to that observed by Kupelian et al (21), the prostate movement patterns vary from stable positioning at baseline (Fig. 3a), continuous drift (Fig. 3b), transient excursion (Fig. 3c), persistent excursion (Fig. 3d), and high-frequency excursions (Fig. 3e). Some patterns are simply too irregular to categorize into any of the above classes (Fig. 3f).

It should be noted that, for a given patient, the above classification of the prostate movement pattern is somewhat arbitrary and it may change from fraction to fraction or even from data set to data set within the same treatment fraction. Figure 4 shows the prostate movement behavior for one of the patients. For this patient, there are five fractions, and each fraction contains two data sets. Data sets 2, 4, 5 are continuous drift; data set 3 is transient excursion; data sets 1, 7, 8 consist of two continuous drifts; data sets 6 and 9 are high-frequency excursions followed by a stable positioning at baseline; and data set 10 shows a continuous drift followed by a stable positioning at baseline. In general, it seems that the prostate motion is random and has no fixed pattern to follow.

A useful way to present the prostate motion data is to show the histogram of the fiducial isocenter movement distance in different directions. As seen in Fig. 5 the prostate is more stable in the LR direction, which is consistent with pelvic and prostate anatomy. A large number of data sets are under 0.5 mm movement in this direction. Generally, the shift distribution in SI direction is similar to that in AP direction, but in the case of AP motion, the prostate tends to move more in posterior direction, presumably due to the rectal and bladder volume changes. This is consistent with the observation that motion of the prostate is oblique in the longitudinal mid-plane of the pelvis and subjects to the effects of bladder and rectal filling (9, 21). The mean shift in each direction, averaged over all patients, was 1.55 ± 1.28 mm, 0.87 ± 1.17 mm, 1.80 ± 1.44 mm in the superior-inferior (SI), lateral (LR), and anterior-posterior (AP) dimensions, respectively. The average shift length is 2.61 ± 1.94 mm. Table 1 summarizes the statistical characterization of the data for each direction and the shift length.

An alternative way to present the data of Fig. 5 is to illustrate the histogram of the prostate position as a function of displacement and time as shown in Fig. 6. Each color represents a specific time segment. It is clear that as the time elapses, the spatial distribution of the prostate becomes more spreaded. From these plots, it is also clear that SI and AP movements are similar, whereas the LR curve is more concentrative.

A rolling average (25) of total movement value was computed in equal time interval stamp to further illustrate the prostate movement tendency. Since the average image acquisition interval is 40 s, according to the Nyquist acquisition theory (26), a time interval of 20 s is used to calculate the rolling average curve. The rolling average window was set to be 120 s. Thus, the average shift at 0 s is a result of shifts from 0 s to

60 s, and the average shift at 100 s represents the contributions from 40 s to 160 s. Since there are not enough data for rolling average calculation at the end of the time duration, the calculation stopped at 1400 s in Fig. 7. The curve in Fig. 7 represents a logarithmic fit of the data. It can also be seen from this figure that the prostate movement increases with time.

Influence of prostate deformation

Prostate deformation is of a practical concern. To a certain extent, the deformation can be characterized by the change of the distance between the implanted fiducials as a function of time. In Fig. 8 the distance of each pair of fiducials relative to its value at the CT simulation stage is plotted for two data sets of one of the patients. The tendencies of the distance change over time for the 3 pairs of fiducials are similar. The maximum distance change for this patient is of the order of 1 mm, indicating that the deformation of prostate is not an issue here. No pronounced deformation was observed for any of other patients.

DISCUSSION

To cope with the uncertainty in prostate patient setup and tumor target localization, commonly used method is to add a population based safety margin to the target and sensitive structures to ensure adequate dose coverage of the target under the uncertainty, which significantly compromises the success of radiation therapy (27). Indeed, many studies have indicated that the margin used for treatment is either too small for a significant fraction of the prostate patients, which seriously underdoses the target

and reduces the chance of curing these patients, or too large for another large fraction of the patients, which may overdose the adjacent sensitive organs such as the rectum and bladder and lead to undesirable clinical complications. Because of the proximity of the prostate to the rectum and bladder, a robust strategy in locating the tumor target are necessary to more accurately target the tumor, so that the radiation dose to the prostate can be escalated to substantially enhance the probability of curing the patients without damaging the sensitive structures. Stereoscopic imaging of implanted metallic fiducials is a useful way to locating the prostate target in nearly real-time fashion. A clinically important question in stereoscopic image guided prostate treatment is what is the optimal imaging frequency that minimizes the patient exposure while not missing any significant residual movement of the prostate during the beam-off interval of the imaging X-ray(28). To better understand the issue, let us examine the movement of the prostate for one of the patients. As shown in Fig. 9(a), during the treatment of the patient, the image pairs are updated every 3 nodes (the minimum sampling rate of the CyberKnife is 30 s). Now suppose that the images are acquired every other time point in the original acquisition schedule, the prostate movement curve would look quite different, as indicated in the dashed one in Fig. 9(a). Figure 9(b) shows another example of the prostate movement captured by two different sampling rates. The peak in the solid curve revealed by a higher sampling rate disappears when the sampling rate is reduced. Given the nature of intra-fractional prostate motion, in order to avoid missing any major prostate movement, it seems necessary to image the patient frequently.

In reality, a few factors may influence the selection of the sampling rate of the X-ray imaging, which include the dose rate, patient specific characteristics, the fractionation

scheme, etc. A tradeoff between imaging frequency and target position accuracy needs to be made. A rule of thumb is that the movement of prostate within the interval of two consecutive images should be less than a pre-specified criterion, say 1 or 2 mm. Due to the randomness of the prostate movement, this decision can only be made based on a statistical basis. The sampling rate should be chosen in such a way that the number of data sets with displacement exceeding a pre-specified motion range should be statistically small. Figure 10 shows a plot of the percentage for the prostate target to move more than 1mm (red), 2mm (green), 3mm (blue), 4mm (light green), 5mm (magenta), ..., at 30 s, 60 s, 90 s, 120 s, This figure is useful in helping us to find out the suitable sampling rate for a pre-specified prostate motion range. For example, if a motion larger than 2mm is permissible for less than 5% of the data sets (in other words, if it is desired to keep 95% of the data sets to have a motion less than 2 mm), from Fig. 10, it is seen that a 30 s sampling duration should be used. If a 60 s duration is used, 7.5% of the data sets will have a motion larger than 2mm. For 90 s and 120 s durations, the percentage having motion greater than 2mm will be increased to 11% and 14%, respectively. For convenience, the percentage of data sets having motion greater than 1mm to 5mm is summarized in table 2 for a few sampling durations of interest.

There are several drawbacks associated with fiducial based image guided prostate radiation therapy. Other than the fact that it involves an invasive procedure of fiducial implantation, the fiducial tracking used in CyberKnife or Calypso system is limited to “rigid” tumors. While our data indicated that the deformation of the prostate gland during the hypofractionated treatment is negligible and the center of mass of the three implanted fiducials can be used to describe the prostate position, it is important to remind that

locating the prostate is only part of the overall task in prostate radiation therapy. In reality, tracking the motion of various involved sensitive structures represents the other side of the “coin” and is also of critical importance to the success of IGRT. After all, it is the adjacent sensitive structures that limit the dose deliverable to the target. Therefore, knowing the spatial location and geometric shapes of the sensitive structures is critical for us to customize the dose distribution to maximize the dose to the target while sparing the adjacent sensitive structures. On a fundamental level, the motion of prostate target is often caused by the motion or physiological change of the sensitive structures.

This study and most of previous, if not all, studies are focused on the prostate-only treatment. Clinically, the treatment of intermediate and advanced stage prostate cancer often involves the irradiation of seminal vesicle and regional lymph nodes. The implanted fiducials in these cases are less helpful in locating the seminal vesicle nodes. Better imaging method capable of providing 3D anatomy is highly desirable. On-board cone beam CT (CBCT) has recently become available to provide volumetric information of a patient in the treatment position(29), and holds promises for improved target localization and irradiation dose verification(30). CBCT is valuable in providing 3D or even 4D patient model before treatment and affords a useful solution to reduce the adverse effect of inter-fraction organ motion(17, 28, 31-34). However, acquiring real time patient geometry information during the radiation delivery process using an on-board imaging device is still improbable. A combined use of pre-treatment patient geometric model derived from 3D/4D CBCT and real-time stereoscopic X-ray projection data may be useful to estimate the location of target and adjacent sensitive structures. This investigation is still in progress and will be reported in the future.

CONCLUSION

Intra-fractional organ motion has long been recognized as one of the major limiting factors of prostate dose escalation in conformal radiation therapy. A detailed knowledge of prostate motion would help to understand the nature and degree of the adverse influence of the uncertainty and provide guidance in dealing with the issue. In this work, we have studied the intra-fractional prostate motion in the hypofractionated CyberKnife treatments of 21 prostate cancer patients. The study emphasizes the importance of real-time imaging during prostate radiation therapy, in particularly a hypofractionated treatment. Given the magnitude and random nature of prostate motion as well as the recent technical advancements in various related fields, real-time monitoring of prostate position to adaptively compensate the motion should be part of future prostate radiation therapy to ensure adequate dose coverage of the prostate target while maintaining an adequate sparing of the sensitive structures.

ACKNOWLEDGEMENT

This work was supported in part by grants from the Department of Defense (PC040282) and National Cancer Institute (1R01 CA98523 and CA104205).

REFERENCES

1. Alan M. Nichol, Kristy K. Brock, Gina A. Lockwood, *et al.* A Magnetic Resonance Imaging Study of Prostate Deformation Relative to Implanted Gold Fiducial Markers. *Int J Radiat Oncol Biol Phys* 2007;67:48-56.
2. Zietman AL, DeSilvio M, JD S. Comparison of conventional-dose vs high-dose conformal radiation therapy in clinically localized adenocarcinoma of the prostate: A randomized controlled trial. *JAMA* 2005;294:1233–1239.
3. Pollack A, Zagars GK, G S. Prostate cancer radiation dose response: Results of the M. D. Anderson phase III randomized trial. *Int J Radiat Oncol Biol Phys* 2002;53:1097–1105.
4. Christopher R. King, Joerg Lehmann, John R. Adler, *et al.* CyberKnife Radiotherapy for Localized Prostate Cancer: Rationale and Technical Feasibility. *Technology in Cancer Research & Treatment* 2003;2:25-29.
5. Van den Heuvel F, Powell T, Seppi E , *et al.* Independent verification of ultrasound based image-guided radiation treatment, using electronic portal imaging and implanted gold markers. *Med Phys.* 2003;30:2878-2887.
6. Chen J, Lee RJ , Handrahan D , *et al.* Intensity-modulated radiotherapy using implanted fiducial markers with daily portal imaging: assessment of prostate organ motion. *Int J Radiat Oncol Biol Phys.* 2007;68:912-919.
7. Langen K, Jones DT. Organ motion and its management. *Int. J. Radiation Oncology Biol. Phys.* 2001;50:265–278.
8. Albert Y. C. Fung, Komanduri M. Ayyangar, David Djajaputra, *et al.* Ultrasound-Based Guidance of Intensity-Modulated Radiation Therapy. *Medical Dosimetry* 2006;31:20-29.
9. Anurag Chandra, Lei Dong, Eugene Huang, *et al.* Experience of Ultrasound-Based Daily Prostate Localization. *Int. J. Radiation Oncology Biol. Phys.* 2003;56:436–447.
10. Langen K, Pouliot J, Anezinos C. Evaluation of ultrasound-based prostate localization for image-guided radiotherapy. *Int J Radiat Oncol Biol Phys* 2003;57:635- 644.
11. Langen KM, Meeks SL, Poole DO, *et al.* The use of megavoltage CT (MVCT) images for dose recomputations. *Phys Med Biol* 2005;50:4259-4276.
12. Meeks S, Harmon JJ, Langen K, *et al.* Performance characterization of megavoltage computed tomography imaging on a helical tomotherapy unit. *Medical Physics* 2005;32:2673-2681.
13. Pouliot J, Bani-Hashemi A, Chen J, *et al.* Low-dose megavoltage cone-beam CT for radiation therapy. *Int J Radiat Oncol Biol Phys* 2005;61:552-560.
14. Litzenberg DW, Balter JM, Lam KL, *et al.* Retrospective analysis of prostate cancer patients with implanted gold markers using off-line and adaptive therapy protocols. *Int J Radiat Oncol Biol Phys* 2005;63:123-133.
15. Balter JM, Lam KL, McGinn CJ, *et al.* Improvement of CT-based treatment-planning models of abdominal targets using static exhale imaging. *Int J Radiat Oncol Biol Phys* 1998;41:939-943.

16. Wong JR, Grimm L, Uematsu M, *et al.* Image-guided radiotherapy for prostate cancer by CT–linear accelerator combination: Prostate movements and dosimetric considerations. *Int. J. Radiation Oncology Biol. Phys.* 2005;61:561–569.
17. Per Rugaard Poulsen, Ludvig Paul Muren, Høyer M. Residual set-up errors and margins in on-line image-guided prostate localization in radiotherapy. *Radiation and Oncology* 2007;accepted.
18. Poulsen P HH, Hoyer M. Accuracy of prostate localization using implanted gold markers and Varian's On-Board Imager system *Radiotherapy and Oncology* 2006;81:S145-S146.
19. Elstram UV PJ, Poulsen P, *et al.* Feasibility of adaptive image-guided IMRT for head and neck cancer using cone-beam CT obtained at the treatment couch *Radiotherapy and Oncology* 2006;81:S219.
20. Balter JM, Wright JN, Newell LJ, *et al.* Accuracy of a wireless localization system for radiotherapy. *Int J Radiat Oncol Biol Phys* 2005;61:933-937.
21. Kupelian P, Willoughby T, Mahadevan A, *et al.* Multi-institutional clinical experience with the Calypso System in localization and continuous, real-time monitoring of the prostate gland during external radiotherapy. *Int. J. Radiation Oncology Biol. Phys.* 2007;67:1088-1098.
22. Willoughby T, Kupelian P, Pouliot J, *et al.* Target localization and real-time tracking using the calypso 4D localization system in patients with localized prostate cancer. *Int. J. Radiation Oncology Biol. Phys.* 2006;65:528-534.
23. Dieterich S. Dynamic Tracking of Moving Tumors in Stereotactic Radiosurgery. In: Mould RF, editor. *Robotic Radiosurgery*. Vol 1. pp. 51-63.
24. Sonja Dieterich YS. Tumor Motion Ranges Due to Respiration and Respiratory Motion Characteristics. In: Harold C. Urschel JJK, James D. Luketich, Lech Papiez, Robert D. Timmerman, editor. *Treating Tumors that Move with Respiration*; 2007. pp. 1-13.
25. Riley JD. Evaluation of travel time estimates derived from automatic vehicle identification tags. Department of Civil Engineering: Virginia Polytechnic Institute; 1999. pp. 98-102.
26. Jones NB, Watson M. *Digital Signal Processing: Principles, Devices, and Applications*: IET.1990.
27. Rasch C, Steenbakkers R, Herk Mv. Target Definition in Prostate, Head, and Neck. *Seminars in Radiation Oncology* 2005;5:136-145.
28. Xing L, Thorndyke B, Schreiber E, *et al.* Overview of image-guided radiation therapy. *Med Dosim* 2006;31:91-112.
29. Jaffray DA, Siewerdsen JH, Wong JW, *et al.* Flat-panel cone-beam computed tomography for image-guided radiation therapy. *Int J Radiat Oncol Biol Phys* 2002;53:1337-1349.
30. Yang Y, Schreiber E, Li T, *et al.* Evaluation of on-board kV cone beam CT (CBCT)-based dose calculation. *Phys Med Biol* 2007;52:685-705.
31. Li T, Koong A, Xing L. Enhanced 4D cone-beam CT with inter-phase motion model. *Med Phys* 2007;34:3688-3695.
32. Li T, Schreiber E, Yang Y, *et al.* Motion correction for improved target localization with on-board cone-beam computed tomography. *Phys Med Biol* 2006;51:253-267.

33. Sonke JJ, Zijp L, Remeijer P, *et al.* Respiratory correlated cone beam CT. *Med Phys* 2005;32:1176-1186.
34. Li T, Xing L. Optimizing 4D cone-beam CT acquisition protocol for external beam radiotherapy. *Int J Radiat Oncol Biol Phys* 2007;67:1211-1219.

FIGURE CAPTIONS

Figure 1 Flowchart of the CyberKnife treatment process.

Figure 2 Histogram of the time span of the studied data sets.

Figure 3 Patterns of prostate movement: (a) continuous drift, (b) transient excursion, (c) stable target at baseline, (d) persistent excursion, (e) high-frequency excursions, (f) irregular. (red: SI direction; green: LR direction; blue: AP direction; black: length).

Figure 4 Prostate movement behaviors for one of the patients at different time points.

Figure 5 Histogram of the fiducial isocenter movement distance in different directions.

Figure 6 Histogram of the prostate movement as a function of displacement and time

Figure 7 Rolling average of prostate movement data.

Figure 8 Distances between three pairs of implanted fiducials as a function of time for one of the treatment session of a patient.

Figure 9 Prostate movement behaviors depicted by stereoscopic imaging of two different image frequencies for two patients.

Figure 10 A plot of the percentage of data sets for the prostate target to move more than 1mm (red), 2mm (green), 3mm (blue), 4mm (light green), 5mm (magenta), ..., for sampling durations of 30 s, 60 s, 90 s, 120 s,

Figure 11 Average time duration against displacement threshold.

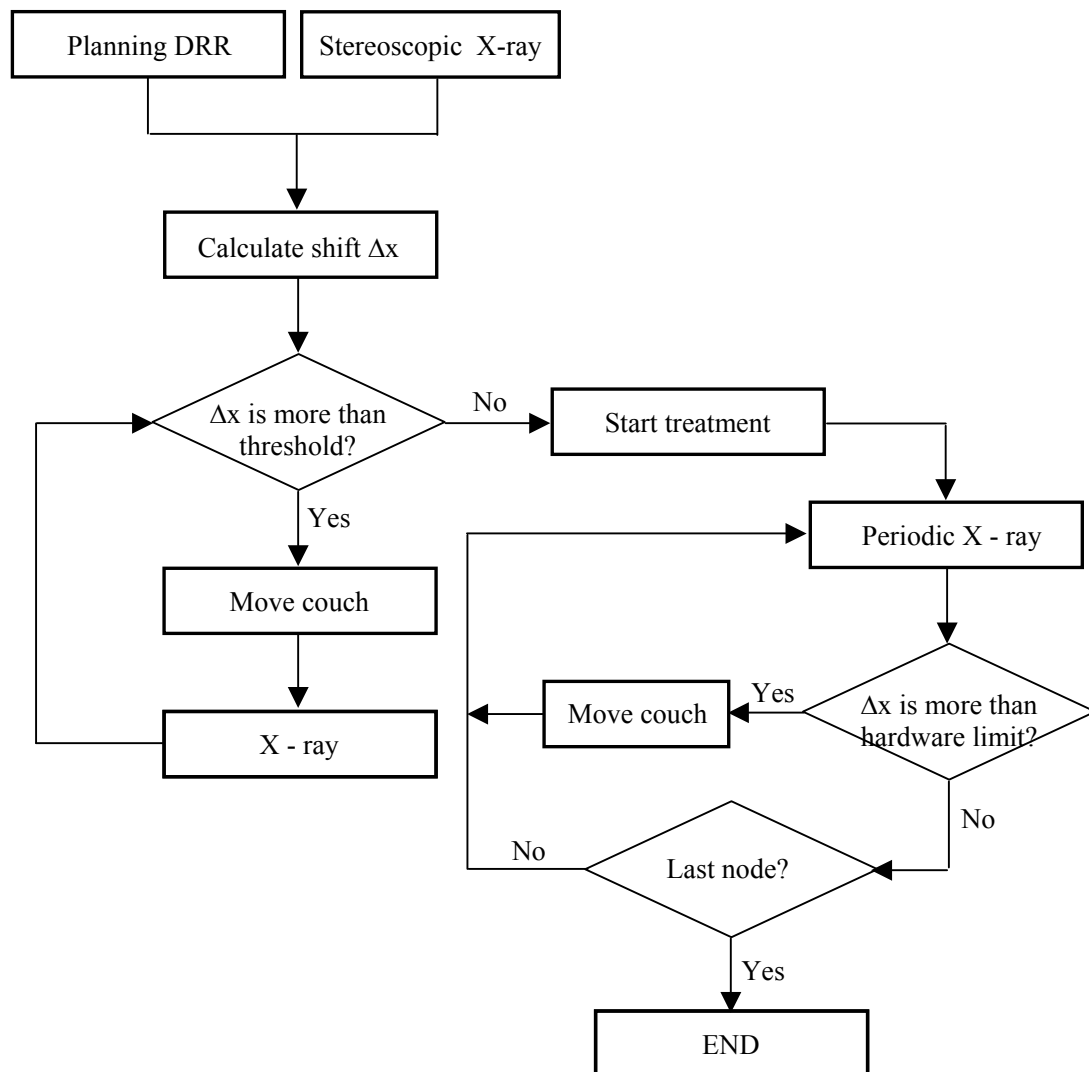


Figure 1

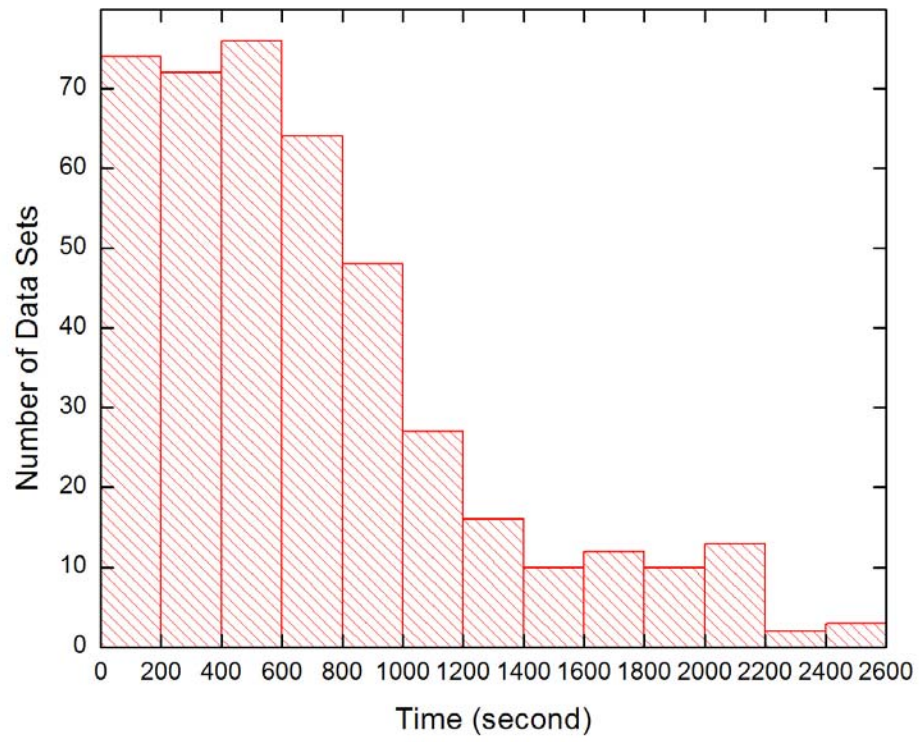


Figure 2

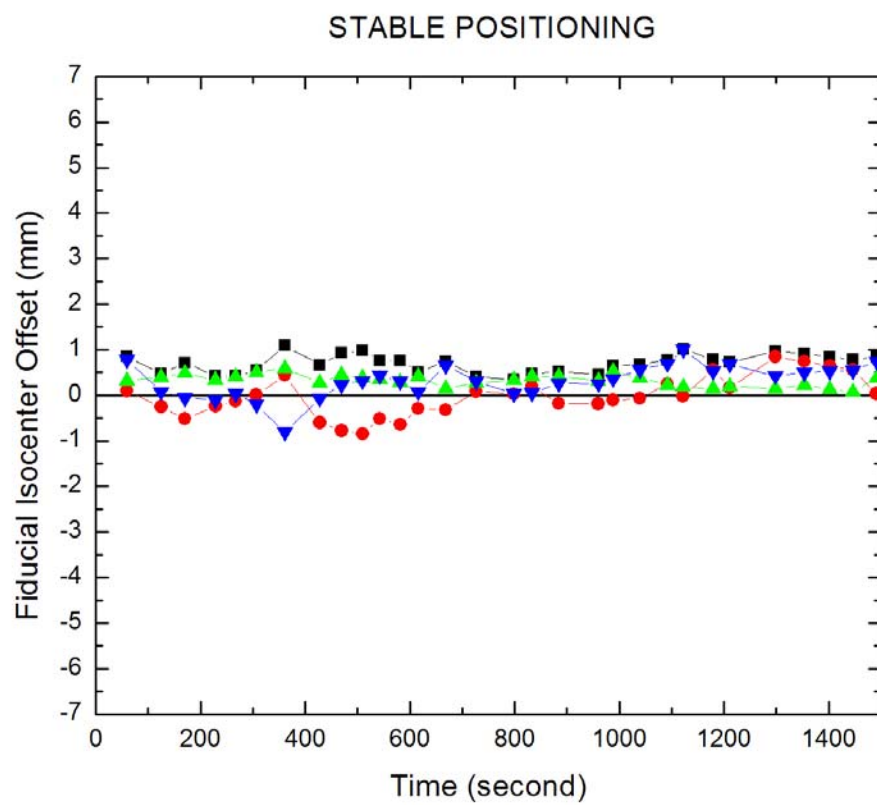


Figure 3(a)

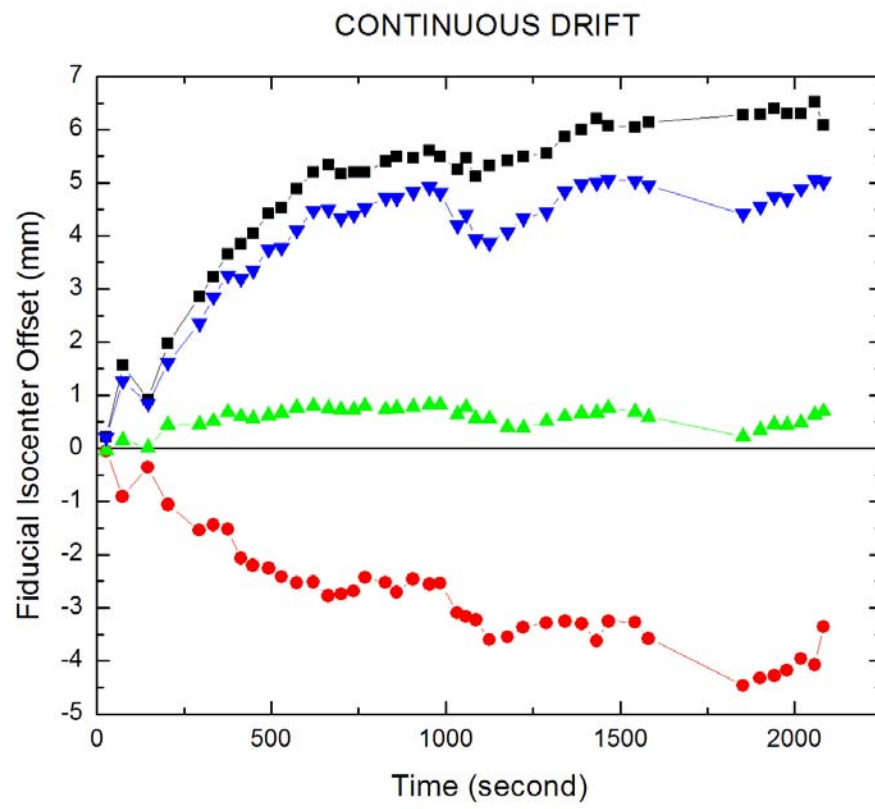


Figure 3(b)

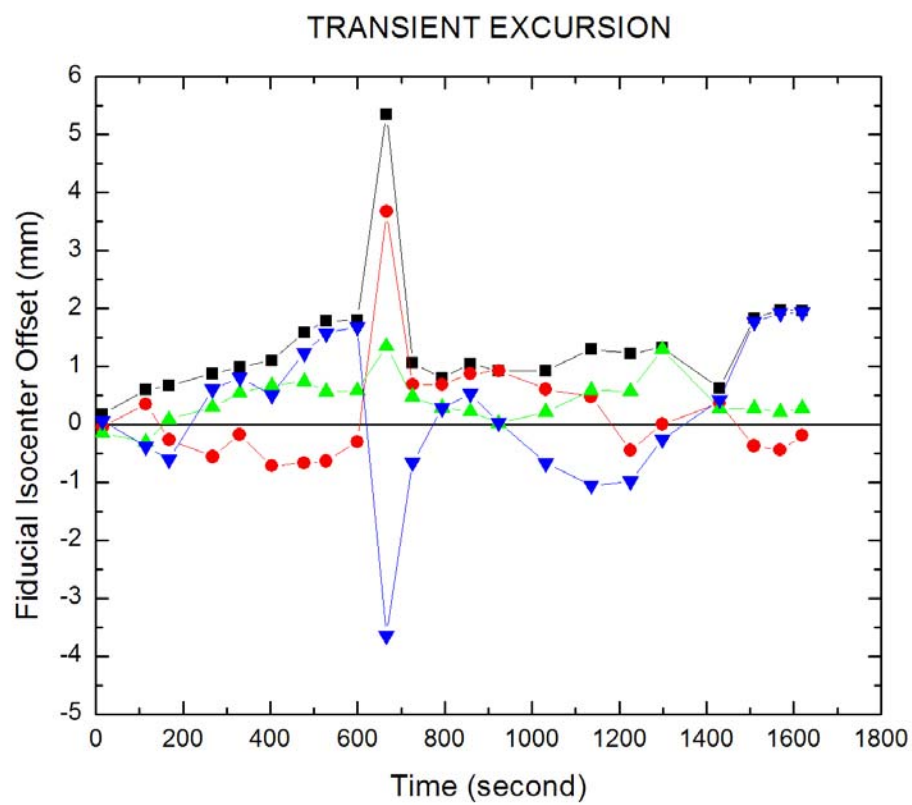


Figure 3(c)

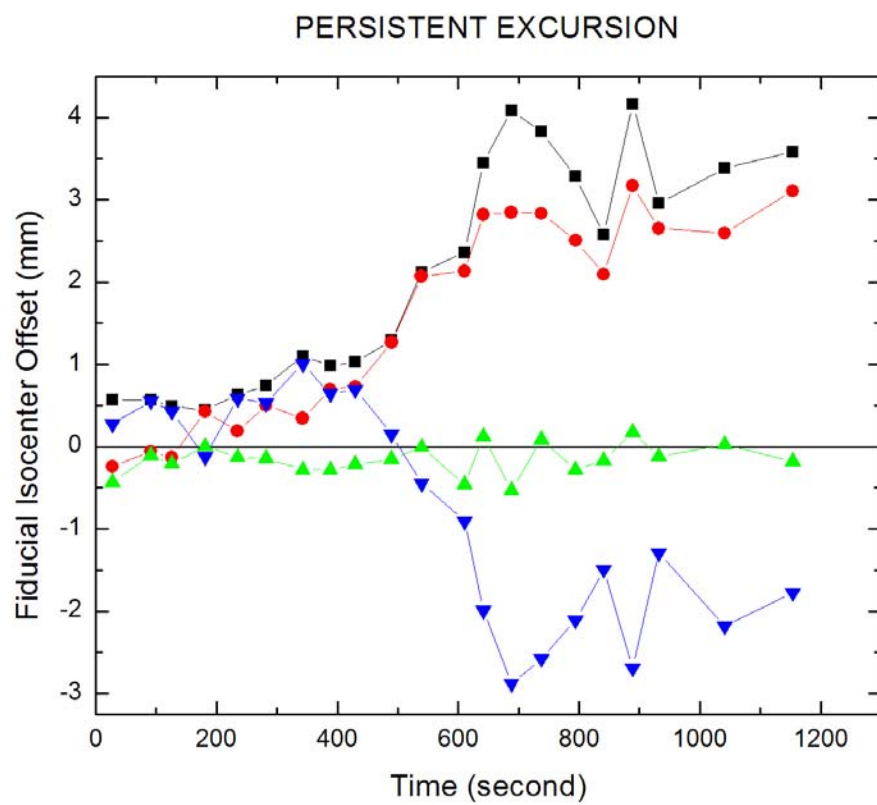


Figure 3(d)

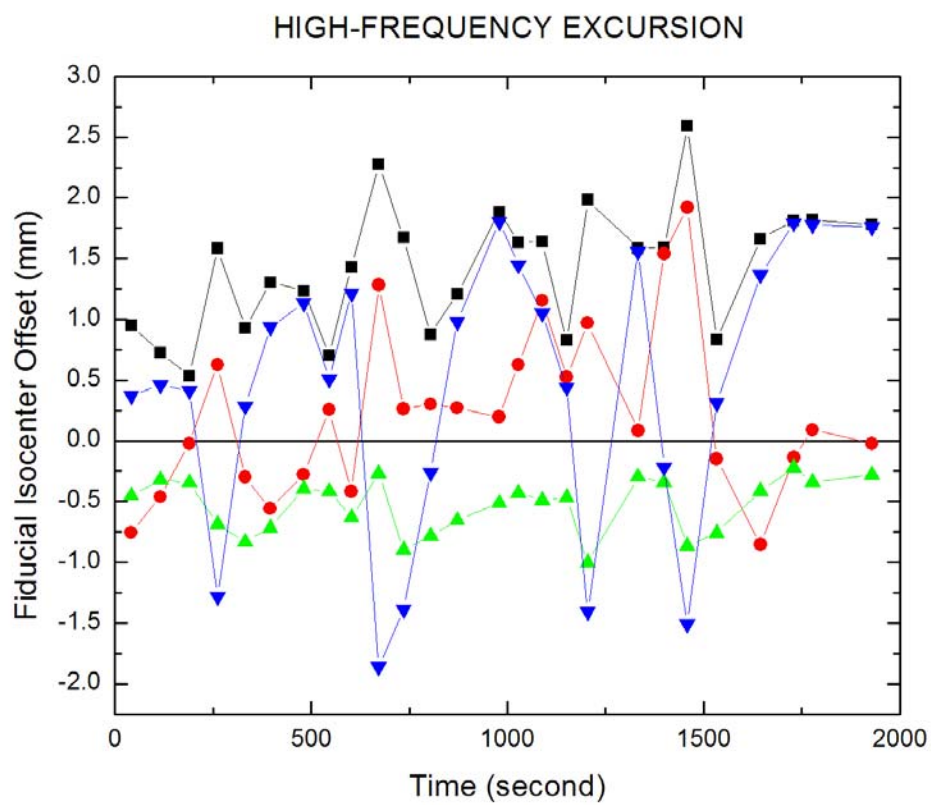


Figure 3(e)

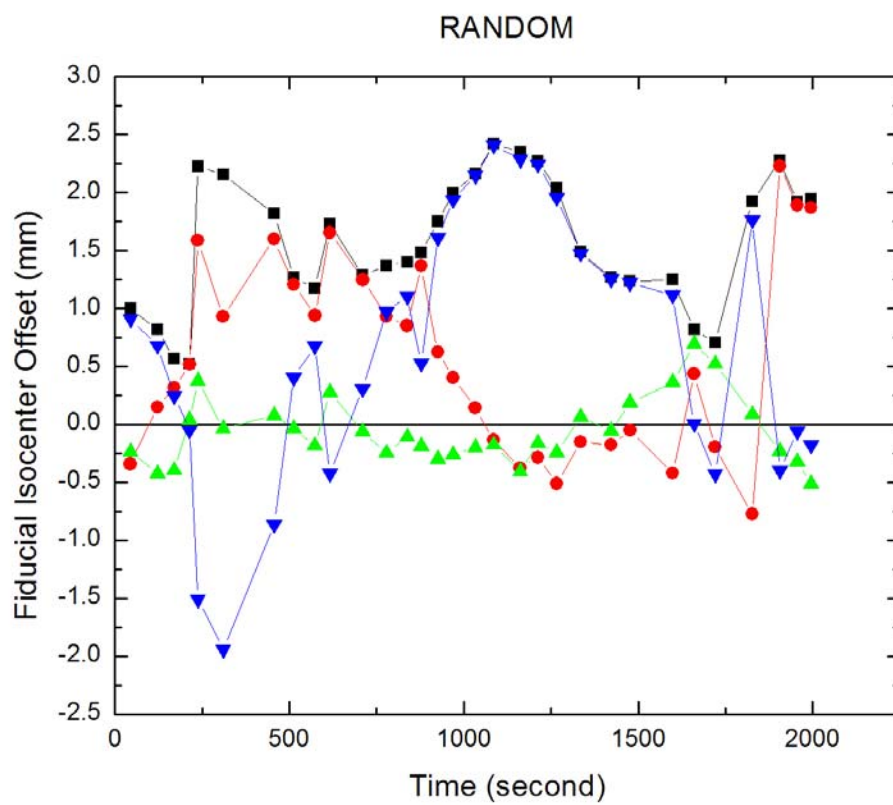


Figure 3(f)

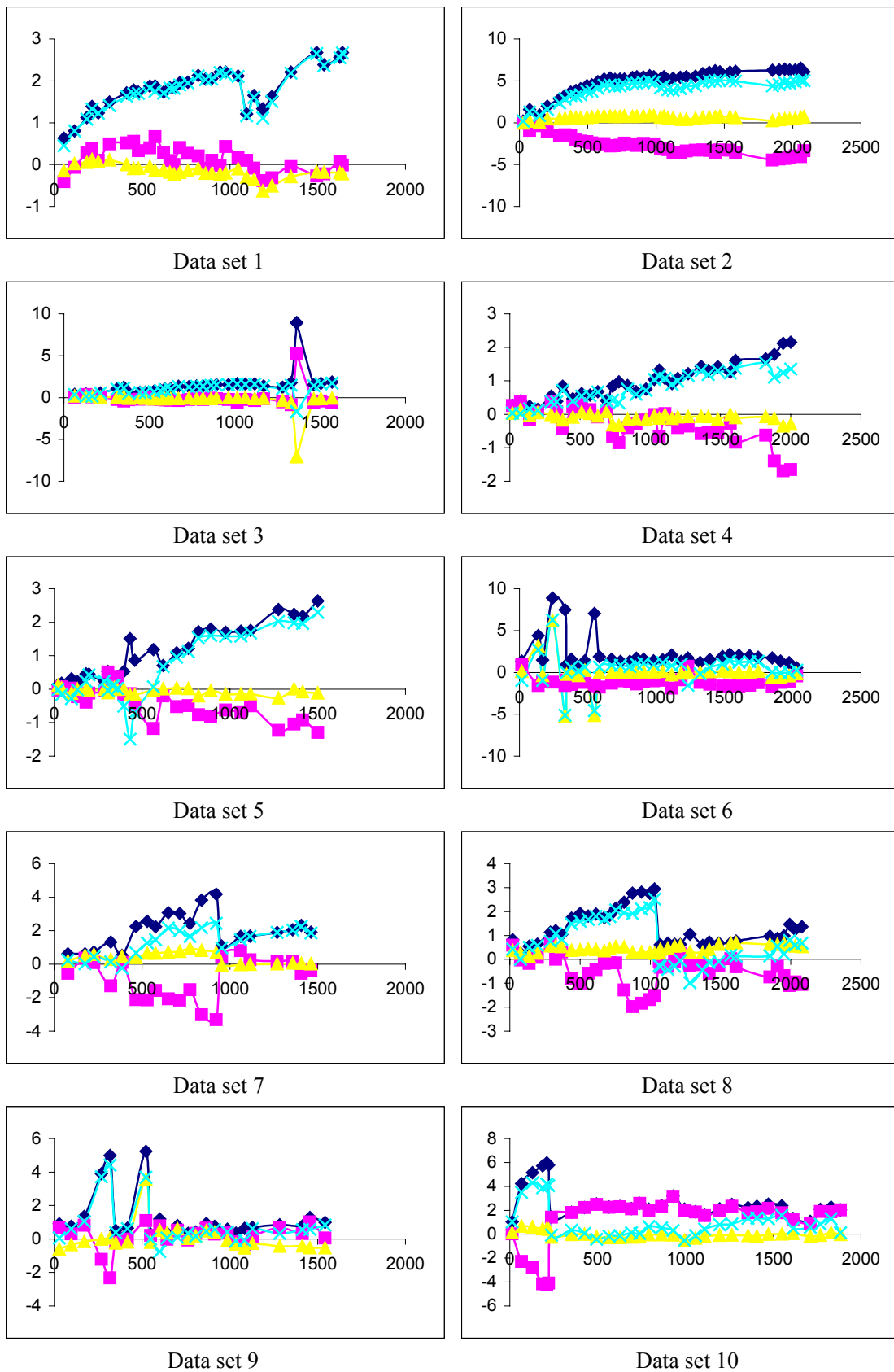


Figure 4

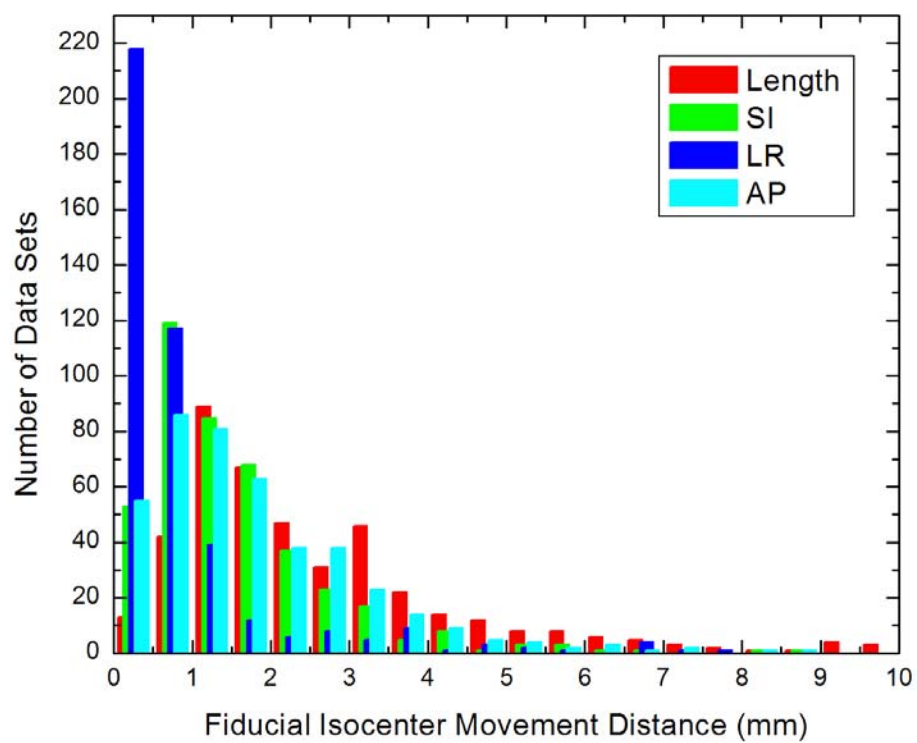


Figure 5

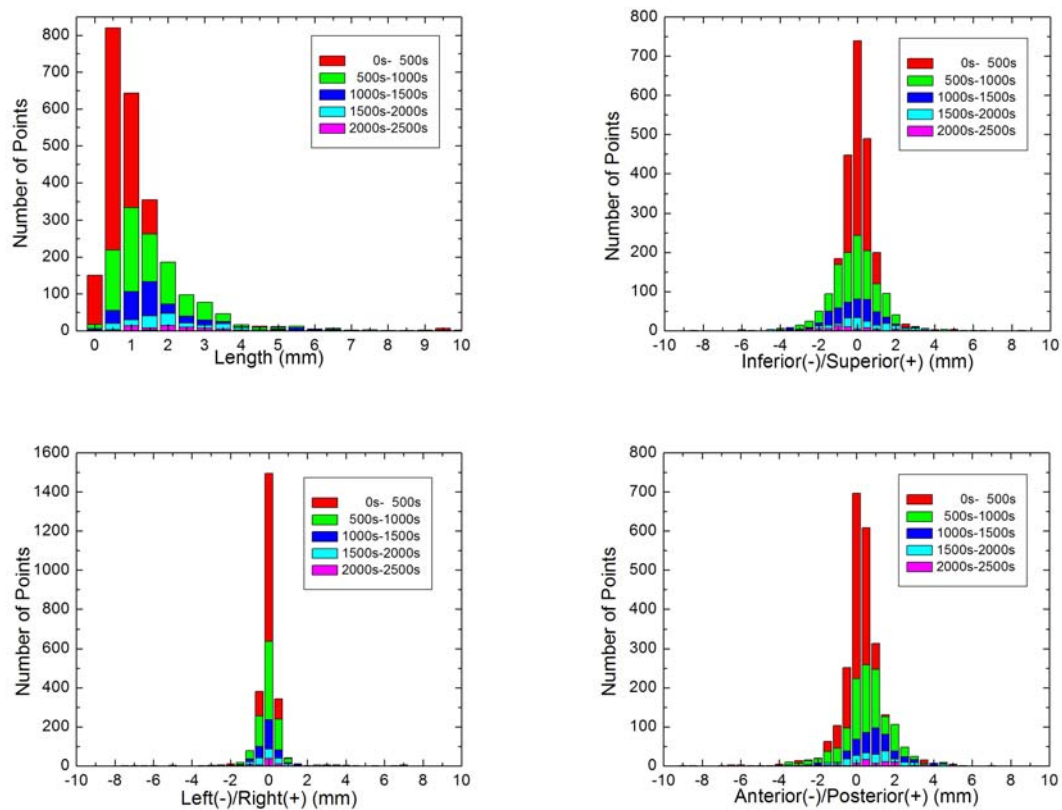


Figure 6

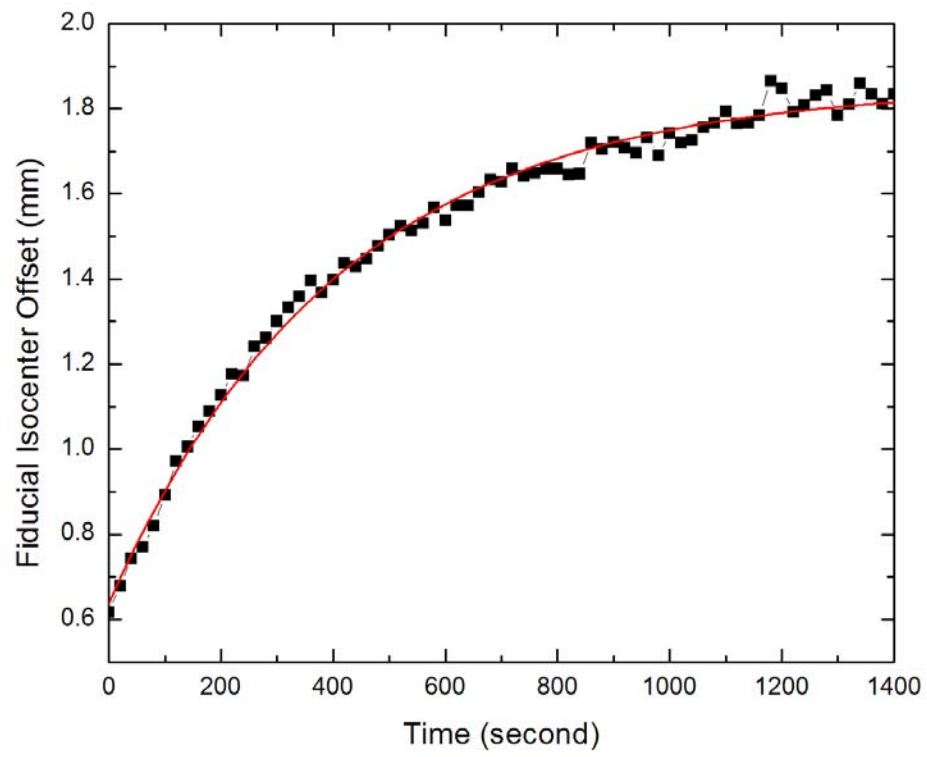
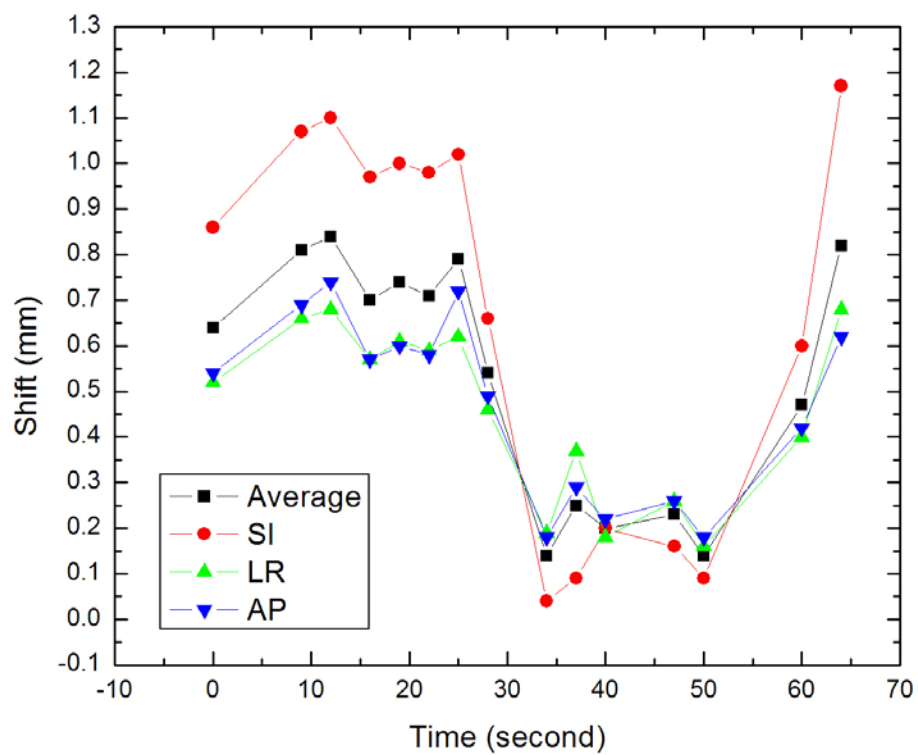
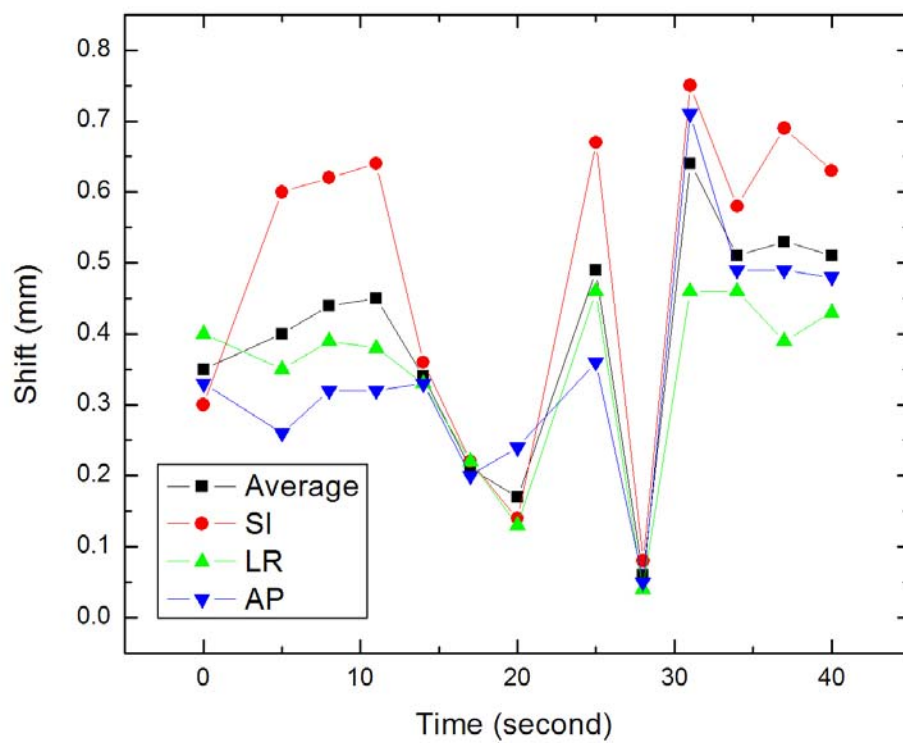


Figure 7

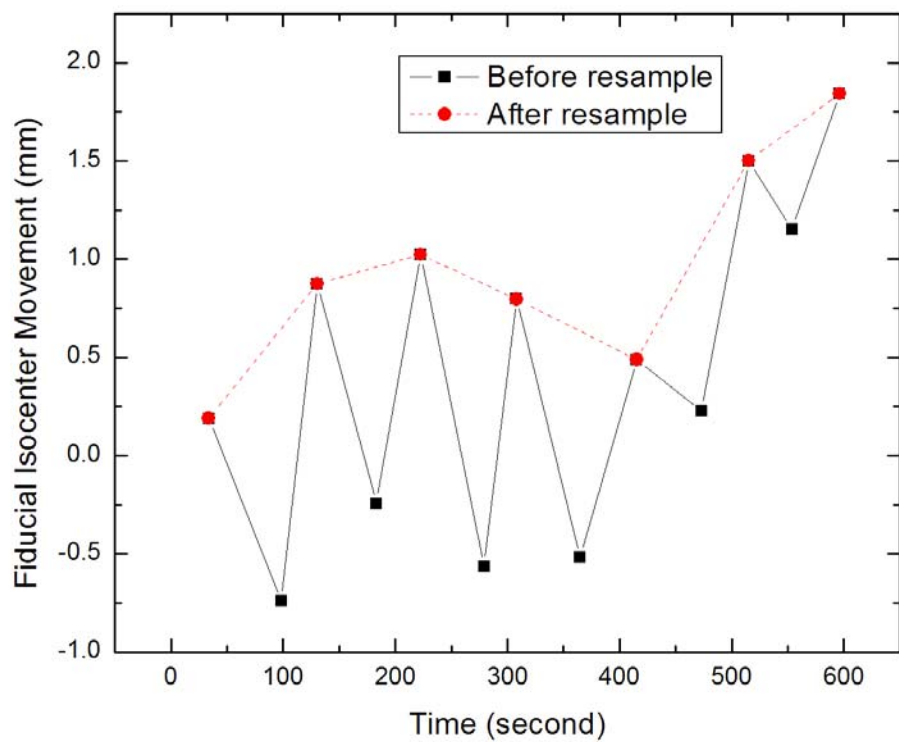


(a)

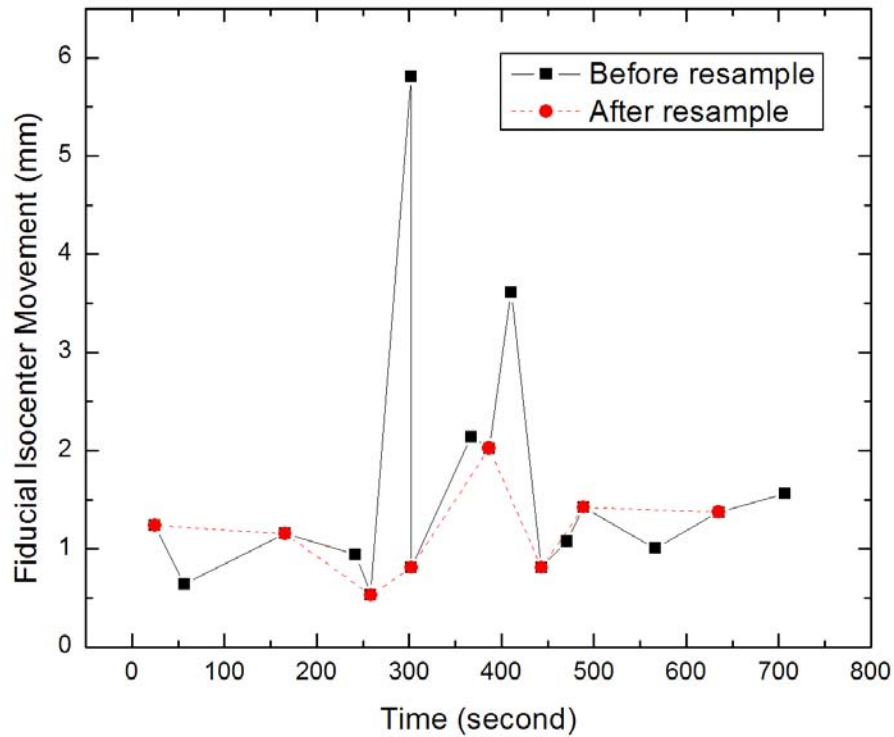


(b)

Figure 8



(a)



(b)

Figure 9

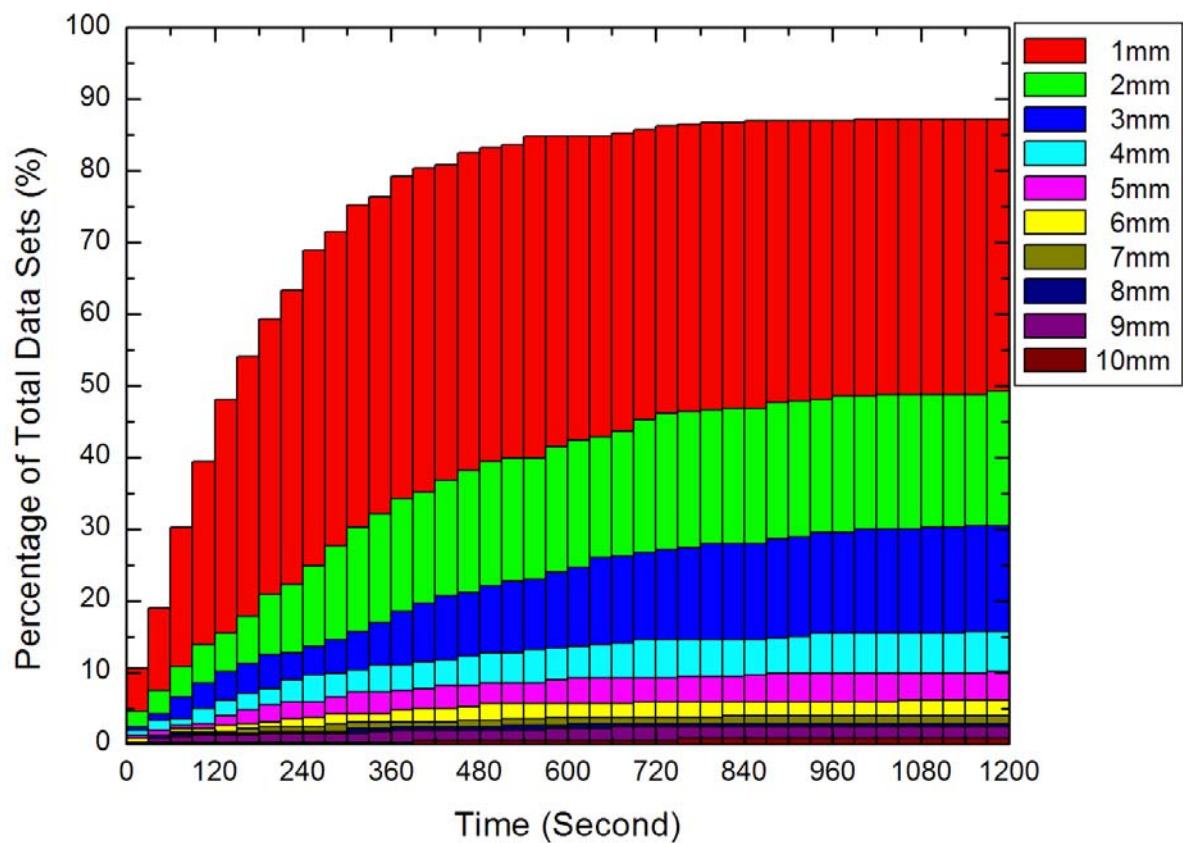


Figure 10

Table. 1 Statistical characterization of the 427 data sets for each direction and the total value of prostate movement

	SI	LR	AP	Length
Average (mm)	1.55	0.87	1.80	2.61
SD (mm)	1.28	1.17	1.44	1.94

Table 2 the percentage of data sets having motion greater than 1mm to 5mm for a few sampling durations of interest.

	1mm	2mm	3mm	4mm	5mm
30s	10.5	4.4	2.3	1.9	1.2
60s	19.0	7.5	4.2	3.2	1.9
90s	30.2	10.8	6.6	3.5	2.6
120s	39.3	13.8	8.4	4.9	2.8

Table 3 Average time duration for different displacement threshold and the number of data sets to account

	1	2	3	4	5	6	7	8	9	10
Average Time(s)	179	350	428	344	313	330	233	202	226	303
Number	372	216	138	70	44	28	17	12	10	3

Feature-Based Rectal Contour Propagation from Planning CT to Cone Beam CT for Adaptive Radiotherapy



Yaoqin Xie Ph.D., Ming Chao Ph.D., Percy Lee MD., and Lei Xing Ph.D.*

* Author to whom correspondence should be addressed.

Stanford University School of Medicine

Department of Radiation Oncology

875 Blake Wilbur Drive

Stanford, CA 94305-5847

E-mail: lei@reyes.stanford.edu

Phone: (650) 498-7896

Fax: (650) 498-4015

ABSTRACT

Purpose: The purpose of this work is to develop a novel registration strategy to automatically map the rectal contours from planning CT (pCT) to cone beam CT (CBCT) for adaptive radiotherapy.

Methods and Materials: The rectal contours were manually delineated in the pCT. A narrow band with the delineated contours as its interior surface was then constructed. The correspondence contours in the CBCT was found by using a feature-based registration algorithm, which consists of two steps: (1) automatically searching for control points in the pCT and CBCT based on the feature of the surrounding tissue and matching the homologous control points using the Scale Invariance Feature Transformation (SIFT); (2) using the control points for a Thin Plate Spline (TPS) transformation to warp the narrow band and finding the corresponding contours from pCT to CBCT.

Results: A robust rectal contour propagation method has been developed. It was able to correctly identify sufficient number of homologous control points in the two input images and enabled accurate warping of the narrow band. Digital phantom study indicated that an average accuracy of 1.2 mm is readily achievable. For clinical cases, the method also yielded satisfactory results even when there were significant rectal content changes between the pCT and CBCT scans.

Conclusion: Exclusion of the volume inside the rectum and efficient detection of image features are two key factors for successful rectal contour mapping. The proposed

technique provides a powerful tool for adaptive radiotherapy of prostate, rectal and gynecological cancers in the future.

Key words: Image-guided radiotherapy (IGRT) ; Adaptive radiotherapy ; Deformable registration ; Contour mapping ; Scale Invariance Feature Transformation (SIFT).

INTRODUCTION

Patients treated with radiotherapy for cancers such as prostate, rectal, and gynecological cancers experience significant day-to-day changes in their rectal volumes due to motion, distention, and filling. Due to variations in the image content, an exact correspondence between two image sets acquired at different time points may not exist. Thus any deformable model relying on the use of information contained in the entire image may not be adequate in dealing with these patients. The artifacts-induced disjoint between the images also makes the auto-propagation of contours outlined in one set of images to another highly difficult with conventional strategies. With continued enthusiasm for adaptive radiotherapy, the ability to reliably and efficiently map the rectum outlined in the pCT to the on-treatment CBCT images now becomes a bottleneck and needs to be resolved in order for many patients with cancer within the pelvis to benefit from the novel adaptive re-planning strategy (1, 2).

The issue of rectal motion and deformation in conformal radiation therapy is described in various publications. Lee et al (3) evaluated the CBCT as a tool to quantify the accuracy and precision of a simulated IMRT treatment delivery model for rectal cancer when rectal motion due to filling and deformation was taken into account. The mean deformation variation of 0.71 and 0.94 cm in the LAT and AP directions was reported. Foskey et al (4) shrank the rectal gas region to a virtual point in order to make the correspondence of the rectal volumes in two sets of images. Similar to that reported by Schreibmann et al (5), Gao et al (6) used an automatic image intensity modification procedure to create artificial gas pockets in the pCT images. The major drawbacks of these types of approaches are the artificial introduction of image features within the rectal

volume and the potentially inaccurate association of the artificial image features. As a consequence, the concordance between the rectal volumes after deformable registration and the manually segmented rectum was found to be less than 80%.

In this work, we propose to use the image information in the neighborhood outside the rectal wall as the driving force to guide the rectal contour propagation from the pCT to CBCT. Because the content in the region outside the rectal wall should be conserved, regardless of any changes in the rectal filling and distension, this strategy seems to be physically sensible. Coupled with a powerful feature-based deformable registration model, which identifies homologous tissue features shared by the pCT and CBCT images, the novel approach captures the key issues of the system and provides a natural solution to the above stated problem. Application of the proposed algorithm to a number of digital phantoms and clinical cases demonstrates that the technique is accurate and robust and may be useful for future adaptive therapy planning.

MATERIALS AND METHOD

Software platform

The proposed contour mapping algorithm was implemented using the Insight Toolkit (7, 8) and the Visualization Toolkit (VTK) (9), which are open source cross-platform C++ software toolkits sponsored by the National Library of Medicine (NLM). They are freely available for research purposes (<http://www.itk.org> for ITK and <http://public.kitware.com/VTK/> for VTK). ITK provides various basic algorithms to perform registration and segmentation for medical images. The programs contained in ITK are highly extendable, making it an ideal platform for development of image

registration and processing techniques. VTK is primarily used for image visualization (including contours).

Narrow band representation of the rectal wall

Inconsistency in rectal contents between two input image sets could severely reduce the performance of a deformable registration algorithm. Co-registering an empty rectum without bowel gas to a rectum filled with bowel gas using any deformable model could be problematic, for example. A natural strategy is to exclude the volume inside the rectal wall. In practice, the template rectal contour in the pCT image has been manually contoured as a part of the routine treatment planning process, thus making it a straightforward matter to exclude the volume inside the rectal wall. Figure 1 shows the proposed contour mapping process. After manual segmentation in the pCT, a narrow band as sketched in Fig. 2 is constructed with the manually segmented rectum representing the inner surface of the band. On an axial slice, the contour has a polygon shape and the vertices of the polygon form the basis for constructing the narrow band. The distance between the neighboring vertices on the contour is typically 2-10 mm depending on the shape of the contour. In generating the narrow band, we first create cubes with side length of d for each vertex, as depicted by points A and B in figure 2b. In order to obtain a smooth band, between A and B three more cubes, cornered at points C , D , and E , are inserted. Point C is chosen to be the middle point between A and B . Point D is the point between A and C , and point E is the point between B and C . More interpolated vertex points can be similarly introduced when needed. The blue area in Fig. 2a stands for the narrow band.

The narrow band in our approach is used as a compact representation of the rectal surface. As will be detailed in the next subsection, a feature-based deformable registration algorithm is employed to find the correspondence of the band in the CBCT images. Upon successful registration, the deformation field is utilized to propagate the pCT contour to the CBCT. Because only the image features outside the rectum is used, a narrow band shown in Fig. 2 permits us to take advantage of the regional calculation algorithm yet avoiding the nuisance of rectum/bladder filling.

Feature-based warping of the narrow band

As illustrated in figure 1, the process of contour mapping is to warp the narrow band constructed above in such a way that its best match in the CBCT images is found. Mathematically, this constitutes an optimization problem, in which a group of transformation parameters that transform the points within the band in pCT to their corresponding points in CBCT. The input to the contour mapping software includes the narrow band and the CBCT images, which are described by the image intensity distributions $I_a(\mathbf{x})$ and $I_b(\mathbf{x})$, respectively.

To find the transformation matrix, $T(\mathbf{x})$, that maps an arbitrary point in the band to the corresponding point in the CBCT images (or *vice versa*), a Thin Plate Spline (TPS) deformable model is employed. But other models should also be applicable to model the deformation of the band. Currently, the TPS method still needs manual placement of control points and this work automates the control point selection by using the SIFT tissue feature searching (see next subsection for details). Roughly, 300 control points are selected based on the prominent tissue features.

The detailed description of the TPS transformation can be found in Ref. (10-13). Briefly, a weighting vector $W=(w_1, w_2 \dots w_n)$ and the coefficients a_1, a_u, a_v are computed from a series of matrices which are constructed using n pairs of SIFT-selected control points in the pCT image (x_i, y_i) and in the CBCT image (u_i, v_i) , respectively. The function transforming a voxel in the pCT to a new coordinate in the CBCT is obtained from

$$f(u', v') = a_1 + a_u u + a_v v + \sum_{i=0}^n w_i U(p_i - (u, v)), \quad (1)$$

where p is the matrix of the control points coordinates in the pCT and U is a basis function to measure the distance. Some major steps of the TPS calculation are:

(1) Assuming $P_1 = (x_1, y_1), P_2 = (x_2, y_2), \dots, P_n = (x_n, y_n)$ are the n control points in the pCT images. The distance between point i and j is given by $r_{ij} = |P_i - P_j|$.

Define matrices

$$P = \begin{bmatrix} 1 & x_1 & y_1 \\ 1 & x_2 & y_2 \\ \dots & \dots & \dots \\ 1 & x_n & y_n \end{bmatrix}, \quad (2)$$

$$K = \begin{bmatrix} 0 & U(r_{12}) & \dots & U(r_{1n}) \\ U(r_{21}) & 0 & \dots & U(r_{2n}) \\ \dots & \dots & \dots & \dots \\ U(r_{n1}) & U(r_{n2}) & \dots & 0 \end{bmatrix}, \quad (3)$$

and

$$L = \begin{bmatrix} K & P \\ P^T & O \end{bmatrix}, \quad (4)$$

where O is a 3×3 matrix of zeros and U is a basic function $U(r) = r^2 \log r^2$.

(2) Letting $Q_1 = (u_1, v_1)$, $Q_2 = (u_2, v_2)$, ..., $Q_n = (u_n, v_n)$ be n corresponding control points in the CBCT image. We construct matrices

$$V = \begin{bmatrix} u_1 & u_2 & \cdots & u_n \\ v_1 & v_2 & \cdots & v_n \end{bmatrix}, \quad (5)$$

$$Y = (V \mid 0 \ 0 \ 0)^T. \quad (6)$$

The weighting vector $W = (w_1, w_2, \dots, w_n)$ and the coefficients a_1 , a_u , and a_v can be computed by the equation

$$L^{-1}Y = (W \mid a_1 \ a_u \ a_v)^T. \quad (7)$$

(3) Using the elements of $L^{-1}Y$ to define a function $f(u', v')$ everywhere as given in Eq. (1). This function transforms a voxel in the pCT volume to a new coordinate in the CBCT image. Upon successful registration, the deformation field is extracted and utilized to transform the manual rectal contours to CBCT.

Scale-Invariant Features Transformation (SIFT)

The feature-based deformable registration is an essential part of the proposed contour mapping process. While the TPS deformable registration is relative simple and doesn't require iterations and intensive calculation for each individual voxel, it relies on the use of homologous control points in the two input image sets to be co-registered. In reality, the interactive identification of the control points in both images is tedious, difficult, and often a source of error. Here we automate the control point selection by using the SIFT-based tissue feature searching. Because of the efficient use of *a priori* system knowledge, the approach greatly enhances the robustness of the narrow band warping algorithm.

The SIFT method was introduced by Lowe (14) to characterize the local tissue features. The method utilizes both image intensity and local gradient information to characterize the neighborhood property of a point. The algorithm includes scale-space extrema detection, control point localization, orientation assignment and control point descriptor. In 2D case, for example, the method uses the orientation histograms of the four quadrants surrounding a point (containing 64 pixels) to characterize the inherent tissue feature of the point (see Fig. 3). To obtain the histogram for a quadrant, as illustrated in Fig. 3, the gradient of each of the 16 pixels in a quadrant is computed. An eight-bin histogram, with first bin representing the number of pixels whose gradients fall between 0° and 45° , and so forth, is then constructed. For illustration, the histogram of each of the four quadrants is displayed schematically in the right panel of Fig. 3 as an eight-vector plot. In total, 32 vectors are calculated in 2D case. In extending the SIFT method from 2D to 3D, total of 192 vectors are needed. These vectors represent the local feature and serve as a signature of the point. The SIFT descriptor is considered as one of the most effective descriptors currently available(15, 16).

Theoretically, the SIFT descriptor can be computed for each voxel in an image. However, this is computationally expensive. The commonly used sampling strategy is to compute the descriptor every 2 to 3 voxels in x , y and z directions. After the SIFT descriptors are computed in both input images, the points having the most similar SIFT descriptors in the two images are then identified. For a given point, indexed by n , in the pCT image, the least-squares difference of the SIFT descriptor of the point and that of a potential association point n' in the CBCT, $S_{n,n'}$, is first computed according to

$$S_{n,n'} = \sqrt{\sum_{\alpha=1}^k |(\nabla I_n)_\alpha - (\nabla I_{n'})_\alpha|^2}, \quad (8)$$

where I represents the pixel intensity. α index the bins of the SIFT histogram of a point and the summation over α runs from 1 to 32 for 2D case, and 192 for 3D case. After $S_{n,n'}$ is computed for all n' in the CBCT, two points n'_1 and n'_2 that have the least histogram difference with point n are identified. If the ratio of these two values is less than 80%, the point that has the lowest S value is chosen tentatively as the correspondence of the point n , otherwise, no association is made for the point. Note that the criterion of 80% here is an empirical value. If the value is too large, the number of false association increases. Conversely, many true associations may be missed. In general, this criterion should be determined on an organ specific basis. For lung, for example, it was found that a criterion of 50% is adequate to find sufficient number of associations.

To further increase the accuracy of control point association, a bi-directional mapping strategy is developed based on the fact that if a point in the pCT is mapped correctly to the CBCT, it will be default to be mapped back to the original control point in the pCT when an inverse map is applied to the corresponding control point in the CBCT. Therefore, after the original association of control points as described above, the mapped points in CBCT is inversely co-registered to the pCT. If the correspondence still exists, the control point pair is labeled a match. Otherwise, they are considered as a mismatch and deleted from the list of correspondence points. Upon the association of the points, the associated points are employed as control points for TPS as described above.

Evaluation of the models using digital phantom and existing patient data

The performance of the above model is evaluated by a number of 2D digital phantoms and archived clinical cases. In the digital phantom experiments, two

deformations are introduced. A virtue of this approach is that the “ground truth” solutions exist and the transformation matrices are known, thus making the evaluation straightforward. The mathematical transformations used to deform the phantom is generated using a formula (17):

$$x'(x, y) = (1 + b \cos m\theta)x \quad (9)$$

$$y'(x, y) = (1 + b \cos m\theta)y \quad (10)$$

Here $\theta = \tan^{-1} \frac{y}{x}$. Two parameters, m and b , are used to characterize a deformation.

Generally, they describe the complexity and magnitude of a deformation, respectively. The contour outlined in the original image is then mapped to the deformed image. The accuracy of the contour mapping calculation is assessed by comparing directly with the contour from the known transformation matrix.

Contour propagation from pCT to CBCT is studied by using a prostate cancer and a rectal cancer case. The pCT is acquired with a GE Discovery-ST CT scanner (GE Medical System, Milwaukee, WI) approximately two weeks prior to the initiation of the radiotherapy. The on-treatment CBCT images are acquired using the Varian TrilogyTM (Varian Medical Systems, Palo Alto, CA). Each slice of pCT or CBCT is discretized into 512×512 pixels. The images are transferred through DICOM to a high-performance personal computer (PC) with a Xeon (3.6 GHz) processor for image processing. The manually outlined contours in the pCT images are mapped to CBCT images using the proposed technique. In general, quantitative validation of a deformable registration algorithm for a clinical case is difficult due to the lack of the ground truth for clinical testing cases. For the cases studied here, visual inspection method is employed to assess the success of the proposed algorithm.

RESULTS

2D digital phantom experiment

The proposed algorithm is first tested using a 2D digital phantom (Fig. 4a) with two intentionally introduced deformations of the image shown in Figs. 4b and 4c, respectively. The rectal contour in pCT is manually delineated and shown in Fig. 4a in red. The deformation shown in Figs. 4b and 4c are obtained by setting the parameters b and c in Eqs. (9) and (10) to $(b = 2, m = 2)$ and $(b = 2, m = 3)$, respectively. The green contours in Figs. 4b and 4c represent the auto-mapped contour. Overall, the mapped contours can capture the main features of the two dramatic deformations, and conform snugly to the boundary of the rectum in both cases.

In obtaining the result shown in Fig. 4b, a total of 200 control points were identified by the bi-directional SIFT calculation as described in method. For clarity, a selection of the SIFT-identified control point associations are displayed in Fig. 5. The total number of control points identified here are far more than that commonly used in TPS calculation (11), allowing an improved deformable warping of the narrow band. The displacement field derived by using the TPS method is shown in Fig. 6a. For comparison, the known displacement field from Eqs. (9) and (10) is plotted in Fig. 6b. The subtraction between the TPS-derived displacement field and the known field is shown in Fig. 6c. It is found that the average deviation of the SIFT-TPS displacement from the known solution is less than 1.2mm.

Clinical case study

The contour propagation study from pCT to CBCT for the prostate case is presented in Fig. 7. The top row shows the pCT image with manually delineated contours (green curves). The auto-mapped contours overlaid in the CBCT are displayed in the bottom row (red curves). As mentioned in the introduction, the propagation of rectum wall is often complicated by the fact that the physical one-to-one correspondence may not exist due to the addition or subtraction of some contents within the rectum. Figure 8 exemplifies this and shows that the rectal filling at the time of CBCT acquisition is quite different from that of pCT. As can be intuitively conceived, this image content change could severely reduce the performance of a conventional deformable registration(18-20). The narrow band approach described in this work circumvents the problem by excluding the rectal volume affected by the rectum/bladder filling. As a result in Fig. 7, the mapped contours closely conform to the rectal wall change and the final contours are clearly clinically sensible.

In practice, rectal volume motion and deformation can cause significant uncertainties pertaining to the adequacy of actual dose delivered to the gross tumor volume (GTV) as well as to the surrounding normal structures. This issue has been a major obstacle in the implementation of IMRT in rectal cancer. In Fig. 8 the three axial pCT and CBCT images of a rectal cancer patient acquired in an interval of two weeks are shown. Significant target volume motion and deformation are observed from Fig. 8. The rectal volume in the pCT is found to be more than 3 times that of the rectal volume in the CBCT and thus represents a challenging situation for any deformable model. The rectal contours are manually drawn in the pCT and mapped to the subsequent CBCT using the

proposed method. The upper row of Fig. 8 shows three axial slices of the pCT with manually delineated contours (green curves). The results of contour propagation from the pCT to the CBCT are shown in the lower row of Fig. 8 (red curves).

DISCUSSION

In this work, an effective feature-based rectal contour mapping algorithm has been described. An indispensable step toward online or offline adaptive re-planning with consideration of the patient’s dose delivery history and on-treatment anatomy is the expedite organ segmentation of CBCT images (7, 21-25). While this task is, in principle, achievable using deformable registration of the pCT and CBCT images, the accuracy of the registration and therefore the contour mapping, is often adversely affected by the presence of image contents in one image that do not have correspondence in the other image. The propagation of rectum wall is an example of this. For prostate, rectal, or gynecological cancer patients for example, the presence and absence of bowel gas can vary daily. Co-registering an empty rectum without bowel gas to a rectum filled with bowel gas (or vice versa) using any deformable model could be problematic and large errors could occur.

We describe a regional contour propagation algorithm taking into account possible organ deformation and anatomic changes. Because the narrow band contains only the image features outside the rectum, this method is not affected by the rectum filling changes. The proposed approach relies on the assumption that a narrow band surrounding the manually segmented rectal contour can capture sufficient information to drive the finding of its counterpart in the subsequent CBCT. Obviously, this assumption

is valid when the band is sufficiently wide so that enough image features are involved in the warping calculation.

The use of SIFT descriptor enhances our ability to find the correspondence of the narrow band because of the effective utilization of image intensity and gradient information. In contrast to the conventional intensity-based image registration, which only uses intensity information of the voxels, the feature-based registration extracts information regarding image structure, including shape, texture, etc. Therefore, the feature-based image registration is generally more effective in correctly identifying corresponding voxels compared to the intensity-based image registration.

The proposed contour mapping technique is applied to digital phantoms and clinical cases and, in all cases, the contour mapping results are found to be clinically acceptable. It is important to emphasize that in these test cases, the rectal deformations are quite significant and thus present challenges to any deformable model or contour mapping technique. It is impressive that a simple approach with a narrow band and SIFT descriptor can capture the main feature of the rectal contour and help to find the correspondence contours in the CBCT images.

In this study, a bi-directional SIFT descriptor are employed to examine the reliability and robustness of the calculations. The bi-directional mapping further enhances the degree of success of a contour propagation algorithm. It is useful to note that the bi-directional mapping is a necessary (but not sufficient) test. In a rare but possible situation, the bi-directional mapping may not be able to find an error occurred in the contour mapping process. A visual inspection of the mapped result is always helpful in practice.

CONCLUSION

Significant inter-fractional patient setup uncertainty and anatomy changes have been reported in numerous studies, and are widely recognized as one of the major limiting factors for maximum exploitation of modern radiation therapy techniques such as IMRT and IGRT. The advent of onboard volumetric imaging devices promises to improve the situation by providing valuable 3D (or even possibly 4D) geometric data of the patient in the treatment position and allows for the adaptive modification of treatment plan during a course of treatment.

In this work, an effective feature-based rectal contour mapping algorithm has been described. The method yielded satisfactory mapping for both digital phantom and clinical cases. It is impressive that the algorithm is able to successfully map the contours from pCT to CBCT even for some very challenging cases in which the deformation and/or image content change are dramatic. The two salient features of the described algorithm are: (1) the use of inherent tissue feature as *a priori* knowledge for deformable registration; and (2) limiting the ROI to exclude the volume inside the rectum and focusing on the adjacent neighborhood of the rectal contour. The algorithm should be extendable for contour propagation of organs with similar features, such as the bladder and stomach.

ACKNOWLEDGEMENT

This work was supported in part by grants from the Department of Defense (PC040282) and National Cancer Institute (1R01 CA98523 and CA104205).

REFERENCES

1. Xing L, Thorndyke B, Schreibmann E, *et al.* Overview of image-guided radiation therapy. *Med Dosim* 2006;31:91-112.
2. Zerda ADL, Armbruster B, Xing L. Formulating adaptive radiation therapy (ART) treatment planning into a closed-loop control framework. *Phys Med Biol* 2007;52:4137-4153.
3. Lee P, Xing L, Pawlicki T, *et al.* Image-guided radiation therapy (RT) for rectal cancer using cone beam CT (CBCT) [abstract]. *Int J Radiat Oncol Biol Phys* 2006;66 (Suppl. 1):S276-S276.
4. Foskey M, Davis B, Goyal L. Large deformation three-dimensional image registration in image-guided radiation therapy. *Phys Med Biol* 2005;50:5869-5892.
5. Schreibmann E, Xing L. Narrow band deformable registration of prostate magnetic resonance imaging, magnetic resonance spectroscopic imaging, and computed tomography studies. *Int J Radiat Oncol Biol Phys* 2005;62:595-605.
6. Gao S, Zhang L, Wang H, *et al.* A deformable image registration method to handle distended rectums in prostate cancer radiotherapy. *Med Phys* 2006;33:3304-3312.
7. Kass M, Witken A, Terzopoulos D. Snakes: active contour models. *Int J Comput Vis* 1988;4:321-331.
8. Ibanez L, Schroeder W, Ng L. ITK Software Guide: Kitware Inc.; 2003. <http://www.itk.org>.

9. Schroeder W, Martin K, Lorensen B. The Visualization Toolkit: An Objective-Oriented Approach To 3D Graphics. <http://public.kitware.com/VTK/>.
10. Bookstein FL. Principal Warps: Thin Plate Splines and the Decomposition of Deformations. *IEEE Trans. Pattern Anal Mach Intell* 1989;11:567-585.
11. Lian J, Xing L, Hunjan S, *et al*. Mapping of the prostate in endorectal coil-based MRI/MRSI and CT: a deformable registration and validation study. *Med Phys* 2004;31:3087-3094.
12. Fei B, Wheaton A, Lee Z, *et al*. Automatic MR volume registration and its evaluation for the pelvis and prostate. *Phys Med Biol* 2002;2002:823-838.
13. Fei B, Kemper C, Wilson DL. A comparative study of warping and rigid body registration for the prostate and pelvic MR volumes. *Comp Med Imag Graph* 2003;4:267-281.
14. Lowe DG. Object Recognition from Local Scale-Invariant Features. Proc. of the International Conference on Computer Vision. Corfu; 1999.
15. Mikolajczyk K, Schmid C. A Performance Evaluation of Local Descriptors. *IEEE Trans. Pattern Anal Mach Intell* 2005;27:1615~1630.
16. Wu G, Qi F, Shen D. A General Learning Framework for Non-rigid Image Registration. In: Yang G-Z, editor. MIAR. Vol LNCS; 2006. pp. 219-227.
17. Lu W, Chen ML, Olivera GH, *et al*. Fast free-form deformable registration via calculus of variations. *Phys Med Biol* 2004;49:3067-3087.
18. Court LE, Dong L. Automatic registration of the prostate for computed-tomography-guided radiotherapy. *Med Phys* 2003;30:2750-2757.

-
19. Lu W, Olivera G, Chen Q. Automatic re-contouring in 4D radiotherapy. *Phys Med Biol* 2006;51:1077-1099.
 20. Schreibmann E, Chen GT, Xing L. Image interpolation in 4D CT using a BSpline deformable registration model. *Int J Radiat Oncol Biol Phys* 2006;64:1537-1550.
 21. Pekar V, McNutt T, Kaus M. Automated model-based organ delineation for radiotherapy planning in prostatic region. *Int J Radiat Oncol Biol Phys* 2005;60:973-980.
 22. Coote T, Hill A, Taylor C, *et al.* The use of active shape models for locating structures in medical images. *J Image Vis Computation* 1994;12:355-366.
 23. Xu C, Prince JL. Snakes, Shapes, and Gradient Vector Flow. *IEEE Trans. Image Processing* 1998;7:359-369.
 24. Liu F, Zhao B, Kijewski P. Liver segmentation for CT images using GVF snake. *Med Phys* 2005;32:3699-3706.
 25. Weese J, Kaus M, Lorenz C. Shape constrained deformable models for 3D medical image segmentation. *Lecture Notes in Computer Science* 2001;2082:380-387.

FIGURE CAPTIONS

Figure 1 Overall process of rectal contour propagation.

Figure 2 A sketch of narrow band. (a) a narrow band image surrounding a manually segmented rectal contour; (b) a narrow band construction is illustrated for two vortex points A and B .

Figure 3 A sketch of orientation histogram in SIFT method.

SIFT—Scale Invariance Feature Transformation

Figure 4 Rectal contour propagation from the pCT to two dramatically deformed images. (a) original contour, the red curve represents the manually delineated contour; (b) and (c) its optimal mapping in the two deformed images (green curves). For comparison, the original contour from the pCT is also shown in the deformed images (red curves).

PCT—planning CT

Figure 5 Control points in the 2D contour mapping

2D—two dimensional

Figure 6 Displacement fields. (a) TPS-derived displacement field for the 2D digital phantom study; (b) intentionally introduced displacement field; and (c) subtraction of TPS derived and the known displacement fields.

TPS—Thin Plate Spline

2D—two dimensional

Figure 7 3D contour mapping for the rectum of a man with prostate cancer. The top row is the three transactions in the planning CT image with manually delineated contours (green contours), the bottom row is corresponding transactions in the CBCT image with auto-mapped contour (red contours). The left column is the axial plane, the middle column is the coronal plane, and the right column is the sagittal plane.

3D—three dimensional

CT—computational tomography

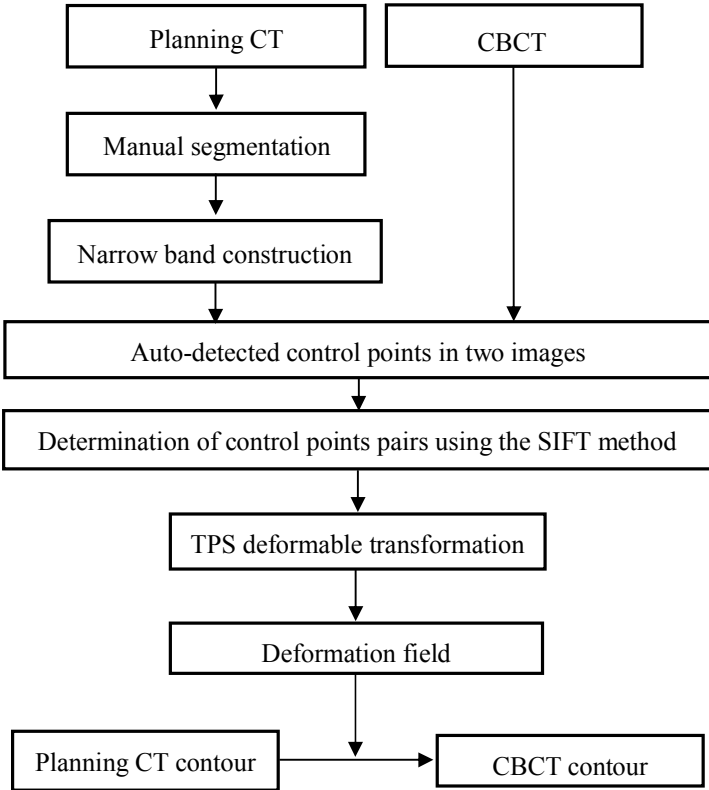
CBCT—cone beam computational tomography

Figure 8 Rectal contour mapping for a rectal cancer case. The top row shows several axial slices in the pCT image with manually delineated contours (green contours). The bottom row is the corresponding slices in the CBCT image with auto-mapped contours (red contours).

PCT—planning CT

CBCT—cone beam computational tomography

Figure
[Click here to download Figure: fig1.doc](#)



Figure

[Click here to download Figure: fig2a.doc](#)

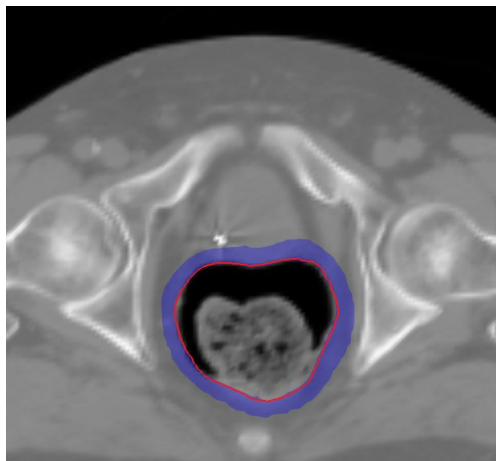


Figure
[Click here to download Figure: fig2b.doc](#)

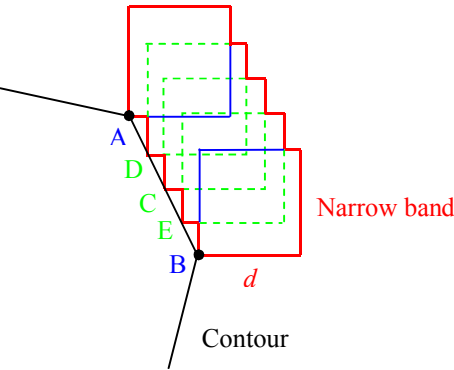
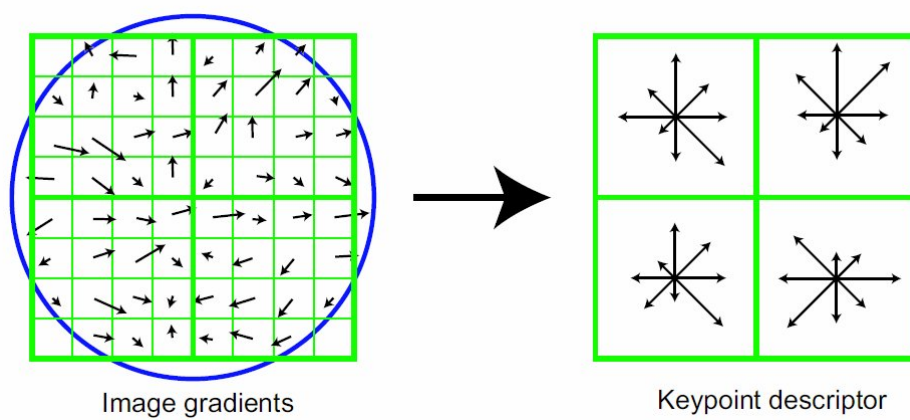
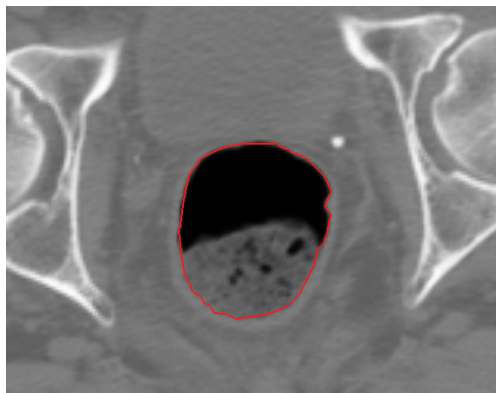


Figure
[Click here to download Figure: fig3.doc](#)



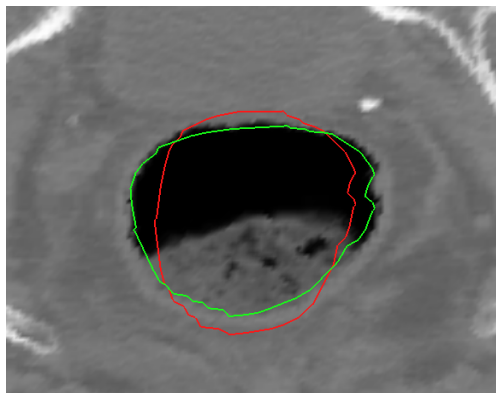
Figure

[Click here to download Figure: fig4a.doc](#)



Figure

[Click here to download Figure: fig4b.doc](#)



Figure

[Click here to download Figure: fig4c.doc](#)

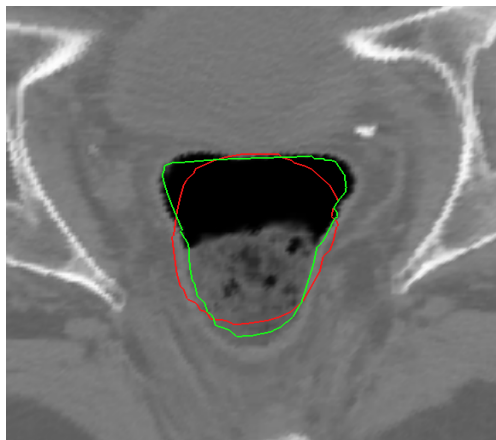


Figure
[Click here to download Figure: fig5a.doc](#)

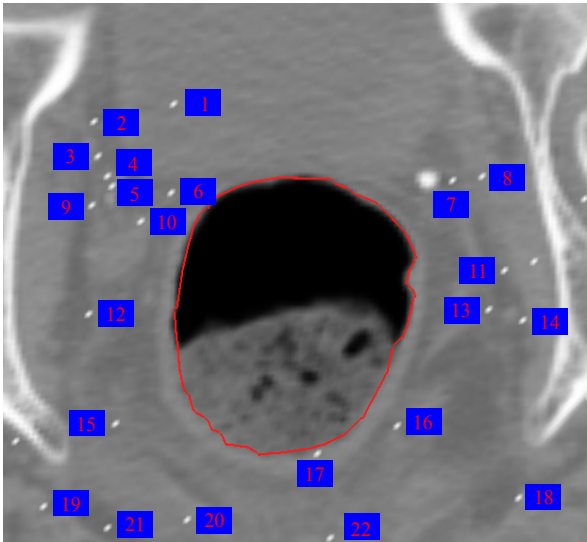
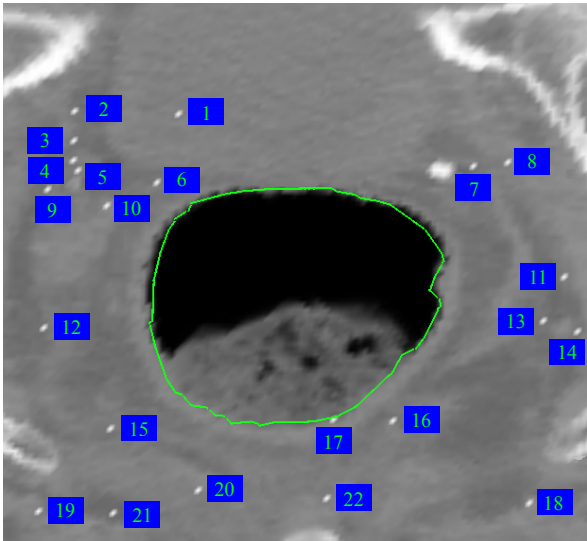
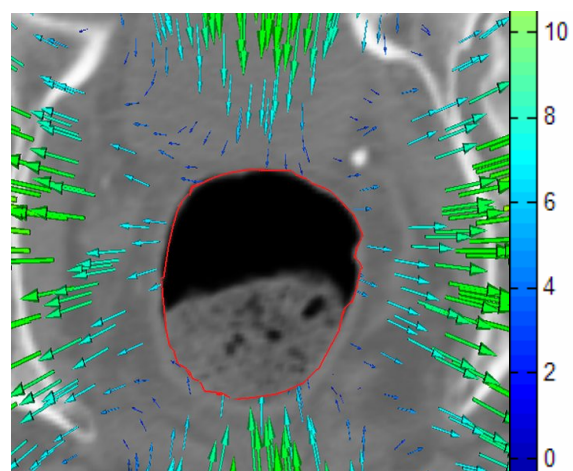


Figure
[Click here to download Figure: fig5b.doc](#)



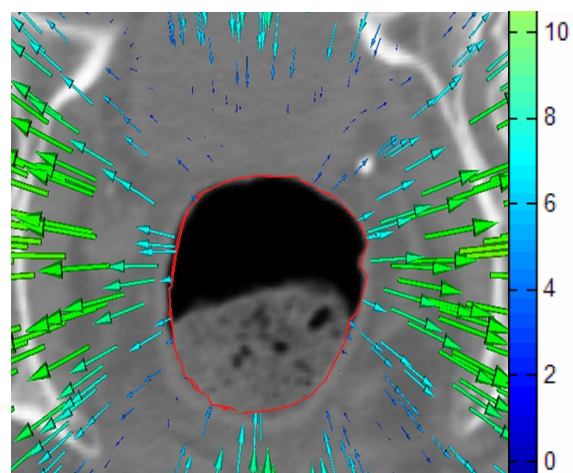
Figure

[Click here to download Figure: fig6a.doc](#)



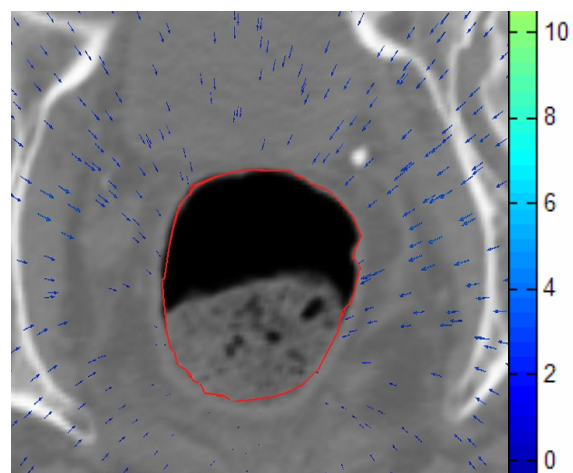
Figure

[Click here to download Figure: fig6b.doc](#)



Figure

[Click here to download Figure: fig6c.doc](#)



Figure

[Click here to download Figure: fig7.doc](#)

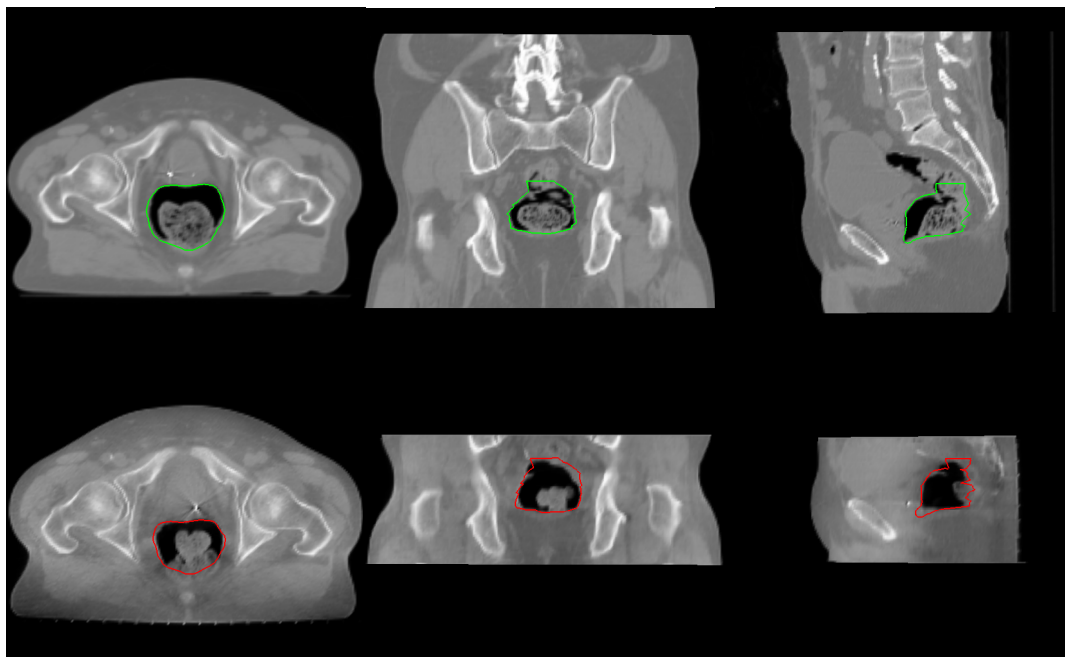
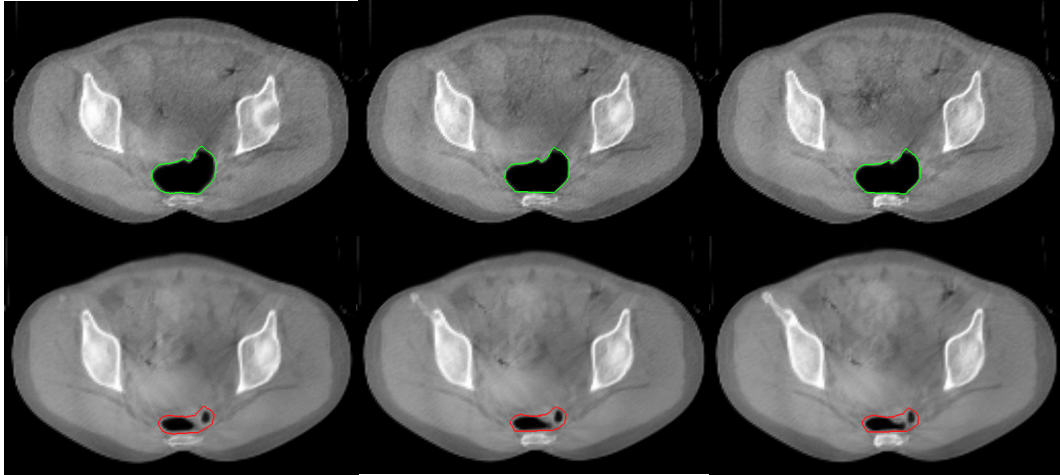


Figure
[Click here to download Figure: fig8.doc](#)



The use of EPID-measured leaf sequence files for IMRT dose reconstruction in adaptive radiation therapy

Louis Lee, Weihua Mao, and Lei Xing

Department of Radiation Oncology, Stanford University School of Medicine, Stanford, CA 94305, USA

E-mail: louislee@stanford.edu

Submitted to: Physics in Medicine and Biology

Short title: EPID-measured leaf sequence files for IMRT dose reconstruction

Keywords: EPID, leaf sequence file, IMRT, dose reconstruction, adaptive radiation therapy

Abstract

For intensity modulated radiation treatment (IMRT) dose reconstruction, multileaf collimator (MLC) log-files have been shown applicable for deriving delivered fluence maps. However, MLC log-files are dependent on the accuracy of leaf calibration and only available from one linear accelerator manufacturer. In this paper, we present a proof of feasibility and principles in (1) using an amorphous silicon electronic portal imaging device (aSi-EPID) to capture the MLC segments during an IMRT delivery and (2) re-constituting a leaf sequence (LS) file based on the leaf end positions calculated from the MLC segments and their associated fractional monitor units. These EPID-measured LS files are then used to derive delivered fluence maps for dose reconstruction. The developed approach was tested on a pelvic phantom treated with a typical prostate IMRT plan. The delivered fluence maps, which were derived from the EPID-measured LS files, showed slight differences in the intensity levels compared with the corresponding planned ones. The dose distribution calculated with the delivered fluence maps showed a discernible difference in the high dose region when compared to that calculated with the planned fluence maps. The maximum dose in the former distribution was also 2.5% less than that in the latter one. The EPID-measured LS file can serve the same purpose as a MLC log-file does for the derivation of the delivered fluence map and yet is independent of the leaf calibration. The approach also allows users who do not have access to MLC log-files to probe the actual IMRT delivery and translate the information gained for dose reconstruction in ART.

1. Introduction

An advantage of the fractionation scheme in radiation treatment is that it offers room for adaptive radiation therapy (ART). ART is a radiation treatment strategy of which the subsequent fractional delivery can be adaptively modified based on a closed-loop control framework using systematic feedback of geometric and dosimetric information (de la Zerda *et al.*, 2007; Webb, 2008; Yan *et al.*, 1997a). The ultimate goal of ART is to maintain adequate target coverage with a desired dose and ensure doses received by normal tissue are within tolerance at the conclusion of treatment. The adaptive strategy comes into play at different levels of complexity depending on techniques and resources available. It ranges from the most accessible form of adapting treatment margins based on daily portal images (Yan *et al.*, 1997b) to the most sophisticated one of re-optimization or re-planning of treatment plans (de la Zerda *et al.*, 2007; Webb, 2008). Common to all these strategies is the execution of dose reconstruction at some stage during the ART process. Through this, the dose deposited to a patient in a particular fraction can be correlated or mapped to a reference set of computed tomography, ideally by deformable registration, contributing to an accumulated dose delivered so far, which is a key parameter for the feedback mechanism in ART framework.

However, in most intensity modulated radiation treatments (IMRTs) employing ART strategies, the dose reconstruction is tacitly based on an assumption that the delivery of fluence maps are as planned (Langen *et al.*, 2005; Yang *et al.*, 2007; Yoo and Yin, 2006). This assumption might not be necessarily valid. For instance, in IMRT using step-and-shoot mode, the expected delivery of fluence maps might not be realized due to intrinsic errors associated with the multileaf collimator (MLC) kinematics and beam control communication resulting in overshoot, undershoot segmental monitor units, dropped segments, and beam delivery during leaf motion (Ezzell and Chungbin, 2001; Litzenberg *et al.*, 2007; Wiersma and Xing, 2007; Xia *et al.*, 2002). In order to incorporate these errors in the dose reconstruction, our group (Lee *et al.*, 2008) and

Litzenberg *et al* (2007) have demonstrated a pragmatic approach of using MLC log-files to reconstruct the IMRT dose actually delivered. This is based on that the MLC log-files have been validated to faithfully reflect the actual delivery process of MLC-based IMRT (Li *et al.*, 2003; Stell *et al.*, 2004). Because the MLC log-file is only available from one commercial linear accelerator (linac) manufacturer (Varian Medical Systems, Palo Alto, CA); users with linacs from other manufacturers are deprived of this straightforward approach to reconstruct the delivered IMRT dose. Furthermore, the leaf position data recorded in a MLC log-file is taken from the same encoders used to position the leaves, making the reported position dependent on the leaf position calibration and by no means an absolute measure of the leaf position. Any systematic error introduced in the MLC calibration might lead to actual leaf positions different from the expected ones resulting in dose errors (Parent *et al.*, 2006; Woo and Nico, 2005).

In order to circumvent this dependence and provide a universal approach of probing the actual delivery of a fluence map, we propose using an amorphous silicon electronic portal imaging device (aSi-EPID) to capture every segment of the fluence map during the treatment. For each captured segment, the leaf positions for each pair of leaves are found by an edge detection algorithm; the fractional monitor units (fMU) associated with this particular segment is also sampled. After all the segments have been analyzed, a leaf sequence (LS) file is re-constituted using the segmental leaf positions and their associated fMU based on the sequence the segments are delivered. The EPID-measured LS files can then be loaded to the treatment planning system (TPS) to derive the delivered fluence maps and reconstruct the delivered IMRT dose. aSi-EPIDs are geometrically and functionally stable, giving undistorted images of high resolution and contrast (McCurdy *et al.*, 2001; Menon and Sloboda, 2004). The proposed approach is based on that the use of the aSi-EPID in measuring leaf end positions to a high degree of accuracy has been proven, leading to its widespread applications in MLC quality assurance

(Budgell *et al.*, 2005; Chang *et al.*, 2004), leaf calibrations (Baker *et al.*, 2005; Clarke and Budgell, 2008), and leaf motion tracking (Parent *et al.*, 2006; Sonke *et al.*, 2004).

The objective of this work is two-fold: (1) to present a proof of feasibility and principles in re-constituting an EPID-measured LS file which serves the same purpose for deriving the delivered fluence map as a MLC log-file does and (2) to demonstrate the dose reconstruction essential for adaptive radiation therapy using the delivered fluence maps literally calculated from the MLC segments captured by an EPID during an IMRT delivery.

2. Methods

2.1. Description of the MLC and EPID

All experiments were done on a Trilogy linac (Varian Medical Systems, Palo Alto, CA) equipped with a Millennium 120-leaf MLC and kilovoltage/megavoltage EPIDs. The Millennium 120-leaf MLC consists of two banks of 60 leaves. The leaf widths for the central 40 leaf pairs and the outer 10 leaf pairs are 0.5 cm and 1.0 cm respectively. The leaves can travel a maximum of 16.5 cm across the beam central axis, and the maximum leaf span between the two leaves on the same carriage is 14.5 cm. All measurements are referred to the isocentric plane. The leaf calibration procedure recommended by Graves *et al.* (Graves *et al.*, 2001) was performed to ensure the MLC indicated field edge positions agreed with the radiation field edges to within 0.3 mm before the experiments (Yang and Xing, 2004).

The megavoltage (MV) EPID (Varian aS1000 flat panel detector) was used to acquire images for the experiments. The EPID is mounted on retractable arms attached to the gantry. It has a detector area of $40 \times 30 \text{ cm}^2$ with a matrix of 1024 by 768 pixels resulting in a physical pixel size of 0.392 mm. The EPID consists of: (1) a 1.0 mm thick copper plate for build-up, (2) a phosphor screen of gadolinium oxysulphide doped with terbium (Kodak Lanex Fast Screen) to convert incident radiation to visible photons, (3) a pixel array implanted on an amorphous silicon

substratum where each pixel is made up of a photodiode and thin film transistor to convert the light photons to electric charges and (4) electronics for readout. The electrical signals are digitized by a 14 bit analog-to-digital converter and processed into image data.

2.2. Geometric status of the EPID

Baker *et al.* (2005) and Parent *et al.* (2006) reported that a systematic tilt of the EPIDs was observed in their studies and indicated that it was likely to occur for all different EPIDs; Clarke and Budgell (2008) have also demonstrated the effect of the gantry angle on the EPID sag. Therefore, it is expected that the imaging geometry for the EPID at different gantry angles might deviate from an ideal configuration that we base on for the measurement of the leaf end position. We need to establish the geometric status of the EPID before we can accurately measure the leaf end position from an EPID image. Recently, our group has developed a geometric quality assurance phantom and an automated analysis program (gQA tool) to study the geometric integrity of the on-board imager (Mao *et al.*, 2008). This gQA tool was used in this work to study the changes in the overall imaging geometry of the EPID including the source-to-imager distance (SID), the EPID center, and the tilt of the EPID for every 10° of a full rotation of the gantry. Based on the geometric information provided by the gQA tool, positional corrections were incorporated into the measurement of the leaf end position. This procedure has been used in a project of tracking fiducial markers using combined kV/MV imaging technique (Wiersma *et al.*, 2008).

2.3. Measurement of the leaf end position

The co-ordinate systems used to describe the imaging geometry of the EPID are shown in figure 1. The (x, y) plane denotes the isocentric plane with the origin at the isocenter (figure 1(a)). The (μ , ν) plane pertains to the EPID with the origin O at the center of the EPID (figure 1(b)). Both

the (x, y) and (μ , v) planes rotate with the gantry angle ω . The μ' - and v' -axes are defined for a tilted EPID; the angles γ and θ represent the tilt of the μ' - and v' -axes respectively (figures 1(c) and 1(d)).

Suppose a leaf end P (assumed to be a point) is projected to A on the EPID plane (μ , v) (figure 2(a)). The projection of A on the μ - and v - axes are A_μ and A_v respectively. The distances of A_μ and A_v are at μ_1 and v_1 from O respectively. Now consider a vertical plane passing through the x-ray source (S), isocenter (I) and the point A_μ (figure 2(b)), and if we assume the imager is in perfect horizontal alignment; the position of the leaf end on the x-axis of the isocentric plane can be calculated.

From similar triangles SIC and SOA $_\mu$,

$$x_1 = \mu_1 \times \frac{SAD}{SID} . \quad (1)$$

Similarly,

$$y_1 = v_1 \times \frac{SAD}{SID} . \quad (2)$$

Now assume the imager is tilted to an angle γ , the leaf end is projected to a point B on the tilted EPID instead of A on the horizontal EPID. The projection of B on the μ' -axis is B $_\mu$, which is at a distance of μ'_1 from O.

From similar triangles SDB $_\mu$ and SOA $_\mu$, the position of the leaf end (μ_1) on the μ -axis can be found by

$$\mu_1 = \mu'_1 \cos \gamma \times \frac{SID}{SID - \mu'_1 \sin \gamma} . \quad (3)$$

Using equation (1), the corresponding leaf end position on x-axis (x_1) of the isocentric plane is

$$x_1 = \mu'_1 \cos \gamma \times \frac{SAD}{SID - \mu'_1 \sin \gamma} . \quad (4)$$

And if we further incorporate the EPID offset distance ($d_{\mu'}$) along the μ' -axis into equation (4), we have

$$x_1 = (\mu'_1 + d_{\mu'}) \cos \gamma \times \frac{SAD}{SID - (\mu'_1 + d_{\mu'}) \sin \gamma} . \quad (5)$$

Without loss of generality, the corresponding leaf end position on y-axis (y_1) of the isocentric plane is

$$y_1 = (v'_1 + d_{v'}) \cos \theta \times \frac{SAD}{SID - (v'_1 + d_{v'}) \sin \theta} . \quad (6)$$

In a perfect imaging geometry where the tilts γ and θ equal to zero ($\mu'=\mu$; $v'=v$), and there is no offsets of the EPID center; the equations (5) and (6) reduce to equations (1) and (2) respectively.

2.4. Software development

A step-and-shoot IMRT field is made up of a number of segments; each segment is specified by prescribed leaf positions and a fraction of the total monitor units (fMU) to be delivered for this segment. For the experiments, a step-and-shoot IMRT field with an open segment of 10 cm high by 1 cm wide ('open gap' field) was designed to step through a distance of 10 cm from -5 cm to 5 cm on the x-axis of the isocentric plane. Five MU was assigned to each segment. The leaf motion was parallel to the μ -axis of the imager. This IMRT field was delivered to a pelvic phantom with its center aligned to the isocenter at a gantry angle of 0° (IEC scale). The 6 MV beam was used at a dose rate of 300 MU/minute. The EPID was positioned at a SID of 150 cm. During the IMRT delivery, EPID images were acquired at a frame rate of 6.7 frames per second, and the acquisition was synchronized with the beam. All EPID images were processed with the dark-field and flood-field corrections. The delivery was repeated three times at this angle and also at other orthogonal angles of 90° , 180° , and 270° in order to study the effect of gravity on the measurement of the leaf position from the EPID images.

An in-house program written in MatLab code (MathWorks, Inc., Natick, MA) was developed to re-constitute the EPID-measured LS file. The program first identifies different segments from a series of EPID images captured from the IMRT field by performing morphologic comparison. The same images of a segment are grouped together; the first and last images are taken as the starting and ending shapes for that particular segment. For each segment image, the positions of the leaf ends are searched near the penumbral regions by a maximum gradient edge detection algorithm in a scanline fashion for the pixel rows. The maximum gradient in intensity in the penumbral region of a portal image has been confirmed to correspond to the 50% intensity level (Bijhold *et al.*, 1991; Partridge *et al.*, 1998) that depicts the dosimetric leaf edge (ICRU, 1976). The pixel location (column number, row number) of the leaf end found is spatially converted and projected back to the isocentric plane with the positional corrections using equations (5) and (6). Only the pixel rows that correspond to the central one-third of the leaf are calculated to avoid the influence of the interleaf transmission (James *et al.*, 2000; Vieira *et al.*, 2002); the final leaf end position is defined as an average of the positions of the leaf ends found from the set of pixel rows that belong to the same leaf (Baker *et al.*, 2005; James *et al.*, 2000; Vieira *et al.*, 2002). The leaf positions of each pair of MLC leaves for each segment image are then coupled with the fMU associated with that particular segment by referring to the synchronized beam on signal and cumulative MU sampled from the beam control circuitry and MLC workstation respectively (Partridge *et al.*, 1998; Woo *et al.*, 2003). After all the segments in one delivered field have been analyzed, an EPDI-measured LS file is re-constituted in a format readable by the TPS using the segmental leaf positions and fMU values. The EPDI-measured LS file, which reflects the actual delivery, is then used to derive the delivered fluence map for dose reconstruction.

The assessment of the developed software on the measurement of the leaf end position was performed by comparing the measured and expected leaf end positions from the ‘open gap’ field experiments.

2.5. Dose reconstruction

A typical prostate step-and-shoot IMRT plan with seven co-planar fields was copied from a patient case and applied to a pelvic phantom. The treatment was delivered to the pelvic phantom as in a routine clinical setting on a Trilogy linac using the 6 MV photon beam at a dose rate of 300MU/minute. EPID images were acquired during the entire delivery as described previously. For each delivered field, there were about 9 to 13 segments depending on the modulation of the fluence map, and there were about 4-6 EPID images captured for each individual segment making a total of about 40 to 80 EPID images for each delivered field. A typical prostate IMRT would result in about 450 EPID images. These images were discarded once the analysis was done to save computer space. The EPID images were analyzed by the developed software, and the re-constituted LS files were loaded back to the Eclipse TPS (Varian Medical Systems, Palo Alto) to derive the delivered fluence maps. The delivered and planned fluence maps were compared. Dose reconstruction was then performed on the pelvic phantom using the delivered fluence maps. The workflow is shown schematically in figure 3. Dose reconstruction was also performed using the planned fluence maps. The dose distributions from the two dose reconstructions on the three orthogonal planes through the isocenter were compared. Note that the plan was not optimized for the pelvic phantom, it is merely used to show the difference in dose reconstruction from using the delivered against planned fluence maps.

3. Results

3.1. 'Open gap' field experiments

For each MLC segment in the 'open gap' field, the mean deviation (σ) of the leaves (leaf m to leaf n) forming the gap on each bank from their expected positions is defined as

$$\sigma = \sqrt{\frac{\sum_{i=m}^n (x_i - x_{i,expected})^2}{n - m + 1}}, \quad (7)$$

where x_i and $x_{i,expected}$ are the measured and expected leaf end positions of the i^{th} leaf respectively.

The mean deviations of the leaves for the 10 segments (Banks B and A) delivered at the gantry angle 0° were about 0.6 mm to 1.0 mm and were reproducible for the three repeated measurements (Table 1). The mean deviations of the leaves for the 10 segments (Banks B and A) delivered at the four principal orthogonal gantry angles were of the same order of magnitude (Table 2). However, we noticed that whilst the mean deviations for the gantry angle 270° were similar to that at the gantry angle 0° ; the mean deviations for the gantry angles of 90° and 180° were found to be smaller (~ 0.3 mm to 0.7 mm).

3.2. Prostate IMRT delivery: MLC segments captured by EPID

Figure 4 shows a series of 13 segments (only the first image of each segment is shown) captured by the EPID for the delivered field at the gantry angle 0° in the prostate IMRT delivery. The corresponding leaf end positions calculated by the developed software for each individual segment are shown in figure 5. The calculated leaf end positions were well within 1.0 mm of their expected positions.

3.3. Derivation of fluence maps and dose reconstruction

The delivered fluence maps derived from the EPID-measured LS files for the seven IMRT fields are shown in figure 6(a); there were slight differences (arrows) in the intensity levels when compared to the corresponding planned fluence maps from the original plan.

The dose reconstruction using the delivered fluence maps showed no discernible difference for all the isodose lines except the one for the 105% when compared to the expected dose distribution (Figure 7). The volumes pertaining to a dose level of 105% or above were 12 cm^3

and 27 cm^3 for the delivered and expected dose distributions respectively. The maximum dose in the delivered dose distribution was 2.5 % lower than that in the expected dose distribution.

4. Discussion

We have shown the feasibility in re-constituting an EPID-measured LS file and using it to derive the delivered fluence map for dose reconstruction. The approach is equivalent to using the MLC log-files for dose reconstruction (Lee *et al.*, 2008; Stell *et al.*, 2004) and yet avoiding the dependency of the recorded leaf positions on the leaf calibration.

At the outset, our main concern was the influence of EPID sag and tilt at different gantry angles on the measurement of the leaf end position. Clark and Budgell (2008) and Woo *et al.* (2003) have solved this problem by calibration techniques. For us, with the use of our developed gQA tool, we were able to quantify the EPID sag and tilt to a reasonable accuracy (Mao *et al.*, 2008) and incorporate this information in the calculation of the leaf end positions.

From the results of the ‘open gap’ field experiments, we found that the mean deviation of the leaves was about 1.0 mm which was expected of a MLC-based IMRT delivery (Eilertsen, 1997; Vieira *et al.*, 2002) taking into account that (1) a tolerance of 1.5 mm in the leaf position was allowed during the actual delivery, (2) the associated image noise that somewhat compromised the accurate measurement of the leaf end at the penumbral region and (3) the slight effect of leaf sagging at various gantry angles (Clarke and Budgell, 2008). The projected pixel size at the isocentric plane is 0.26 mm, which means that the mean deviation was about 4 pixels. We found that the mean deviations of the leaves at gantry angle 90° and 180° ($\sim 0.6 \text{ mm}$) were in general smaller than that at the gantry angle 0° and 270° , and there was no discernible difference in the mean deviations for the two different banks when the gantry was horizontally placed (gantry angle 90° and 270°). Under the present experimental setup, the data we acquired was insufficient for us to explain this phenomenon; one possible explanation could be that the routine leaf

calibration is done at the gantry angle 0° and it might deviate from the ideal scenario at other gantry angles. Moreover, a smaller mean deviation does not necessarily mean it is more accurate in the leaf position at these gantry angles; it simply means the condition of the leaf positioning was different from that at the gantry angle 0° and 180° . Further work needs to be done to find out the causes for this phenomenon.

In an ideal step-and-shoot IMRT delivery, the MLC segment is supposed to be stationary whilst the beam is on and only to change shape whilst beam is held off. However, it is well aware that some leaves do actually move whilst the beam is on (Li *et al.*, 2003; Stell *et al.*, 2004; Zeidan *et al.*, 2004). Therefore, in re-constituting the LS file, we adopted to use the first and last images of a segment as the two control points in the LS file trying to capture the movement of the leaves that might have occurred during the beam-on time. The results showed that it was impossible to distinguish whether the movement detected was due to an actual leaf displacement between the two control points or simply the uncertainty of the leaf end position confounded by the image noise at the penumbral region. Nevertheless, the movements we found were all less than 0.2 mm (\sim one pixel size), which led us to presume that they truly reflected the real situation and incorporate these in the LS file. This is a limitation typically encountered when one tries to extract spatial information from a noisy image.

In the comparison of the delivered fluence maps with the planned ones, the differences in the intensity levels seen were attributable to the combined effect of leaf deviations in each of the contributing segments and the inherent fMU redistribution (Stell *et al.*, 2004; Xia *et al.*, 2002); the dosimetric impact of these differences was reflected in the dose reconstruction using the delivered fluence maps. The differences in the 105% isodose level and the maximum dose between the delivered and expected dose distributions indicate that a need for employing the delivered rather than planned fluence maps for dose reconstruction in ART is warranted.

One might argue that dose reconstruction should be accomplished by in-vivo exit portal dosimetry (McDermott *et al.*, 2007; McDermott *et al.*, 2008; van Elmpt *et al.*, 2007), but the technique is still in its development and impeded by some unresolved issues such as dosimetric non-linearities of the aSi-EPID (Budgell *et al.*, 2005; McDermott *et al.*, 2006a) that require tedious calibration and correction (Nijsten *et al.*, 2007) and the correction of scatter from the patient (McDermott *et al.*, 2006b; McDermott *et al.*, 2008). Compared to these dosimetric methods, our approach is based on a well-proven superiority of aSi-EPID in spatial determination of the leaf end position; it is also straightforward and easy to implement at a clinic. In addition, the proposed approach is equally well suited for IMRT dose verification purposes.

5. Conclusions

We presented here a proof of feasibility and principles in re-constituting a leaf sequence file that reflects the actual delivery of an IMRT based on the MLC segments captured by an EPID. This EPID-measured LS file can serve the same purpose as a MLC log-file does for the derivation of the delivered fluence map and is independent of the leaf calibration. The approach also allows users who do not have access to MLC log-files to probe the actual IMRT delivery and translate the information gained for dose reconstruction in ART.

Acknowledgements

This work is supported in part by grants from the Department of Defense (W81XWH-05-1-0041), Komen Breast Cancer Foundation (BCTR0504071), and National Cancer Institute (5R01 CA98523 and 1R01 CA98523). Support from the Sir Robert Black Postdoctoral Fellowship and the Hong Kong Hospital Authority Overseas Training Allowance for the first author are also gratefully acknowledged. We would also like to thank Mark Wanlass and Bill Cheng, our linac engineers, for offering technical advice on the control of the linac and MLC.

References

- Baker S J, Budgell G J and MacKay R I 2005 Use of an amorphous silicon electronic portal imaging device for multileaf collimator quality control and calibration *Phys Med Biol* **50** 1377-92
- Bijhold J, Gilhuijs K G, van Herk M and Meertens H 1991 Radiation field edge detection in portal images *Phys Med Biol* **36** 1705-10
- Budgell G J, Zhang Q, Trouncer R J and Mackay R I 2005 Improving IMRT quality control efficiency using an amorphous silicon electronic portal imager *Med Phys* **32** 3267-78
- Chang J, Obcemea C H, Sillanpaa J, Mechalakos J and Burman C 2004 Use of EPID for leaf position accuracy QA of dynamic multi-leaf collimator (DMLC) treatment *Med Phys* **31** 2091-6
- Clarke M F and Budgell G J 2008 Use of an amorphous silicon EPID for measuring MLC calibration at varying gantry angle *Phys Med Biol* **53** 473-85
- de la Zerda A, Armbruster B and Xing L 2007 Formulating adaptive radiation therapy (ART) treatment planning into a closed-loop control framework *Phys Med Biol* **52** 4137-53
- Eilertsen K 1997 Automatic detection of single MLC leaf positions with corrections for penumbral effects and portal imager dose rate characteristics *Phys Med Biol* **42** 313-34
- Ezzell G A and Chungbin S 2001 The overshoot phenomenon in step-and-shoot IMRT delivery *J Appl Clin Med Phys* **2** 138-48
- Graves M N, Thompson A V, Martel M K, McShan D L and Fraass B A 2001 Calibration and quality assurance for rounded leaf-end MLC systems *Med Phys* **28** 2227-33
- ICRU 1976 Determination of absorbed dose in a patient irradiated by beams of x- or gamma-rays in radiotherapy procedures (Bethesda, MD: ICRU)

- James H V, Atherton S, Budgell G J, Kirby M C and Williams P C 2000 Verification of dynamic multileaf collimation using an electronic portal imaging device *Phys Med Biol* **45** 495-509
- Langen K M, Meeks S L, Poole D O, Wagner T H, Willoughby T R, Kupelian P A, Ruchala K J, Haimlerl J and Olivera G H 2005 The use of megavoltage CT (MVCT) images for dose recomputations *Phys Med Biol* **50** 4259-76
- Lee L, Le Q T and Xing L 2008 Retrospective IMRT dose reconstruction based on cone-beam CT and MLC log-file *Int J Radiat Oncol Biol Phys* **70** 634-44
- Li J G, Dempsey J F, Ding L, Liu C and Palta J R 2003 Validation of dynamic MLC-controller log files using a two-dimensional diode array *Med Phys* **30** 799-805
- Litzenberg D W, Hadley S W, Tyagi N, Balter J M, Ten Haken R K and Chetty I J 2007 Synchronized dynamic dose reconstruction *Med Phys* **34** 91-102
- Mao W, Lee L and Xing L 2008 Development of a QA phantom and automated analysis tool for geometric quality assurance of on-board MV and kV x-ray imaging systems *Med Phys* In press.
- McCurdy B M, Luchka K and Pistorius S 2001 Dosimetric investigation and portal dose image prediction using an amorphous silicon electronic portal imaging device *Med Phys* **28** 911-24
- McDermott L N, Nijsten S M, Sonke J J, Partridge M, van Herk M and Mijnheer B J 2006a Comparison of ghosting effects for three commercial a-Si EPIDs *Med Phys* **33** 2448-51
- McDermott L N, Wendling M, van Asselen B, Stroom J, Sonke J J, van Herk M and Mijnheer B J 2006b Clinical experience with EPID dosimetry for prostate IMRT pre-treatment dose verification *Med Phys* **33** 3921-30

- McDermott L N, Wendling M, Sonke J J, van Herk M and Mijnheer B J 2007 Replacing pretreatment verification with in vivo EPID dosimetry for prostate IMRT *Int J Radiat Oncol Biol Phys* **67** 1568-77
- McDermott L N, Wendling M, Nijkamp J, Mans A, Sonke J J, Mijnheer B J and van Herk M 2008 3D in vivo dose verification of entire hypo-fractionated IMRT treatments using an EPID and cone-beam CT *Radiother Oncol* **86** 35-42
- Menon G V and Sloboda R S 2004 Quality assurance measurements of a-Si EPID performance *Med Dosim* **29** 11-7
- Nijsten S M, van Elmpt W J, Jacobs M, Mijnheer B J, Dekker A L, Lambin P and Minken A W 2007 A global calibration model for a-Si EPIDs used for transit dosimetry *Med Phys* **34** 3872-84
- Parent L, Seco J, Evans P M, Dance D R and Fielding A 2006 Evaluation of two methods of predicting MLC leaf positions using EPID measurements *Med Phys* **33** 3174-82
- Partridge M, Evans P M, Mosleh-Shirazi A and Convery D 1998 Independent verification using portal imaging of intensity-modulated beam delivery by the dynamic MLC technique *Med Phys* **25** 1872-9
- Sonke J J, Ploeger L S, Brand B, Smitsmans M H and van Herk M 2004 Leaf trajectory verification during dynamic intensity modulated radiotherapy using an amorphous silicon flat panel imager *Med Phys* **31** 389-95
- Stell A M, Li J G, Zeidan O A and Dempsey J F 2004 An extensive log-file analysis of step-and-shoot intensity modulated radiation therapy segment delivery errors *Med Phys* **31** 1593-602
- van Elmpt W J, Nijsten S M, Dekker A L, Mijnheer B J and Lambin P 2007 Treatment verification in the presence of inhomogeneities using EPID-based three-dimensional dose reconstruction *Med Phys* **34** 2816-26

- Vieira S C, Dirkx M L, Pasma K L and Heijmen B J 2002 Fast and accurate leaf verification for dynamic multileaf collimation using an electronic portal imaging device *Med Phys* **29** 2034-40
- Webb S 2008 Adapting IMRT delivery fraction-by-fraction to cater for variable intrafraction motion *Phys Med Biol* **53** 1-21
- Wiersma R D and Xing L 2007 Examination of geometric and dosimetric accuracies of gated step-and-shoot intensity modulated radiation therapy *Med Phys* **34** 3962-70
- Wiersma R D, Mao W and Xing L 2008 Combined kV and MV imaging for real-time tracking of implanted fiducial markers *Med Phys* In press.
- Woo M K, Lightstone A W, Shan G, Kumaraswamy L and Li Y 2003 Automatic verification of step-and-shoot IMRT field segments using portal imaging *Med Phys* **30** 348-51
- Woo M K and Nico A 2005 Impact of multileaf collimator leaf positioning accuracy on intensity modulation radiation therapy quality assurance ion chamber measurements *Med Phys* **32** 1440-5
- Xia P, Chuang C F and Verhey L J 2002 Communication and sampling rate limitations in IMRT delivery with a dynamic multileaf collimator system *Med Phys* **29** 412-23
- Yan D, Vicini F, Wong J and Martinez A 1997a Adaptive radiation therapy *Phys Med Biol* **42** 123-32
- Yan D, Wong J, Vicini F, Michalski J, Pan C, Frazier A, Horwitz E and Martinez A 1997b Adaptive modification of treatment planning to minimize the deleterious effects of treatment setup errors *Int J Radiat Oncol Biol Phys* **38** 197-206
- Yang Y and Xing L 2004 Quantitative measurement of MLC leaf displacements using an electronic portal image device *Phys Med Biol* **49** 1521-33
- Yang Y, Schreiber E, Li T, Wang C and Xing L 2007 Evaluation of on-board kV cone beam CT (CBCT)-based dose calculation *Phys Med Biol* **52** 685-705

- Yoo S and Yin F F 2006 Dosimetric feasibility of cone-beam CT-based treatment planning compared to CT-based treatment planning *Int J Radiat Oncol Biol Phys* **66** 1553-61
- Zeidan O A, Li J G, Ranade M, Stell A M and Dempsey J F 2004 Verification of step-and-shoot IMRT delivery using a fast video-based electronic portal imaging device *Med Phys* **31** 463-76

Figure captions

Figure 1. Co-ordinate systems describing the imaging geometry of the EPID. (a) Isocentric plane (x, y) and gantry angle ω as viewed from the couch end. (b) EPID (μ, ν) plane as viewed in the beam's eye view. (c) EPID's μ -axis tilt γ as viewed from the couch end. (d) EPID's ν -axis tilt θ as viewed from the side. *SAD: source-to-axis distance; SID: source-to-imager distance.*

Figure 2. Schematic diagrams showing the projection of a leaf end P on the EPID (μ, ν) plane (a) and the geometrical relationship of various parameters in the calculation of the leaf end position on the isocentric plane (b). *SAD: source-to-axis distance; SID: source-to-imager distance.*

Figure 3. Schematic diagram showing the workflow from the acquisition of the MLC segments to the dose reconstruction in the prostate IMRT delivery.

Figure 4. A series of 13 MLC segments captured by the EPID for the delivered field at the gantry angle 0° for the prostate IMRT delivery.

Figure 5. A series of leaf end positions for each individual MLC segment from figure 4.

Figure 6. (a) Delivered fluence maps from EPID-measured leaf sequence files. (b) Planned fluence maps. The differences in the intensity levels between the delivered and planned fluence maps are highlighted by the arrows.

Figure 7. (a) Delivered dose distribution calculated with fluence maps derived from EPID-measured leaf sequence files. (b) Expected dose distribution calculated with planned fluence

maps. The differences in the dose distribution (105% level) between the delivered and expected dose distributions for the three orthogonal planes are highlighted by the arrows.

Table 1. The mean deviations of the leaves (Banks B and A) for the 10 segments of the ‘open gap’ field delivered at the gantry angle 0° in three repeated deliveries.

Mean deviation of leaves (mm) from expected positions											
		Segment									
		1	2	3	4	5	6	7	8	9	10
Bank B	Delivery 1	0.8	0.7	0.7	0.8	0.9	0.7	0.8	0.8	0.9	0.8
	2	0.8	0.7	0.7	0.8	0.9	0.8	0.7	0.8	0.9	0.8
	3	0.8	0.6	0.7	0.8	0.9	0.7	0.8	0.8	0.9	0.8
Bank A	Delivery 1	0.8	0.8	0.8	0.8	1.0	0.8	0.8	0.9	0.9	1.0
	2	0.8	0.7	0.8	0.8	1.0	0.9	0.8	1.0	1.0	1.0
	3	0.8	0.7	0.8	0.8	1.0	0.9	0.9	1.0	0.9	0.9

Table 2. The mean deviations of the leaves (Banks B and A) for the 10 segments of the ‘open gap’ field delivered at the four principal orthogonal gantry angles.

Mean deviation of leaves (mm) from expected positions											
		Segment									
		1	2	3	4	5	6	7	8	9	10
Bank B	Gantry 0°	0.8	0.7	0.7	0.8	0.9	0.7	0.8	0.8	0.9	0.8
	90°	0.4	0.4	0.5	0.5	0.7	0.5	0.5	0.6	0.5	0.6
	180°	0.3	0.5	0.5	0.7	0.6	0.6	0.6	0.7	0.7	0.6
	270°	0.8	0.7	0.7	1.0	0.9	0.7	0.8	0.8	0.8	0.8
Bank A	Gantry 0°	0.8	0.8	0.8	0.8	1.0	0.8	0.8	0.9	0.9	1.0
	90°	0.4	0.4	0.5	0.5	0.7	0.5	0.5	0.5	0.6	0.4
	180°	0.4	0.5	0.6	0.7	0.6	0.6	0.7	0.6	0.7	0.7
	270°	0.8	0.7	0.8	0.8	0.8	0.7	0.8	0.7	0.8	0.8

Figure 1

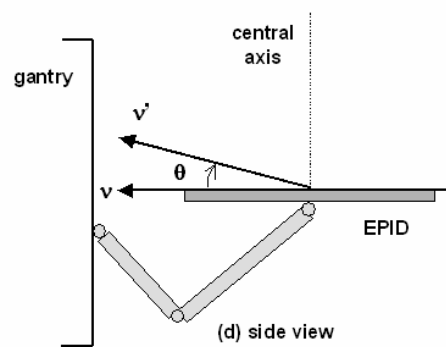
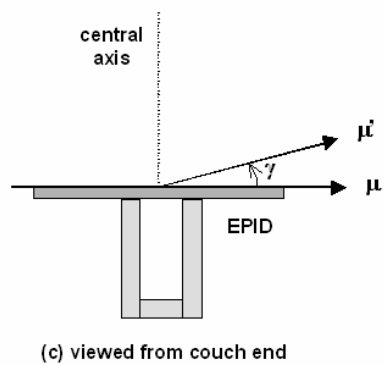
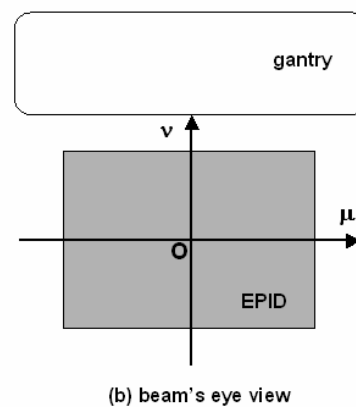
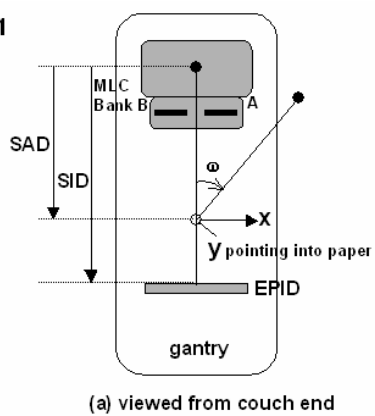


Figure 3

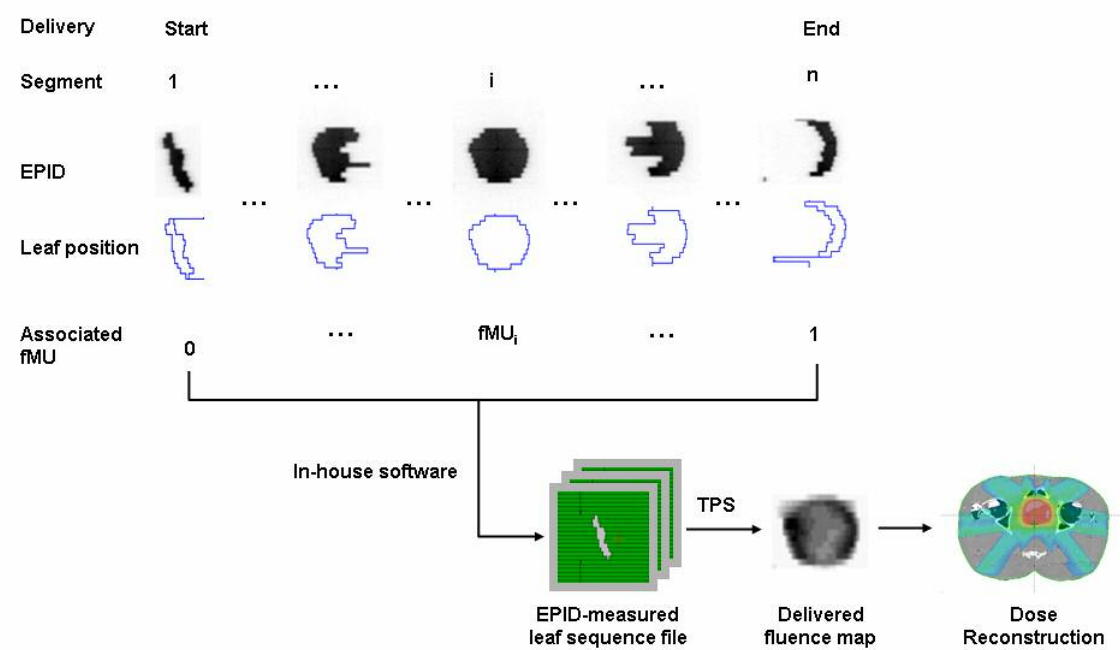


Figure 4

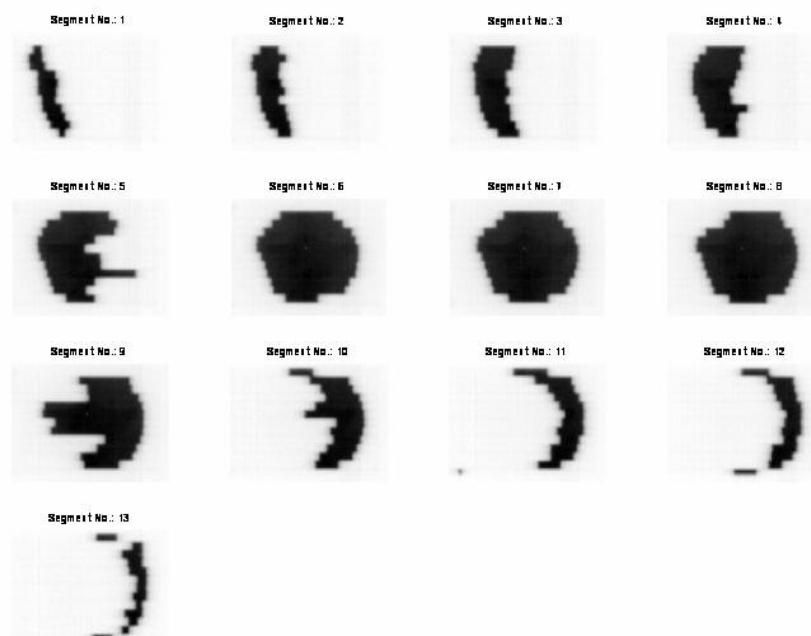


Figure 5

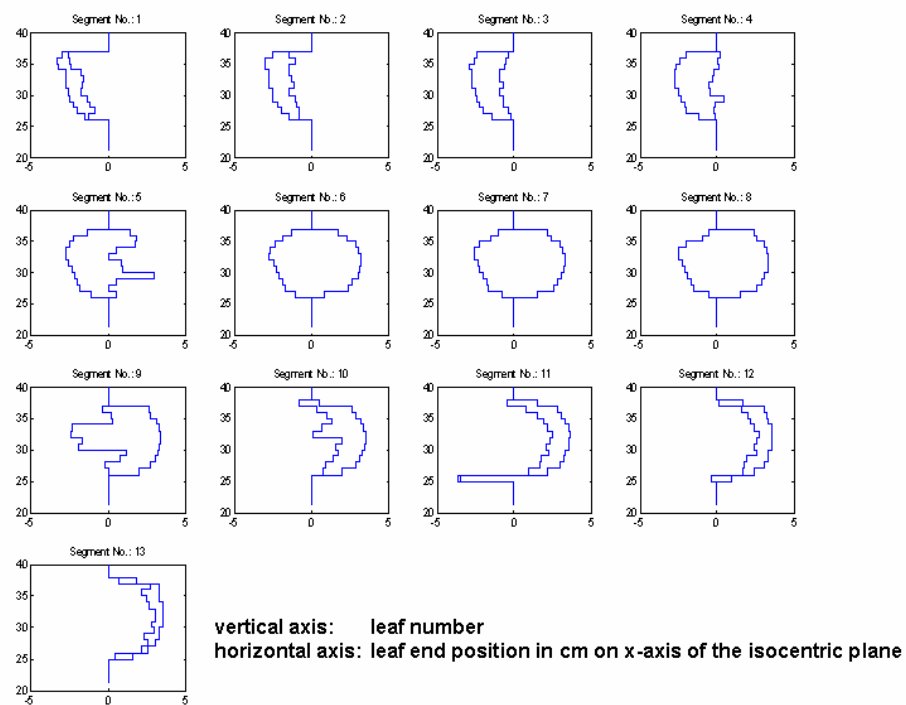


Figure 6

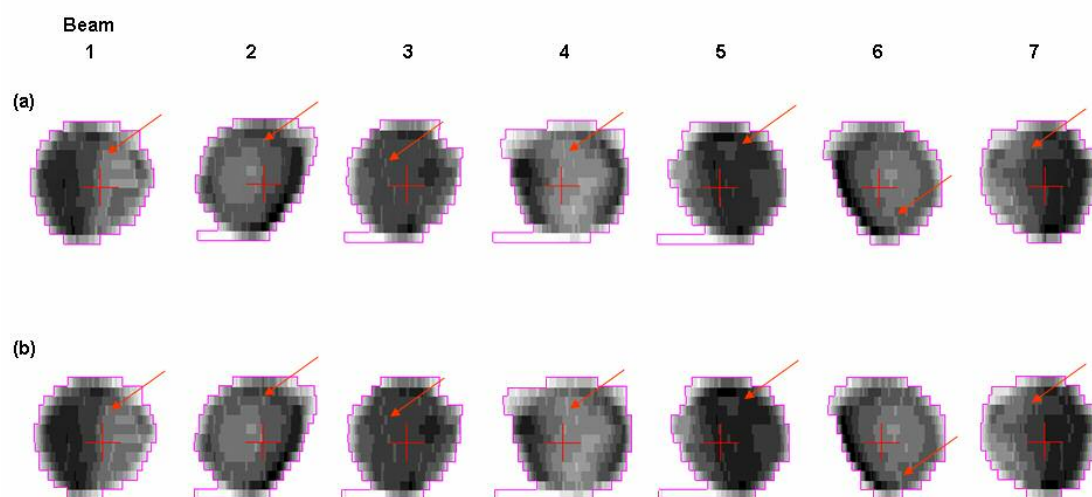
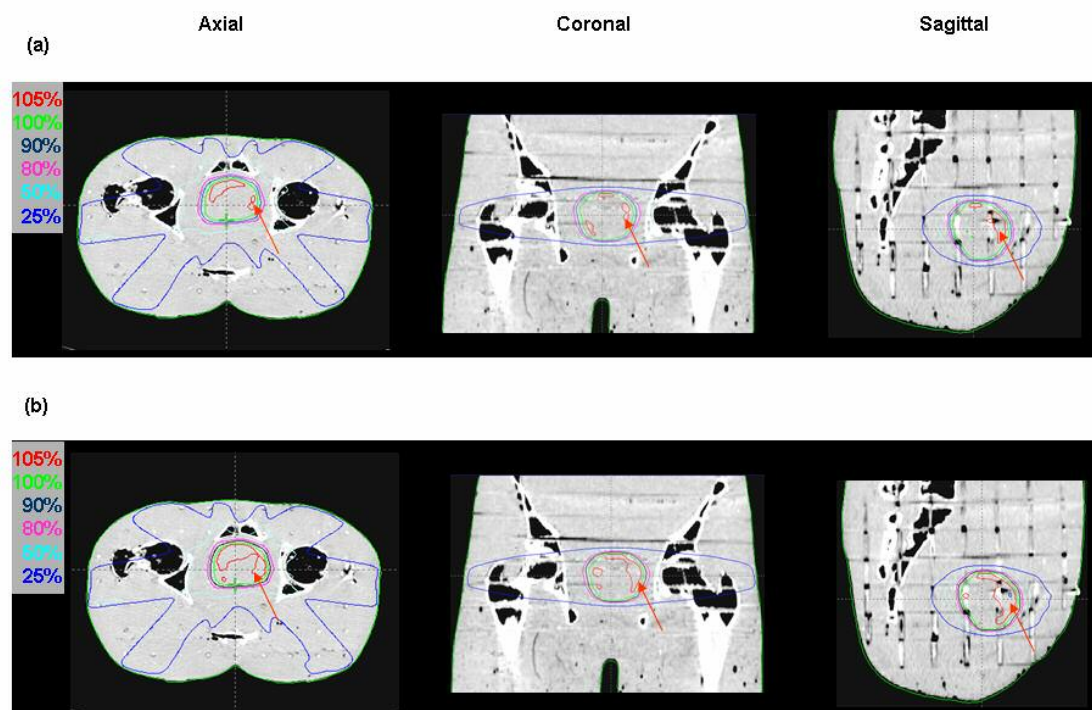


Figure 7





Dose reduction for kilovoltage cone-beam computed tomography in radiation therapy

Jing Wang ¹, Tianfang Li ², Zhengrong Liang³, Lei Xing ^{1, a}

¹ Department of Radiation Oncology
Stanford University School of Medicine, Stanford, CA 94305

² Department of Radiation Oncology
University of Pittsburgh Medical Center, Pittsburgh, PA 15901

³ Department of Radiology
State University of New York, Stony Brook, NY 11794

^{a)} Author to whom correspondence should be addressed:

Department of Radiation Oncology
Stanford University School of Medicine,
Clinical Cancer Center
875 Blake Wilbur Drive, Rm CC-G204
Stanford, CA 94305-5847
Telephone: (650) 498-7896
Fax: (650) 498-4015
Email: lei@reyes.stanford.edu

Short title: Dose reduction for CBCT

Abstract

Kilovoltage cone-beam computed tomography (kV-CBCT) has shown potentials to improve accuracy of patient setup in radiotherapy. However, daily and repeated use of CBCT will deliver high extra radiation doses to patients. One way to reduce the patient dose is to lower mAs when acquiring projection data. This, however, degrades the quality of low-mAs CBCT images dramatically due to excessive noises. In this work, we aim to improve the CBCT image quality from low mAs scans. Based on the measured noise properties of the sinogram, a penalized weighted least-squares (PWLS) objective function was constructed, and the ideal sinogram were then estimated by minimizing the PWLS objection function. To preserve the edge information in the projection data, an anisotropic penalty term was designed using the intensity difference between neighboring pixels. The effectiveness of the presented algorithm was demonstrated by two experimental phantom studies. Noise in the reconstructed CBCT image acquired with the low-mAs protocol was greatly suppressed after the proposed sinogram-domain image processing, without noticeable sacrifice of the spatial resolution.

Keywords: cone-beam CT, dose reduction, PWLS, anisotropic penalty

I. Introduction

Integration of the kilovoltage cone-beam computed tomography (kV-CBCT) with linear accelerator makes it possible to acquire high resolution volumetric image of a patient at treatment position. There is growing interests in using on-board kV-CBCT for patient treatment position setup and dose reconstruction in radiotherapy (Xing *et al.*, 2006; Yang *et al.* 2007; Lee *et al.* 2008). However, the repeated use of kV-CBCT during the course of a treatment has raised concerns of extra radiation dose delivered to patients (Brenner and Hall, 2007; Islam *et al.*, 2006; Wen *et al.*, 2007). It has been reported (Wen *et al.*, 2007) that the dose delivered from a Varian's kV-CBCT system with current clinical protocols is more than 3 cGy for central tissue and about 5 cGy for most of the peripheral tissues during an IMRT (intensity modulated radiation therapy) treatment course for prostate cancer. The extra radiation exposure to normal tissue during kV-CBCT will significantly increase the probability of stochastic risk of inducing cancer and genetic defects. Based on the ALARA (As Low As Reasonably Achievable) principle, the unwanted kV-CBCT dose should be minimized to fully realize its advantages of precise target localization during radiotherapy (Murphy *et al.*, 2007).

One way to reduce the radiation dose delivered to patients during kV-CBCT procedure is to acquire CT projection data with a lower mAs level (can be realized by reducing the tube current or pulse time). However, the image quality of the projection image and the reconstructed CBCT image will be degraded due to excessive quantum noise as a result of low mAs protocol. Conventionally, noise in CT is suppressed by using a low-pass filter to attenuate the high-frequency component of the projection data during reconstruction.

High frequency component contains information of both noise and edges, where a simple low-pass filter can not differentiate edge information from noise. Therefore, noise reduction using a low-pass filter will result in loss of edges, which is not desirable for CT imaging. Several edge-preserving filters (Hsieh, 1998; Kachelriess *et al.*, 2001; Zhong *et al.*, 2004) have been proposed to reduce noise in CT images based on local characteristics of the projection data elements. More recently, statistics-based image-domain (Li *et al.*, 2005a) and sinogram domain restoration algorithms (Li *et al.*, 2004; La Riviere, 2005; La Riviere and Billmire, 2005; Wang *et al.*, 2006) have shown advantages in noise reduction and edge preservation for low-dose fan-beam CT. In the mean time, noise properties of CT projection data have been under investigation (Li *et al.*, 2004; Whiting *et al.*, 2006) and the noise model of the sinogram data in Radon space (i.e., line integrals) has been validated by experimental studies (Wang *et al.*, 2008). In this work, we aim to improve low-dose CBCT image quality by reducing noise in CBCT sinogram before image reconstruction. The noise reduction algorithm incorporates the noise modeling of the CT sinogram data in Radon space (line integrals) to construct a penalized weighted least-squares (PWLS) objective function (FESSLER, 1994; Sukovic and Clinthorne, 2000). The ideal solution of the line integrals is then estimated by minimizing the PWLS objective function. The weighted least square is based on the first and second moments of the noise in the sinogram data and an anisotropic penalty is designed to preserve the edges in sinogram. CBCT images are reconstructed by using the FDK (FELDKAMP *et al.*, 1984) algorithm after all sinogram images are processed by PWLS criterion sequentially. The effectiveness of the PWLS-based noise reduction algorithm is demonstrated by two experimental phantom studies.

II. Methods and Materials

A. CBCT Sinogram Smoothing

Ideally, the line integral of attenuation coefficients can be calculated by

$$p_i = \ln \frac{N_{i0}}{N_i} \quad (1)$$

where N_{i0} and N_i are the incident photon number and detected photon number at detector bin i respectively. For the ease of presentation, we refer the measurement as photon number.

In a real X-ray CBCT system, the measured signal is total energy deposit on the flat-panel detector. In the following of this paper, we refer the value of p_i as the sinogram datum at detector bin i . Mathematically, the PWLS cost function in sinogram domain can be written as:

$$\Phi(p) = (\hat{y} - \hat{p})^T \Sigma^{-1} (\hat{y} - \hat{p}) + \beta R(p). \quad (2)$$

The first term in equation (2) is a weighted least-squares criterion, where \hat{y} is the vector of the measured sinogram data and \hat{p} is the vector of ideal sinogram data to be estimated. Symbol T denotes the transpose operator. The matrix Σ is diagonal matrix and its i th element is the variance of sinogram data at detector bin i . The second term in equation (2) is a smoothness penalty or *a priori* constraint, where β is the smoothing parameter which controls the degree of agreement between the estimated and the measured data.

The element of the diagonal matrix Σ is the variance of the corresponding sinogram datum and it determines the contribution of each sinogram datum to the cost function. Based on the sinogram noise modeling in (Li *et al.*, 2004) and (Wang *et al.*, 2008), the variance of the sinogram dataum can be estimated by:

$$\sigma_i^2 = \exp(p_i) / N_{i0}, \quad (3)$$

For a fixed incident photon number N_{i0} , a sinogram datum with a larger value will have a larger variance and therefore less contribution to the cost function since the weight of that measured datum is $1/\sigma_i^2$ as defined in (2). This can be understood by the following observation. A larger sinogram datum value p_i at detector bin i indicates less X-ray photons being detected, i.e., smaller N_i in equation (1), or more photons being attenuated along the projection path i . A detector bin receiving less photons will be associated with a smaller signal-to-noise ratio (SNR) based on the Poisson noise nature of the detected X-ray photons. Therefore, the weighted least-squares criterion reflects the above observation that the measured datum with a lower SNR will contribute less for estimation of its ideal sinogram datum.

To calculate the sinogram datum variance at detector bin i via equation (3), we need to estimate the incident photon number N_{i0} for calculation of the sinogram variance. The incident photon number is mainly determined by the protocols of tube current and duration of X-ray pulse (*i.e.* mAs). Ideally the incident X-ray flux from the tube would be calibrated as uniform as possible across the FOV, i.e., N_{i0} is a constant for all the detector bins. In reality, the X-ray flux is modulated to consider the concavity shape of the human body by the bow-tie attenuating filter prior to arrival at the patients. Therefore, the incident photon number will not be a constant across the FOV. To estimate the incident intensity over the FOV at a specific mAs level, we performed the air scan and then average the projection image over all projection view angles. Figure 1 shows the incident X-ray intensity with the tube current 80

mA and duration of pulse 10 ms. The incident X-ray intensity can then be used for estimation of sinogram data variance $\{\sigma_i^2\}$.

The penalty term in equation (2) is a prior or smoothing constraint, which encourages the equivalence between neighboring data elements. In (Li *et al.*, 2004; Wang *et al.*, 2006), a penalty of quadratic form with equal weights for all neighbors has been used for sinogram smoothing of fan-beam CT:

$$R(p) = \sum_n w_{in} (p_i - p_n)^2. \quad (4)$$

where n represents four nearest neighbors around pixel i and w_{in} is the weight for neighbor n . With an equal weight for the four nearest neighbors, these neighbors play equivalent role in constraining the solution. As such, it provides a uniform regularization without considering details of intensity variation and possibly presence of edges in the sinogram image. To preserve the edge information in the sinogram image of CBCT, we propose to use anisotropic weights for different neighbors in the sinogram image. The weight of the neighbor is determined by the magnitude of difference between neighbors and the concerned pixel. For a larger difference between the neighbor and the pixel, then coupling between them should be weaker and the weight w_{in} should be smaller. This form of the weight is chosen the same as the conducting coefficient in the well-known anisotropic diffusion filter (PERONA and MALIK, 1990):

$$w_{in} = \exp\left[-\left(\frac{p_i - p_n}{\delta}\right)^2\right]. \quad (5)$$

where the gradient determines the strength of the diffusion during each iteration and the parameter δ was chosen as the 90% of histogram of the gradient magnitude of the sinogram to be processed (PERONA and MALIK, 1990).

Minimization of the objective function (2) can be performed efficiently by iterative Gauss-Seidel updating strategy. The updating formula for solution of \hat{p} is given by:

$$p_i^{(k+1)} = \frac{y_i + \beta \sigma_i^2 \left(\sum_{n \in N_i^1} w_{in} p_n^{(k+1)} + \sum_{n \in N_i^2} w_{in} p_n^{(k)} \right)}{1 + \beta \sigma_i^2 \sum_{n \in N_i} w_{in}} \quad (6)$$

where index k represents iterative number, N_i^1 denotes those two nearest neighbors of i whose index is smaller than i , N_i^2 denotes those two nearest neighbors of i whose index is larger than i , and N_i denotes these four nearest neighbors of pixel i in the sinogram image. The initial of \hat{p} is given by the measured data \hat{y} .

B. On-board kV-CBCT

The cone-beam CT projection data was acquired by the ExactArms (kV source/detector arms) of a Trilogy™ treatment system (Varian Medical Systems, Palo Alto, CA). The number of projections for a full 360° rotation is around 634. The dimension of each acquired projection image 397 mm × 298 mm, containing 1024 × 768 pixels. The system has a field of view (FOV) of 25 cm × 25 cm (full-fan mode) in the transverse plane and 17 cm in the longitudinal direction, which can be increased to 45 cm × 45 cm in the transverse plane by shifting the detector laterally (half-fan mode).

Two phantoms were used to evaluate the performance of the proposed PWLS algorithm in this study. The first phantom is a commercial calibration phantom CatPhan® 600 (The Phantom Laboratory, Inc., Salem, NY). Details about the CatPhan® 600 phantom can be found in (Li *et al.*, 2005a). The second one is an anthropomorphic head phantom (see Figure 2). For each phantom, the X-ray tube current was set at 10 mA (low-dose) and 80 mA (high-dose) during acquisition of CBCT projection images. At both mA levels, the duration of the x-ray pulse at each projection view was 10 ms. The tube voltage was set to 125 kVp during all data acquisitions. After each sinogram acquired with low mAs protocol was processed by the PWLS algorithm described above, the CBCT image was reconstructed by the FDK algorithm. The voxel size in the reconstructed image is $0.5 \times 0.5 \times 0.5 \text{ mm}^3$.

III. Results

A. CatPhan® 600 phantom

We first tested the proposed algorithm on the CatPhan® 600 phantom. Several representative slices of the reconstructed CBCT are shown in Figures 3, 4 and 6. In each of these figures, (a) is the FDK reconstructed image from the projection data acquired with 10 mA tube current; (b) is the FDK reconstructed image from the sinogram processed by the proposed PWLS sinogram smoothing algorithm; and (c) is the FDK reconstructed image from the sinogram obtained with 80 mA tube current.

Figure 3 shows one slice of image contains a point-like object, which mimics a fiducial marker. In Figure 3 (a), the point source is difficult to be observed. After sinogram were processed by the PWLS algorithm, the reconstructed image (Figure 3(b)) is very similar to that of the one obtained with high mA protocol (Figure 3(c)). The point source was well-recovered and easy to be detected.

Figure 4 shows one slice of image contains several strips with different sizes and contrasts, which can be used to study the edge information in the reconstructed images. The CT image reconstructed from the PWLS processed sinogram is comparable to that obtained with 80 mA protocol in terms of detectability of the strips, see the ROI2 in figure 4(c). To show the difference between Figure 4 (a), (b) and (c), in Figure 5 we plotted horizontal profiles along the central strips (see ROI1 of Figure 4(c)). It can be observed that the edges are well preserved (compare profiles through Figure 3(b) and 3(c)) while noise is effectively suppressed (compare profiles through figure 3(a) and 3(b)).

To further quantitatively evaluate the effectiveness of the PWLS sinogram smoothing algorithm, we calculated the contrast to noise ratio (CNR) at different regions of interest (ROIs) in the images shown in Figure 6. The CNR is defined as:

$$CNR = \frac{|\mu_s - \mu_b|}{\sqrt{\sigma_s^2 + \sigma_b^2}} \quad (7)$$

where μ_s is the mean value of the signal and μ_b is the mean value of background. Four circular objects (indicated by arrows in Figure 6) with different intensities were chosen to calculate CNRs. Table I lists the CNRs of these five ROIs. After 10 mA sinogram were

processed by the PWLS algorithm, CNR in the reconstructed image improve significantly. It can be observed that the CNR of PWLS processed 10 mA image is comparable to that of the image acquired with 80 mA protocol.

Table I: CNRs of 4 ROIs in Figure 5.

	ROI1	ROI2	ROI3	ROI4	ROI5
80 mA	1.83	7.31	4.75	1.51	0.89
10 mA	0.82	2.70	1.68	0.49	0.36
PWLS 10 mA $\beta=0.05$	1.92	6.88	4.75	1.33	0.85

B. Anthropomorphic head phantom

Results of the anthropomorphic head phantom are shown in Figure 7. Figure 7 (a) shows one slice of the reconstructed images from projection data acquired with 10 mA protocol. Figure 7(c) shows the reconstructed image from PWLS processed 10 mA sinogram. Figure 7(d) shows the same slice of the image reconstructed from sinogram obtained with 80 mA. It can be observed that noise in 10 mA CT images is efficiently suppressed after the sinogram are processed by the PWLS algorithm. The processed low-dose CT (10 mA) image is very similar to that of its corresponding high-dose image (80 mA) by visual judgment. Standard deviation of the noise in a uniform ROI (as indicated by an arrow in Figure 7(d)) is 2.8×10^{-3} in low-dose (10mA) image and 0.951×10^{-3} in its corresponding high-dose image. After the low-dose sinogram is processed by the PWLS algorithm with smoothing parameter $\beta = 0.05$, the standard deviation of the same ROI is 0.955×10^{-3} , which is fairly close the noise level of the 80 mA image.

To further illustrate how the edge information is affected by the PWLS sinogram smoothing, in Figure 7(e) we show the difference image between Figure 7(a) and (c). In the difference image, random noise is dominant and no edge or structure can be observed. This indicates edge information is well preserved in the PWLS processed images.

IV. Discussion

Generally, noise reduction for CT imaging can be performed in three spaces: projection data (either before or after logarithmic transform), filtered projection data (before backprojection operation during reconstruction), and reconstructed CT images. During filtering and backprojection operation, the noise properties will change significantly. Then noise modeling, such as distribution of noise and variance of noise, is difficult in filtered projection data and reconstructed image. Therefore, in this work we chose to work on the log-transformed data to fully utilize the noise model of the projection data in Radon space (Li *et al.*, 2004; Wang *et al.*, 2008).

Accurate noise modeling of measurement is fundamentally important in statistics-based image processing algorithms. Meanwhile, the regularization term also plays an important role for the performance of the algorithm. In CT sinogram processing, a commonly used regularization takes a quadratic form with equal weights for neighbors of equal distance (La Riviere, 2005; La Riviere and Billmire, 2005; Li *et al.*, 2004; Wang *et al.*, 2006). Such quadratic penalty simply encourages the equivalence between neighbors without considering discontinuities in the image and may lead to over-smoothing around sharp edges or boundaries. In the presented algorithm, we proposed an anisotropic penalty to consider the

difference among neighbors. The idea was inspired by the well-known anisotropic diffusion filter (PERONA and MALIK, 1990), in which the gradient controls the strength of diffusion among neighbors. The coupling between neighbors should be smaller if the absolute value of difference between them is smaller and this kind of neighbor should contribute less to the solution of concerned pixel (see equation (6)). There are many choices that satisfy this behavior of weighting. In this work, the form the anisotropic weight was chosen the same as the conduction coefficients in the anisotropic diffusion filter (PERONA and MALIK, 1990). By such choice, the anisotropic quadratic form penalty discourages the equivalence among neighbors if the gradient between them is large, and the edges or boundaries in the image will be better preserved. This effect is similar to that of anisotropic coefficients in the diffusion filter.

In the presented method, the reconstruction of CT images was performed by analytical FDK algorithm for its speed and accuracy. During FDK reconstruction process, noise can also be suppressed by using low-pass filter. It has been reported (Li *et al.*, 2004; La Riviere, 2005) that statistics-based sinogram smoothing algorithm plus FBP reconstruction is superior to conventional low-pass filters for noise suppression of 2D fan-beam CT. In this work, we also reconstructed the CT image of the anthropomorphic head phantom using Hanning filter with cutoff at 80% Nyquist frequency, see Figure 7(b). It can be observed that image reconstructed from PWLS-processed sinogram is superior to the result of the Hanning filter in terms of noise suppression and structure preservation.

Similar to the cutoff frequency in the conventional low-pass filter during reconstruction, there is also a free parameter β in the presented method which controls the trade-off of the noise level and the structure preservation in reconstructed images. In this work the choice of β is determined by the visual judgment. The optimal choice of the parameter β can be determined by more sophisticated ways such as the received operating characteristic (ROC) study. Nevertheless, the parameter β can be chosen according to the noise level of the sinogram because from equation (6), the solution for the ideal sinogram, we can see that the parameter β and variance σ_i^2 is always coupled together. The noise level of the projection data is mainly determined by two factors: incident photon number and the line integrals. As such, the parameter β could be optimized at certain mAs level and treatment site for patients of similar size. In this work, however, the parameter is chosen empirically, which is justifiable when the dependence of the parameter on the noise level is weak.

The method presented in this paper is based on the noise properties of the sinogram and the smoothing constrain or penalty is applied in sinogram domain. Based on the same noise model, the smoothing constraint can also be applied on the CT image domain, and the statistical iterative reconstruction (SIR) algorithm can be used to obtain the attenuation coefficients map by minimizing the objective function. The SIR-based algorithms showed some advantages over conventional filtered backprojection method for multi-slice helical CT (Thibault *et al.*, 2007). However, an obstacle for practical use of the SIR is the computation burden, especially for large volume datasets of CBCT. It takes more than 10 hours to reconstruct typical volume of multi-slice helical CT using SIR (Thibault *et al.*, 2007). It takes only 3 seconds for the presented sinogram smoothing method to process one projection

image using a PC with 3.0 GHz CPU. Parallel computing can speed up both SIR and sinogram-based algorithms significantly using the Cell Broadband Engine (Knaup *et al.*, 2006) and PC cluster (Li *et al.*, 2005b). It is possible to achieve clinically acceptable time for the presented sinogram smoothing algorithm through parallel computation. It is an interesting research topic to quantitatively compare the performance of the SIR-based CBCT reconstruction algorithm and the statistics-based sinogram smoothing method.

When CBCT is used for patient setup and target localization during radiotherapy, some extra information may be taken into account for dose and noise reduction. For example, complete CT volume dataset with high clarity used for treatment planning is usually available before the treatment. This will provide strong *a priori* information of the patient before each CBCT scan. Prior information of planning 3D CT has been proved useful to improve image quality of 4D CBCT (Li *et al.*, 2007). It is expected that radiation dose of CBCT used for radiotherapy can be further reduced by incorporating the planning CT information into the image restoration or reconstruction algorithms.

In the report of the AAPM task group 75 (Murphy *et al.*, 2007), several dose reduction strategies for image-guided radiotherapy were discussed. For CBCT, dose reduction can be achieved by narrowing field of view to avoid delivering radiation to unnecessary region of patient (Murphy *et al.*, 2007). Compared with those hardware-based approaches, software approaches (such as the one proposed in this paper) provide a more cost-effective means for dose reduction of CBCT. In addition to the statistics-based reconstruction and restoration algorithms, advanced analytical CBCT reconstruction

algorithms (Leng *et al.*, 2007; Zhuang *et al.*, 2006; Zou and Pan, 2004; Zou *et al.*, 2005) may further improve low-dose CBCT image quality.

V. Conclusion

A PWLS algorithm with non-uniform weights was proposed to reduce noise in low-dose onboard CBCT. In this method, sinogram was first processed according to the PWLS criterion. The weight for each measurement was chosen as sinogram datum variance, where variance can be estimated accurately according to the sinogram noise model. To preserve edge information during noise reduction, we proposed an anisotropic quadratic form penalty. The quadratic form penalty encourages equivalence between neighbors and the anisotropic penalty provides the mechanism to control the influence of different neighbors according to its corresponding gradient. The effectiveness of the proposed method is demonstrated by two experimental phantom studies. The quality of the 10 mA CT image after its sinogram processed by the PWLS algorithm is comparable to the image obtained with 80 mA protocol. These experimental results indicate that it is possible to reduce CBCT radiation dose by a factor of 1/8 without loss of useful information for radiotherapy.

Acknowledgement

This work was supported in part by grants from the Department of Defense (PC040282) and National Cancer Institute (1R01 CA98523, CA104205 and CA082402).

Reference:

- Brenner D and Hall E 2007 Current concepts - Computed tomography - An increasing source of radiation exposure *NEW ENGL J MED* **357** 2277-84
- FELDKAMP L, DAVIS L and KRESS J 1984 PRACTICAL CONE-BEAM ALGORITHM *J OPT SOC AM A* **1** 612-9
- FESSLER J 1994 PENALIZED WEIGHTED LEAST-SQUARES IMAGE-RECONSTRUCTION FOR POSITRON EMISSION TOMOGRAPHY *IEEE T MED IMAGING* **13** 290-300
- Hsieh J 1998 Adaptive streak artifact reduction in computed tomography resulting from excessive x-ray photon noise *MED PHYS* **25** 2139-47
- Islam M, Purdie T, Norrlinger B, Alasti H, Moseley D, Sharpe M, Siewerdsen J and Jaffray D 2006 Patient dose from kilovoltage cone beam computed tomography imaging in radiation therapy *MED PHYS* **33** 1573-82
- Kachelriess M, Watzke O and Kalender W 2001 Generalized multi-dimensional adaptive filtering for conventional and spiral single-slice, multi-slice, and cone-beam CT *MED PHYS* **28** 475-90
- Knaup M, Kalender W A and Kachelriebe M 2006 Statistical Cone-Beam CT Image Reconstruction using the Cell Broadband Engine *IEEE Nuclear Science Symposium Conference Record* **5** 2837 - 40
- La Riviere P 2005 Penalized-likelihood sinogram smoothing for low-dose CT *MED PHYS* **32** 1676-83
- La Riviere P and Billmire D 2005 Reduction of noise-induced streak artifacts in X-ray computed tomography through spline-based penalized-likelihood sinogram smoothing *IEEE T MED IMAGING* **24** 105-11
- Lee L, Le Q, Xing L: Retrospective IMRT dose reconstruction based on cone-beam CT and MLC log-file. *International Journal of Radiation Oncology, Biology, Physics*, **70**, 634-644, 2008.
- Leng S, Zhuang T, Nett B and Chen G 2007 Helical cone-beam computed tomography image reconstruction algorithm for a tilted gantry with N-PI data acquisition *OPT ENG* **46** -
- Li T, Koong A and Xing L 2007 Enhanced 4D cone-beam CT with inter-phase motion model *MED PHYS* **34** 3688-95
- Li T, Li X, Wang J, Wen J, Lu H, Hsieh J and Liang Z 2004 Nonlinear sinogram smoothing for low-dose X-ray CT *IEEE T NUCL SCI* **51** 2505-13
- Li T, Schreibmann E, Thorndyke B, Tillman G, Boyer A, Koong A, Goodman K and Xing L 2005a Radiation dose reduction in four-dimensional computed tomography *MED PHYS* **32** 3650-60
- Li X, Ni J and Wang G 2005b Parallel iterative cone-beam CT image reconstruction on a PC cluster *Journal of X-Ray Sci. and Tech.* **13** 63-72
- Murphy M, Balter J, Balter S, BenComo J, Das I, Jiang S, Ma C, Olivera G, Rodebaugh R, Ruchala K, Shirato H and Yin F 2007 The management of imaging dose during image-guided radiotherapy: Report of the AAPM Task Group 75 *MED PHYS* **34** 4041-63
- PERONA P and MALIK J 1990 SCALE-SPACE AND EDGE-DETECTION USING ANISOTROPIC DIFFUSION *IEEE T PATTERN ANAL* **12** 629-39

- Sukovic P and Clinthorne N 2000 Penalized weighted least-squares image reconstruction for dual energy X-ray transmission tomography *IEEE T MED IMAGING* **19** 1075-81
- Thibault J B, Sauer K D, Bouman C A and Hsieh J 2007 A three-dimensional statistical approach to improved image quality for multislice helical CT *MED PHYS* **34** 4526-44
- Wang J, Li T, Lu H and Liang Z 2006 Penalized weighted least-squares approach to sinogram noise reduction and image reconstruction for low-dose X-ray computed tomography *IEEE T MED IMAGING* **25** 1272-83
- Wang J, Lu H, Eremina D, Zhang G, Zhang G, Wang S, Chen J, Manzione J and Liang Z 2008 An experimental study on the noise properties of X-ray CT sinogram data in the Radon space *Proc. SPIE Medical Imaging*
- Wen N, Guan H, Hammoud R, Pradhan D, Nurushev T, Li S and Movsas B 2007 Dose delivered from Varian's CBCT to patients receiving IMRT for prostate cancer *PHYS MED BIOL* **52** 2267-76
- Whiting B, Massoumzadeh P, Earl O, O'Sullivan J, Snyder D and Williamson J 2006 Properties of preprocessed sinogram data in x-ray computed tomography *MED PHYS* **33** 3290-303.
- Xing L, Thorndyke B, Schreibmann E, Yang Y, Li TF, Kim GY, Luxton G, Koong A: Overview of image-guided radiation therapy. *Medical Dosimetry*, **31**, 91-112, 2006.
- Yang Y, Schreibmann E, Li T, Wang C, Xing L: Evaluation of on-board kV cone beam CT (CBCT) based dose calculation. *Physics in Medical Biology*, **52**, 685-705, 2007.
- Zhong J, Ning R and Conover D 2004 Image denoising based on multiscale singularity detection for cone beam CT breast imaging *IEEE T MED IMAGING* **23** 696-703
- Zhuang T, Nett B, Leng S and Chen G 2006 A shift-invariant filtered backprojection (FBP) cone-beam reconstruction algorithm for the source trajectory of two concentric circles using an equal weighting scheme *PHYS MED BIOL* **51** 3189-210
- Zou Y and Pan X 2004 Exact image reconstruction on PI-lines from minimum data in helical cone-beam CT *PHYS MED BIOL* **49** 941-59
- Zou Y, Pan X and Sidky E 2005 Theory and algorithms for image reconstruction on chords and within regions of interest *J OPT SOC AM A* **22** 2372-84

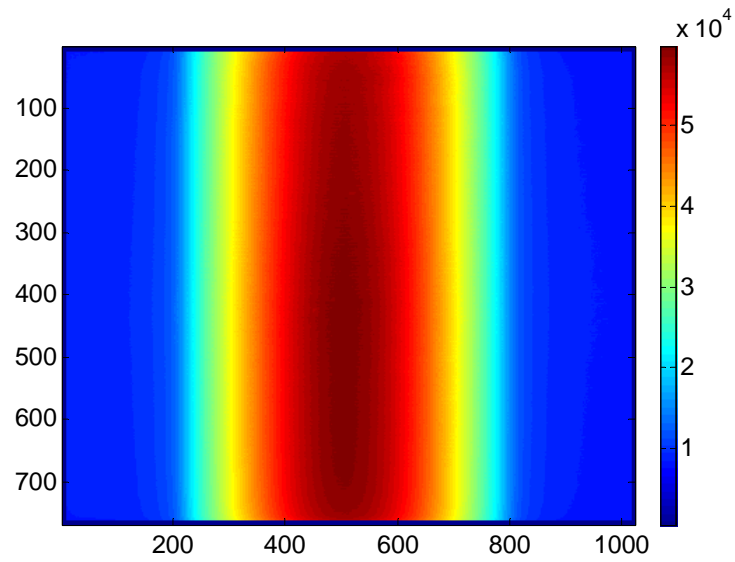


Figure 1: Incident X-ray intensities across the field of view with 80 mA tube current and 10 ms pulse time. Relative intensity is mainly caused by the bow-tie filter.

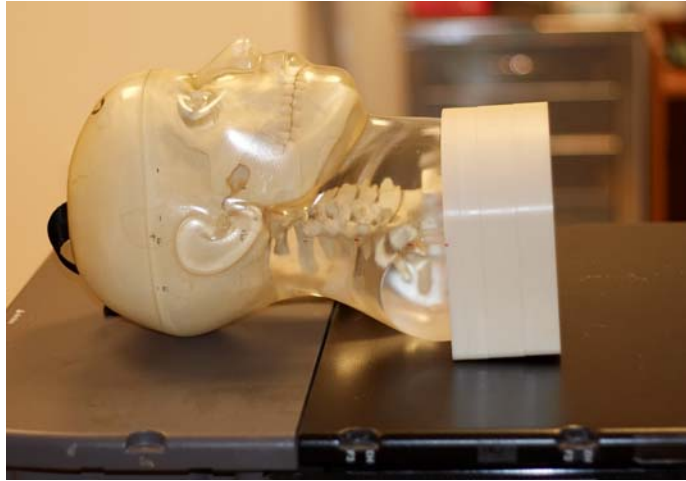


Figure 2: Illustration of the anthropomorphic head phantom used for evaluation the PWLS algorithm.

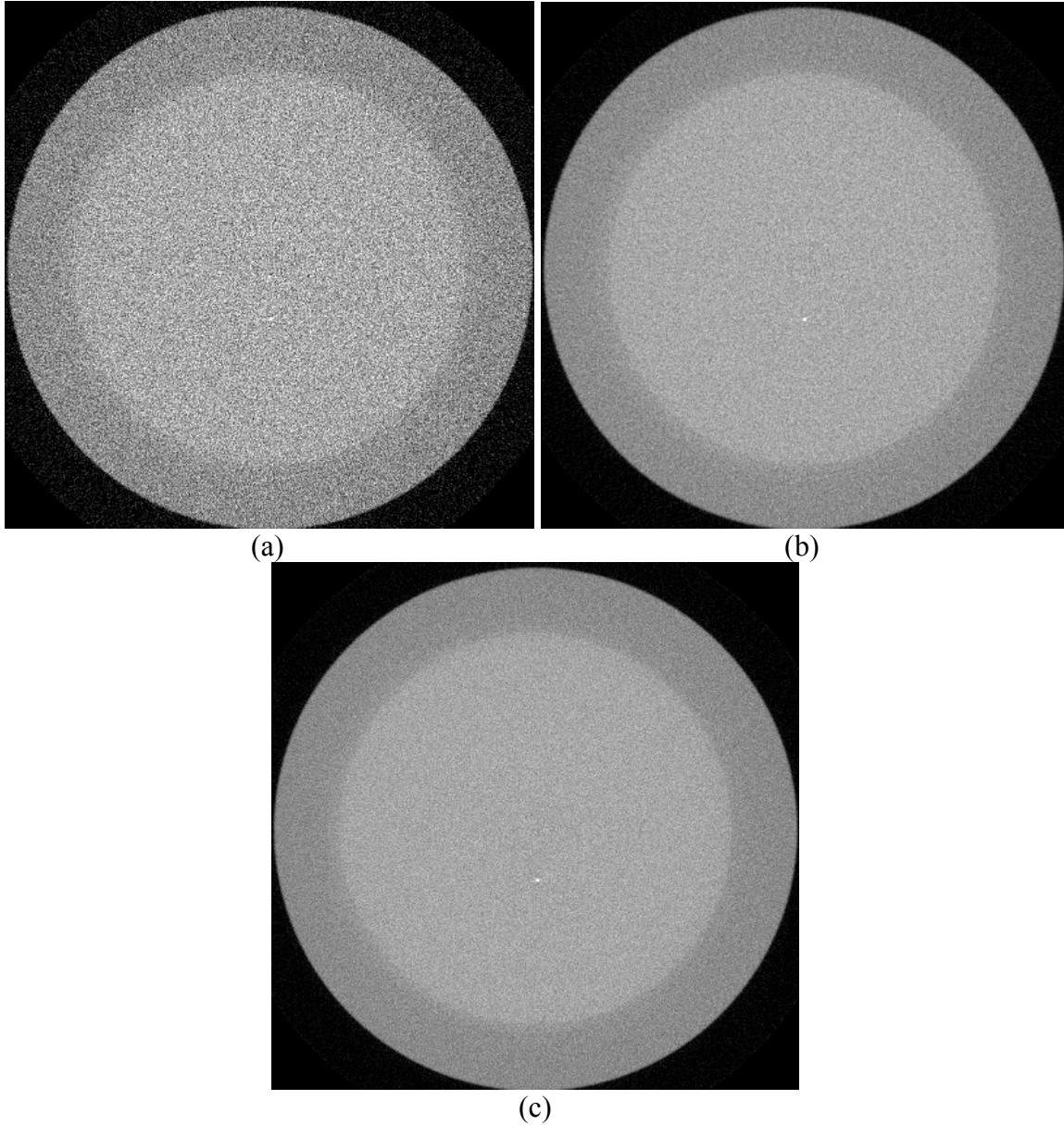


Figure 3: One slice of FDK reconstructed image of the CatPhan® 600 phantom containing a point-like object: (a) from projection images acquired with 10 mA tube current; (b) after sinogram acquired with 10 mA tube current are processed by the PWLS algorithm; and (c) from projection images acquired with 80 mA tube current.

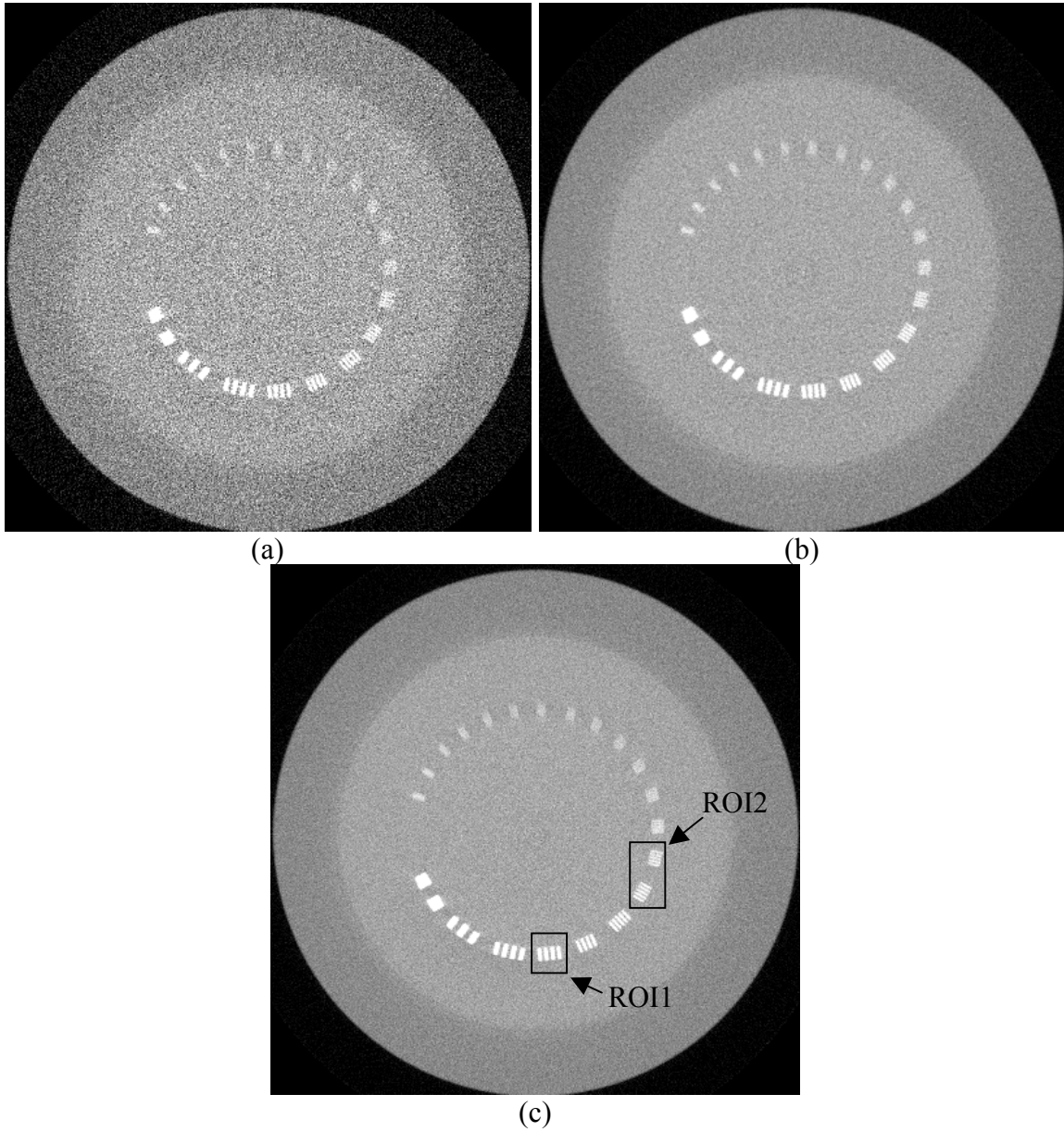


Figure 4: One slice of FDK reconstructed image of the CatPhan® 600 phantom containing several strips: (a) from projection images acquired with 10 mA tube current; (b) after sinogram acquired with 10 mA tube current are processed by the PWLS algorithm; and (c) from projection images acquired with 80 mA tube current.

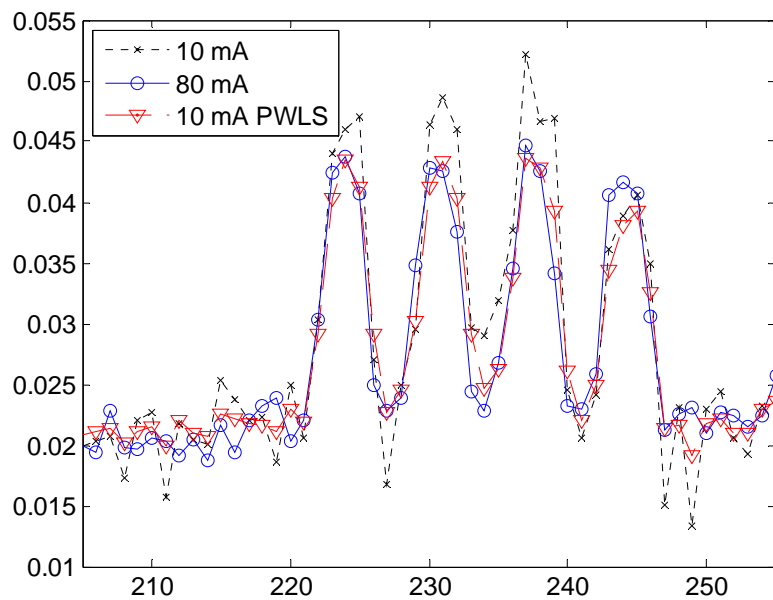


Figure 5: profiles through the central strips in Figure 4 (indicated by ROI1).

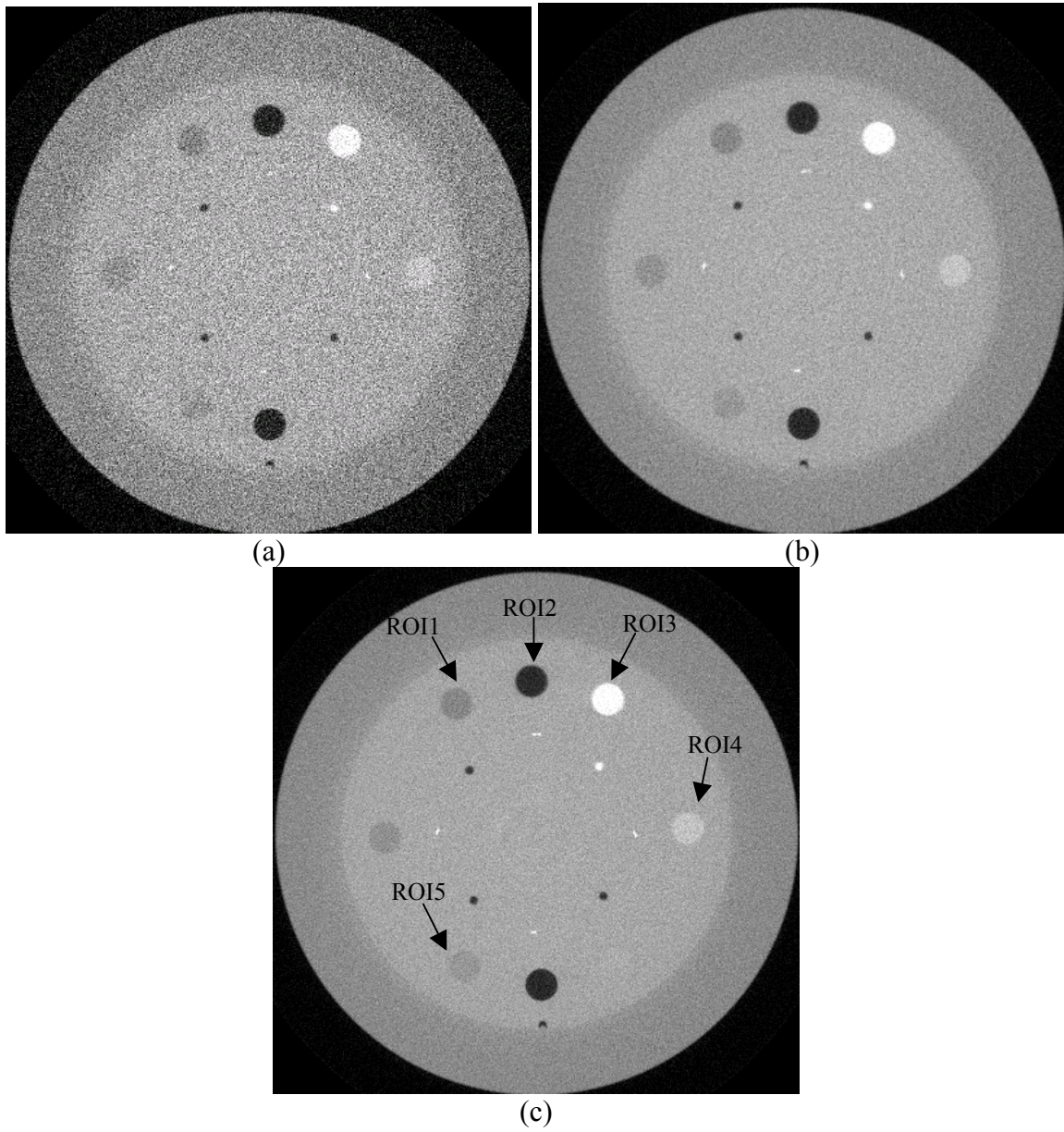


Figure 6: One slice of FDK reconstructed image of the CatPhan® 600 phantom containing several circular objects with different intensities: (a) from projection images acquired with 10 mA tube current; (b) after sinogram acquired with 10 mA tube current are processed by the PWLS algorithm; and (c) from projection images acquired with 80 mA tube current.

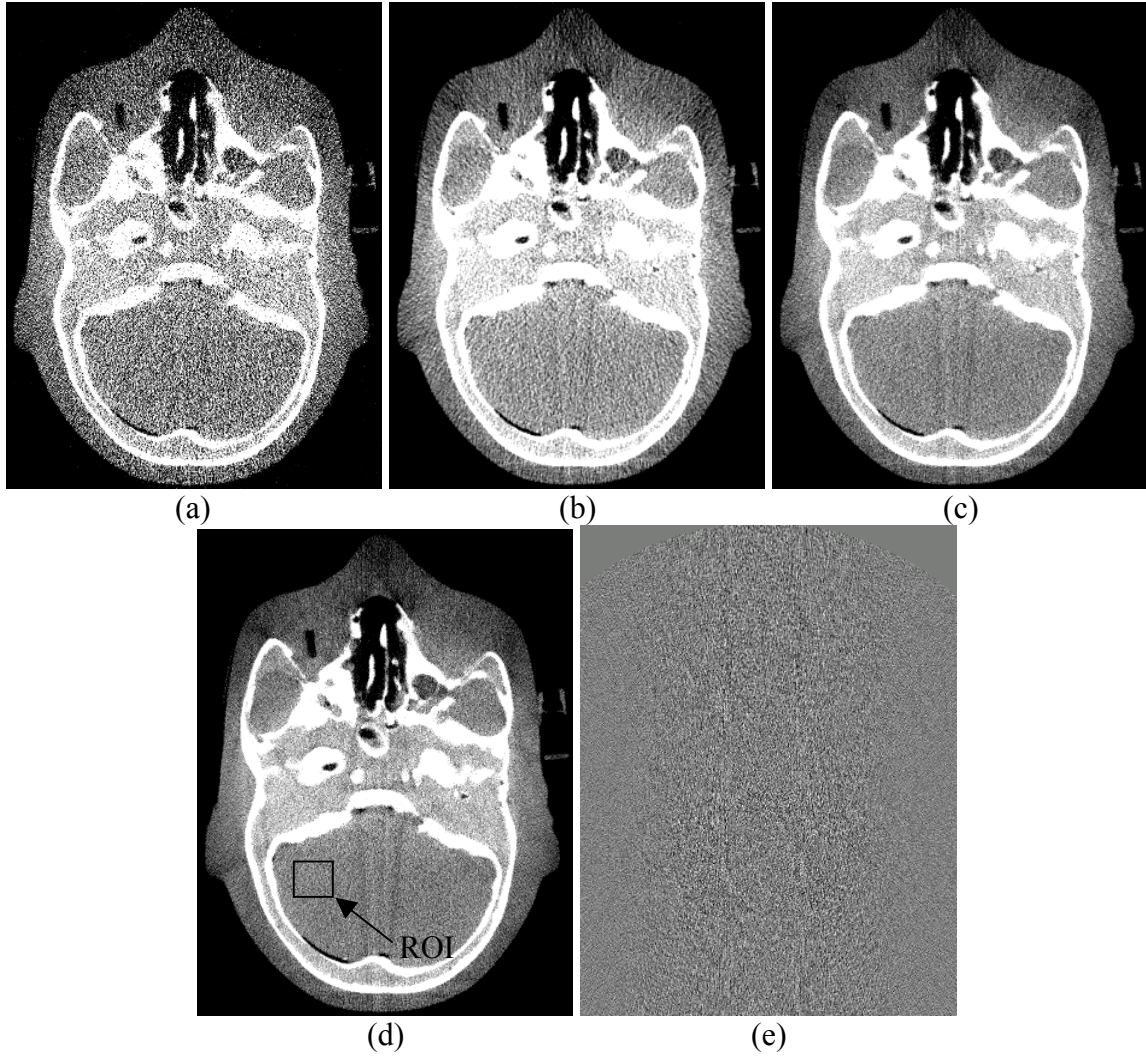


Figure 7: One slice of FDK reconstructed image of the anthropomorphic head phantom: (a) from projection images acquired with 10 mA tube current; (b) using low-pass Hanning filter with cutoff 80% Nyquist frequency; (c) after sinogram acquired with 10 mA tube current are processed by the PWLS algorithm; (d) from projection images acquired with 80 mA tube current; and (e) difference image between (d) and (c).